Development of Electronically Tuned Nanomaterials for Electrocatalysis

A thesis submitted for the degree of

Doctor of Philosophy

By

Abhisek Majumdar

Department of Physics

Indian Institute of Technology Guwahati

Guwahati-781039, India

August 2022

Department of Physics
Indian Institute of Technology Guwahati
Guwahati-781039, India

Declaration

I hereby declare that the thesis work "**Development of Electronically Tuned Nanomaterials for Electrocatalysis**" has been completely carried out by me at the Department of Physics, Indian Institute of Technology Guwahati under the supervision of **Dr Uday Narayan Maiti** and no part of this work has been submitted elsewhere for the award of any degree.

Abhisek Majumdar

Abhisek Majumdar

Roll No.- 166121014
Senior Research Fellow
Department of Physics
Indian Institute of Technology Guwahati
Guwahati-781039, India

Department of Physics
Indian Institute of Technology Guwahati
Guwahati-781039, India

Certificate

This is to certify that the work contained in the thesis "**Development of Electronically Tuned Nanomaterials for Electrocatalysis**" has been completely carried out by **Mr Abhisek Majumdar** at the Department of Physics, Indian Institute of Technology Guwahati. Neither the entire work nor any part of it has been submitted elsewhere for the award of any degree.

Dr. Uday Narayan Maiti

Associate professor
Department of Physics
Indian Institute of Technology Guwahati
Guwahati-781039, India

Acknowledgement

To me, a PhD is a beautiful journey where I gain a lot of knowledge and experience regarding research work and life. During this journey, there were lots of ups and down. However, a bunch of people helped me to overcome those periods, for which I'm extremely grateful to them.

First, I would like to show my sincere gratitude to my supervisor Dr Uday Narayan Maiti, for his immense guidance, continuous support and encouragement with valuable suggestions throughout my PhD journey. He has helped me a lot to grow my scientific knowledge. I admire his deep knowledge, passion and dedication to his work. I am very much thankful to him for giving me the opportunity to work under his supervision and for providing the necessary laboratory facilities. It has been a great experience working under him, and this thesis work would not have been possible without his constant support.

I express my gratitude to my doctoral committee members, Prof. Subhradip Ghosh, Prof. Dilip Pal and Dr Nageswara Rao Peela, for their valuable suggestions, constructive comments and timely review of my work throughout the PhD journey, which immensely help me to enrich my thesis work.

I would also like to thank the Head of the Department of Physics, IIT Guwahati and Central Instrument Facilities (CIF) for providing laboratory and required instrumental facilities to carry out my thesis work. I sincerely appreciate all the faculty members, technical/ scientific officer, non-teaching staff of the Physics department and all the members of CIF for their support and cooperation. I'm also thankful to IIT Guwahati for providing an institute fellowship for the financial assistantship during my PhD period.

I'm thankful to Dr Yongtak Oh from Korea Institute of Science and Technology, Prof. Sang Ouk Kim from Korea Advanced Institute of Science & Technology, Dr Debasis Ghosh from JAIN University, Dr Sambhu Nath Jha and Dr Shilpa Tripathi from Raja Ramanna Centre for Advanced Technology for providing instrumental facility and insightful suggestions. I would also like to acknowledge Pronoy Dutta and Golam Masud Karim from IIT Guwahati for conducting my theoretical calculations.

I am extremely fortunate to have a wonderful laboratory research environment because of selfless research assistance, good company, and constant support from my past and present lab mates. For that, I am highly grateful to Dr Anirban Sikdar, Pronoy, Golam, Sujit, Amalika, Dr Munu Borah, Snehasish, Priyam and Pranab. I would also like to mention my dear friends at IITG, Suman, Lopamudra, Kajal, Dibyendu, Sayandeep, with whom I have had some wonderful times. I would also like to show appreciation to some joyful persons I have met at

IITG, Sayan da, Sovan da and Charu sir. Special appreciation to my childhood friends Soumalya, Sushmita, Bittu, Chinmoy, Anamika, Deepsikha.

I want to express my deepest gratitude to all my family members specially my father, Jyotish Majumdar and mother, Arati Majumdar, because of their selfless love, blessing and support. I am very much grateful to my sister Tanushree di, brother-in-law Biplab da and my little nephew Trinabha for his innocent activities, which always put a smile on me. I am blessed to have Subhasree in my life for love and support in my ups and downs. Thank you for being there with patience and tolerating me during my bad periods. Finally, I would like to thank each and everyone who have helped me in any possible way during my PhD time but forgot to mention them here.

Abhisek Majumdar
IIT Guwahati

Contents

Chapter 4: Microwave Induced Rapid Surface Amorphization of Metal Oxide Nanowire into Sulfides Shell: A New Design Strategy for Electronically Modulated Efficient Hydrogen Evolution Catalyst

Chapter 5: Microwave Induced Rapid Recrystallization process for Universal Development of Metal Chalcogenides and Phosphides Towards Outstanding Oxygen Evolution Reaction

Chapter 6: Summary and Outlook

Abstract

A green energy-dependent sustainable future can be promised by converting and storing renewable energies in terms of chemical fuels like hydrogen through electrochemical water splitting. However, the requirements of high overpotential to overcome the energy barriers of both hydrogen and oxygen evolution reactions (HER & OER) restrict the overall efficiency of hydrogen generation by electrocatalysis of water. Noble metal based electrocatalysts (platinum, iridium, ruthenium) have been believed as ideal electrocatalysts due to their high activity, selectivity and optimal adsorption ability for HER, OER reaction intermediates. However, their high cost and scarcity compelled scientists to search for new, cost-effective and simple strategies for the development of efficient electrocatalysts. In this regard, rational design of heterostructures and anchoring single-atom catalysts (SAC) on adequate support are the two successful strategies to lower the overpotentials for HER and OER processes. Though substantial work has been presented in the literature based on efficient heterostructure and SAC development, the used conventional methods are extremely time-consuming, energy inefficient and complex. In addition, high quality atomistic interfacing in heterostructure development is difficult to realize due to the multi-step process requirement of the conventional strategies. Stabilization of SACs over a proper support is also very challenging yet important to synergistically enhance catalytic activity of the system specially in the dynamic OER environment where usually reconstruction of the catalyst happens. These challenges drastically reduce the efficiency of the catalysts and increase the required overpotential for HER and OER and thus realization of catalysts with high current density for practical application become very difficult. Therefore, for practical adaptation of these catalysts we need to focus not only on the optimization of performances but also in new technologies to do the processing of the catalyst at low cost. The current thesis thoroughly addresses the described challenges by inventing radically new processes for the development of heterostructures and SACs and by providing theoretical understanding of synergistic electronic coupling for the enhancement of catalytic activity. For instance, atomic interfacing between molybdenum selenide ($MoSe_2$) and nickel cobalt selenide ($NiCo_2Se_4$) has been achieved by selenization induced dealloying process. This results in vertical orientation of inter-spaced $MoSe_2$ on conducting $NiCo_2Se_4$ support which drastically enhances the HER catalytic activity due to its unique structural configuration and synergistic heterostructure formation as confirmed from density functional theory (DFT) thus requires only overpotential of 89 mV to get a current density 10 mA cm^{-2}, and a Tafel slope of 65 mV dec^{-1}. Further, interfacing between crystalline and amorphous structure has been

presented here to achieve an advanced crystalline-amorphous core-shell heterostructure of amorphous molybdenum sulfide (a-MoS_x) and crystalline molybdenum tungsten oxide (MoWO) via microwave induced rapid surface amorphization process. From the DFT analysis we found that the core not only provides sufficient conductivity and increases the HER activity of the active site of amorphous a-MoS_x but also substantially increases the number of HER active sites. This results in excellent catalytic activity for HER and exhibits an overpotential of 136 mV at 10 mA cm^{-2} in the acid electrolyte, which is much lower than the overpotential of parent oxide (356 mV) and its fully sulfurized crystalline counterpart (163 mV), and the same catalyst can be extended to operate in various pH conditions as well. In addition, we have realized a rapid and energy efficient recrystallization strategy based on microwave irradiation for the universal development of nickel-iron based chalcogenide and phosphides. This strategy results in biphasic structure of iron doped Ni_3S_2/NiS which shows exceptionally high OER activity requiring only 187 mV for 10 mA cm^{-2} and commercial level current density of 500 mA cm^{-2} at 289 mV. The comprehensive analysis indicates the phase evolution of NiS to amorphous Ni-(oxy)hydroxide during OER process to generate iron doped Ni_3S_2/NiOOH heterostructure is the reason for its high activity. Furthermore, single atom iridium has been photochemically decorated on the surface of $MoSe_2$@$NiCo_2Se_4$ heterostructure which on electrochemical surface reconstruction displays outstanding OER activity, requiring only 200 mV overpotentials for 10 mA cm^{-2}. A series of post-OER characterizations have been done to understand how iridium single atoms stabilize over the surface of base material and the structure realized from these findings has been used in DFT to understand the origin of high activity of this catalyst. We believe, this present thesis work will provide a new direction for the development of electrocatalysts via new efficient strategies and lay the platform for the development of highly active practical electrocatalysts not only in water electrolysis application but also in diverse fields like sea water splitting, fuel cell and metal-air batteries.

List of Abbreviations

HER	Hydrogen evolution reaction
OER	Oxygen evolution reaction
SAC	Single atom catalyst
GO	Graphene oxide
RGO	Reduced graphene oxide
SCE	Saturated calomel electrode
LSV	Linear sweep voltammetry
CV	Cyclic voltammetry
EIS	Electrochemical impedance spectroscopy
EDAX	Energy dispersive X-ray spectroscopy
FESEM	Field emission scanning electron microscopy
FETEM	Field emission transmission electron microscopy
HRTEM	High resolution transmission electron microscopy
STEM	Scanning transmission electron microscopy
XRD	X–ray diffraction
XPS	X–ray photoelectron spectroscopy
XAS	X-ray absorption spectroscopy
XANES	X-ray absorption near edge structure
EXAFS	Extended X-ray absorption fine structure

List of publications

Journal publications

1. A. Majumdar, P. Dutta, A. Sikdar, H. Lee, D. Ghosh, S. N. Jha, S. Tripathi, Y. Oh, U. N. Maiti, "Impact of Atomic Rearrangement and Single Atom Stabilization on MoSe2@NiCo2Se4 Heterostructure Catalyst for Efficient Overall Water Splitting", Small, 2022, 18, 2200622.

2. A. Majumdar, G. M. Karim, P. Dutta, H. Lee, S. K. Deb, A. Sikdar, Y. Oh, U. N. Maiti, "Microwave Induced Rapid Surface Amorphization of Metal Oxide Nanowire into Sulfides Shell for Electronically Modulated Efficient Hydrogen Evolution Catalyst", Catalysis Today, https://doi.org/10.1016/j.cattod.2022.11.023

3. A. Majumdar, P. Dutta, Y. Kang, G. M. Karim, S. K. Deb, U. N. Maiti, S. O. Kim "Energy-efficient Recrystallization and Generic Phase Evolution in Seconds for the Design of Highly Efficient Oxygen Evolution Catalysts", Applied Surface Science, https://doi.org/10.1016/j.apsusc.2023.156622

4. A. Sikdar, A. Majumdar, A. Gogoi, P. Dutta, M. Borah, S. Maiti, C. Gogoi, K. A. Reddy, Y. Oh, U. N. Maiti, "Diffusion driven nanostructuring of metal-organic frameworks (MOFs) for graphene hydrogel based tunable heterostructures: Highly active electrocatalyst for efficient water oxidation", J. Mater. Chem A, 2021, 9, 7640-7649.

5. M. Borah, A. Sikdar, S. Kapse, A. Majumdar, P. Dutta, G. M. Karim, S. K. Deb, R. Thapa, U. N. Maiti, "Stable and boosted oxygen evolution efficiency of mixed metal oxide and borate planner heterostructure over heteroatom (N) doped electrochemically exfoliated graphite foam", Catal. Today, 2021, 370, 83-92.

6. A. Sikdar, A. Majumdar, P. Dutta, M. Borah, S. O. Kim, U. N. Maiti, "Ultra-large area graphene hybrid hydrogel for customized performance supercapacitors: High volumetric, areal energy density and potential wearability", Electrochimica Acta, 2020, 332, 135492.

7. P. Dutta, A. Sikdar, A. Majumdar, M. Borah, N. Padma, S. Ghosh, U. N. Maiti, "Graphene aided gelation of MXene with oxidation protected surface for supercapacitor electrodes with excellent gravimetric performance", Carbon, 2020, 169, 225.

8. A. Sikdar, S. K. Deb, A. Gogoi, A. Majumdar, P. Dutta, K. Anki Reddy, U. N. Maiti, "Polyaniline-Graphene Hydrogel Hybrids via Diffusion Controlled Surface Polymerization for High Performance Supercapacitor", ACS Appl. Nano Mater. 2020, 3, 12, 12278.

9. A. Sikdar, P. Dutta, S. K. Deb, A. Majumdar, N. Padma, S. Ghosh, U. N. Maiti, "Spontaneous three-dimensional self-assembly of MXene and graphene for impressive energy and rate performance pseudocapacitors", Electrochimica Acta, 2021, 391, 138959.

10. P. Dutta, A. Patra, S. K. Deb, A. Sikdar, A. Majumdar, G. M. Karim, U. N. Maiti, "Freestanding MXene-hydrogels prepared via critical density-controlled self-assembly: high-performance energy storage with ultrahigh capacitive vs. diffusion-limited contribution", Journal of Materials Chemistry A, 2021, 9, 25013-25023.

11. P. Dutta, S. K. Deb, A. Patra, A. Majumdar, G. M. Karim, C. K. Parashar, M. K. Mohanta, M. Qureshi, U. N. Maiti, "Electric Field Guided Fast and Oriented Assembly of MXene into Scalable Pristine Hydrogels for Customized Energy Storage and Water Evaporation Applications", Advanced Functional Materials, 2022, 2204622

12. G. M. Karim, P. Dutta, A. Majumdar, A. Patra, S. K. Deb, S. Das, N. V. Dambhare, A. K. Rath, U. N. Maiti, "Ultra-fast electro-reduction and activation of graphene for high energy density wearable supercapacitor asymmetrically designed with MXene", Carbon, 2023, 203, 191-201.

Works presented in conference

1. Abhisek Majumdar, Uday Narayan Maiti, "Topotactic Chemical Conversion of Nanowire Based Bimetallic Leafy Structure for Excellent Hydrogen Evolution Catalysis", International Conference on Optoelectronic and Nano Materials for Advanced Technology (ICONMAT-2019), January 3-5, 2019, CUSAT, Kochi, India.

2. Abhisek Majumdar, Uday Narayan Maiti, "Electronically Modified CoNiS Cactus Like Structure for Highly Efficient Hydrogen Evolution Reaction", International Conference on Nano Science and Technology (ICONSAT-2020), March 5-7, 2020, S.N. Bose National Centre for Basic Sciences, Kolkata, India.

Chapter 1

Introduction

Chapter 1

Introduction

1.1 Introduction

Rapid exhaustion of fossil reservoirs, growing environmental pollution, and ever-rising energy demands due to technological advancement and population outbursts have compelled scientists to explore more clean and renewable energies like solar, wind and geothermal energies.[1] But, the intermittence of these energy sources forces everyone to utilize them at a particular time in the day and season. In addition, the amount of energy generated by renewable energy sources in a short amount of time is also very low to meet the requirement of today's application. Thus, it is extremely essential to store the energies from renewable sources at their peak time and use them according to the requirement. Storing renewable energies in terms of chemical fuels like hydrogen is an excellent strategy to overcome the challenges due to its large specific energy density, excellent energy conversion productivity and zero carbon dioxide emission ability.[2] Electrochemical water splitting has attracted much attention for generating hydrogen fuel (H_2) in a very simple process. Thus, combining renewable energy sources with an easy electrochemical water splitting process can bring a sustainable way to meet the future energy demand and replace fossil fuels.

Water electrolysis is a combination of hydrogen evolution reaction (HER) at cathode and oxygen evolution reaction (OER) at anode.[3] Nevertheless, the efficiency of this process is largely reliant on the catalytic capabilities of the cathode and anode materials. Presently state-of-the-art electrocatalysts for HER and OER are noble metals Pt, Ir and Ru-based catalysts because they possess high catalytic activity and exceptional durability.[4,5] But, the high price and rarity of these precious materials limit their use in large-scale implementation of water splitting process. Hence, efforts are being made to lower the utilization of noble metals while preserving the high catalytic performance of future electrocatalysts. In this direction, decreasing the catalyst's size to single-atom catalysts (SAC) for improving the catalytic activity and selectivity through higher exposed active sites and modified electronic structure has drawn a lot of attraction.[6,7] In a parallel way, researchers are also exploring highly efficient and earth-abundant non-noble metal-based electrocatalysts for both HER & OER.[8,9]

This chapter emphasizes on brief outlook on the major aspect of energy conversion through the electrocatalytic water splitting process. Recent advances in transitional metal-

based catalysts and single-atom catalyst development with efficient available strategies are also summarized. Current challenges to develop efficient electrocatalyst has been incorporated. A brief characterization technique for efficient electrolysis of water is also included. At the end of this chapter, the motivation and objectives of this thesis work have also been discussed.

1.2 Fundamentals of electrocatalysis of water

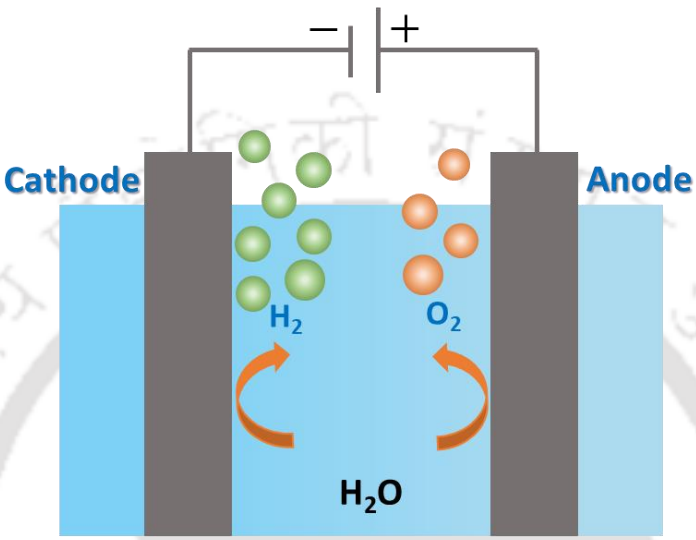

Figure 1.1. Representation of an electrolytic cell containing cathode, anode & electrolyte

Figure 1.1 shows a typical electrolysis cell consisting of a cathode, anode and electrolyte for the electrocatalysis of water. On applying an external potential between cathode and anode, two half-reactions occur: HER & OER at cathode and anode respectively. Based on the pH of the solution, the overall water electrolysis process can be expressed as,[10]

Overall reaction	$2H_2O \rightarrow 2H_2 + O_2$	1.1
In acidic solution		
Cathode	$2H^+ + 2e^- \rightarrow H_2$	1.2
Anode	$2H_2O \rightarrow O_2 + 4H^+ + 4e^-$	1.3
In alkaline solution		
Cathode	$2H_2O + 2e^- \rightarrow H_2 + 2OH^-$	1.4
Anode	$4OH^- \rightarrow O_2 + 2H_2O + 4e^-$	1.5

Overall water splitting at 25˚ C and 1 atm, irrespective of the pH of the electrolyte, requires a thermodynamic voltage of 1.23 V. However, in practice, extra potential on the cell is required for a successful water splitting process, and the operational potential can be expressed as,

$$V_{op} = 1.23\,V + \eta_a + |\,\eta_c\,| + \eta_{IR} \qquad 1.6$$

Where, η_{IR} corresponds to the internal resistance of the cell consisting of contact resistance and solution resistance and thus can be reduced by modifying the electrolyzer cell design. η_a and $|\,\eta_c\,|$ are the extra potential that is required to address the intrinsic energy hurdle of anode and cathode. This hurdle can be substantially lowered by utilizing highly active electrocatalysts.

1.2.1 Hydrogen Evolution Reaction

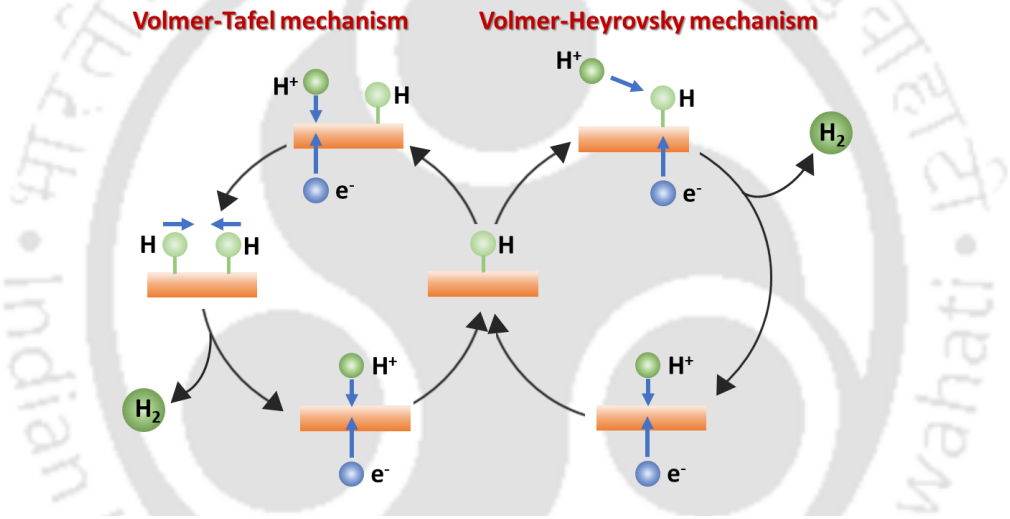

Figure 1.2. HER mechanism on the electrode surface in acidic electrolyte

HER is a two-electron transfer process taking place on cathode surface and comprises three elementary steps known as Volmer reaction followed by either Heyrovsky reaction or Tafel reaction. In Volmer reaction, a proton is adsorbed over the surface of cathode by combining an electron to produce adsorbed hydrogen intermediate (H_{ads}) as shown in Figure 1.2. Then this adsorbed hydrogen couples with another proton/water molecule and an electron simultaneously to produce hydrogen molecule in Heyrovsky reaction. Instead of Heyrovsky reaction two nearby adsorbed hydrogens can also couple to generate hydrogen molecule by Tafel reaction. All the reaction pathways are as follows,[10]

Volmer reaction (electrochemical hydrogen adsorption)

$$* + H^+ + e^- \rightarrow H^* \quad \text{(in acidic solution)} \qquad 1.7$$

$$* + H_2O + e^- \rightarrow H^* + OH^- \text{ (in alkaline solution)} \quad 1.8$$

Heyrovsky reaction (electrochemical desorption)

$$H^* + H^+ + e^- \rightarrow * + H_2 \text{ (in acidic electrolyte)} \quad 1.9$$

$$H^* + H_2O + e^- \rightarrow * + OH^- + H_2 \text{ (in alkaline electrolyte)} \quad 1.10$$

Tafel step (chemical desorption)

$$H^* + H^* \rightarrow H_2 \quad 1.11$$

Due to the dissociation of water prior to the formation of H^*, the HER in alkaline conditions is considerably slower than under acidic conditions. Regardless of the pH, the free energy of hydrogen adsorption (ΔG_{H^*}) is generally recognized as an indicator for hydrogen-evolving materials. For HER, ΔG_{H^*} of an ideal material (like Pt) need to be close to zero as too weak adsorption corresponds to poor interaction of protons and electrode surface, whereas strong adsorption requires high energy to break the bonds between hydrogen and catalyst surface and thus slows down H_2 desorption process.[11] Thus, the activity of a catalyst for HER can be dependent on strength of the adsorption of proton over electrode surface and can be graphically understood by volcano relationship plotted by ΔG_{H^*} of numerous catalysts determined from density functional theory (DFT) versus the logarithm of their corresponding exchange current densities ($\log j_0$) as shown in Figure 1.3. The so-called volcano diagram provides a simple way

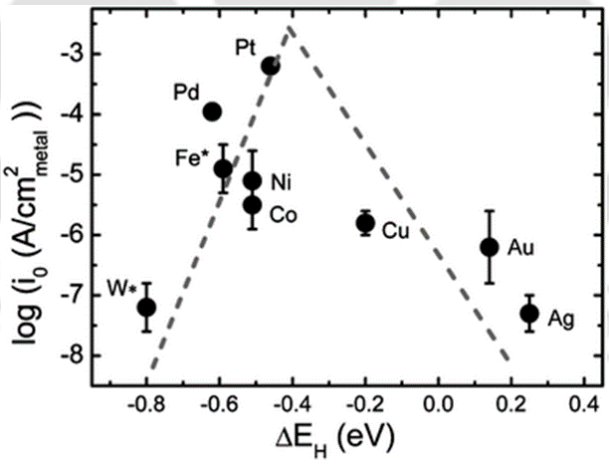

Figure 1.3. HER Volcano plot in alkaline solution on metal electrodes.[12]

of visualizing and comparing the activities of various metals and suggesting that platinum has the highest HER activity and thus enabling us to optimize the material design.

1.2.2 Oxygen Evolution Reaction

Oxygen evolution reaction (OER) occurs on the anode surface and consists of four electron processes. Due to its complex multistep processing, OER shows sluggish kinetics compared to HER reaction. OER reaction involves three adsorbed intermediates OH*, O* and OOH* on the electrode surface, and the most accepted reaction paths in acidic and alkaline solution can be given as,[13]

In acidic electrolyte

$$* + H_2O \rightarrow OH^* + H^+ + e^- \quad (1.12)$$

$$OH^* \rightarrow O^* + H^+ + e^- \quad (1.13)$$

$$O^* + H_2O \rightarrow OOH^* + H^+ + e^- \quad (1.14)$$

$$OOH^* \rightarrow * + O_2 + H^+ + e^- \quad (1.15)$$

In alkaline electrolyte

$$* + OH^- \rightarrow OH^* + e^- \quad (1.16)$$

$$OH^* + OH^- \rightarrow O^* + H_2O + e^- \quad (1.17)$$

$$O^* + OH^- \rightarrow OOH^* + e^- \quad (1.18)$$

$$OOH^* \rightarrow * + O_2 + H_2O + e^- \quad (1.19)$$

So, in a basic medium, OH is adsorbed over the catalyst surface by oxidation of hydroxide ions (Figure 1.4). Then this -OH* is converted to -O* via removal of proton. This -O* then takes

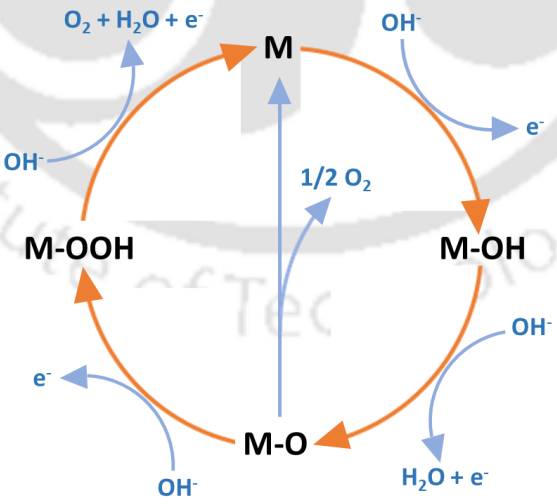

Figure 1.4. Oxygen evolution reaction mechanism on the electrode surface in alkaline electrolyte

hydroxide ion to produce -OOH*, which finally generates O_2 by reacting with hydroxide ion and the active sites become available for the next round of reaction. OER under basic condition

is more favourable than in acid conditions due to availability of plenty of OH^- ions in the electrolyte, which can be directly adsorbed on the catalyst surface forming OH^* intermediate. Regardless of the pH, ΔG value of different intermediates should be optimum for efficient OER catalysis.[14] To understand the OER activity of different metal oxide catalysts, volcano plot between $\Delta G_{O^*} - \Delta G_{OH^*}$ and overpotential has been shown in Figure 1.5, which suggests RuO_2, IrO_2 have the highest OER activity. So, to do the OER process efficiently, catalysts with high activity and stability are highly beneficial to address the high energy blockade for oxygen evolution.

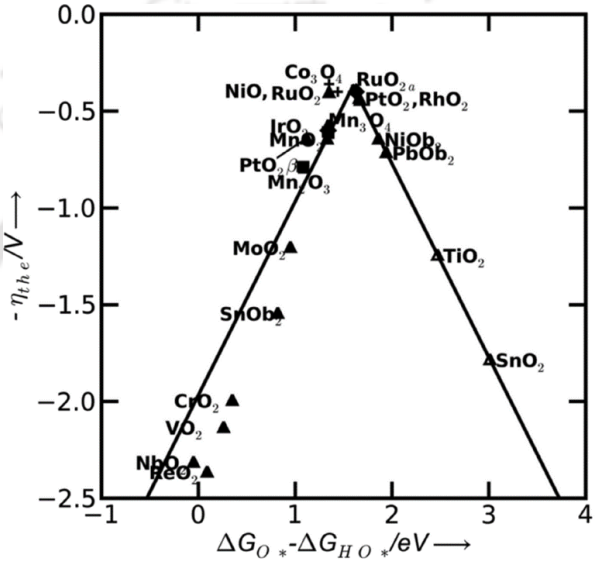

Figure 1.5. OER Volcano plot in alkaline solution on different metal oxide electrodes.[15]

1.2.3 Experimental setup

Three-electrode electrochemical cell systems are being used to precisely assess the intrinsic activity, which can't be done in two-electrode system. In actual electrolyzers i.e. in a two-electrode setup, voltage is applied between two electrodes and it prevents the determination of overpotential of each electrode. To measure the specific and mass activities of catalysts, a three-electrode system which may accurately characterize the overpotential of the working electrode should be utilized. A three-electrode cell for electrocatalysis contains working electrode (WE), counter electrode (CE), and reference electrode (RE).

To build a three-electrode setup, choosing the right cell material is very important because cells made of glass can be used for acid and neutral electrolytes. However, alkaline electrolyte corrodes the glassware; thus, polytetrafluoroethylene or polyoxymethylene should

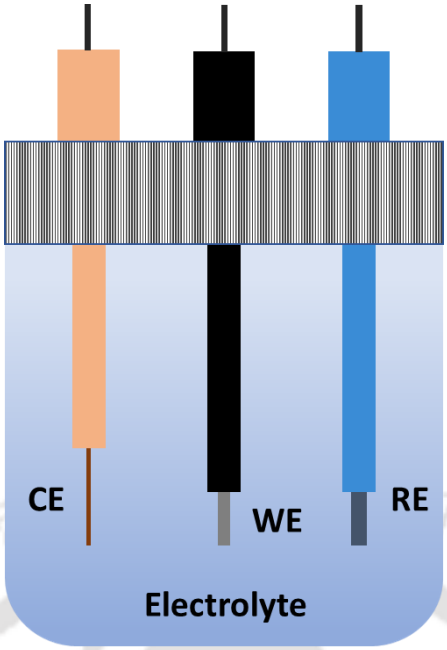

Figure 1.6. Representation of a three-electrode electrochemical cell having working electrode, counter electrode & reference electrode

be used to make a cell for alkaline solution.[16] The WE is monitored against a RE, which must consist of a steady and precise potential in order to correctly determine or regulate the potential applied to catalysts. The saturated calomel electrode (SCE) and the silver chloride reference electrode (Ag/AgCl) are two of the most often used reference electrodes. Counter electrode should be chosen such that it does not restrict the reaction at the working electrode and it should quickly provide electrons for the reaction. Therefore, Pt wires, meshes and foils are frequently used by researchers as counter electrodes since they can withstand significant currents during both HER and OER. For performance assessment of HER and OER catalysts, we need to focus on some catalytic parameters which have been given below.

1.2.4 Overpotential (η)

The thermodynamic equilibrium potential for the half-reactions of water splitting i.e. HER and OER are 0 and 1.23 V respectively corresponding to reversible hydrogen electrode (RHE) in acidic electrolyte. However, in practice, an extra potential known as overpotential (η) is required to address the energy barriers for electrochemical water splitting.[17] There are different contributions that are being added to the overpotential, like activation overpotential, concentration overpotential and resistance overpotential. The activation overpotential is related to the electrocatalyst itself and is dependent on its intrinsic energy barrier that it needs to overcome during catalysis. By choosing a proper electrocatalyst, this overpotential can be

highly reduced. For example, noble metal-based catalyst shows very low activation overpotential. The concentration overpotential occurs during the electrocatalysis process when a sudden drop in ion concentration happens near the electrocatalyst surface. It can be reduced by continuous stirring of electrolyte throughout the catalysis process. The resistance overpotential is involved with the resistance drop coming from the contact resistance of the electrocatalyst and measurement system. This overpotential can be eliminated by including a compensation term known as iR compensation. The overpotential is typically determined by using the polarisation curve between current density and potential for a given current. Lower the value of overpotential better is the performance. For the catalytic redox reaction, the applied potential can be given by the Nernst equation,

$$E = E^0 + \frac{RT}{nF} \ln \frac{C_0}{C_R} \quad 1.20$$

Where n is the number of electrons exchanged, E^0 is the reaction's standard potential, T is the reaction's absolute temperature, R is the universal gas constant, C_0 and C_R are the oxidized and reduced reagents, respectively, and F is the Faraday constant. The overpotential (η) can be defined as,

$$\eta = E - E^{eq} \quad 1.21$$

Where, E^{eq} is defined as equilibrium potential. In literature, overpotential at 10 mA cm^{-2} current density is being reported for general comparison with other catalysts.

1.2.5 Tafel Slope

To understand the kinetics of electrocatalysis reaction Tafel slope is being calculated from the Tafel equation,[18]

$$\eta = a + b \log j \quad 1.22$$

Where, η corresponds to overpotential, a is constant, b denotes Tafel slope, and j signifies current density. Lower the value of Tafel slope, faster is the charge transfer kinetics and thus it requires smaller value of overpotential to achieve similar current density. From equation 1.22, exchange current density can be calculated by putting η equal to zero, and the corresponding j value gives the exchange current density (j_0), which corresponds to the rate of electron transfer between electrolyte and electrocatalyst. Higher the value of exchange current density, higher

is the activity of the electrocatalyst for water electrocatalysis. Therefore, for efficient electrocatalysis, low overpotential, low Tafel slope and high exchange current density is desirable.

1.2.6 Electrochemical active surface area (ECSA)

Electrochemical active surface area (ECSA) is generally used to determine the active surface area of the working electrode that is responsible for electrocatalysis during water electrolysis. The higher the value of ECSA, the more catalytic reaction happens due to the availability of more active sites and thus quicker the reaction kinetics. To estimate the value of ECSA, double layer capacitance (C_{dl}) was calculated through observing the cyclic voltammetry curves (CV) in a potential range free from any faradaic region having a potential window of usually 0.1 V. Half of the difference of anodic current (J_a) and cathodic current (J_c) at middle of the potential window was plotted against the scan rate. The slope of the above curve provides C_{dl} value which is also estimated to be proportional to ECSA of electrocatalysts.

1.2.7 Activity

To recognize the activity of an electrocatalyst, mass and specific activities must be calculated. As the activity of different catalysts can be different depending on the catalyst loading, so it is necessary to measure the mass activity by normalizing the current by its loading mass in ampere per gram (A g^{-1}). However, to recognize the intrinsic catalytic activity of a catalyst, current is normalized by ECSA to give rise specific activity of a catalyst. These parameters are important to compare the activity of the catalyst with other reported electrocatalysts and state-of-the-art electrocatalysts.

1.2.8 Turnover frequency

The number of molecules reacted at each active site per unit of time is referred to as turnover frequency (TOF). This shows the intrinsic activity of each active site. The TOF can be given as,[19]

$$TOF = jA/\alpha Fn \qquad 1.23$$

Where, j is the current density at a particular overpotential, A represents the surface area of the electrode, α signifies the electron number of the electrocatalyst (electrons mol^{-1}), F corresponds to Faraday constant (96 485.3 C mol^{-1}) and n is the molar amount of electrocatalyst. Since it is impossible to count all of the accessible active sites that are

participating in the actual reaction, it is challenging to calculate the precise TOF value. As a result, a viable method for determining the TOF is based solely on the quantity of atoms on the surface or the quantity of the material's readily accessible electrocatalytic sites.

1.2.9 Stability

In the application of electrocatalysis, it is highly important to know if the catalysts are able to maintain their activity for a long-time of operation. There are mainly two types of stability: long-term cyclic voltammetry (CV) and long-term galvanostatic/potentiostatic measurement. In long-term CV, the catalyst goes through several repetitive cycles (usually more than 3000 cycles) and during that the stability of the catalyst is being monitored. In case of long-term galvanostatic/potentiostatic measurement, a constant potential (chronoamperometry) or a constant current (chronopotentiometry) is provided to the catalyst for a long time (usually more than 10 hours) and the variation in the corresponding current or potential is being monitored for that time. A stable catalyst is expected to endure this kind of operational stability for long-term.

1.2.10 Electrochemical impedance spectroscopy (EIS)

The EIS is used by many electrochemical studies, which is based on applying an alternative current signal to the working electrode and identifying the corresponding response. In the experimental procedure, an impedance spectrum (impedance vs frequency) is acquired by giving a potential signal at the working electrode. This impedance spectra are dependent on the equivalent circuit diagram of the cell consisting of resistors (R), capacitors (C) and inductors (L). In electrocatalysis of water, the most important plot is the Nyquist plot which corresponds to imaginary impedance (Z'') versus real impedance (Z'). From this plot, the resistance at onset potential for HER and OER can be obtained as,

$$R = R_s + R_{ct} \qquad 1.24$$

Where, R_{ct} is the charge transfer resistance between electrode surface and electrolyte. Lower value of R_{ct} suggests better charge transfer at the interface and thus better kinetics can be expected. Whereas, R_s corresponds to any solution resistance at the electrolyte and the contact resistance between electrode and measurement system. Thus, R_s increases the overpotential for HER and OER and can be compensated by iR_s term to get the actual overpotential of the electrocatalyst.

1.3 Noble metal-based electrocatalysts for water splitting

Pt metal and Pt-based nanomaterials are highly active HER catalyst,[20,21] while Ru/Ir-based oxides are the most active OER catalysts [22–24] because of their optimal surface energy for ideal adsorption of HER and OER reaction intermediates.[25,26] This can be further understood by observing the volcano plot for different HER and OER catalysts, which suggests Pt, Ru, Ir, Pd, Au, and Rh-based catalysts possess the highest activity and optimum surface energy (Figures1.3 & 1.5). However, due to their high cost and scarcity, it has been a great challenge to use them for commercial purposes.[22] Also, some of the noble metal-based catalysts display less stability for durable operation in harsh catalytic environments.[27,28] Therefore, researchers have been trying to utilize them through different strategies over the past few years without sacrificing their high activity and also to increase their operational stability. Among them, noble metal-based alloys, oxides/phosphides/sulfides/selenides, different composites, doping, and single-atom catalyst (SAC) development have been studied extensively.

Noble metal-based multimetallic nanoparticles, which are produced via mixing secondary metal elements with noble metal systems, have become an alternative to noble metals over the past few decades. Due to their better catalytic activity for synergistic effect and endurance compared to their monometallic counterparts, these nanoparticles have gained a lot of consideration.[29,30] In addition to the increase in catalytic efficiency, this strategy also helps to lower the loading amount of noble metals from the system, thus decreasing the overall price for developing the catalysts compared to only noble metal-based catalysts. In the past few years, noble metal-based bimetallic alloys like Pt-Co, Pt-Fe, Pt-Ni, Cu-Ir, Ir-Ni, Ir-Co, Ir-W, Ru-Co and Ru-Ni have been reported which are expected to show good catalytic activity towards water splitting.[31–39] For instance, Wei et al. have developed a hollow nanospheres of Pt-Co alloy with 1:1 molar ratio through a sequential reduction method with an intermediate structure of amorphous complex Co-B-O.[40] This catalyst showed an excellent HER metrix in acidic media with 2.8 times higher mass activity related to commercially used Pt/C. The extremely accessible electron/mass transport path, exposed active spots on the ultra-thin shells, and strain effect caused by the hollow sphere structure are mostly to account for the Pt-Co hollow nanospheres' exceptional activity for HER. In another work, Pi et al. developed IrM (M: Co, Ni, Fe) metal-based nanoclusters by a simple wet chemical large scalable process.[41] These developed catalysts showed an outstanding performance for both HER and OER, specially IrNi nanocluster achieved a current density of 10 mA cm^{-2} at a potential 1.58 V for overall water splitting making it a potential bifunctional catalyst. For using a catalyst in

different pH conditions, iridium tungsten alloy having nanodentritic structure (IrW ND) has been created by Lv et al. which acted as a bifunctional electrocatalyst.[37] They measured the hydrogen generation rate to be two times higher for IrW ND than the commercial Pt/C electrode, irrespective of the pH of the electrolyte. Furthermore, IrW ND displayed an excellent OER activity with superb stability compared to only Ir counterpart and the structure achieved a current density of 10 mA cm^{-2} at a low potential of 1.48 V for overall water splitting. The reason for enhanced performance of catalysis has been studied through DFT calculation which suggested a suitable binding energy for reaction intermediates accelerating the reaction kinetics. In addition, alloying Ir with W stabilized Ir in the structure, which improved the Ir corrosion during catalysis measurement thus increased its durability. Yang et al. adopted a core-shell structure having Ru-Ni alloy core with ultrathin Ru shell through a wet chemical method.[39] This catalyst showed excellent activity and stability in various pH electrolytes. To understand the high activity of this catalyst, they have done DFT calculations which revealed a downshift of d band center after the incorporation of Ni in the system thus reducing the binding energy for HER and OER intermediates on the catalyst surface resulting an easy H-H and O-O formation.

Numerous research efforts indicated that incorporation of third transition metal in binary alloy system could increase the catalytic activity further by tuning the adsorption energy.[42,43] For instance, Feng et al. have compared a series of catalysts like single metal (Ir), bi-metallic alloys (IrCo, IrNi) and tri-metallic alloy (IrCoNi) for OER and found the highest activity for IrCoNi alloy.[44] From the DFT calculation, they found the adsorption energy of OER intermediates on different catalyst surfaces as, IrCoNi < IrCo < IrNi < Ir. Thus, IrCoNi alloy surface provides an optimal surface energy and shows the best OER performance among other catalysts. In this direction, several multimetallic alloys have been reported, which are highly active HER and OER catalysts. For example, Co-doped IrCu octahedral nanocages have been developed by Lee group for efficient OER catalysis in acid media.[45] IrNiFe nanoparticles have been synthesized and used as highly active HER and OER catalysts by Fu et al.[42] Wang group developed Pt-based trimetallic nanochains (PtNiCu) which is 5 times more electrocatalytically active for HER than commercial Pt.[46]

According to recent studies, the insertion of non-metallic elements (S, P, and Se) into a noble metal-based matrix may also be utilized for electronic tuning, in addition to alloying heterogeneous metal components with noble metals for increasing electrocatalytic activity. For example, The Rh_2P nanocubes with P termination have been studied as a HER catalyst which

possesses the optimal structure for H adsorption, confirmed by DFT studies.[47] Furthermore, this novel Rh_2P catalyst can be used as excellent pH independent HER electrocatalyst requiring an overpotential of 14, 30 and 38 mV to achieve 10 mA cm^{-2} current density in acid, basic and neutral solutions and thus stand as a promising replacement to state-of-the-art catalysts. Similarly, other catalysts like IrP_2, Pd_3P and PtP_2 in carbon support for overall water splitting were also developed via two-step annealing starting with $IrCl_4$, $PdCl_2$, and $PtCl_4$ by Qin et al.[48] In another work, Zheng et al. synthesized lithium (Li) incorporated iridium selenide (Li-$IrSe_2$) for overall water splitting in a variety of pH conditions.[49] This catalyst has shown remarkable overall catalytic activity requiring a cell voltage of only 1.44 V and 1.5 V for acidic and neutral electrolytes. The enhanced performance originated due to high surface area, high porosity and existence of Se vacancies in the catalyst.

An attractive way to further increase the catalytic activity, stability and to improve the utilization of noble metals is to combine them with proper support that possesses large surface area, high conductivity and can also show synergistic effects for tuning catalytic capabilities. Among different supports, most potential ones are graphene, MXene, metal organic framework (MOF), metal chalcogenides and metal (oxy)hydroxides. In this direction, Su et al. synthesized a bimetallic nanoalloys of Co and Ru encapsulated in N-doped graphene (RuCo@NC).[38] This bimetallic alloy catalyst displayed an exceptional HER performance requiring an overpotential of 28 mV for 10 mA cm^{-2} current density and was stable even after 10000 cycles in alkaline electrolyte. From the DFT calculation, they have showed that Ru incorporation in the system increases the electron transfer to graphene from Co core and thus, the C-H bond energy got boosted lowering the ΔG_{H^*} for HER on graphene surface. Jiang et al. developed an efficient HER catalyst by growing Pt-Ni nanowires on the MXene sheets with variable Pt composition ($Pt_xNi@Ti_3C_2$).[50] This catalyst showed excellent performance in both acidic and alkaline media requiring one of the lowest overpotential (18.55 mV for 10 mA cm^{-2}) and Tafel slope (13.37 mV dec^{-1}) in acidic solution. From the DFT calculation and XPS analysis, the adsorption energy for hydrogen is observed to be optimized close to zero in acidic media due to electron transfer between MXene sheets and Pt-Ni alloy. Furthermore, the Ti_3C_2 nanosheets' surface vacancies from the removal of F-containing groups in alkaline environments served as active sites for water dissociation, which significantly increased HER activities. In another work, Wang eta al. reported a heterostructure of Pt_3Ni alloy and NiS structure via direct sulfurization of Pt-Ni nanowires.[51] This heterostructure was showing much better performance compared to only Pt_3Ni alloy and also showing 9.7 times higher current density compared to commercial

Pt/C at 0.07 V in 1M KOH solution. DFT calculation revealed that NiS in the heterostructure boosted H^+ creation by easily dissociating water and Pt_3Ni lowered the potential requirement to produce H_2 from H^+ thus overcoming the energy barrier for HER synergistically. Recently Zhang et al. have started with ZIF 67 (cobalt MOF) nanorods which under annealing converted to nitrogen-doped carbon nanotubes (N-CNT).[52] Via galvanic replacement, they have replaced some of the cobalt cations with platinum cations which under high-temperature annealing alloyed with cobalt (Pt_3Co) to sub- 10 nm nanoparticles and supported on N-CNT making a catalyst Pt_3Co@NCNT. The host N-CNT not only provided large surface area and high conductivity but also prevented ultrasmall Pt_3Ni alloys from agglomeration. Thus, this catalyst displayed an outstanding HER catalysis in both acidic and basic solutions, which was also supported by optimized ΔG_{H^*} value from DFT calculation.

The intrinsic activity of nanoparticle catalysts is determined by the exposed corners/edges and the heterojunctions. However, by reducing the size of the catalysts, catalytic activity and selectivity can be vastly improved due to the increased exposed active sites and modified electronic structure.[53,54] To this purpose, single-atom catalysts (SACs) of noble metals have drawn considerable interest and proven to be a promising material for electrochemical energy storage and conversion.[55,56] However, isolated atoms must be anchored to the proper supports in order to form stable structures with uniform atomic distribution.[57,58] The supports should possess a large surface area and good conductivity for decorating the single atoms to the great extent. Thus, when the active metal atoms are spread atomically on the supports, the catalysts will maximize atom use efficiency and lower the cost of large-scale applications. For instance, using atomic layer deposition, Sun et al. successfully loaded isolated single Pt atoms on N-doped graphene (Pt/NGNs, 2.1 wt percent).[59] The number of deposition cycles was utilized for simple control over Pt sizes, ranging from a single atom to clusters and nanoparticles. In comparison to a Pt cluster on N-doped graphene and a commercial Pt catalyst, the generated Pt/NGNs showed outstanding HER activity and stability in 0.5 M H_2SO_4. Data demonstrated by XANES and DFT analysis confirmed the electron transfer between the Pt single atom and N-doped graphene not only helped to enhance the HER activity but also stabilize the Pt single atom. In another work, isolated Pt was incorporated within a nitrogen-doped porous carbon matrix (Pt@PCM) through electrostatic contact between the Pt species and the support.[60] In comparison to commercial Pt/C for HER, the lattice-confined Pt@PCM catalyst demonstrated a substantial mass activity improvement. The DFT calculations shed more light on the isolated Pt decoration's catalytic role, showing that Pt

atom decoration might activate the nearby C/N by controlling their electronic distribution as HER active sites. Xing et al. used a straightforward liquid redox method to chemically activate the MoS_2 surface plane through spontaneous atomic palladium interfacial doping.[61] The Pd-MoS_2 had much higher HER activity than the 2H-MoS_2 due to the combination of the 2H to 1T phase shift, an increase in sulphur vacancy sites, and the addition of additional Pd-S* sites. According to the DFT calculation, the improvement of HER activity was not only due to the incorporation of single atom Pd but also due to regulation of adsorption energy at the S vacancy sites, which also actively participated in the catalytic reaction. Recently Zhang eta al. generalized the synthesis of single-atom catalyst via electrochemical deposition.[62] In the work, they have developed a series of noble metal-based SAC (Ir, Ru, Rh, Pd, Ag, Pt, and Au) on the surface of $Co(OH)_2$ nanosheets and utilized them for efficient HER and OER catalysis. Wang et al. also loaded Ir SAC on the surface of NiO for OER with a high loading of 18 wt %, which stabilized over the support by forming a covalent Ir-O bonding.[63] DFT calculation suggested Ir SACs not only acted as a high catalytic site but also regulated the electronic structure of base NiO, which increased its reactivity and thus overall catalytic activity of the system.

1.4 Earth-abundant transition metal-based electrocatalysts for water splitting

Transition metals (TM) like cobalt (Co), nickel (Ni), iron (Fe), molybdenum (Mo), tungsten (W) and copper (Cu) have received a lot of attention in electrocatalysis because of their low cost, abundant sources along with durable and promising electrocatalytic properties. It is simple to control the electronic structure of TM-based electrocatalysts and change their oxidation state as well. Because of this, the development and synthesis of highly efficient and stable non-precious metal-based electrocatalysts have featured prominently in modern research. Different classifications by which TM-based catalysts (TMXs, X=O, OH, S, Se, P, N, C) are utilized are metals/alloys, oxides, hydroxides/oxyhydroxides, chalcogenides (sulfide, selenide), phosphides, nitrides, carbides and their performances were further improved by doping, defect creation and heterostructure formation to tune their electronic structure.

TM-based metal/alloy catalysts possess high intrinsic conductivity and can speed up the electron transfer process during catalysis with adsorbed oxygen. However, they easily get corroded in acid and basic solutions and thus require some stable support to address the stability issue. So, TM-based monometallic or alloys are often decorated on some stable support like carbon. For instance, by easily annealing the MOF, Xu et al. created a highly effective OER electrocatalyst with Ni nanoparticles (NPs) enclosed in N-doped graphene.[64] By utilizing the

synergistic effect of metals, metal alloys typically display higher catalytic activity compared to single metal. In that direction, Wang et al. constructed NiFe alloy nanoparticles (NPs) with carbon shells doped with N.[65] This NiFe alloy catalyst showed high activity for OER with a low overpotential of 226 mV for driving a current density of 10 mA cm^{-2}. In search of a highly active TM-based alloy catalyst for HER, Ni_3Fe alloy encapsulated in carbon nanotube supported on N-doped carbon nanofiber was fabricated by Li et al.[66] This optimized Ni_3Fe@N-C NT/NFs structure displayed better HER performance compared to single metal-based (Ni/Fe) catalyst due to favourable ΔG_{H^*} value of only -0.14 eV (ΔG_{H^*} for Ni and Fe based catalysts are -0.23 and -0.52 eV). Yang et al. reported a series of single-metal, bi-metal alloys and tri-metal alloys wrapped in graphene by high-temperature annealing of MOF.[67] Among all the synthesized materials, FeCoNi alloy exhibited highest activity towards HER and OER. To understand the effect of alloying in OER catalysis, they have plotted a volcano diagram consisting of overpotential as a function of ΔG_{O^*}- ΔG_{HO^*} and observed highest activity for multi-metal alloying. DFT calculation further confirmed that number of electrons transferred between alloy and graphene can be tuned by adjusting metal ratio in FeCoNi alloy or by adjusting the degree of freedom of the alloy.

Among many electrocatalysts, TM-oxides are very capable materials for electrocatalytic OER reactions in basic electrolyte. One of the most prevalent states in nature is TM-oxides, and the volcano plot shows that its activity is high for OER (Figure 1.5). However, the low conductivity limits its use in catalysis applications. Recently 2-Dimensional (2D) transition metal-based sulfides, selenides, phosphides, nitrides and carbides have received a lot of attraction due to their intrinsic high activity and conductivity and thus have grown to be one of the most researched materials for electrocatalysis. Additionally, during the OER process, the surface of TM-based sulfides, selenides, and phosphides are reconfigured through the concurrent leaching of some lattice ions or by producing highly active surface amorphous hydroxide/(oxy)hydroxide phases, which exhibit significantly higher catalytic activity than their directly synthesized ones.[68–70] However, the intrinsic catalytic performance of TM-based catalysts is still not comparable to the state-of-the-art electrocatalyst. Therefore, proper tuning in their electronic structure along with new catalyst design is highly required for TMXs-based catalysts to compete with state-of-the-art catalysts. In this regard, doping, defect introduction and interface engineering have been extensively researched in the past few years.

Incorporation of heteroatom (transition metal or non-metal) in TMXs can greatly enhance the electrochemical HER & OER performance by hybridizing the energy levels of

original catalyst and the doping element.[71] Chemical doping generally comprises altering the active site's valence state, band structure, d-band centers, charge redistribution, and formation energy of intermediates as well as improving the wettability qualities that enable efficient H_2 and O_2 evolution.[72–74] Zhang et al. demonstrated NiCo phosphide with tuned nitrogen and phosphorous doping to manipulate Fermi energy and conductivity of the pristine catalyst.[75] This realized structure accelerated the water splitting with high stability in harsh acid and alkaline solution for 100 h due to its increased active centres with synergistic electronic modification, confirmed by numerical simulation. Xu et al. incorporated three heteroatoms boron (B), nitrogen (N) and sulfur (S) on a cobalt phosphide (CoP) nanoparticle supported on porous carbon, graphene composite (C@rGO) generated by pyrolysis of cobalt MOF and graphene oxide (GO) composite.[73] This B,N,S-CoP@C@rGO catalyst displayed very low overpotential of 112 and 264 mV to achieve a current density of 10 mA cm^{-2} for HER and OER, which is better than the activity of single heteroatom doping (N) and bi heteroatom doping (B,N). The enhancement in the performance correlated to the stronger charge transfer ability with a low energy barrier due to optimization of the electronic structure where porous carbon matrix along with rGO prevented agglomeration of CoP nanoparticles. In addition to non-metal doping, adding transition-metal atoms to TMXs can also enhance their electrocatalytic activity. For instance, Jaramillo group have done a theoretical work to understand the doping effect of iron in the transition metal phosphide structure by calculating ΔG_{H^*} of a series of variable Fe-doped cobalt phosphide (CoP).[76] Their finding suggested that $Fe_{0.5}Co_{0.5}P$ has the highest activity close to Pt/C and is placed at the top of the volcano plot for hydrogen evolution among all other compared catalysts. This research demonstrated the activity of transition metal phosphides produced by various metallic dopants and offered a theoretical basis for the development of high-efficiency Fe-doped catalysts. Their finding was also later confirmed by different Fe-doped CoP structures developed experimentally.[77,78] Co and Fe were co-doped into $NiSe_2$ porous nanosheets through topotactical transformation employing vapour salinization as the synthetic process.[79] Numerous additional active sites with enhanced charge transfer properties were observed due to uniform distribution of Fe and Co on $NiSe_2$ nanosheet. This optimized catalyst showed 92 and 251 mV overpotential for 10 mA cm^{-2} current density for HER and OER catalysis.

Defect engineering in the form of vacancies, grain boundaries, line defects, dislocation or etching of catalyst is an alternative way to increase the electrical conductivity and catalytic activity of the catalyst by modifying its electronic structure.[80] Generally, in the structure, these

defect sites play the most catalytic active regions for efficient HER and OER compared to the other surfaces.[81] For example, oxygen vacancy in cobalt iron oxide ($CoFe_2O_4$) tuned the adsorption energy for H_2O and ΔG_{H^*} is also being optimized for efficient water splitting.[82] Moreover, an increase in density of states was observed at the Fermi level after the incorporation of oxygen vacancies, which enhanced the electron transportation. MoS_2, WS_2 are highly active HER catalysts, but their catalytic activity is limited to their edges only with basal planes mostly inactive due to unavailability of unsaturated Mo/ W atoms.[83] To increase their activity, sulfur vacancies have been created on their basal planes in different reports which increases the overall activity of the catalyst not just by increasing the number of active sites but also by regulating their electronic structure.[84–86] Self-reconstruction of structure and etching of cations and anions during a highly oxidative OER environment is another route for developing highly active OER catalyst. For example, Wang et al. have developed a core-shell structure of $NiFe/NiFeO_x$ nanoparticles on $NiMoO_4$ supported by amorphous carbon (NiMoFeO@NC).[70] This structure rapidly self-reconstructed during OER process by etching of MoO_4^{2-} from $NiMoO_4$ cores and simultaneous inclusion of iron in the Ni-(oxy)hydroxide shells. This reconstructed structure showed excellent performance towards OER and achieved high current density of 100 mA cm^{-2} at 290 mV overpotential and maintained that current without decay for 24 h of stability test.

Interface engineering or heterostructure formation of two TM-based materials can provide favourable adsorption sites for both HER and OER reaction intermediates due to synergistic coupling. This heterostructure engineering not only overcomes the demerits of individual catalysts but can also provide numerous catalytically active rich heterojunctions. These techniques can effectively improve the catalytic activity, electrical conductivity and facile charge transfer characteristics of the transition metal-based electrodes. For instance, Xiong et al. developed a biphasic heterostructure of Ni_3S_2 and MnO_2 supported on Ni foam via two-step hydrothermal process.[87] This heterostructure exhibited exceptional HER and OER catalytic activity and also required very low voltage of 1.52 V to get 10 mA cm^{-2} current density for overall water splitting. The origin of its high activity was investigated by DFT calculation which suggested that highly exposed numerous heterojunctions facilitated easy adsorption and dissociation of water molecules. Li et al. have synthesized a core-shell heterostructure of NiFe alloy shell on Ni(Cu) nanotube core through selective electrodeposition on nickel foam which acted as a highly active bifunctional catalyst.[88] $NiSe_2$-Ni_2P heterostructure has been generated by three steps hydrothermal method where first nickel hydroxide has been grown over Ni

foam.[89] This $Ni(OH)_2$ was then converted to $NiSe_2$, which again partially converted to Ni_2P to produce final heterostructure of $NiSe_2$-Ni_2P. This heterostructure has shown excellent performance for HER ($\eta_{10} = 102\ mV$) and OER ($\eta_{50} = 220\ mV$) in alkaline media due to optimization of hydrogen and water adsorption over the catalyst surface after interface engineering. Recently Wang et al. have developed a FeS_2@MoS_2 heterostructure for efficient HER catalysis, which showed better performance compared to the individual components.[90] This has been supported by DFT calculation which revealed adsorption energy for hydrogen has drastically reduced for FeS_2@MoS_2 (0.08 eV) heterostructure compared to FeS_2 (0.98 eV) and MoS_2 (0.25 eV) structures. In another work MoP/MoS_2 heterostructure has been developed by first growing MoS_2 on carbon cloth hydrothermally and then phosphorizing this at high-temperature annealing.[91] This catalyst displayed excellent HER activity in all pH conditions requiring an overpotential of 69, 54 and 96 mV for 10 mA cm^{-2} current density in acid, alkaline and neutral solutions. The origin of high performance was correlated to the presence of large number of active sites on the heterointerface of heterostructure, good electron transport property due to conducting MoP, and presence of plenty of nanopores in the structure facilitated easy mass transfer, which has been supported by XPS result and DFT calculation. Zhou et al. have developed Ni–Fe disulfide@oxyhydroxide core-shell heterostructure by in-situ surface reconstruction of the Ni-Fe disulfide structure.[92] Ni-Fe sulfide was prepared through hydrothermal and then high-temperature sulfidation process which was then undergone through 100 cyclic voltammetry cycles in oxidative environment to partially reconstruct the sulfide surface to oxyhydroxide. The constructed catalyst showed excellent catalytic activity for OER and durability for 50 h due to its synergistic core-shell structure where the shell acted as a highly active OER catalyst and the core Ni-Fe sulfide provided easy electron transfer.

1.5 Existing challenges in development of efficient electrocatalysts

Although the development of electrocatalysts for efficient water splitting has grown significantly over the past decade, as detailed in the previous section, there is still a substantial barrier present to their facile development with effective utilization and commercialization. Therefore, the current challenges in developing catalysts based on transition metals and noble metals have been highlighted below.

- *Requirement of new efficient process for the development of electrocatalysts*

Electrocatalysts that are being used at commercial level are mainly based on noble metals. However, recently more and more catalysts based on earth-abundant transition metals are being

studied. They have been primarily synthesized by conventional methods like hydrothermal/solvothermal, and chemical vapor deposition (CVD). But these synthesis techniques are non-energy efficient, complex and require multi-step processing and long-time, thus increasing the cost of the material synthesis. Therefore, to achieve low-cost catalyst, we need to focus not only on performance optimization but also on new technologies that can process the development of catalysts at a low cost. So, new radical processing is required to overcome the current challenges faced by conventional methods for development of efficient electrocatalysts.

- *Demand of new strategies to develop efficient heterostructures for water electrolysis*

To further achieve high performances for HER and OER, recently heterostructures are being studied extensively. However, the growth of atomistic interfacing between components of a heterostructure is difficult and thus to realize high performance as well. Most of the heterostructures are constructed by sequential method i.e. depositing different components one above another via conventional methods. This leads to an increase in number of synthesis steps and cost of material development compared to the development of single-component sulfide, selenide and phosphides through conventional methods where usually a single step is used. Therefore, heterostructure development needs some comprehensive strategy where low-cost approach must be invented, and the electronic coupling should be adjusted in such a way that the performance is optimized for commercial application.

- *Complexity in single atom decoration & its stabilization to achieve high performance*

Due to the high price and low natural abundance of noble metals, it is highly required to minimize its usage amount and maximize its efficiency. To achieve that, different strategies like formation of alloys and nanoparticles have emerged over the past few years. To further increase the atomic utilization efficiency of noble metals, single-atom catalyst (SAC) development has become a promising approach toward efficient electrocatalysis of water. However, the processing that has been adapted for SAC development is complicated. In addition, less focus has been given to the base, which can influence its stability and performance. Most of the reported SACs have been decorated over carbon matrix, but the role of transition metal-based sulfides, selenides or phosphides as a support is less studied. In addition, transition metal-based structures are gone through intensive surface reconstruction during OER. So, it is highly important to understand the state of those SACs after the dynamic OER process, which is also limited in the literature. Therefore, there should be some facile

strategy for the decoration of single atoms, and the base material should be optimized such that adequate electronic coupling between them can be achieved for high performance in electrocatalysis.

- *Requirement of high current density and stability of electrocatalysts for commercial purpose*

Achieving a high current density is still a challenge mainly due to two reasons: material stability and inaccessibility of active sites at high current density due to rapid reaction rate. At high current density large amounts of H_2 and O_2 are being generated. Therefore, if the material surface structure is such that it cannot easily release the generated H_2 and O_2, then catalytic active sites will be inaccessible for the next round of reaction and noise can be seen in LSV curves at high current density. So, most of the catalysts focus on getting the onset potential or overpotential at low current density. But a practical electrolyzer operates at high current density. Therefore, achieving a high current density at low overpotential is also important, along with developing suitable processing for the electrocatalysts. In addition, long-term stability of materials is an important aspect of electrocatalysis application. However, most of the reported catalysts display good stability at low current density. But, stability at high current density is a concern for most of the electrocatalysts for their commercialization which needs to be addressed.

- *Lack of theoretical understanding for the origin of high catalytic performance*

Recently significant improvement has been observed in the enhancement of catalytic performance. However, very less theoretical based understanding has been given to support the high catalytic activity and for further scope toward modulation of those catalysts. Theoretical understanding through DFT calculation can provide substantial information on the advantages and disadvantages of an electrocatalyst which is sometimes not possible via experimental analysis and thus can help to tune the material efficiently. Therefore, more and more theoretical-based understanding along with new processing for development of highly active catalysts are urgently required to address the current bottleneck in the field of electrocatalysis of water.

1.6 Objectives of this thesis work

To overcome the existing challenges in the field of electrocatalysis, as discussed in the previous section, some compositional modification or conventional processing may not be enough.

There needs some radical new strategy for the development of catalysts with proper adequate tuning, which can achieve high performance at low overpotential. In view of that, we have taken some objectives as below,

- Development of heterostructure having uniform atomistic interfacing with suitable electronic coupling between components and abundant active sites via in situ dealloying process.
- Development of molybdenum-tungsten based core-shell heterostructure through a simple, unique and fast processing for efficient pH universal catalyst.
- Fast recrystallization strategy for universal generation of metal sulfide, selenide and phosphides to achieve commercial level current density at low overpotential.
- Stabilization of iridium single atoms over heterostructure to get electronic synergy for overcoming the high energy barrier of OER.
- Theoretical understanding of the electronic synergy and their effect on electrocatalytic HER and OER reactions.

- **Discussion of the objectives**

The undertaken objectives are anticipated to surpass the current challenges in the field of electrocatalysis. Firstly, rather than depositing structures one above another for heterostructure development, we have introduced a dealloying process where a single component has been dealloyed so that atomistic interfacing is generated, which is very different compared to the conventional method. Here, we have started with a mixed metal oxide/hydroxide and via selenization strategy developed a heterostructure of $MoSe_2$ and $NiCo_2Se_4$ where $MoSe_2$ layers are vertically standing over the selenide substrate. Exposure of vertical nature of $MoSe_2$ like this has not been done previously and is expected to show very good HER catalytic activity due to exposure of its active edges. This unique strategy can be extended for other mixed metal oxides as well to develop a heterostructure efficiently. Secondly, microwave-induced simple and unique processing has been adapted to develop molybdenum-tungsten-based core-shell heterostructure where amorphous a-MoS_x has been coated on a crystalline MoWO structure on a second scale. This type of advanced core-shell heterostructure has not been developed yet, and the conventional methods usually result in crystalline-crystalline core-shell heterostructure. Due to interface engineering between amorphous and crystalline structures, this type of structure is expected to show synergistic effect for electrocatalysis and can be used in different pH conditions. Thirdly, we have introduced an energy-efficient rapid microwave

phase evolution processing which can instantly recrystallize metal hydroxides into metal sulfide, selenide and phosphides as completely different to the conventional methods, which require high energy, long time and laborious multi-step processing. In addition, this unique processing gives rise to biphasic system, which under OER reconstructs into highly active OER catalyst with interesting surface reconstruction for electrocatalysis. This facile and novel processing can be extended to develop other transition metal-based chalcogenides as well. Fourthly, simple photochemical method has been adopted to decorate single-atom iridium on the surface of a heterostructure which is expected to show excellent OER performance due to the synergistic coupling of single-atom Ir and the base heterostructure. During the OER measurement, the base heterostructure is expected to be self-reconstructed to metal hydroxide/oxyhydroxide, thus can provide the opportunity to understand the stabilization of single atom Ir on the dynamically reconstructed support during OER. Finally, theoretical understanding regarding introduction of any electronic synergy and enhancement in electrocatalytic activity on different catalytic surfaces originating via such strategies would be beneficial to address the current bottleneck in the field of electrocatalysis.

1.7 Conclusion

Electrocatalysts play an important role in the efficient water splitting process for future hydrogen-based economy. Different strategies and synthesis routes have been adopted by researchers to enhance the efficiency of electrocatalysts. However, several challenges are still there as discussed in previous section, which need to be addressed for commercialization of these catalysts. While developing such electrocatalysts, the focus should be two-fold. Firstly, simple and low-cost strategies should be adopted for the development of highly active catalysts. And secondly, a detailed understanding of the catalyst through proper advanced characterization and theoretical correlation should be given. In conclusion, further research should be committed to developing novel strategies and electrocatalyst designs to solve the pre-existing issues associated with sustainable hydrogen generation applications.

1.8 Organization of the thesis

This thesis focuses on the facile development of electronically tuned earth-abundant catalysts by heterostructure formation and coupling of noble metal-based single-atom catalysts with adequate catalytic support for application in efficient water electrolysis technology. The entire thesis work has been divided into six different chapters starting with a brief introduction to the state-of-art technologies and challenges in producing highly efficient electrocatalysts, and the

rest of the chapters discuss the strategies to overcome these challenges. This thesis ends with concluding remarks and future prospects in the area of water electrolysis process. A brief description of each chapter is presented below.

Chapter 1: Chapter 1 provides an overview of state-of-art energy conversion technologies. Recent advances in the development of electrocatalysts based on earth-abundant transition metals and noble metal-oriented catalysts toward the application of overall water splitting process have been described. The design philosophy of catalyst architecture for commercial applications has been refined. At the end of this chapter, the motivation and objectives of the present work have been illustrated.

Chapter 2: In chapter 2, we describe how selenization-induced atomic rearrangement of mixed metal oxide/hydroxide nanosheets (MoO_3/Ni-$Co(OH)_2$) led to the development of heterostructure of $MoSe_2$ and $NiCo_2Se_4$ nanosheets. This strategy triggers the growth of longitudinal and expanded $MoSe_2$ nanosheet arrays perpendicular to the $NiCo_2Se_4$ nanosheet substrate, which displays an excellent HER performance. Density functional theory (DFT) calculation reveals the advantages of structural features and heterostructure formation. Thus, in this chapter, we have presented a very simple selenization-induced heterostructure formation technique which can trigger new developments in broad area of electrocatalyst.

Chapter 3: In chapter 3, we have presented a bifunctional electrocatalyst by decorating Ir single atoms (SAC-Ir) on the surface of $MoSe_2$@$NiCo_2Se_4$ having a high surface area, as demonstrated in chapter 2. This introduction of SAC-Ir boosts the OER activity of the catalyst. The origin of high OER activity is related to the in-situ surface activation of selenide into amorphous Ni-Co-oxyhydroxide by selective leaching of molybdenum and suitable electronic coupling with single atom iridium, as analyzed by extensive post OER characterizations and comprehensive understanding through DFT calculations.

Chapter 4: In chapter 4, we have described a fast method for growing an ultrathin amorphous a-MoS_x shell over crystalline molybdenum tungsten oxide (MoWO) nanowire core in a matter of seconds. High microwave absorption ability of partially reduced graphene oxide was utilized for radiative heating and transient surface reaction of MoWO with the sulfur source, which gave rise to crystalline/amorphous core-shell structure. This as-developed core-shell heterostructure shows excellent HER activity in different pH conditions with superb stability. A detailed theoretical understanding of catalytic activity of the amorphous a-MoS_x and the

function of the crystalline MoWO core in enhancing the activity of various catalytic sites is described in this chapter. This fast, simple, and cost-effective process is expected to serve as a practical technology for core-shell-based active electrocatalysts development.

Chapter 5: In chapter 5, we present a versatile, low cost and very fast strategy involving domestic microwave for the development of highly efficient metal sulphide, selenide and phosphide-based OER catalysts. Partially reduced graphene oxide was used for this strategy which rapidly heated up to a high temperature in a matter of seconds and initiated rapid crystallization and phase transformation. All these developed chalcogenides exhibit excellent OER catalytic activity and deliver practically required high current at lower overpotentials as compared to most of the previous reports. The origin of very high OER activity was investigated in detail and correlated with this unique heterostructure and the in-situ phase evolution during OER. Thus, this rapid recrystallization strategy can lay the platform for the development of new efficient catalysts in this direction.

Chapter 6: Chapter 6 summarizes the important findings of this thesis work with concluding remarks. The future prospects in the area of developing efficient electrocatalysts for energy conversion technologies have been presented at the end of this thesis.

References

[1] J. A. Turner, *Science (80-.).* **2004**, *305*, 972.

[2] K. T. Møller, T. R. Jensen, E. Akiba, H. wen Li, *Prog. Nat. Sci. Mater. Int.* **2017**, *27*, 34.

[3] N. T. Suen, S. F. Hung, Q. Quan, N. Zhang, Y. J. Xu, H. M. Chen, *Chem. Soc. Rev.* **2017**, *46*, 337.

[4] M. S. Faber, S. Jin, *Energy Environ. Sci.* **2014**, *7*, 3519.

[5] Y. Lee, J. Suntivich, K. J. May, E. E. Perry, Y. Shao-Horn, *J. Phys. Chem. Lett.* **2012**, *3*, 399.

[6] C. Dong, X. Zhang, J. Xu, R. Si, J. Sheng, J. Luo, S. Zhang, W. Dong, G. Li, W. Wang, F. Huang, *Small* **2020**, *16*, 1905328.

[7] P. Xi, B. Huang, J. Yin, J. Jin, M. Lu, H. Zhang, Y. Peng, C. H. Yan, *J. Am. Chem. Soc.* **2020**, *142*, 18378.

[8] Z. P. Wu, X. F. Lu, S. Q. Zang, X. W. Lou, *Adv. Funct. Mater.* **2020**, *30*, 1910274.

[9] H. Zhang, Y. Luo, P. K. Chu, Q. Liu, X. Liu, S. Zhang, J. Luo, X. Wang, G. Hu, *J. Alloys Compd.* **2022**, *922*, 166113.

[10] A. Lasia, *Handb. Fuel Cells* **2010**.

[11] M. Hakala, R. Kronberg, K. Laasonen, *Sci. Reports 2017 71* **2017**, *7*, 15243.

[12] W. Sheng, M. Myint, J. G. Chen, Y. Yan, *Energy Environ. Sci.* **2013**, *6*, 1509.

[13] S. Trasatti, *Electrochim. Acta* **1984**, *29*, 1503.

[14] Z. W. She, J. Kibsgaard, C. F. Dickens, I. Chorkendorff, J. K. Nørskov, T. F. Jaramillo, *Science (80-.).* **2017**, *355*.

[15] E. Fabbri, A. Habereder, K. Waltar, R. Kötz, T. J. Schmidt, *Catal. Sci. Technol.* **2014**, *4*, 3800.

[16] K. J. J. Mayrhofer, G. K. H. Wiberg, M. Arenz, *J. Electrochem. Soc.* **2008**, *155*, P1.

[17] S. Anantharaj, S. R. Ede, K. Sakthikumar, K. Karthick, S. Mishra, S. Kundu, *ACS Catal.* **2016**, *6*, 8069.

[18] Y. Shi, B. Zhang, *Chem. Soc. Rev.* **2016**, *45*, 1529.

[19] X. Zou, Y. Zhang, *Chem. Soc. Rev.* **2015**, *44*, 5148.

[20] J. N. Hansen, H. Prats, K. K. Toudahl, N. Mørch Secher, K. Chan, J. Kibsgaard, I. Chorkendorff, *ACS Energy Lett.* **2021**, *6*, 1175.

[21] N. Cheng, S. Stambula, D. Wang, M. N. Banis, J. Liu, A. Riese, B. Xiao, R. Li, T. K. Sham, L. M. Liu, G. A. Botton, X. Sun, *Nat. Commun. 2016 71* **2016**, *7*, 1.

[22] Y. Lee, J. Suntivich, K. J. May, E. E. Perry, Y. Shao-Horn, *J. Phys. Chem. Lett.* **2012**, *3*, 399.

[23] K. A. Stoerzinger, R. R. Rao, X. R. Wang, W. T. Hong, C. M. Rouleau, Y. Shao-Horn,

Chem **2017**, *2*, 668.

[24] T. Reier, M. Oezaslan, P. Strasser, *ACS Catal.* **2012**, *2*, 1765.

[25] H. Zhang, X. Wu, C. Chen, C. Lv, H. Liu, Y. Lv, J. Guo, J. Li, D. Jia, F. Tong, *Chem. Eng. J.* **2021**, *417*, 128069.

[26] H. Kim, T. Y. Yoo, M. S. Bootharaju, J. H. Kim, D. Y. Chung, T. Hyeon, *Adv. Sci.* **2022**, *9*, 2104054.

[27] J. Yi, W. H. Lee, C. H. Choi, Y. Lee, K. S. Park, B. K. Min, Y. J. Hwang, H. S. Oh, *Electrochem. commun.* **2019**, *104*, 106469.

[28] S. M. Galani, A. Mondal, D. N. Srivastava, A. B. Panda, *Int. J. Hydrogen Energy* **2020**, *45*, 18635.

[29] M. Zhou, C. Li, J. Fang, *Chem. Rev.* **2021**, *121*, 736.

[30] K. D. Gilroy, A. Ruditskiy, H. C. Peng, D. Qin, Y. Xia, *Chem. Rev.* **2016**, *116*, 10414.

[31] P. Wu, H. Zhang, Y. Qian, Y. Hu, H. Zhang, C. Cai, *J. Phys. Chem. C* **2013**, *117*, 19091.

[32] Y. Zeng, Z. Shao, H. Zhang, Z. Wang, S. Hong, H. Yu, B. Yi, *Nano Energy* **2017**, *34*, 344.

[33] H. H. Li, Q. Q. Fu, L. Xu, S. Y. Ma, Y. R. Zheng, X. J. Liu, S. H. Yu, *Energy Environ. Sci.* **2017**, *10*, 1751.

[34] C. Wang, Y. Hou, J. Kim, S. Sun, *Angew. Chemie Int. Ed.* **2007**, *46*, 6333.

[35] C. Wang, Y. Sui, G. Xiao, X. Yang, Y. Wei, G. Zou, B. Zou, *J. Mater. Chem. A* **2015**, *3*, 19669.

[36] S. M. Alia, S. Shulda, C. Ngo, S. Pylypenko, B. S. Pivovar, *ACS Catal.* **2018**, *8*, 2111.

[37] F. Lv, J. Feng, K. Wang, Z. Dou, W. Zhang, J. Zhou, C. Yang, M. Luo, Y. Yang, Y. Li, P. Gao, S. Guo, *ACS Cent. Sci.* **2018**, *4*, 1244.

[38] J. Su, Y. Yang, G. Xia, J. Chen, P. Jiang, Q. Chen, *Nat. Commun. 2017 81* **2017**, *8*, 14969.

[39] J. Yang, Q. Shao, B. Huang, M. Sun, X. Huang, *iScience* **2019**, *11*, 492.

[40] M. Wei, L. Huang, S. Huang, Z. Chen, D. Lyu, X. Zhang, S. Wang, Z. Q. Tian, P. K. Shen, *J. Catal.* **2020**, *381*, 385.

[41] Y. Pi, Q. Shao, P. Wang, J. Guo, X. Huang, *Adv. Funct. Mater.* **2017**, *27*, 1700886.

[42] L. Fu, G. Cheng, W. Luo, *J. Mater. Chem. A* **2017**, *5*, 24836.

[43] N. Du, C. Wang, X. Wang, Y. Lin, J. Jiang, Y. Xiong, N. Du, C. Wang, X. Wang, Y. Lin, J. Jiang, Y. Xiong, *Adv. Mater.* **2016**, *28*, 2077.

[44] J. Feng, F. Lv, W. Zhang, P. Li, K. Wang, C. Yang, B. Wang, Y. Yang, J. Zhou, F. Lin, G.-C. Wang, S. Guo, J. Feng, F. Lv, W. Zhang, P. Li, K. Wang, C. Yang, B. Wang, Y. Yang, J. Zhou, F. Lin, S. Guo, G. Wang, *Adv. Mater.* **2017**, *29*, 1703798.

[45] T. Kwon, H. Hwang, Y. Jin Sa, J. Park, H. Baik, S. Hoon Joo, K. Lee, T. Kwon, H.

Hwang, J. Park, K. Lee, Y. J. Sa, S. H. Joo, H. Baik, *Adv. Funct. Mater.* **2017**, *27*, 1604688.

[46] X. Cao, Y. Han, C. Gao, Y. Xu, X. Huang, M. Willander, N. Wang, *Nano Energy* **2014**, *9*, 301.

[47] F. Yang, Y. Zhao, Y. Du, Y. Chen, G. Cheng, S. Chen, W. Luo, F. Yang, Y. Zhao, Y. Du, Y. Chen, G. Cheng, S. Chen, W. Luo, *Adv. Energy Mater.* **2018**, *8*, 1703489.

[48] Q. Qin, H. Jang, L. Chen, P. Li, T. Wei, X. Liu, J. Cho, *ACS Appl. Mater. Interfaces* **2019**, *11*, 16461.

[49] T. Zheng, C. Shang, Z. He, X. Wang, C. Cao, H. Li, R. Si, B. Pan, S. Zhou, J. Zeng, *Angew. Chemie* **2019**, *131*, 14906.

[50] Y. Jiang, X. Wu, Y. Yan, S. Luo, X. Li, J. Huang, H. Zhang, D. Y. Yang Jiang, X. Wu, Y. Yan, S. Luo, X. Li, J. Huang, H. Zhang, D. Yang, *Small* **2019**, *15*, 1805474.

[51] P. Wang, X. Zhang, J. Zhang, S. Wan, S. Guo, G. Lu, J. Yao, X. Huang, *Nat. Commun. 2017 81* **2017**, *8*, 14580.

[52] S. L. Zhang, X. F. Lu, Z. P. Wu, D. Luan, X. W. Lou, *Angew. Chemie Int. Ed.* **2021**, *60*, 19068.

[53] Y. Le, F. Mehmood, S. Lee, J. Greeley, B. Lee, S. Seifert, R. E. Winansl, W. Elám, R. J. Meyer, P. C. Redfern, D. Teschner, R. Schlö'Gl, M. J. Pellin, L. A. Curtiss, S. Vajda, *Science (80-.).* **2010**, *328*, 224.

[54] J. Cai, R. Javed, D. Ye, H. Zhao, J. Zhang, *J. Mater. Chem. A* **2020**, *8*, 22467.

[55] X. F. Yang, A. Wang, B. Qiao, J. Li, J. Liu, T. Zhang, *Acc. Chem. Res.* **2013**, *46*, 1740.

[56] H. Zhang, G. Liu, L. Shi, J. Ye, *Adv. Energy Mater.* **2018**, *8*, 1701343.

[57] Y. Peng, B. Lu, S. Chen, *Adv. Mater.* **2018**, *30*, 1801995.

[58] J. Cordón, G. Jiménez-Osés, J. M. López-De-Luzuriaga, M. Monge, *Nat. Commun. 2017 81* **2017**, *8*, 1657.

[59] N. Cheng, S. Stambula, D. Wang, M. N. Banis, J. Liu, A. Riese, B. Xiao, R. Li, T. K. Sham, L. M. Liu, G. A. Botton, X. Sun, *Nat. Commun.* **2016**, *7*, 13638.

[60] H. Zhang, P. An, W. Zhou, B. Y. Guan, P. Zhang, J. Dong, X. W. Lou, *Sci. Adv.* **2018**, *4*.

[61] Z. Luo, Y. Ouyang, H. Zhang, M. Xiao, J. Ge, Z. Jiang, J. Wang, D. Tang, X. Cao, C. Liu, W. Xing, *Nat. Commun. 2018 91* **2018**, *9*, 2120.

[62] Z. Zhang, C. Feng, C. Liu, M. Zuo, L. Qin, X. Yan, Y. Xing, H. Li, R. Si, S. Zhou, J. Zeng, *Nat. Commun. 2020 111* **2020**, *11*, 1215.

[63] Q. Wang, X. Huang, Z. L. Zhao, M. Wang, B. Xiang, J. Li, Z. Feng, H. Xu, M. Gu, *J. Am. Chem. Soc.* **2020**, *142*, 7425.

[64] Y. Xu, W. Tu, B. Zhang, S. Yin, Y. Huang, M. Kraft, R. Xu, Y. Xu, W. Tu, S. Yin, R. Xu, B. Zhang, Y. Huang, M. Kraft, *Adv. Mater.* **2017**, *29*, 1605957.

[65] C. Wang, H. Yang, Y. Zhang, Q. Wang, *Angew. Chemie Int. Ed.* **2019**, *58*, 6099.

[66] T. Li, G. Luo, K. Liu, X. Li, D. Sun, L. Xu, Y. Li, Y. Tang, T. Li, G. Luo, K. Liu, X. Li, D. Sun, L. Xu, Y. Li, Y. Tang, *Adv. Funct. Mater.* **2018**, *28*, 1805828.

[67] Y. Yang, Z. Lin, S. Gao, J. Su, Z. Lun, G. Xia, J. Chen, R. Zhang, Q. Chen, *ACS Catal.* **2017**, *7*, 469.

[68] J. Chen, H. Chen, T. Yu, R. Li, Y. Wang, Z. Shao, S. Song, *Recent Advances in the Understanding of the Surface Reconstruction of Oxygen Evolution Electrocatalysts and Materials Development*, Vol. 4, Springer Singapore, **2021**.

[69] B. R. Wygant, K. Kawashima, C. B. Mullins, *ACS Energy Lett.* **2018**, *3*, 2956.

[70] Y. Wang, Y. Zhu, S. Zhao, S. She, F. Zhang, Y. Chen, T. Williams, T. Gengenbach, L. Zu, H. Mao, W. Zhou, Z. Shao, H. Wang, J. Tang, D. Zhao, C. Selomulya, *Matter* **2020**, *3*, 2124.

[71] J. Wang, T. Liao, Z. Wei, J. Sun, J. Guo, Z. Sun, *Small Methods* **2021**, *5*, 2000988.

[72] A. Jiang, B. Zhang, Z. Li, G. Jin, J. Hao, *Chem. – An Asian J.* **2018**, *13*, 1438.

[73] H. Xu, H. Jia, B. Fei, Y. Ha, H. Li, Y. Guo, M. Liu, R. Wu, *Appl. Catal. B Environ.* **2020**, *268*, 118404.

[74] N. Yao, P. Li, Z. Zhou, R. Meng, G. Cheng, W. Luo, *Small* **2019**, *15*, 1901993.

[75] R. Zhang, J. Huang, G. Chen, W. Chen, C. Song, C. Li, K. Ostrikov, *Appl. Catal. B Environ.* **2019**, *254*, 414.

[76] J. Kibsgaard, C. Tsai, K. Chan, J. D. Benck, J. K. Nørskov, F. Abild-Pedersen, T. F. Jaramillo, *Energy Environ. Sci.* **2015**, *8*, 3022.

[77] X. Guo, X. Yu, Z. Feng, J. Liang, Q. Li, Z. Lv, B. Liu, C. Hao, G. Li, *ACS Sustain. Chem. Eng.* **2018**, *6*, 8150.

[78] L. M. Cao, Y. W. Hu, S. F. Tang, A. Iljin, J. W. Wang, Z. M. Zhang, T. B. Lu, *Adv. Sci.* **2018**, *5*, 1800949.

[79] Y. Sun, K. Xu, Z. Wei, H. Li, T. Zhang, X. Li, W. Cai, J. Ma, H. J. Fan, Y. Li, *Adv. Mater.* **2018**, *30*, 1802121.

[80] H. Zhang, R. Lv, *J. Mater.* **2018**, *4*, 95.

[81] Y. Jia, K. Jiang, H. Wang, X. Yao, *CHEMPR* **2019**, *5*, 1371.

[82] C. Guo, X. Liu, L. Gao, X. Ma, M. Zhao, J. Zhou, X. Kuang, W. Deng, X. Sun, Q. Wei, *J. Mater. Chem. A* **2019**, *7*, 21704.

[83] J. Zhu, Z. C. Wang, H. Dai, Q. Wang, R. Yang, H. Yu, M. Liao, J. Zhang, W. Chen, Z. Wei, N. Li, L. Du, D. Shi, W. Wang, L. Zhang, Y. Jiang, G. Zhang, *Nat. Commun. 2019 101* **2019**, *10*, 1348.

[84] C. Tsai, H. Li, S. Park, J. Park, H. S. Han, J. K. Nørskov, X. Zheng, F. Abild-Pedersen, *Nat. Commun.* **2017**, *8*, 15113.

[85] L. Li, Z. Qin, L. Ries, S. Hong, T. Michel, J. Yang, C. Salameh, M. Bechelany, P. Miele, D. Kaplan, M. Chhowalla, D. Voiry, *ACS Nano* **2019**, *13*, 6824.

[86] C. Kong, Y. X. Han, L. jie Hou, P. J. Yan, *Int. J. Hydrogen Energy* **2022**, *47*, 242.

[87] Y. Xiong, L. Xu, C. Jin, Q. Sun, *Appl. Catal. B Environ.* **2019**, *254*, 329.

[88] Y. Li, K. Dastafkan, Q. Sun, Y. Ma, X. Wang, X. Yang, Z. Wang, C. Zhao, *Electrochim. Acta* **2021**, *379*, 138042.

[89] P. Wang, Z. Pu, W. Li, J. Zhu, C. Zhang, Y. Zhao, S. Mu, *J. Catal.* **2019**, *377*, 600.

[90] D. Wang, Y. Song, T. Guo, R. Liu, Z. Wu, *Sustain. Energy Fuels* **2022**, *6*, 2243.

[91] A. Wu, Y. Gu, Y. Xie, C. Tian, H. Yan, D. Wang, X. Zhang, Z. Cai, H. Fu, *ACS Appl. Mater. Interfaces* **2019**, *11*, 25986.

[92] M. Zhou, Q. Weng, X. Zhang, X. Wang, Y. Xue, X. Zeng, Y. Bando, D. Golberg, *J. Mater. Chem. A* **2017**, *5*, 4335.

Chapter 2

Atomic Rearrangement of Mixed Metal Oxide/Hydroxide Nanosheet to Develop $MoSe_2@NiCo_2Se_4$ Heterostructure for Efficient Hydrogen Evolution Reaction

Chapter 2

Atomic Rearrangement of Mixed Metal Oxide/Hydroxide Nanosheet to Develop $MoSe_2$@$NiCo_2Se_4$ Heterostructure for Efficient Hydrogen Evolution Reaction

The successful implementation of hydrogen-based alternative energy solutions depends critically on the design and synthesis of active, stable and affordable materials for efficient hydrogen production. Rational design of heterostructures based on earth-abundant transition metals is a successful strategy to achieve this goal, but realization of such advanced nanostructures with adequate electronic control is challenging. Here, we present the heterostructure of edge-oriented molybdenum selenide ($MoSe_2$) and nickel-cobalt-selenide ($NiCo_2Se_4$) realized through selenization of mixed metal oxide/hydroxide. As-developed sheet-on-sheet heterostructure shows excellent HER performance, requiring an overpotential of 89 mV to get a current density 10 mA cm^{-2}, and a Tafel slope of 65 mV dec^{-1}. Density functional theory calculation reveals the importance of rational heterostructure design for efficient HER electrocatalysis.

2.1 Introduction

Hydrogen generation by electrolysis of water provides a suitable pathway to convert and store intermittent renewable energy like solar or wind.[1] However, efficiency of this process heavily relies on the catalytic performance and stability of the catalysts.[2] Noble metals such as platinum (Pt) based electrocatalysts show the highest performance in HER with excellent durability, but its high cost and scarcity are serious concerns for the practical implementation of hydrogen fuel-based economy.[3] Although enormous research efforts have already been paid to develop alternative HER catalysts based on earth-abundant transition metal oxides, sulphides, selenides and phosphides to replace noble metals, but their performances are still not satisfactory.[4–8] In this circumstances, highly effective technology that has emerged for efficient water electrolysis is heterostructure formation of earth-abundant catalysts for tailorable properties via synergistic electronic coupling, which cannot be obtained with the single component.[9,10] However, complex multistep processing, adequate catalytic configuration challenges, and/or intrinsic performance limitations of earth-abundant

catalysts still hamper the progress of these heterostructure systems for HER reactions. In order to come up with the next generation of water electrolysis induced hydrogen generation, these existing problems need to be resolved.

Heterostructure consists of complementing properties that can address the aforementioned challenges if active sites are made to expose preferentially, and electronic highway is established up to these active sites. For example, the edges of molybdenum selenide ($MoSe_2$) are known to be the active sites for HER catalysis,[11] thus its edge-oriented vertical structure is anticipated to be ideal configuration to maximize hydrogen evolution, provided the base nanomaterial of the heterostructure offer low resistive path for the electrons to reach from the external circuit to those edge sites. In particular, bimetallic transition metal selenides like nickel cobalt selenide ($NiCo_2Se_4$) could be an excellent choice as the base of the heterostructure, as it shows a low resistive metallic property.[12]

Here, we present a heterostructure of $MoSe_2$ and $NiCo_2Se_4$ nanosheets via selenization-induced atomic rearrangement of mixed metal oxide/hydroxide nanosheets (MoO_3/Ni-$Co(OH)_2$). Selenization of MoO_3/Ni-$Co(OH)_2$ nanosheets triggers the growth of longitudinal $MoSe_2$ nanosheet arrays perpendicular to the $NiCo_2Se_4$ nanosheet substrate. Importantly, $MoSe_2$ shows a distinctive interlayer-expanded structure as compared to its bulk form. This particular $MoSe_2$ layer structure (vertical orientation and interlayer expansion) ensures a large surface area with accessible catalytic edges. Density functional theory (DFT) calculation reveals that this unique structural feature allows the energy barrier reduction for HER reaction as compared to its bulk counterpart. This vertical structure is also utilized as the charge carrier pathway from catalytic active edges to the conducting highway of $NiCo_2Se_4$, bypassing the interlayer hopping within $MoSe_2$. This ensured high HER activity with a very small overpotential of 89 mV at a current density of 10 mA cm^{-2}.

2.2 Experimental Section

2.2.1 Materials

Cobalt (II) chloride hexahydrate ($CoCl_2.6H_2O$), platinum (20 wt %) on graphitized carbon (Pt/C) and Nafion (5 wt%) were purchased from Sigma-Aldrich. Nickel chloride hexahydrate ($NiCl_2.6H_2O$), sodium molybdate dihydrate ($Na_2MoO_4.2H_2O$) were purchased from Alfa-Aesar. Urea (CH_4N_2O), ammonium fluoride (NH_4F), potassium

hydroxide pellets (KOH) were bought from Merck. Nickel foam (NF) having a thickness of 1.6 mm have been obtained from MTI. All the chemicals have been used without further purification. A Millipore type III deionized water with a resistance of 18.2 MΩ was used throughout all the experiments.

2.2.2 Fabrication of $MoSe_2$@$NiCo_2Se_4$ sheet in sheet heterostructure

NF (2 cm × 6 cm) was cleaned with 3M HCl, ethanol and water under ultrasonication for 15 min each to remove surface impurities. 1 mmol $NiCl_2.6H_2O$, 4 mmol $CoCl_2.6H_2O$, 1.5 mmol $Na_2MoO_4.2H_2O$, 20 mmol urea and 10 mmol NH_4F were dissolved in 70 ml distilled water and stirred for 15 min in room temperature to make a homogeneous solution. Then the mixed solution along with the washed NF was transferred to a 100 ml autoclave and heated to 120˚C for 6h. After the reaction autoclave was allowed to cool naturally to room temperature and NF was taken out and washed with water, ethanol and then dried in a vacuum oven at room temperature to obtain purple coloured MoO_3/Ni-$Co(OH)_2$ sheets on NF substrate. Finally, $MoSe_2$@$NiCo_2Se_4$ sheet in sheet heterostructure on NF was prepared by transferring MoO_3/Ni-$Co(OH)_2$ (1 cm × 3 cm) into a 25 ml autoclave with a mixed solution of 0.1 M selenium powder, 0.13 g of sodium borohydride ($NaBH_4$) in 15 ml water. After the hydrothermal reaction at 140˚C for 2h, a black product on NF surface was obtained which was then washed with water, ethanol and dried in vacuum oven at room temperature to acquire $MoSe_2$@$NiCo_2Se_4$ heterostructure on NF.

2.2.3 Material characterizations

Powder XRD patterns have been taken by Rigaku X-ray diffractometer at room temperature with Cu Kα radiation (λ=1.5418 Å). FESEM images were captured with Zeiss Sigma 300 FESEM whereas energy dispersive X-ray spectroscopic investigation was conducted in Ametek EDAX attached with Zeiss Sigma 300 FE-SEM. HRTEM analysis and STEM analysis were done in Titan TM 80-300 (FEI) with probe Cs corrector. For elemental analysis and ionic state determination, XPS was done in ESCALAB Xi+ (Thermo Fisher) instrument. Raman vibrational study was performed in Horiba LabRam HR with a 514 nm laser source.

2.2.4 Electrochemical measurements

Electrocatalytic HER performance was tested in three-electrode configuration with saturated calomel electrode (CHI 150) as reference electrode, Pt wire as counter electrode and 1M KOH as electrolyte in a PARSTAT 3000A-DX potentiostat. A piece of 1×1 cm^2 of synthesized samples on NF was directly used as the working electrode. All polarisation curves are taken at 5 mV s^{-1} scan rate and have been corrected through iR compensation. All the potentials were referred against reversible hydrogen electrode (RHE) according to the formula,

$$E_{RHE} = E_{SCE} + 0.059 \times 14 + 0.242 \quad 2.1$$

Impedance spectroscopy of samples were measured in a frequency range of 10 kHz to 0.1 Hz at an AC amplitude of 10 mV.

The double layer capacitance (C_{dl}) was calculated by observing cyclic voltammetry curves (CV) in a potential range of 1.1-1.2 V vs. RHE free from any faradaic region. Half of the difference of anodic current (J_a) and cathodic current (J_c) was plotted against potential vs. RHE at a potential of 1.15 V vs. RHE. Slope of the above curve provides C_{dl} value which is also estimated to be proportional to ECSA of samples.

2.2.5 Computational details

All the calculations were performed using spin polarized DFT as implemented in the Quantum Espresso package with ultrasoft pseudopotentials.[13,14] Grimme's D3 dispersion correction was used to account for the long-range van der Waal's interactions.[15] Perdew-Burke-Ernzerhof (PBE) generalized gradient approximation (GGA) was employed for exchange correlation functional with a kinetic energy cutoff of 550 eV for the plane waves.[16] The basal plane of the HER catalyst was modeled using monoclinic $NiCo_2Se_4$ with optimized lattice parameters of a = 12.5 Å b = 3.6 Å c= 6.2 Å. A 2x2 monolayer of 2H-$MoSe_2$ was vertically aligned over the (100) plane of 30 atom 1x2 $NiCo_2Se_4$ supercell to model the hetero-structure. Hydrogen adsorption studies were performed on Mo edge along with Mo edges with 50% and 100% Se coverage.[17] To address the strong interaction in localized d-orbitals of transition metals in $NiCo_2Se_4$, an effective U parameter of 6.6 eV for Ni 3d and 3.7 eV for Co 3d states were used as reported in previous studies.[18–20] All the structures were relaxed until the force on each atom was less than 0.02 eV/ Å along with a total energy tolerance of 10^{-6} eV/atom. Vacuum spacing of 15 Å was applied to separate the periodic slabs in all the structural models. The hydrogen adsorption free energies (ΔG_H) were determined using the following equation

$$\Delta G_H = \Delta E_H + \Delta E_{ZPE} - T\Delta S_H \quad 2.2$$

where, the chemisorption energy of hydrogen, ΔE_H is defined as,

$$\Delta E_H = \Delta E_{Surface+H} - \Delta E_{Surface} - \frac{1}{2}\Delta E_{H2} \quad 2.3$$

where, $\Delta E_{Surface+H}$ and $\Delta E_{Surface}$ are the total energies of surfaces with and without adsorbed H atom respectively. ΔE_{ZPE} and ΔS_H is the zero-point energy and entropy difference between adsorbed hydrogen and hydrogen in the gas phase respectively. Considering the above parameters, the Gibbs free energy for hydrogen adsorption can finally be written as [21],

$$\Delta G_{ZPE} = \Delta E_H + 0.24 \quad 2.4$$

2.3 Result and Discussion

2.3.1 Morphological analyses

Mixed oxide/hydroxide nanosheets of molybdenum, and nickel/cobalt (MoO_3/Ni-$Co(OH)_2$) were uniformly grown over nickel foam via hydrothermal process. Pristine MoO_3/Ni-$Co(OH)_2$ structure is successfully transformed into uniform $MoSe_2$@$NiCo_2Se_4$ heterostructure through selenization as indicated by field emission scanning electron microscope (FESEM) images (Figure 2.1a and b). Before selenization, MoO_3/Ni-$Co(OH)_2$ structure exhibited thin-nanosheets-induced porous network structure with homogeneous surface (Figure 2.1a). Selenization transformed this morphology into hierarchical structure in which ~3 nm thick nanosheets were found to grow on base nanosheets network (Figure 2.1b). Through high resolution transmission electron microscope (HRTEM) (Figure 2.2a and b), the vertical orientation of $MoSe_2$ is observed in the form of parallel lattice fringes (2.8 nm) which is similar to the estimated thickness of this layered structure from FESEM. Lattice fringes from HRTEM well represent the layer structure of $MoSe_2$, but the average interlayer distance

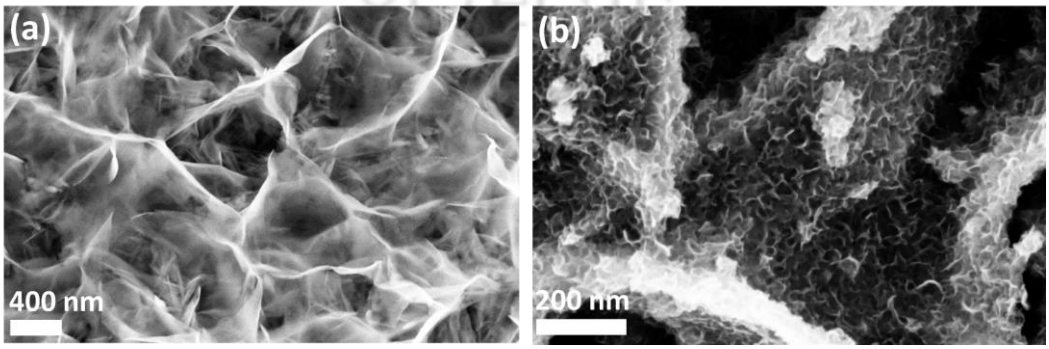

Figure 2.1. Morphological characterisation: FESEM images of (a) MoO_3/Ni-$Co(OH)_2$ showing sheet like structure, (b) $MoSe_2$@$NiCo_2Se_4$ heterostructure showing sheet-on-sheet structure.

(0.78 nm) is different from the theoretical interlayer spacing of bulk $MoSe_2$ (0.64 nm).[22] This shows that, the expanded $MoSe_2$ structures were realized via selenization induced process.

HRTEM image of $MoSe_2@NiCo_2Se_4$ (Figure 2.2a and b) further reveals that these lattice fringes exist as a bundle of multi-layers (3-6 layers) with (002) planes being perpendicular to the basal plane of $NiCo_2Se_4$ sheet, indicating vertically oriented $MoSe_2$ edge structure. Magnified view of the sample through Cs corrected HRTEM analysis (Figure 2.2c) shows inter-planner spacing of 0.197 nm and 0.173 nm, corresponding to (311) and (-313) crystal planes of $NiCo_2Se_4$, respectively. Selected area electron diffraction pattern (SAED) (Figure 2.2d) shows concentric rings with inter-planar spacing of (002), (311) and (-311) of $NiCo_2Se_4$. These cumulative evidences suggest the well-developed $MoSe_2@NiCo_2Se_4$ heterostructure with the unique structural features of $MoSe_2$ vertical orientation and polycrystalline $NiCo_2Se_4$ substrate.

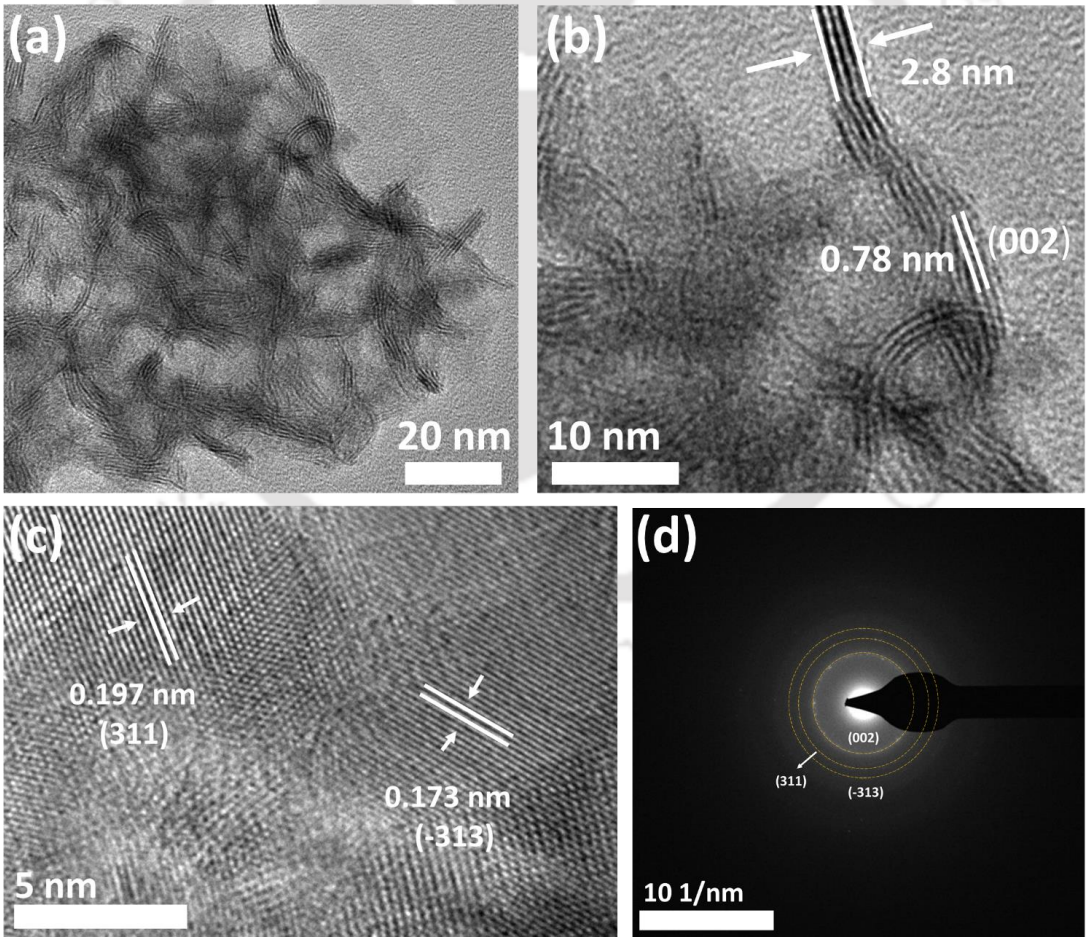

Figure 2.2. Morphological characterisation: (a) HRTEM image, (b) magnified HRTEM image and (c) Cs corrected HRTEM image of $MoSe_2@NiCo_2Se_4$. (d) SAED pattern of $MoSe_2@NiCo_2Se_4$ confirming the planes (002), (311) and (-313) of $NiCo_2Se_4$ in the heterostructure.

2.3.2 Structural analyses

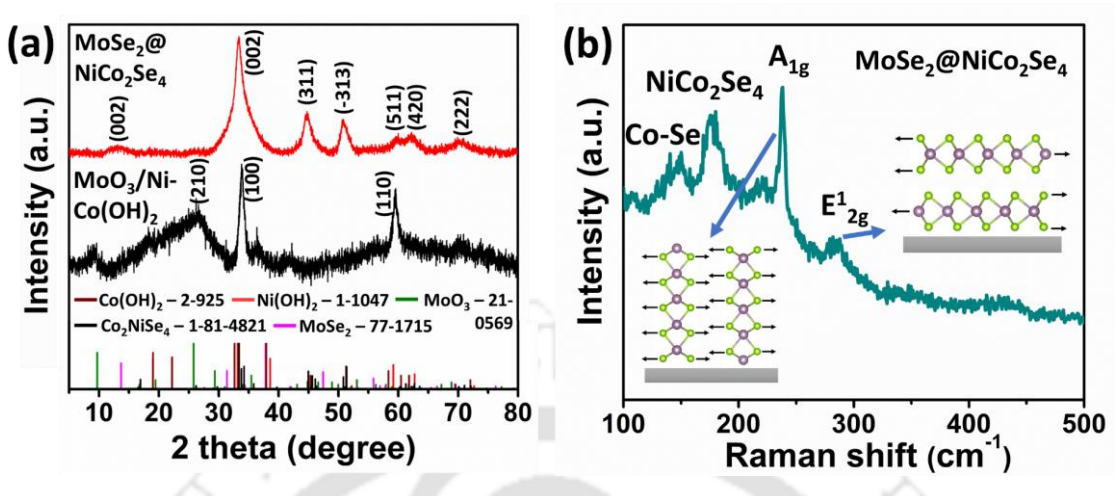

Figure 2.3. Structural characterisation: (a) XRD pattern of MoO_3/Ni-$Co(OH)_2$ and $MoSe_2$@$NiCo_2Se_4$. (b) Raman spectra of $MoSe_2$@$NiCo_2Se_4$.

The crystalline phase of the as-synthesized materials (before and after selenization) was also confirmed from X-ray diffraction pattern (XRD). XRD pattern (Figure 2.3a) shows that the starting material consists of nickel-cobalt hydroxide (Ni-$Co(OH)_2$) and molybdenum oxide (MoO_3) mixed phases. On the other hand, $MoSe_2$@$NiCo_2Se_4$ is entirely dominated by the peaks of $NiCo_2Se_4$ and the peaks at 33.4º, 44.6º, 50.7º, 59.8º, 62.3º, 70.3º correspond to (002), (311), (-313), (511), (420) and (222) planes of monoclinic $NiCo_2Se_4$ (JCPDS Card No. 01-081-4821). However, a low intensity broad peak at 12.8º correspond to (002) plane of $MoSe_2$ (JCPDS Card No. 77-1715) of the heterostructure can also be observed for $MoSe_2$@$NiCo_2Se_4$ (Figure 2.3a). These XRD results confirm the phases of $MoSe_2$ and $NiCo_2Se_4$ which is consistent with the phase information from HRTEM lattice images, indicating the successful selenization reaction throughout the whole sample specimen.

Vertical edge-oriented structure of $MoSe_2$ was further confirmed by analysing Raman spectra. The peaks of $MoSe_2$@$NiCo_2Se_4$ (Figure 2.3b) at 238 cm^{-1}, 285 cm^{-1} correspond to Mo-Se out of plane vibration (A_{1g}) and Mo-Se in-plane vibration (E^1_{2g}), whereas peaks at 152 cm^{-1} and 180 cm^{-1} remarks Co-Se vibration and F_{2g} mode of $NiCo_2Se_4$, respectively.[23–26] The high intensity of A_{1g} compared to E^1_{2g} confirms the vertical edge orientation of $MoSe_2$ which is consistent with HRTEM result.[23,24] The affirmative presence of vertical $MoSe_2$ arrays from $MoSe_2$@$NiCo_2Se_4$ suggest the strong connection between selenization process and vertical rearrangement of

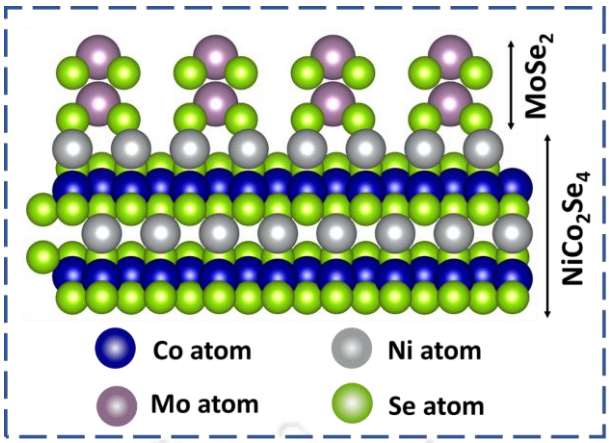

Figure 2.4. Illustration for heterostructure of ultrathin sheet ($MoSe_2$) on sheet ($NiCo_2Se_4$) structure.

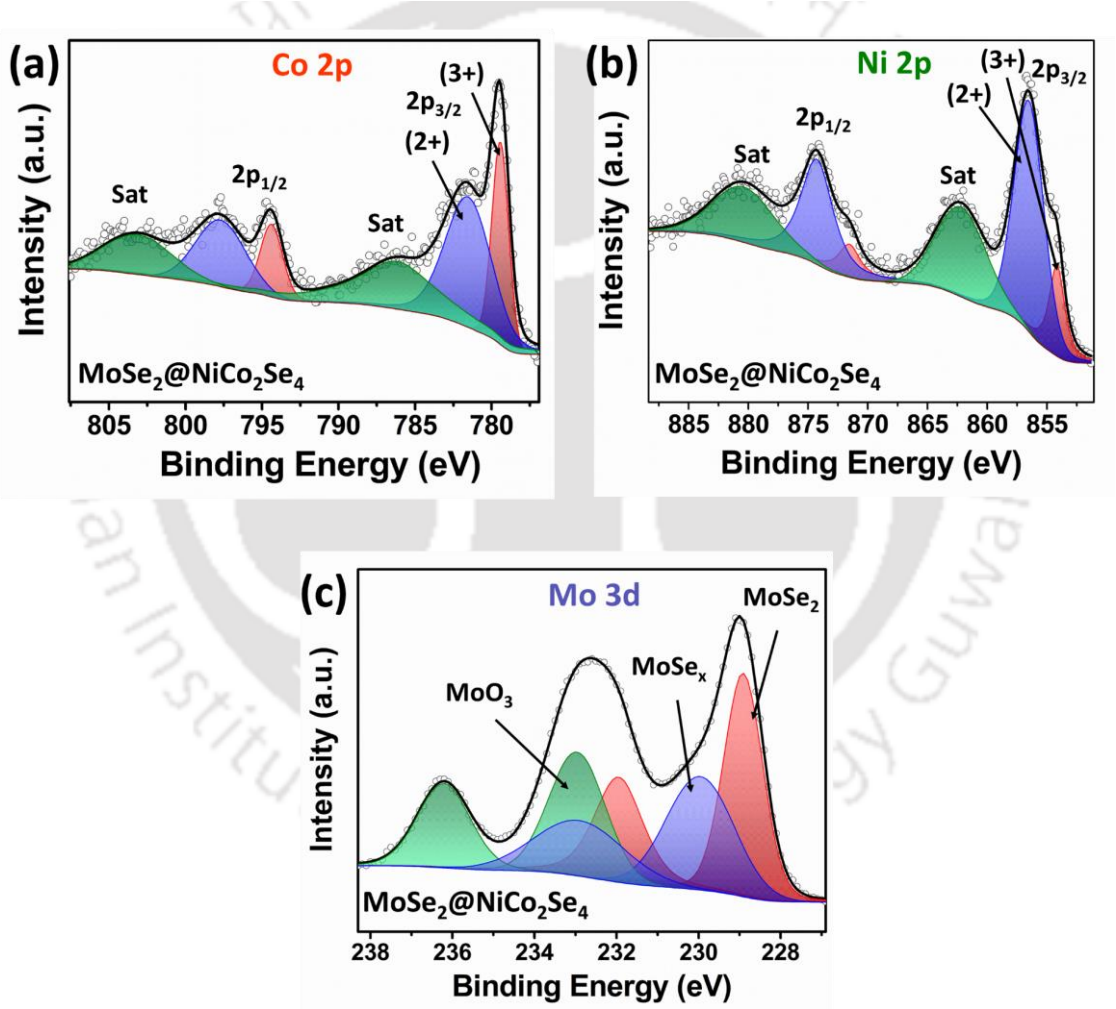

Figure 2.5. XPS study: high resolution XPS spectra for (a) Co 2p, (b) Ni 2p and (c) Mo 3d of $MoSe_2@NiCo_2Se_4$ with their peak fitting.

molybdenum structure; molybdenum having higher atomic radii expels out of the oxide/hydroxide structure and form edge oriented $MoSe_2$ while Ni-Co forms the base

selenide substrate, thereby forming $MoSe_2$@$NiCo_2Se_4$ heterostructure as demonstrated by the schematic representation in Figure 2.4.

Chemical composition and the oxidation states of the elements of as-developed catalysts were investigated through X-ray photoelectron spectroscopy (XPS). For $MoSe_2$@$NiCo_2Se_4$ (Figure 2.5a & b), the deconvoluted core level spectrum of Co 2p (Ni 2p) consists of two sets of spin orbit splitting peaks ($2p_{3/2}$ & $2p_{1/2}$) corresponding to Co^{2+} (Ni^{2+}) at 781.5 eV & 797.7 eV (854.2 eV & 871.6 eV) and Co^{3+} (Ni^{3+}) at 779.4 eV & 794.4 eV (856.5 eV & 874.3 eV) respectively.[27,28] This confirms the presence of $NiCo_2Se_4$ phase within the pristine selenization sample.

Meanwhile, high resolution Mo 3d XPS spectra (Figure 2.5c) of $MoSe_2$@$NiCo_2Se_4$ has been splitted into $3d_{5/2}$ and $3d_{3/2}$ which correspond to the Mo^{4+} (doublet at 228.9 eV and 231.9 eV) from $MoSe_2$,[29] Mo^{6+} (doublet at 232.9 eV and 236.2 eV) from MoO_3,[30] and Mo^{5+} (229.9 eV and 232.9 eV)[31] linked to amorphous $MoSe_x$ present in the system.

2.3.3 HER catalytic performance

HER catalytic activity of $MoSe_2$@$NiCo_2Se_4$ grown over nickel foam was evaluated in 1M KOH solution along with parent MoO_3@Ni-$Co(OH)_2$ phase and commercial Pt/C as the reference. Linear sweep voltammetry (LSV) curves in Figure 2.6a show that $MoSe_2$@$NiCo_2Se_4$ has the highest HER activity, requiring an overpotential of 89 mV to deliver a current density of 10 mA cm^{-2}. This overpotential is substantially lower than the overpotential required for MoO_3@Ni-$Co(OH)_2$ (189 mV) and is comparable to Pt/C (35 mV). Notably, it requires only 156 mV and 227 mV for $MoSe_2$@$NiCo_2Se_4$ to achieve a very high current density of 100 mA cm^{-2} and 500 mA cm^{-2}, signifying its excellent HER catalytic activity.

Catalytic efficiency was further investigated by estimating the Tafel slope (Figure 2.6b) of materials. $MoSe_2$@$NiCo_2Se_4$ shows Tafel slope of 65 mV dec^{-1} whereas MoO_3/Ni-$Co(OH)_2$ (95 mV dec^{-1}) shows relatively higher values, suggesting significantly improved HER kinetics upon selenization (Table 2.1). The outstanding performance of $MoSe_2$@$NiCo_2Se_4$ heterostructure surpasses many other state-of-the-art earth abundant catalysts, possessing superior HER performance metrics (Figure 2.6c and Table 2.2).[32–41] Importantly, the as-developed $MoSe_2$@$NiCo_2Se_4$ heterostructure

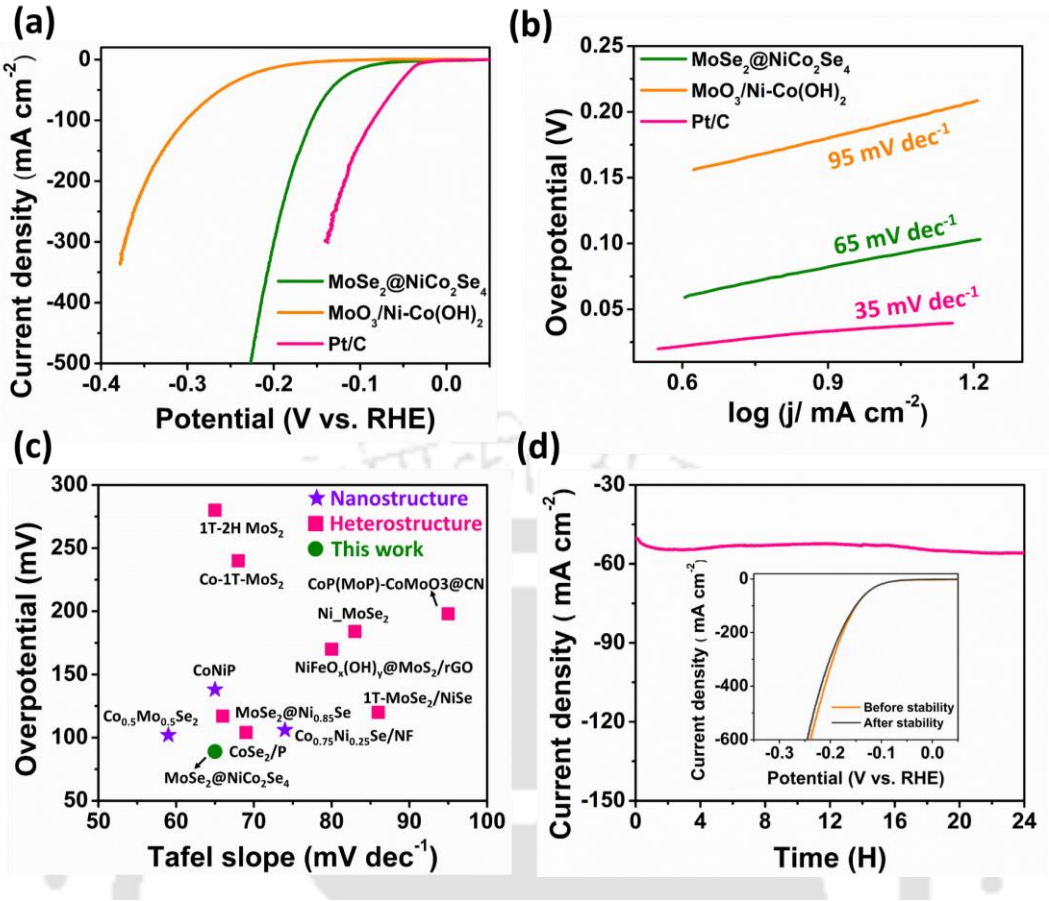

Figure 2.6. Electrochemical HER performance: (a) HER polarisation curves with *iR* correction for $MoSe_2@NiCo_2Se_4$, MoO_3/Ni-Co(OH)$_2$ and Pt/C in 1 M KOH solution, (b) corresponding Tafel plots of different catalysts. (c) Comparison of overpotential and Tafel slope of different reference materials at a current density of 10 mA cm^{-2} in 1M KOH solution. (d) Long term chronoamperometry test at -0.135 V vs. RHE recorded for 24 h. Inset shows the LSV curves before and after stability test.

displays excellent operational stability for long duration (Figure 2.6d), maintaining 50 mA cm^{-2} current density throughout the 24 h operation at a constant potential of -0.135

Table 2.1: Summary of HER performance of different synthesized samples

Samples	η_{10} (mV)	η_{100} (mV)	η_{500} (mV)	Tafel slope (mV dec^{-1})	R_s (Ω)	R_{ct} (Ω)
$MoSe_2@NiCo_2Se_4$	89	156	227	65	1.08	1.14
MoO_3/Ni-Co(OH)$_2$	189	301	-	95	1.23	4.52

Table 2.2: Comparison of HER overpotentials at different current densities and Tafel slope for various reported electrocatalysts

Samples	η_{10} (mV)	η_{100} (mV)	Tafel slope (mV dec^{-1})	Reference
$MoSe_2@NiCo_2Se_4$	89	156	65	**This work**
1T-2H MoS_2	280	-	65	[41]
Co-1T-MoS_2	240	330[a)]	110	[36]
CoP(MoP)-$CoMoO_3$@CN	198	-	95	[37]
$NiMoSe_2$	184	-	83	[35]
$NiFeO_x(OH)_y@MoS_2$/rGO	170	-	34	[42]
1T-$MoSe_2$/NiSe	120	252[a)]	86	[38]
CoNiP	138	-	65	[40]
$MoSe_2@Ni_{0.85}Se$	117	205	66	[33]
Ni_{SA}-MoS_2	98	-	75	[43]
$Co_{0.75}Ni_{0.25}Se$/NF	106	218[a)]	74	[34]
$Co_{0.5}Mo_{0.5}Se_2$	102	162	59	[39]
$MoS_2/Co_9S_8/Ni_3S_2$/Ni	113	-	85	[44]
$NiSe_2$/Ti	96	200[a)]	82	[45]
Ni_5P_4	150	-	53	[46]
$CoSe_2$/P	104	177[a)]	69	[32]

[a)] *(Data have been collected from HER LSV curve)*

V vs RHE. The LSV curve after stability test (inset of Figure 2.6d) does not deteriorate suggesting its practical use for long-term operation.

To inspect the origin of high HER activity, cyclic voltammetry (CV) scans were taken to measure the electrical double layer capacitance C_{dl}, and hence to evaluate electrochemically active surface area (ECSA). The value of C_{dl} (Figure 2.7a) for $MoSe_2@NiCo_2Se_4$ (15.37 mF cm^{-2}) is much higher in relation to MoO_3/Ni-$Co(OH)_2$ (9.1 mF cm^{-2}), indicating that selenization induced vertical array heterostructure offer much higher ECSA, and hence high HER activity as compared to bulk parental structure is expected. To understand intrinsic HER activity of synthesized samples $MoSe_2@NiCo_2Se_4$ and MoO_3/Ni-$Co(OH)_2$, ECSA normalised LSV curves are presented in Figure 2.7b. This curve shows $MoSe_2@NiCo_2Se_4$ has lower onset potential and higher ECSA normalised current in any given potential compared to MoO_3/Ni-

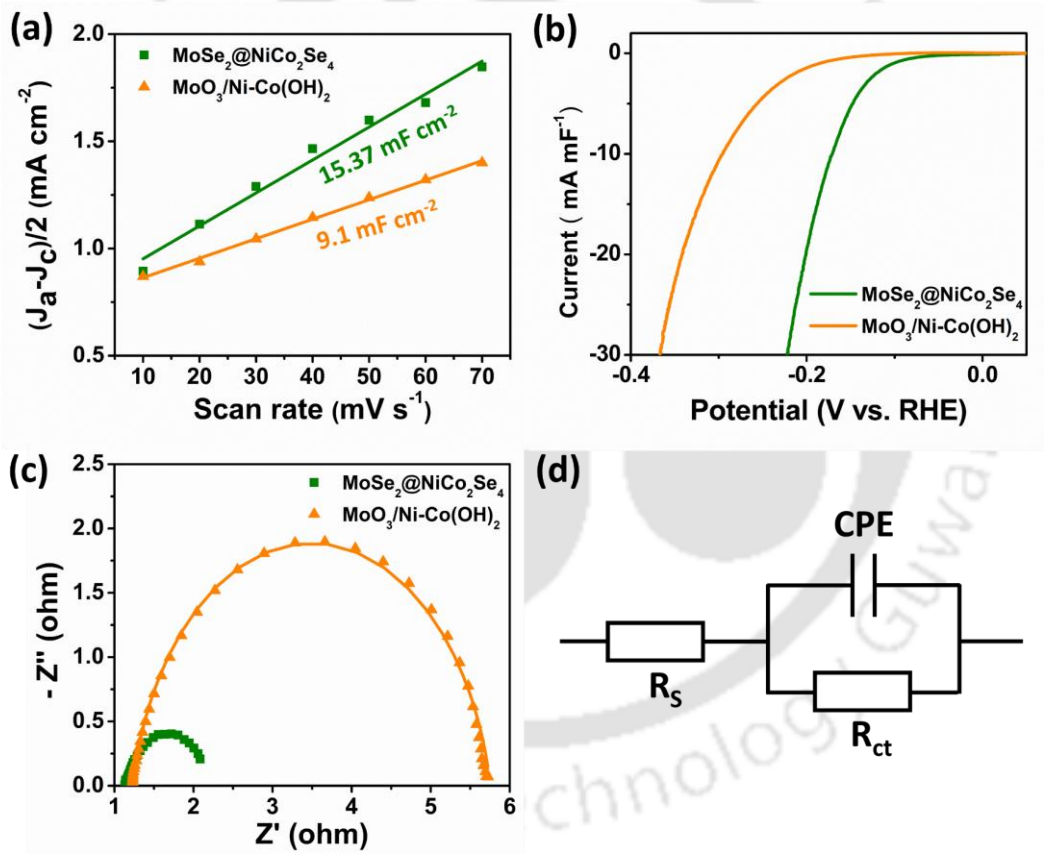

Figure 2.7. Electrochemical HER performance: (a) Different current density versus scan rate plot to estimate the C_{dl} of the ECSA and (b) ECSA normalised HER LSV curves of $MoSe_2@NiCo_2Se_4$ and MoO_3/Ni-$Co(OH)_2$. (c) EIS curves of the corresponding materials with fitting and (d) equivalent circuit diagram used for fitting of the EIS curves measured for HER

$Co(OH)_2$. This suggests after selenization, $MoSe_2@NiCo_2Se_4$ is associated not only with more ECSA value but also with higher intrinsic HER catalytic activity associated with beneficial electronic properties of layer expanded, sheet-on-sheet heterostructure which

is also consistent with our theoretical results as discussed later. Furthermore, charge transfer resistance (R_{ct}) (Figure 2.7c) measured from fitted electrochemical impedance spectra (EIS) according to equivalent diagram as shown in Figure 2.7d, is much lower for $MoSe_2$@$NiCo_2Se_4$ (1.14 Ω) as compared to MoO_3/Ni-$Co(OH)_2$ (4.52 Ω). Fitted values of all the catalysts have been summarized in Table 2.1. The very low value of R_{ct} for the selenide heterostructure confirms beneficial interfacial charge transfer which can activate HER at low overpotential.[47,48] Low R_{ct} value can be related with the adequate electronic structure of the catalyst and open network structure of $MoSe_2$@$NiCo_2Se_4$ (Figure 2.1b) for beneficial mass transport and release of generated H_2 gas.[49] Together with the structural advantage that lead to high ECSA and beneficial release of generated gas, the heterostructure endow unique intrinsic electronic properties related with vertical orientation of $MoSe_2$ and its layer expanded structure, that gives rise to high HER activity. In vertical oriented structure, electron can directly reach to the catalytic edge of $MoSe_2$ from base $NiCo_2Se_4$, bypassing the energy barrier (0.123 V per layer) which arise in conventional $MoSe_2$ structures positioned parallel to the current collector (Figure 2.8).[50,51]

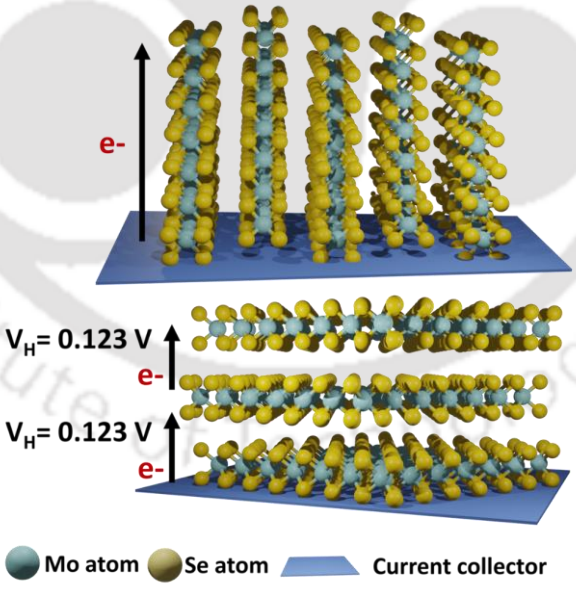

Figure 2.8. Advantage of vertical orientation of $MoSe_2$ compared to non-oriented $MoSe_2$ on substrate

2.4. Theoretical calculation of HER

In order to investigate the electronic benefits of unique features of $MoSe_2$@$NiCo_2Se_4$ heterostructure, subsequent study through detailed density functional theory (DFT) calculation was conducted. This study elucidates the electronic origin of excellent HER activity of $MoSe_2$@$NiCo_2Se_4$ and OER activity of activated Ir-$MoSe_2$@$NiCo_2Se_4$. To investigate the beneficial electronic properties of $MoSe_2$@$NiCo_2Se_4$ to activate HER reaction at low overpotential, at first, the role of expanded interlayer of $MoSe_2$ in

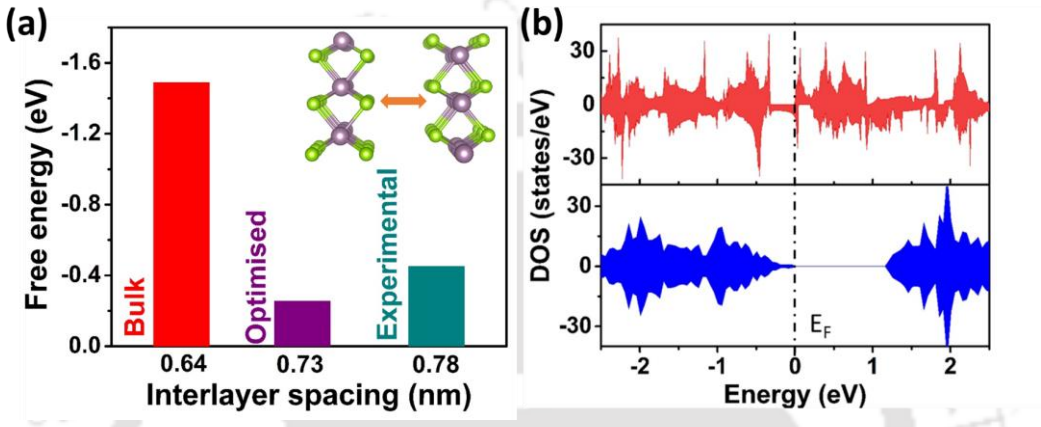

Figure 2.9. DFT analysis of vertical expanded layer $MoSe_2$@$NiCo_2Se_4$ heterostructure: (a) change in Gibbs free energies for H* adsorbed in vertical $MoSe_2$ with different interlayer spacing. (b) DOS of expanded vertical $MoSe_2$ layer (top), DOS of normal $MoSe_2$ surface (bottom).

controlling the rate determining hydrogen adsorption process was investigated. Change in Gibb's free energy (ΔG_H) for the Volmer step ($H^+ + e^- = H^*$) have been extensively used as a descriptor to evaluate the catalytic behaviour of different HER catalyst.[21] Thermodynamically, ΔG_H value to zero provide better environment for HER catalysis

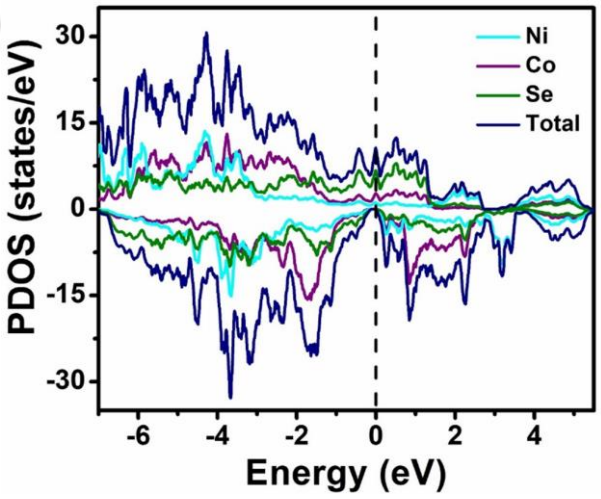

Figure 2.10. Calculated PDOS for $NiCo_2Se_4$

reaction by promoting better hydrogen adsorption site.[52] Based on DFT estimation, the value of ΔG for vertically aligned bulk $MoSe_2$ (Figure 2.9a) with normal layer separation (d_{200}= 0.64 nm) is -1.48 eV. Interestingly, ΔG is only -0.46 eV for vertical $MoSe_2$ having experimentally measured inter-layer separation of 0.78 nm. DFT also predicts that the ideal layer separation is 0.73 nm for which ΔG (-0.254 eV) value is optimal. This largely reduced ΔG_H can be attributed to the appearance of electronic states near the Fermi level in vertically aligned expanded $MoSe_2$ which provides adequate adsorption of hydrogen thus giving rise to high efficiency in HER as compared to bulk with large band gap (Figure 2.9b).[53] On the other hand, ΔG_H for the base $NiCo_2Se_4$ is 0.91 eV, which is higher than lattice expanded vertical $MoSe_2$ but considerably lower than bulk $MoSe_2$. This indicates that the base $NiCo_2Se_4$ sheet also took part in the HER activity. In addition, metallic nature of $NiCo_2Se_4$ sheet, as found from projected DOS (Figure 2.10), offer electronic highway to supply electron from current collector to the $MoSe_2$ edge sites. After confirming beneficial electronic properties of individual components of heterostructure i.e. $MoSe_2$ with layer expanded structure and $NiCo_2Se_4$ for HER, ΔG_H was calculated for complete heterostructure with three different possible edge termination namely Mo sites, Mo sites with 50% ($MoSe_2$@$NiCo_2Se_4$-50Se) and 100% Se ($MoSe_2$@$NiCo_2Se_4$-100Se) coverage as shown in Figure 2.11a. Calculation shows that Mo sites with 50% Se coverage (ΔG_H=0.41eV) and Mo edge sites (-0.56 eV) exhibit beneficial HER catalytic activity compared to basal $NiCo_2Se_4$ (0.91 eV) (Figure 2.11b, Table 2.3).

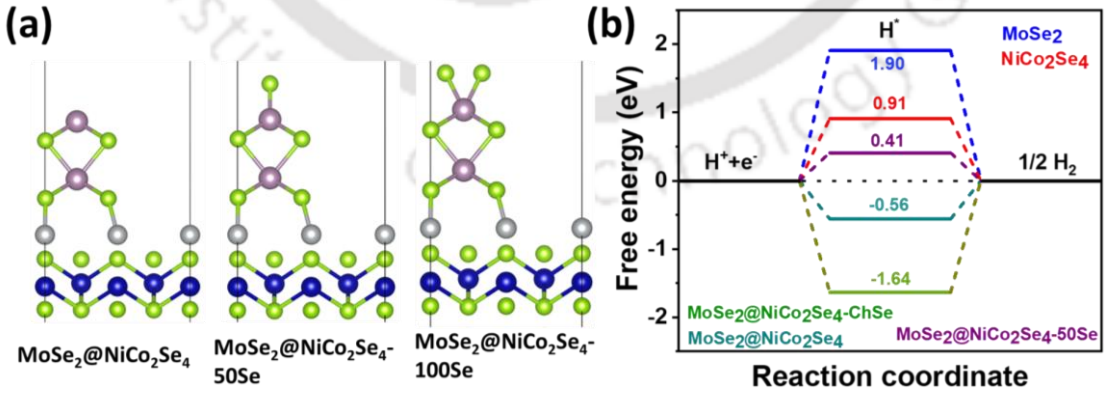

Figure 2.11. (a) Atomic configuration of the $MoSe_2$@$NiCo_2Se_4$ heterostructures with Mo edge, Mo edge with 50% and 100% Se coverage. Here grey, blue, green and purple atoms represent the Ni, Co, Se and Mo atoms respectively. (b) Gibbs free energy for H* at different catalyst active sites.

Interestingly, Se atoms at the surface termination in Mo edge site (0.41 eV) shows much lower Gibbs free energy compared to the Se atoms in the interlayer channels ($MoSe_2$@$NiCo_2Se_4$-ChSe, -1.64 V). This confirms that the exposed edge atoms are the main catalytic active sites. Hence, it can be concluded from the comprehensive structural and electrochemical analysis that (i) both the components of heterostructure contribute to HER activity; (ii) base $NiCo_2Se_4$, together with its own HER activity, offers high theoretical surface area platform for holding vertical $MoSe_2$ structure, and its metallic conductivity offers electronic highway for charge carrier to reach to the $MoSe_2$ edge site; (iii) Layer expanded and edge-oriented structure significantly lower the adsorption energy barrier for hydrogen, thus benefit HER activity. All the aforementioned factors collectively act together to give high HER activity.

Table 2.3: List of ΔG_H at different active sites for HER

Active site	ΔG (eV)
$MoSe_2$@$NiCo_2Se_4$-Mo(50)	0.41
$MoSe_2$@$NiCo_2Se_4$-Mo(100)	0.76
$MoSe_2$@$NiCo_2Se_4$-Mo	-0.56
$MoSe_2$@$NiCo_2Se_4$-Se	-1.64
$NiCo_2Se_4$	0.91
$MoSe_2$	1.9

2.5 Conclusion

In summary, catalysts derived from multi-level atomic re-arrangement were developed via hydrothermal selenization. Selenization converts mixed metal oxide/hydroxide (MoO_3/Ni-$Co(OH)_2$) nanosheets leading to heterostructure comprising of erected $MoSe_2$ nanosheets over $NiCo_2Se_4$ nanosheets. The brilliant HER performance of this heterostructure, with an overpotential of only 89 mV for 10 mA cm^{-2} current density, is associated with the significant lowering of Gibb's free energy for hydrogen adsorption in vertical and interlayer expanded $MoSe_2$ structure as supported by DFT calculation. Due to the generic nature the selenization induced in situ heterostructure process is expected to trigger new developments in broad area of electrocatalyst.

References

[1] J. A. Turner, *Science (80-.).* **2004**, *305*, 972.

[2] N. T. Suen, S. F. Hung, Q. Quan, N. Zhang, Y. J. Xu, H. M. Chen, *Chem. Soc. Rev.* **2017**, *46*, 337.

[3] Y. Lee, J. Suntivich, K. J. May, E. E. Perry, Y. Shao-Horn, *J. Phys. Chem. Lett.* **2012**, *3*, 399.

[4] Y. Pi, Q. Shao, P. Wang, F. Lv, S. Guo, J. Guo, X. Huang, *Angew. Chemie - Int. Ed.* **2017**, *56*, 4502.

[5] C. Dong, X. Zhang, J. Xu, R. Si, J. Sheng, J. Luo, S. Zhang, W. Dong, G. Li, W. Wang, F. Huang, *Small* **2020**, *16*, 1905328.

[6] F. Ming, H. Liang, H. Shi, G. Mei, X. Xu, Z. Wang, *Electrochim. Acta* **2017**, *250*, 167.

[7] F. Bu, W. Chen, M. F. Aly Aboud, I. Shakir, J. Gu, Y. Xu, *J. Mater. Chem. A* **2019**, *7*, 14526.

[8] L. Jiao, Y. X. Zhou, H. L. Jiang, *Chem. Sci.* **2016**, *7*, 1690.

[9] P. Zhai, Y. Zhang, Y. Wu, J. Gao, B. Zhang, S. Cao, Y. Zhang, Z. Li, L. Sun, J. Hou, *Nat. Commun.* **2020**, *11*, 5462.

[10] S. Niu, W. J. Jiang, T. Tang, L. P. Yuan, H. Luo, J. S. Hu, *Adv. Funct. Mater.* **2019**, *29*, 1902180.

[11] J. Kibsgaard, Z. Chen, B. N. Reinecke, T. F. Jaramillo, *Nat. Mater. 2012 1111* **2012**, *11*, 963.

[12] H. Chen, J. Jiang, L. Zhang, H. Wan, T. Qi, D. Xia, *Nanoscale* **2013**, *5*, 8879.

[13] P. Giannozzi, S. Baroni, N. Bonini, M. Calandra, R. Car, C. Cavazzoni, D. Ceresoli, G. L. Chiarotti, M. Cococcioni, I. Dabo, A. Dal Corso, S. De Gironcoli, S. Fabris, G. Fratesi, R. Gebauer, U. Gerstmann, C. Gougoussis, A. Kokalj, M. Lazzeri, L. Martin-Samos, N. Marzari, F. Mauri, R. Mazzarello, S. Paolini, A. Pasquarello, L. Paulatto, C. Sbraccia, S. Scandolo, G. Sclauzero, A. P. Seitsonen, A. Smogunov, P. Umari, R. M. Wentzcovitch, *J. Phys. Condens. Matter* **2009**, *21*, 395502.

[14] D. Vanderbilt, *Phys. Rev. B* **1990**, *41*, 7892.

[15] S. Grimme, *J. Comput. Chem.* **2006**, *27*, 1787.

[16] J. P. Perdew, K. Burke, M. Ernzerhof, *Phys. Rev. Lett.* **1996**, *77*, 3865.

[17] W. Li, G. Liu, J. Li, Y. Wang, L. Ricardez-Sandoval, Y. Zhang, Z. Zhang, *Appl. Surf. Sci.* **2019**, *498*, 143869.

[18] V. I. Anisimov, J. Zaanen, O. K. Andersen, *Phys. Rev. B* **1991**, *44*, 943.

[19] M. Cococcioni, S. De Gironcoli, *Phys. Rev. B - Condens. Matter Mater. Phys.* **2005**, *71*, 35105.

[20] Z. Fang, L. Peng, H. Lv, Y. Zhu, C. Yan, S. Wang, P. Kalyani, X. Wu, G. Yu, *ACS Nano* **2017**, *11*, 9550.

[21] J. K. Nørskov, T. Bligaard, A. Logadottir, J. R. Kitchin, J. G. Chen, S. Pandelov, U. Stimming, *J. Electrochem. Soc.* **2005**, *152*, J23.

[22] M. Jiang, J. Zhang, M. Wu, W. Jian, H. Xue, T. W. Ng, C. S. Lee, J. Xu, *J. Mater. Chem. A* **2016**, *4*, 14949.

[23] P. Gnanasekar, D. Periyanagounder, J. Kulandaivel, *Nanoscale* **2019**, *11*, 2439.

[24] D. Kong, H. Wang, J. J. Cha, M. Pasta, K. J. Koski, J. Yao, Y. Cui, *Nano Lett.* **2013**, *13*, 1341.

[25] J. Masud, A. T. Swesi, W. P. R. Liyanage, M. Nath, *ACS Appl. Mater. Interfaces* **2016**, *8*, 17292.

[26] F. Lu, M. Zhou, W. Li, Q. Weng, C. Li, Y. Xue, X. Jiang, X. Zeng, Y. Bando, D. Golberg, *Nano Energy* **2016**, *26*, 313.

[27] X. Qian, H. Li, L. Shao, X. Jiang, L. Hou, *ACS Appl. Mater. Interfaces* **2016**, *8*, 29486.

[28] H. Chen, S. Chen, M. Fan, C. Li, D. Chen, G. Tian, K. Shu, *J. Mater. Chem. A* **2015**, *3*, 23653.

[29] J. Guo, Y. Shi, X. Bai, X. Wang, T. Ma, *J. Mater. Chem. A* **2015**, *3*, 24397.

[30] F. Xie, W. C. H. Choy, C. Wang, X. Li, S. Zhang, J. Hou, *Adv. Mater.* **2013**, *25*, 2051.

[31] B. Li, L. Jiang, X. Li, Z. Cheng, P. Ran, P. Zuo, L. Qu, J. Zhang, Y. Lu, *Adv. Funct. Mater.* **2019**, *29*, 1806229.

[32] Y. R. Zheng, P. Wu, M. R. Gao, X. L. Zhang, F. Y. Gao, H. X. Ju, R. Wu, Q. Gao, R. You, W. X. Huang, S. J. Liu, S. W. Hu, J. Zhu, Z. Li, S. H. Yu, *Nat. Commun.* **2018**, *9*, 2533.

[33] C. Wang, P. Zhang, J. Lei, W. Dong, J. Wang, *Electrochim. Acta* **2017**, *246*, 712.

[34] S. Liu, Y. Jiang, M. Yang, M. Zhang, Q. Guo, W. Shen, R. He, M. Li, *Nanoscale* **2019**, *11*, 7959.

[35] Y. Yang, X. Zhao, H. Mao, R. Ning, X. Zheng, J. Sui, W. Cai, *Int. J. Hydrogen Energy* **2020**, *45*, 10724.

[36] F. Ma, Y. Liang, P. Zhou, F. Tong, Z. Wang, P. Wang, Y. Liu, Y. Dai, Z. Zheng, B. Huang, *Mater. Chem. Phys.* **2020**, *244*, 122642.

[37] L. Yu, Y. Xiao, C. Luan, J. Yang, H. Qiao, Y. Wang, X. Zhang, X. Dai, Y. Yang, H. Zhao, *ACS Appl. Mater. Interfaces* **2019**, *11*, 6890.

[38] X. Zhang, Y. Y. Zhang, Y. Zhang, W. J. Jiang, Q. H. Zhang, Y. G. Yang, L. Gu, J. S. Hu, L. J. Wan, *Small Methods* **2019**, *3*, 1800317.

[39] S. Prabhakaran, J. Balamurugan, N. H. Kim, J. H. Lee, *Small* **2020**, *16*, 2000797.

[40] Y. Lu, Y. Deng, S. Lu, Y. Liu, J. Lang, X. Cao, H. Gu, *Nanoscale* **2019**, *11*, 21259.

[41] S. Wang, D. Zhang, B. Li, C. Zhang, Z. Du, H. Yin, X. Bi, S. Yang, *Adv. Energy Mater.* **2018**, *8*, 1801345.

[42] F. Zhou, X. Zhang, R. Sa, S. Zhang, Z. Wen, R. Wang, *Chem. Eng. J.* **2020**, *397*, 125454.

[43] Q. Wang, Z. L. Zhao, S. Dong, D. He, M. J. Lawrence, S. Han, C. Cai, S. Xiang, P. Rodriguez, B. Xiang, Z. Wang, Y. Liang, M. Gu, *Nano Energy* **2018**, *53*, 458.

[44] Y. Yang, H. Yao, Z. Yu, S. M. Islam, H. He, M. Yuan, Y. Yue, K. Xu, W. Hao, G. Sun, H. Li, S. Ma, P. Zapol, M. G. Kanatzidis, *J. Am. Chem. Soc.* **2019**, *141*, 10417.

[45] Z. Pu, Y. Luo, A. M. Asiri, X. Sun, *ACS Appl. Mater. Interfaces* **2016**, *8*, 4718.

[46] M. Ledendecker, S. Krick Calderón, C. Papp, H.-P. Steinrück, M. Antonietti, M. Shalom, *Angew. Chemie Int. Ed.* **2015**, *54*, 12361.

[47] D. Merki, H. Vrubel, L. Rovelli, S. Fierro, X. Hu, *Chem. Sci.* **2012**, *3*, 2515.

[48] A. Sikdar, A. Majumdar, A. Gogoi, P. Dutta, M. Borah, S. Maiti, C. Gogoi, K. Anki Reddy, Y. Oh, U. Narayan Maiti, *J. Mater. Chem. A* **2021**, *9*, 7640.

[49] Y. Cui, Y. Xue, R. Zhang, J. Zhang, X. Li, X. Zhu, *J. Mater. Chem. A* **2019**, *7*, 21911.

[50] Y. Yu, S. Y. Huang, Y. Li, S. N. Steinmann, W. Yang, L. Cao, *Nano Lett.* **2014**, *14*, 553.

[51] E. Cappelluti, R. Roldán, J. A. Silva-Guillén, P. Ordejón, F. Guinea, *Phys. Rev. B - Condens. Matter Mater. Phys.* **2013**, *88*, 075409.

[52] M. Hakala, R. Kronberg, K. Laasonen, *Sci. Reports 2017 71* **2017**, *7*, 15243.

[53] A. Parija, Y. H. Choi, Z. Liu, J. L. Andrews, L. R. De Jesus, S. C. Fakra, M. Al-Hashimi, J. D. Batteas, D. Prendergast, S. Banerjee, *ACS Cent. Sci.* **2018**, *4*, 493.

Chapter 3

Single atom iridium stabilization on $MoSe_2@NiCo_2Se_4$ heterostructure catalyst for efficient overall water splitting

Chapter 3

Single atom iridium stabilization on $MoSe_2$@$NiCo_2Se_4$ heterostructure catalyst for efficient overall water splitting

The total efficiency of hydrogen synthesis by electrolysis of water is constrained by the high overpotential requirement of the oxygen evolution reaction process (OER). Single atom catalyst comprising isolated metal atoms uniformly distributed over a support has a significant potential for obtaining high activity and selectivity to reduce this overpotential. However, it is still unclear how single atoms interact with support materials for stability, especially with transition metal-based sulfide/ selenides, which reconstruct during OER process. Here, we photochemically decorated single atom iridium (Ir) over $MoSe_2$@$NiCo_2Se_4$ heterostructure, which on electrochemical surface reconstruction displays outstanding OER activity, requiring only 200 mV and 313 mV overpotentials for 10 mA cm^{-2} and 500 mA cm^{-2} current densities, respectively. A full cell electrolyzer comprising of $MoSe_2$@$NiCo_2Se_4$ as cathode and its SAC-Ir decorated counterpart as anode requires only 1.51 V to attain 10 mA cm^{-2} current density. A series of characterizations after OER and density functional theory calculation reveals the origin of synergistic electronic coupling of single atom iridium with the support and its stabilization over it during OER process.

3.1 Introduction

Electrocatalytic water splitting for generating hydrogen and oxygen, by converting and storing intermittent renewable energies, offers an alluring way to obtain sustainable hydrogen-based economy.[1] However, slow reaction kinetic at the anode, where water is oxidised and the OER takes place, is the fundamental reason that water electrolysis requires high energy barrier.[2] Iridium (Ir) and ruthenium (Ru) oxides are the most efficient OER electrocatalysts at the moment, but they are also rather expensive and scarce.[3] Although significant efforts have been made to create inexpensive alternatives to OER using transition-metal-based catalysts that are found in abundance on Earth, such as metal hydroxides, oxides, sulfides, selenides and phosphides yet their efficiency is not satisfactory. Improvement of these OER systems is therefore greatly desired to achieve high energy efficiency and cost effectiveness in alkaline electrocatalysis.

A productive strategy to increase catalytic activity while drastically lowering the amount of noble metals is to use single-atom catalysts (SACs).[4,5] Single atoms can

significantly enhance the OER performance of support materials like metal, metal oxide and carbon-based materials.[6,7] However, it is still rare to use metal sulfides, selenides or phosphides for anchoring single atoms over it. Under OER circumstances, they go through surface self-reconstruction to create oxyhydroxides rich of oxygen ligands for the anchoring of isolated atoms. Therefore, it makes sense to assume that the structural self-reconstruction of active sites will alter the catalytic activity, particularly for SACs.[8,9] In addition, single atoms will try to agglomerate under this reconstructing environment thus changing the catalytic activity drastically. Therefore, stabilizing isolated atoms under harsh reaction circumstances is a significant obstacle in the design of SACs. However, understanding the state of those isolated active atoms and how they synergize with support under dynamic catalytic environment are rarely reported, but essential for constructing efficient SACs. On the other hand, despite single atom (noble metal) strategy has demonstrated a noticeable enhancement in OER reaction rate, but their overpotential values are still not satisfactory, mostly lies in the range of 220-300 mV at 10 mA cm^{-2} current density.[5,10] Therefore, in order to come up with the next generation of water electrolysis induced hydrogen generation, these existing problems need to be resolved.

Here, we have photochemically decorated iridium single atoms over the surface of $MoSe_2$@$NiCo_2Se_4$ heterostructure that we had developed in the previous chapter. Besides competitive HER activity, resulting $MoSe_2$@$NiCo_2Se_4$ structure also shows good OER activity requiring an overpotential of 255 mV to achieve a current density of 10 mA cm^{-2}, qualifying as a potential bi-functional catalyst. With homogenous decoration of iridium single atom on $MoSe_2$@$NiCo_2Se_4$, the OER overpotential (for 10 mA cm^{-2}) is reduced to 200 mV, which is among the best values reported thus far including single atom iridium samples. The origin of high OER activity is related to the in-situ surface activation of selenide into amorphous Ni-Co-oxyhydroxide by selective leaching of molybdenum and suitable electronic coupling with single atom iridium, as analyzed by extensive post OER characterizations and comprehensive understanding through DFT calculations. A full cell electrolyzer using $MoSe_2$@$NiCo_2Se_4$ as cathode and its SAC-Ir decorated counterpart as anode display a current density of 10 mA cm^{-2} at 1.51 V, which is among the best performances reported thus far. This outstanding performance of $MoSe_2$@$NiCo_2Se_4$/Ir-$MoSe_2$@$NiCo_2Se_4$ catalysts pair demonstrates the importance of heterostructure control for solar to fuel conversion technology.

3.2 Experimental Section

3.2.1 Materials

Iridium (III) chloride hydrate ($IrCl_3.xH_2O$), iridium (IV) oxide (IrO_2), platinum (20 wt %) on graphitized carbon (Pt/C) and Nafion (5 wt%) were purchased from Sigma-Aldrich. Potassium hydroxide pellets (KOH) were bought from Merck. Nickel foam (NF) having a thickness of 1.6 mm was obtained from MTI. All the chemicals were used without further purification. A Millipore type III deionized water with a resistance of 18.2 MΩ was used throughout all the experiments.

3.2.2 Preparation of single atom Ir on $MoSe_2@NiCo_2Se_4$ heterostructure (Ir-$MoSe_2@NiCo_2Se_4$)

Firstly, $MoSe_2@NiCo_2Se_4$ heterostructure that was synthesized in the previous chapter, shifted to a beaker containing an aqueous solution of 2 mM iridium chloride with adjusted pH to 12 by 4M KOH solution. Then the beaker was placed under a monochromatic UV light (output wavelength ~ 254 nm) in a UV chamber. The UV irradiation was continued for a time of 4h in which the solution color changed from yellow to dark blue. Finally, the sample was washed with water and ethanol and dried in vacuum oven at room temperature.

3.2.3 Material characterizations

Powder XRD patterns was taken by Rigaku X-ray diffractometer at room temperature with Cu Kα radiation (λ=1.5418 Å). FESEM images were captured with Zeiss Sigma 300 FESEM whereas energy dispersive X-ray spectroscopic investigation was conducted in Ametek EDAX attached with Zeiss Sigma 300 FESEM. HRTEM analysis and STEM analysis were done in Titan TM 80-300 (FEI) with probe Cs corrector. For elemental analysis and ionic state determination, XPS was done in ESCALAB Xi+ (Thermo Fisher) instrument. Raman vibrational study was performed in Horiba LabRam HR with a 514 nm laser source. Ir L3-edge X-ray absorption spectroscopy (XAS) was carried in Indus-2, a 2.5 GeV synchrotron radiation source facility in Raja Raman Centre for Advanced Technology. All XAS data were inspected using Athena software for background correction, normalisation of XANES and EXAFS spectra. EXAFS data have been fitted with Artemis software. ICP-OES has been done in PerkinElmer Optima 5300 DV made in USA. As the samples have been grown on nickel foam (NF), all the

elemental analysis through ICP-OES have been performed without considering Ni to eliminate the contribution of Ni coming from NF.

3.2.4 Electrochemical measurements

Electrocatalytic HER and OER performances were tested in three-electrode configuration with saturated calomel electrode (CHI 150) as reference electrode, Pt wire as counter electrode and 1M KOH as electrolyte in a PARSTAT 3000A-DX potentiostat. A piece of 1×1 cm^2 of synthesized samples on NF was directly used as the working electrode. All polarisation curves were taken at 5 mV s^{-1} scan rate and corrected through iR compensation. All the potentials were referred against reversible hydrogen electrode (RHE) according to the formula,

$$E_{RHE} = E_{SCE} + 0.059 \times 14 + 0.242 \quad 3.1$$

OER overpotential was calculated with the formula,

$$\eta = E_{RHE} - 1.23\ V \quad 3.2$$

Impedance spectroscopy of samples were measured in a frequency range of 10 kHz to 0.1 Hz at an AC amplitude of 10 mV.

The double layer capacitance (C_{dl}) was calculated by observing cyclic voltammetry curves (CV) in a potential range of 1.1-1.2 V vs. RHE free from any faradaic region. Half of the difference of anodic current (J_a) and cathodic current (J_c) was plotted against potential vs. RHE at a potential of 1.15 V vs. RHE. Slope of the above curve provides C_{dl} value which is also estimated to be proportional to ECSA of samples.

3.2.5 OER calculation

For the OER DFT calculations, GGA-PBE exchange-correlation functional with a kinetic energy cut-off of 680 eV was used to expand the wave functions. All the catalyst surface was modelled using β-NiOOH (001) structure. Co was incorporated in the structure by replacing 2 Ni atoms from a 2x2x2 supercell. Vacuum layer of 15 Å was implemented to separate the periodic images. The Brillouin zone was sampled by Monkhorst-Pack grid with a k point density of 0.2 eV/Å.[11] The convergence criterion was set at 10^{-7} eV for self-consistent field calculations. During structural relaxation calculations, the atomic positions were relaxed until the forces on the atoms were less than 0.02 eV/Å along with a tolerance of 10^{-6} eV/atom for energy. An effective U parameter of 5.5 eV and 3 eV was used for Ni and Co respectively.[12,13]

To calculate the overpotential, a four electron OER mechanism under the alkaline environment was used following the below mentioned reaction paths,

$$* + OH^- = OH^* + e^- \quad 3.3$$

$$OH^* + OH^- = O^* + H_2O(l) + e^- \quad 3.4$$

$$O^* + OH^- = OOH^* + e^- \quad 3.5$$

$$OH^* + OH^- = * + O_2(g) + H_2O(l) + e^- \quad 3.6$$

Here * denotes active sites in the catalyst surface and **OH, *O, *OOH* denotes adsorbed species respectively. The Gibbs free energy was calculated using the equation,

$\Delta G_i = \Delta E_i + \Delta ZPE - T\Delta S$; where i =1-4

Here, ΔE is the DFT calculated energy difference, ΔZPE and ΔS are differences in zero-point energy and entropy. In this study, ΔZPE and ΔS are calculated using reported values in literature.

3.3 Result & Discussion

3.3.1 Morphological analyses

In order to optimize OER catalytic performance, single atom iridium was linked with $MoSe_2$@$NiCo_2Se_4$ via photochemical process in alkaline iridium chloride solution under UV light irradiation. Interestingly, Ir decoration over $MoSe_2$@$NiCo_2Se_4$ does not alter the sheet-on-sheet morphology of $MoSe_2$@$NiCo_2Se_4$ as observed from FESEM image (Figure 3.1). This can also be confirmed from TEM image as shown in Figure 3.2a where, arrays of $MoSe_2$ structure can be observed for Ir-$MoSe_2$@$NiCo_2Se_4$. In addition, same planes (311) and (-313) related to $NiCo_2Se_4$ can also be found in HRTEM

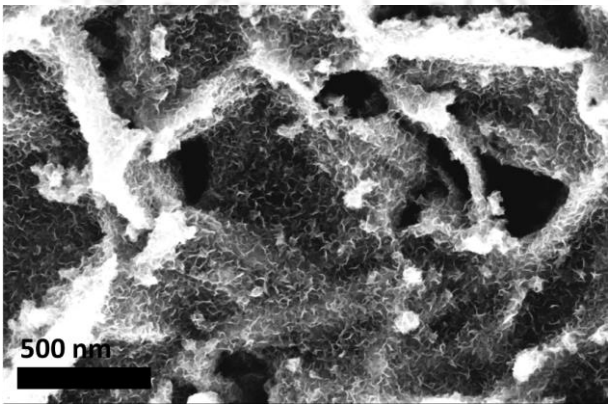

Figure 3.1. Morphological characterisation: FESEM image of Ir-$MoSe_2$@$NiCo_2Se_4$.

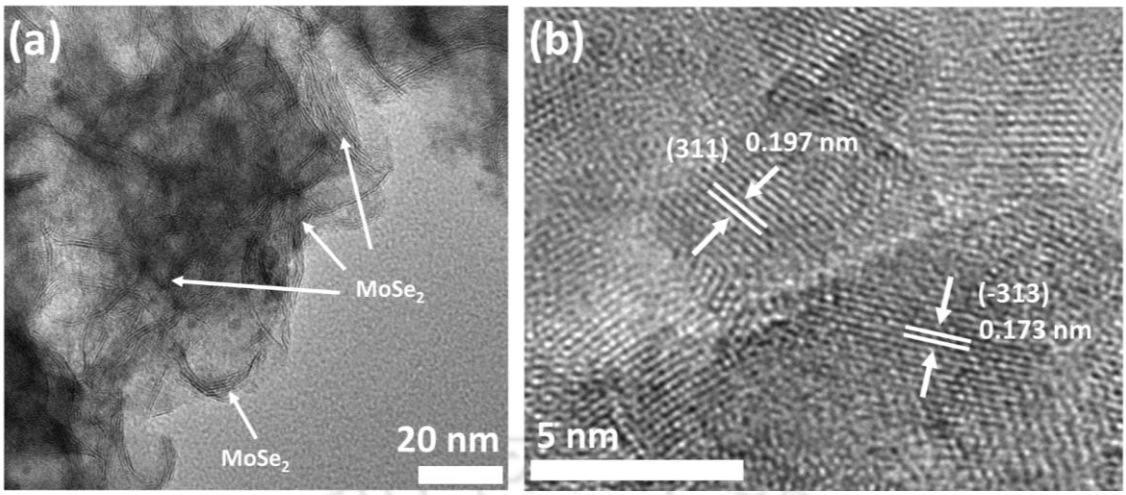

Figure 3.2. Morphological characterisation: (a) HRTEM image of Ir-$MoSe_2$@$NiCo_2Se_4$ showing same sheet in sheet structure as $MoSe_2$@$NiCo_2Se_4$ and (b) Cs corrected HRTEM image of Ir-$MoSe_2$@$NiCo_2Se_4$ showing planes corresponding to $NiCo_2Se_4$

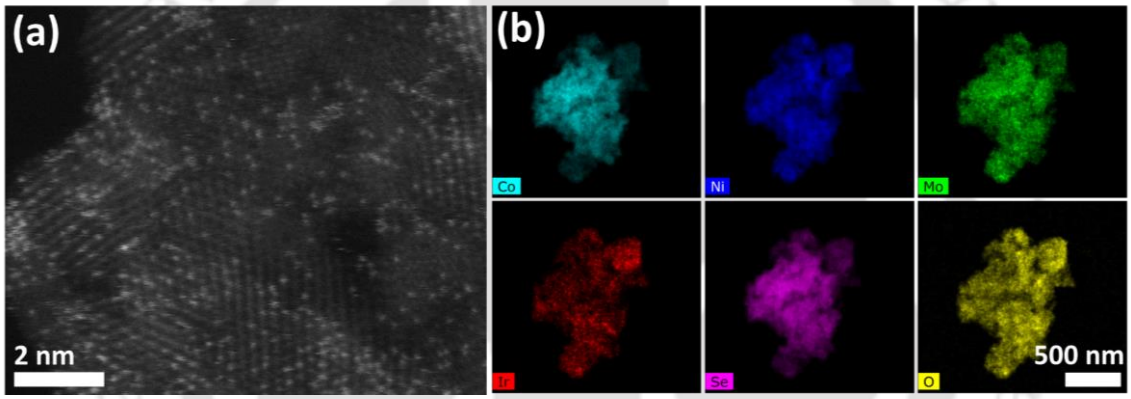

Figure 3.3. (a) HAADF-STEM image of Ir-$MoSe_2$@$NiCo_2Se_4$ showing bright single Ir atoms and (b) represents HAADF-STEM elemental mapping of Ir-$MoSe_2$@$NiCo_2Se_4$.

image (Figure 3.2b) as in the structure before Ir incorporation. Single atomic nature of iridium was confirmed from aberration corrected high-angle annular dark-field scanning transmission electron microscopy (HAADF-STEM) imaging (Figure 3.3a), which shows abundant white atomic dots of iridium uniformly dispersed without any aggregation. STEM energy dispersive X-ray spectroscopy (EDS) elemental mapping (Figure 3.3b) shows uniform dispersion of iridium with other elements (Co, Ni, Mo, Se) of the compound. The atomic percentage of Ir was found to be 1.5% from EDS analysis.

3.3.2 Structural analyses

However, in XRD pattern of Ir-$MoSe_2$@$NiCo_2Se_4$ (Figure 3.4), along with all the peaks related to $NiCo_2Se_4$, an additional broad peak at 13.4º appears which can possibly be

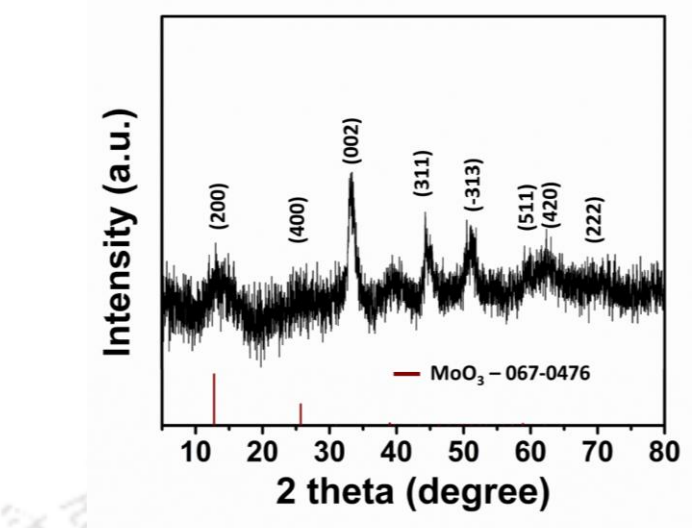

Figure 3.4. Structural characterisation: XRD pattern of Ir-$MoSe_2$@$NiCo_2Se_4$.

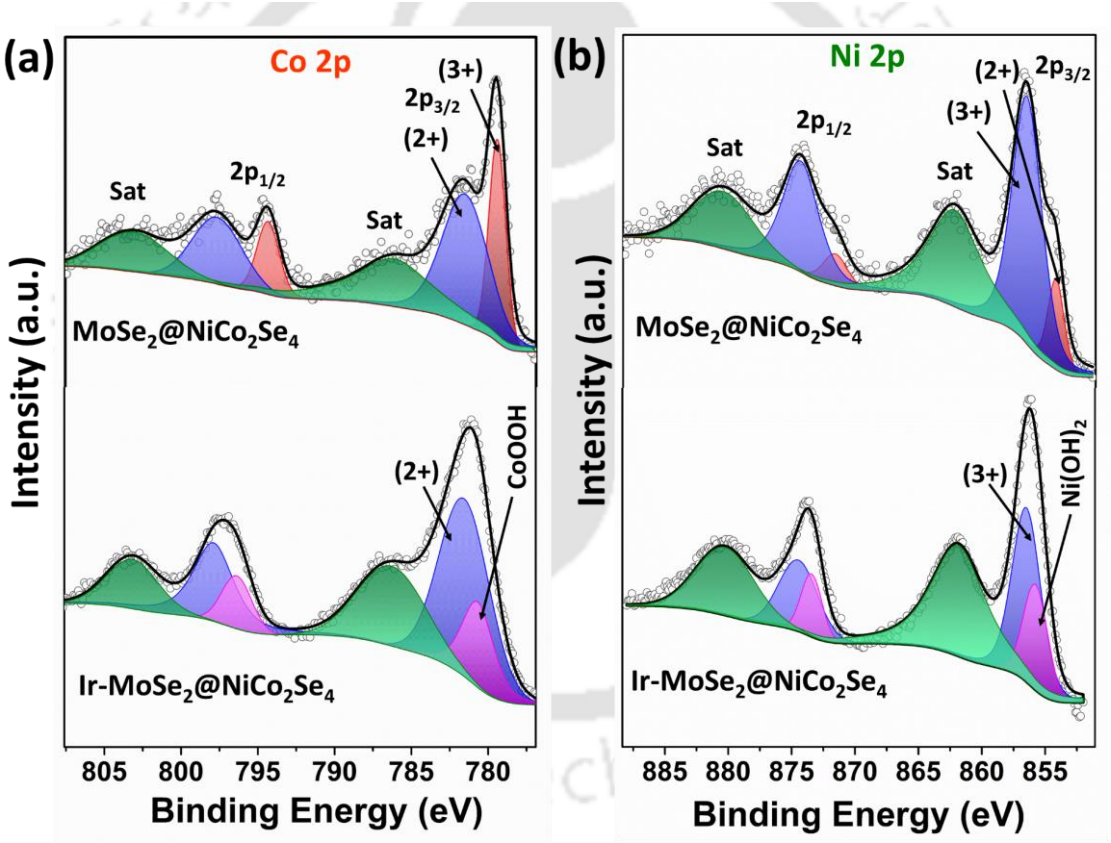

Figure 3.5. Structural characterisations: high resolution XPS spectra for (a) Co 2p, (b) Ni 2p of $MoSe_2$@$NiCo_2Se_4$ and Ir-$MoSe_2$@$NiCo_2Se_4$ with their peak fitting.

associated to molybdenum oxide (MoO_3) phase [JCPDS-067-0476] which may have appeared due to light irradiation assisted partial oxidation of $MoSe_2$ in alkaline condition during SAC-Ir similar to the case observed for molybdenum based anaologous chalcogendies MoS_2.[14] Chemical composition and the oxidation states of the elements of as-developed

catalysts were investigated through X-ray photoelectron spectroscopy (XPS). For $MoSe_2$@$NiCo_2Se_4$ and Ir-$MoSe_2$@$NiCo_2Se_4$ (Figure 3.5a, b), the deconvoluted core level spectrum of Co 2p (Ni 2p) consists of two sets of spin orbit splitting peaks ($2p_{3/2}$ & $2p_{1/2}$). SAC-Ir deposition over $MoSe_2$@$NiCo_2Se_4$ led to significant change in these core level spectra (Figure 3.5a, b), the doublet due to Co^{3+} (Ni^{2+}) of $NiCo_2Se_4$ disappeared and new set of doublets corresponding to oxyhydroxide/hydroxide of Co (Ni) appeared at 780.6 eV & 796.4 eV (855.7 eV & 873.4 eV) respectively.[15,16] Appearance of (oxy)hydroxide phase results from partial conversion of selenide in the alkaline solution used for SAC-Ir deposition. Partial surface conversion into (oxy)hydroxide phase during Ir deposition can also be judged from the relative decrease of selenium content in the hybrid Ir-$MoSe_2$@$NiCo_2Se_4$ as is determined from EDX analysis (Table 3.1). This partial hydroxide conversion offers oxygen ligands to be the bridging site for iridium to be bound to $NiCo_2Se_4$ surface.

Table 3.1. EDX result for atomic percentage of different elements

Samples	Co (%)	Ni (%)	Mo (%)	Ir (%)	Se (%)	O (%)
$MoSe_2$@$NiCo_2Se_4$	13.4	7.3	8.2	-	44	27
Ir-$MoSe_2$@$NiCo_2Se_4$	8.0	5.7	7.7	1.5	36.7	40.5

Meanwhile, high resolution Mo 3d XPS spectra (Figure 3.6a, b) of $MoSe_2$@$NiCo_2Se_4$ and Ir-$MoSe_2$@$NiCo_2Se_4$ have been splitted into $3d_{5/2}$ and $3d_{3/2}$ which correspond to the Mo^{4+} from $MoSe_2$,[17] Mo^{6+} from MoO_3,[18] and Mo^{5+} [19] linked to amorphous $MoSe_x$ present in the system. However, after Ir incorporation, oxide related peak relatively increases compared to selenide related peak (Figure 3.6b) which can be associated to the partial oxidation of $MoSe_2$ during SAC-Ir deposition under UV light irradiation in alkaline condition which is in line with the XRD result. Ir 4f spectrum of Ir-$MoSe_2$@$NiCo_2Se_4$ (Figure 3.6c) are deconvoluted to doublets centered at 65.2 eV and 62.3 eV, which can be related to Ir^{4+} oxidation state indicating high oxidation nature of SAC-Ir.[7]

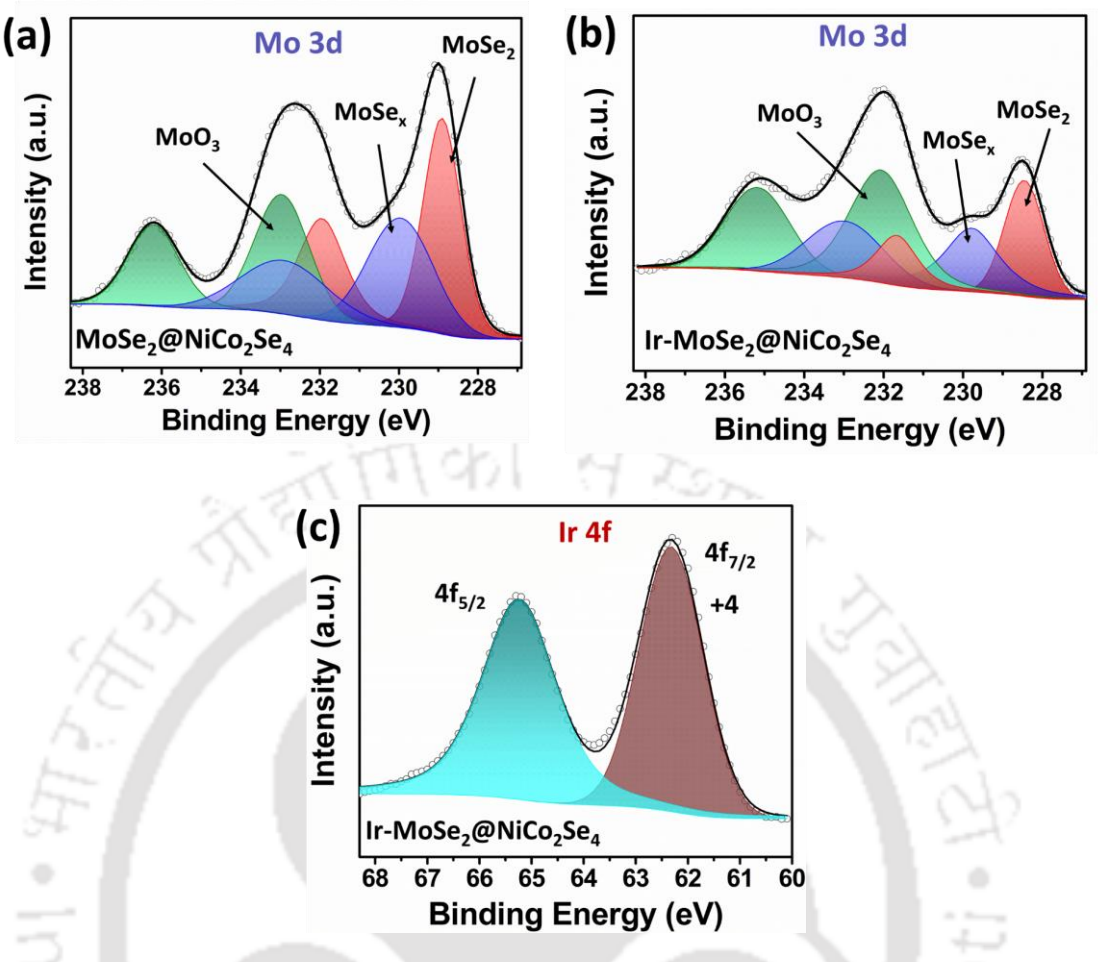

Figure 3.6. Structural characterisations: High resolution XPS spectra of Mo 3d for (a) $MoSe_2@NiCo_2Se_4$ and (b) Ir-$MoSe_2@NiCo_2Se_4$. (c) High resolution XPS spectra of Ir 4f for Ir-$MoSe_2@NiCo_2Se_4$.

To further understand the local electronic and coordination structure, X-ray absorption near edge spectroscopy (XANES) and extended X-ray absorption fine

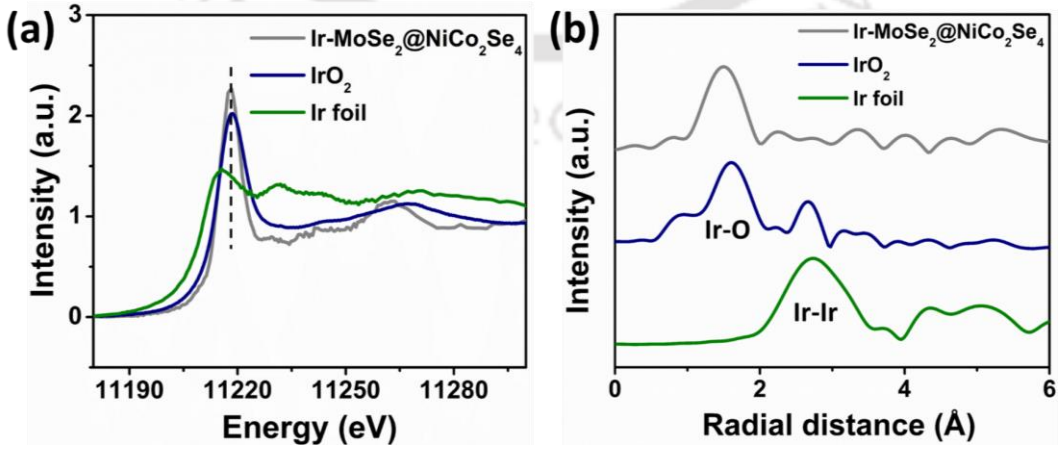

Figure 3.7. Structural characterisations: (a) Normalised XANES Ir L3-edge of Ir foil, IrO_2 and Ir-$MoSe_2@NiCo_2Se_4$ and (b) their corresponding FT-EXAFS spectra.

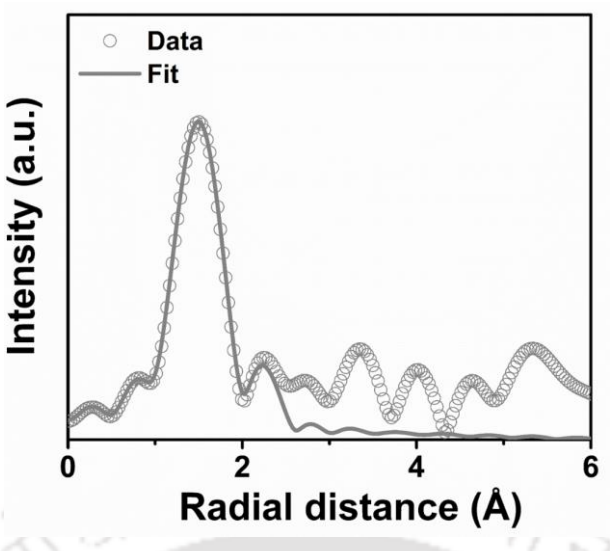

Figure 3.8. Structural characterisations: FT-EXAFS fitting of Ir-$MoSe_2$@$NiCo_2Se_4$.

structure (EXAFS) of Ir-SAC were analysed. The spectra were compared with that of commercial iridium oxide (IrO_2) and metallic Ir foil. The white-line peak position of Ir-$MoSe_2$@$NiCo_2Se_4$ in Ir L3 -edge XANES (Figure 3.7a) is around the same position as commercial IrO_2, confirming +4 oxidation of SAC-Ir, which is also consistent with the XPS result.[7] Fourier transform of EXAFS spectra of Ir-$MoSe_2$@$NiCo_2Se_4$ in Figure 3.7b shows peak at around 1.5 Å (phase uncorrected) which is related to Ir-O scattering path.[20,21] However, no Ir-Ir scattering peak was observed in Ir-$MoSe_2$@$NiCo_2Se_4$, which suggests the presence of isolated Ir single atoms within the sample. The local environment and coordination of single atom Ir in Ir-$MoSe_2$@$NiCo_2Se_4$ can be deeply understood by fitting the EXAFS results. From the fitted EXAFS of Ir-$MoSe_2$@$NiCo_2Se_4$ (Figure 3.8) and the corresponding fitting parameters (Table 3.2), it is clear that SAC-Ir is coordinated with four nearest neighbour oxygen (O) atoms (R=1.999Å), out of which three can be offered by oxygen ligand of oxyhydroxide/hydroxide of Co (Ni) support and the fourth one can be –OH ligand over Ir-atom. The fitting further reveals that Ir-atom is also coordinated with two more O-atoms with higher distance (R=2.744 Å) as compared to nearest neighbour O-atoms. These two O-atoms can be associated with the adsorbed hydroxyl group and they are inevitable in processing of SAC-Ir in aqueous KOH medium.[22] Other small peaks at higher $R_>$ value of EXAFS are due to outer shell of Ir-O (beyond first shell) and also have contribution from the first shell (Ir-O) and they do not match with Ir-Ir spectra which demonstrates single atomic nature of Ir in the sample.

Table 3.2. Fitting parameters of FT-EXAFS spectra of Ir-$MoSe_2$@$NiCo_2Se_4$ (CN: coordination number; σ^2: Debye-Waller factor)

Sample	Shell	CN	R (Å)	σ^2 (Å^2)	R-factor
Ir-$MoSe_2$@$NiCo_2Se_4$	Ir-O	4.2	1.999	0.0014	0.018
	Ir-O	1.9	2.744	0.0021	

3.3.3 OER catalytic performance

Oxygen evolution is the most challenging reaction of overall water electrolysis due to its sluggish reaction kinetics involving four electron transfer process, thus generally require large overpotentials. To estimate the OER performance of the catalysts, linear sweep voltammetry (LSV) measurement was done in 1M KOH solution in three-

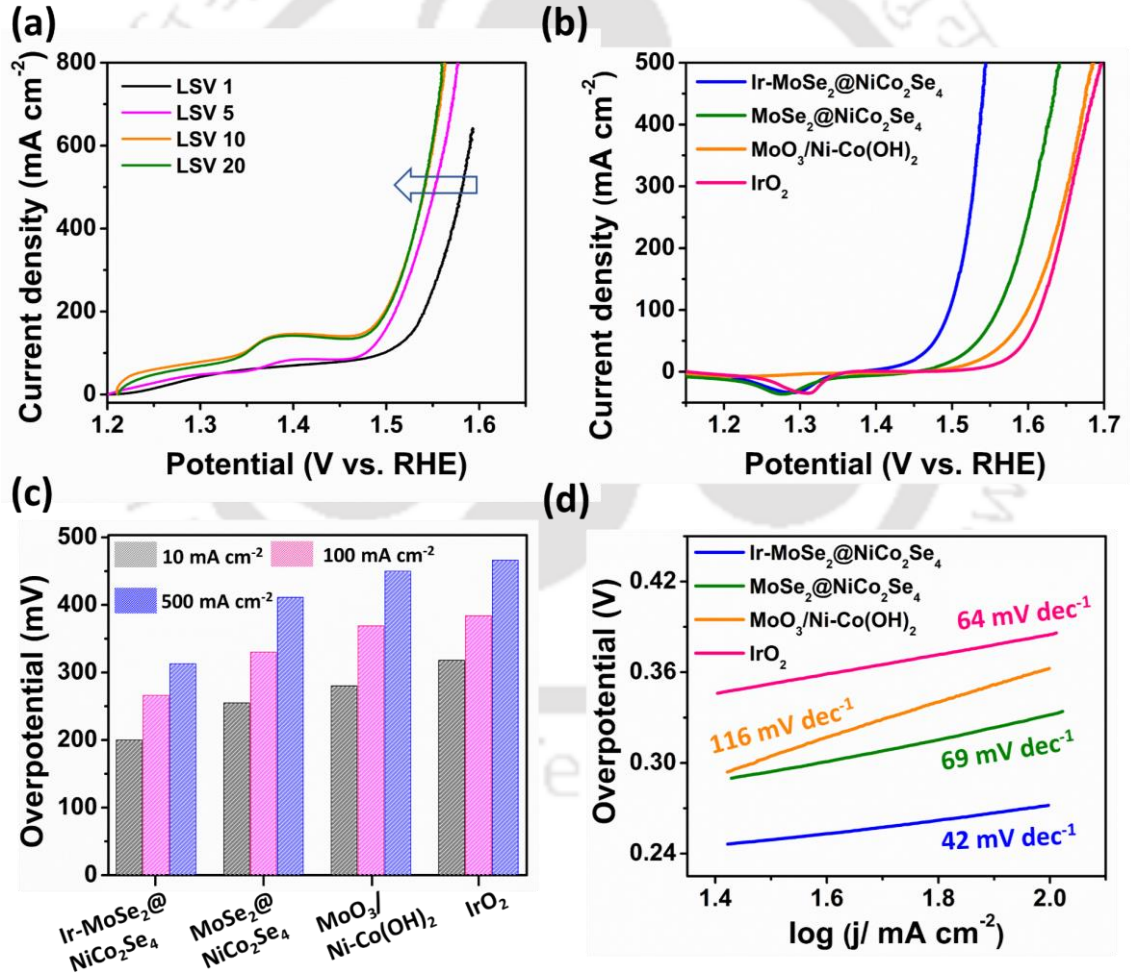

Figure 3.9. Electrochemical OER performance: (a) OER LSV cycles for activating Ir-$MoSe_2$@$NiCo_2Se_4$. (b) OER Polarisation curves for Ir-$MoSe_2$@$NiCo_2Se_4$, $MoSe_2$@$NiCo_2Se_4$, MoO_3/Ni-Co$(OH)_2$ and IrO_2 with *iR* compensation. (c) Bar diagram for required overpotential to reach 10 mA cm^{-2}, 100 mA cm^{-2} and 500 mA cm^{-2} for different catalysts, (d) corresponding Tafel plots.

electrode set-up. A typical transition metal-based selenide, sulphide and phosphide undergo surface reconstruction under OER operation condition, and LSV gets improved in consecutive cycles which is also obvious in other reported journals.[22,23] Thus, consecutive pre-LSV for 20 cycles (Figure 3.9a) were taken till there was no further modification in the curves, and all the data presented here is after this OER induced self-activation. LSV curves as presented in Figure 3.9b demonstrates that $MoSe_2$@$NiCo_2Se_4$ shows good catalytic activity, requiring an overpotential of 226 mV and 255 mV to get a current density of 1mA cm^{-2} (termed as onset potential) and 10 mA cm^{-2} respectively; these values outnumber MoO_3/Ni-$Co(OH)_2$ (238 mV and 280 mV) and commercial IrO_2 (257 mV and 318 mV). Strikingly, SAC-Ir linked heterostructure (Ir-$MoSe_2$@$NiCo_2Se_4$) show dramatic improvement in catalytic efficiency where its onset potential is only 153 mV and it requires an overpotential of only 200 mV to deliver OER current density of 10 mA cm^{-2}. Importantly, Ir-$MoSe_2$@$NiCo_2Se_4$ exhibits commercially demanding high current density at low overpotential (266 mV at 100 mA cm^{-2}, 313 mV at 500 mA cm^{-2}) which is shown at a comparison chart of overpotentials in various current density with pristine $MoSe_2$@$NiCo_2Se_4$, MoO_3/Ni-$Co(OH)_2$, IrO_2 and other high OER active bench mark catalysts (Figure 3.9c, Table 3.3 and Table 3.4).

Table 3.3. Summary of OER performance of different synthesized catalysts

Samples	η_{10} (mV)	η_{100} (mV)	η_{500} (mV)	Tafel slope (mV dec^{-1})	R_s (Ω)	R_{ct} (Ω)
Ir-$MoSe_2$@$NiCo_2Se_4$	200	266	313	42	1.03	0.45
$MoSe_2$@$NiCo_2Se_4$	255	330	411	69	1.05	0.87
MoO_3/Ni-$Co(OH)_2$	280	369	450	116	1.43	1.22

Table 3.4. Comparison of OER overpotentials at different current densities and Tafel slope for various reported electrocatalysts

Samples	η_{10} (mV)	η_{100} (mV)	Tafel slope (mV dec^{-1})	Reference
Ir-$MoSe_2$@$NiCo_2Se_4$	200	266	42	**This work**

Ir_V_G	320	-	52	[24]
Ir_1@Co/NC	260	465[a)]	119	[25]
Ir-NiO	215	260[a)]	38	[7]
$NiCoO_x$	281	-	76	[26]
NG@IrCo/NG	341	-	81	[27]
$SrIrO_3$	300	-	42	[28]
Co_Ni_3N	307	380[a)]	57	[29]
$Co_{1.8}Ni(OH)_{5.6}$	274	-	45	[30]
MoS_2/NiS_2	278	394	92	[31]
Au/NiFe LDH	237	270[a)]	36	[32]
A-Ni@DG	270	-	47	[33]
$NiCo_2S_4$ NA/CC	340	350[a)]	89	[34]
Ni_5P_4	330	-	40	[35]
$NiSe_2$/Ti	295	370[a)]	82	[36]
Co-C_3N_4	380	-	68	[37]

[a)] *(Data have been collected from OER LSV curve)*

Ir-$MoSe_2$@$NiCo_2Se_4$ also display the lowest Tafel slope of 42 mV dec^{-1} as compared to all other aforementioned catalysts, including commercial IrO_2 as shown in Figure 3.9d. The values of overpotentials and Tafel slope of Ir-$MoSe_2$@$NiCo_2Se_4$ are

among the lowest values reported for SAC-Ir and other benchmark catalysts, remarking this material to be the top-tier candidates for water electrolysis catalyst (Table 3.4).

To understand the intrinsic activity of the samples ECSA of Ir-$MoSe_2$@$NiCo_2Se_4$ has been calculated in Figure 3.10a and ECSA normalised LSV curves of catalyst have been shown in Figure 3.10b. In-situ activated Ir-$MoSe_2$@$NiCo_2Se_4$ has highest current

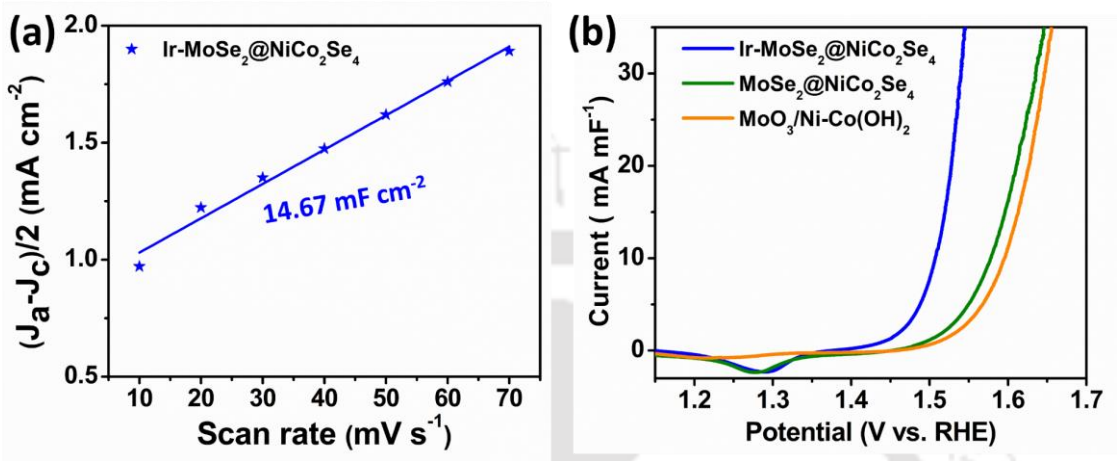

Figure 3.10. Electrochemical OER performance: (a) Current density versus scan rate plot to estimate the C_{dl} of the ECSA of Ir-$MoSe_2$@$NiCo_2Se_4$. (b) ECSA normalised OER LSV curves of Ir-$MoSe_2$@$NiCo_2Se_4$, $MoSe_2$@$NiCo_2Se_4$ and MoO_3/Ni-Co$(OH)_2$.

at any given potential compared to other synthesized samples, which indicate higher intrinsic OER activity of the catalyst. This higher intrinsic activity can be associated with high activity of linked SAC- Ir, and promotional effect coming from its base which get activated in-situ to generate Ni,Co-(oxy)hydroxide that increases density of states around Fermi level of Ir. To investigate the origin of highly boosted OER performance of Ir-$MoSe_2$@$NiCo_2Se_4$, charge transfer resistance (R_{ct}) values of the catalysts were also estimated from fitted EIS spectra. Ir-$MoSe_2$@$NiCo_2Se_4$ shows the lowest value of R_{ct} of 0.45 Ω (Figure 3.11a, Table 3.3), referring to beneficial OER reaction kinetics. Chronoamperometric test (Figure 3.11b) at an applied potential of 1.48 V (RHE) over long duration of 24 h shows excellent stability of the catalyst with practically demanding high current density of 50 mA cm^{-2}. Negligible variation of LSV curve of Ir-$MoSe_2$@$NiCo_2Se_4$ (Figure 3.11c) suggests the stability of performance. For more comprehensive stability test, multistep chronopotentiometry experiment was performed (Figure 3.11d) in which current is being increased in steps with consistent intervals of

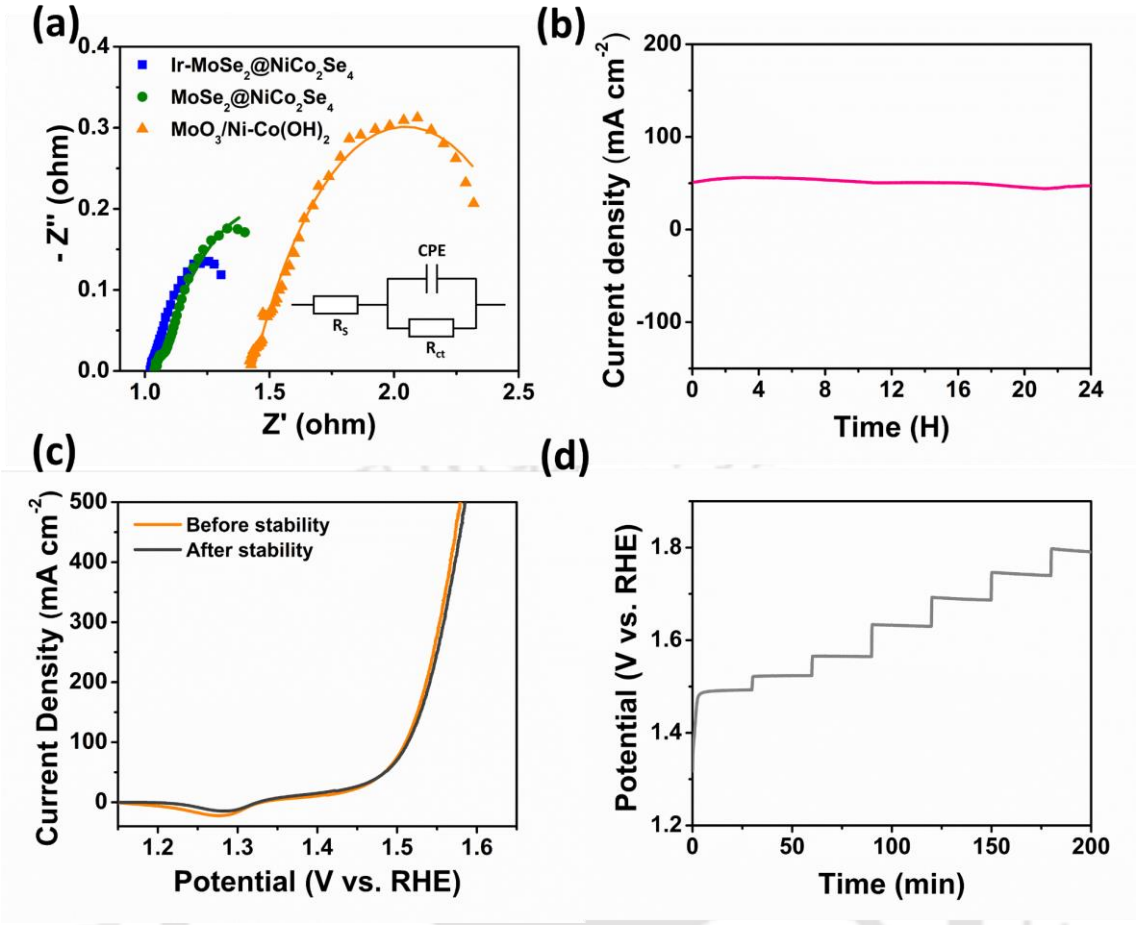

Figure 3.11. Electrochemical OER performance: (a) Nyquist plot of electrochemical impedance spectra in OER for different synthesized catalysts with fitting according to the model shown in the inset, (b) Chronoamperometric curve of Ir-$MoSe_2$@$NiCo_2Se_4$ at an applied potential of 1.48 V for 24 h duration, (c) shows polarization curves of the catalyst before and after stability. (d) Multistep chronopotentiometry test at different current density in step.

time to observe any decay in potential in that range. Throughout the range of 10-200 mA cm^{-2}, potential remains highly stable which also demonstrate stability and durability of sample in harsh operation conditions.

3.3.4 Overall water splitting

With the confirmation of excellent HER and OER activity of $MoSe_2@NiCo_2Se_4$ and self-activated Ir-$MoSe_2@NiCo_2Se_4$, the overall water splitting performance was tested using them as cathode and anode materials, respectively. Polarization curve of the full cell electrolyzer shows that it requires 1.51 V (not iR corrected) to produce OER current density of 10 mA cm^{-2} (Figure 3.12a), which is the lowest value among other bench mark heterostructure catalysts (Figure 3.12b).[24,25,27,28,38–44] Furthermore, this combination of electrodes shows an outstanding stability with negligible variation in current density for a continuous operation of 24 hours (Figure 3.12c). To see the practical implication feasibility, full cell electrolyzer of $MoSe_2@NiCo_2Se_4$ and Ir-

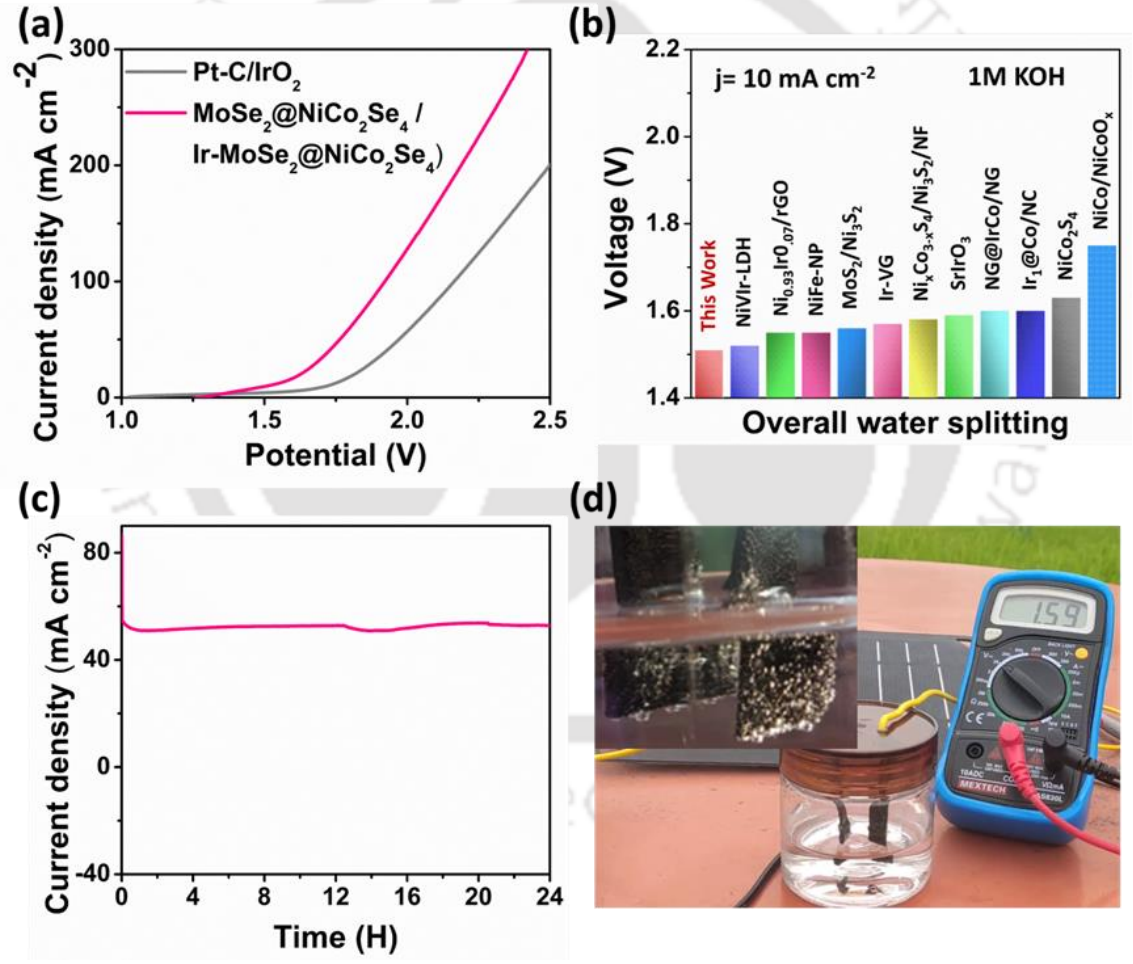

Figure 3.12. Overall water splitting: (a) Comparison of polarisation curves for $MoSe_2@NiCo_2Se_4$/Ir-$MoSe_2@NiCo_2Se_4$ and reference Pt-C/IrO_2 without iR correction for overall water splitting. (b) Comparison of cell voltage at 10 mA cm^{-2} for $MoSe_2@NiCo_2Se_4$/Ir-$MoSe_2@NiCo_2Se_4$ with previously reported catalysts. (c) Chronoamperometric test for overall water splitting at 1.76 V for a long time of 24 h for $MoSe_2@NiCo_2Se_4$/Ir-$MoSe_2@NiCo2Se_4$. (d) Digital photograph of the two-electrode configuration using a self-sustainable solar cell for overall water splitting.

$MoSe_2$@$NiCo_2Se_4$ was operated with commercial solar cell (Figure 3.12d). Continuous evolution of hydrogen and oxygen gas generation has been shown under natural sun light. Thus, the $MoSe_2$@$NiCo_2Se_4$ and in-situ activated Ir-$MoSe_2$@$NiCo_2Se_4$ prove itself to be an excellent platform of fully sustainable and renewable hydrogen generation system.

3.3.5 Post-OER characterizations

The surface of transition metal based sulfide/selenide/phosphides undergo reconstruction during OER process through concurrent leaching of some lattice ions or by generating highly active surface amorphous hydroxide/(oxy)hydroxide phases, which show much better catalytic activity as compared to directly synthesized hydroxide/(oxy)hydroxide counterpart.[8,9,45,46] Thus, linking SAC-Ir with sulfide/selenide/phosphides, and surface reconstruction of these hosts can combine unique advantages of activated amorphous hydroxide/(oxy)hydroxide and SAC-Ir to exhibit excellent OER activity. However, as compared to simple sulfide/selenide/phosphides, there is a highly important question involved with this process regarding the stability of high surface energy SAC-Ir over dynamically evolving reconstructed surface. If SAC-Ir structure still maintain after surface reconstruction, then only high activities of amorphous hydroxide/(oxy)hydroxide and SAC-Ir can be combined. Unfortunately, many of the reports with SAC linked sulfide/selenide/phosphides just refer the activities with the as-developed structures, without considering the final status of SAC or its host.[47,48] Thus, the study of surface reconstruction of SAC-Ir linked $MoSe_2$@$NiCo_2Se_4$ is important to know its surface evolution and the stability of SAC-Ir during this dynamical process. Furthermore, it is also highly important to know, whether the coordination environment and the oxidation state of SAC-Ir changes during this surface reconstruction process.

To inspect the origin of high OER efficiency and thereby shed light on the aforementioned questions, detailed microscopic and spectroscopic analysis were done on the Ir-$MoSe_2$@$NiCo_2Se_4$ sample after 24 h stability test. Morphological feature after stability test was analysed with FE-SEM characterization. From the result, OER reaction processed Ir-$MoSe_2$@$NiCo_2Se_4$ shows network of bigger sheets without the smaller sheets of $MoSe_2$ on its top (Figure 3.13a). This indicates significant crystalline modification happened in OER, and dissolution of $MoSe_2$ occurred in-situ.

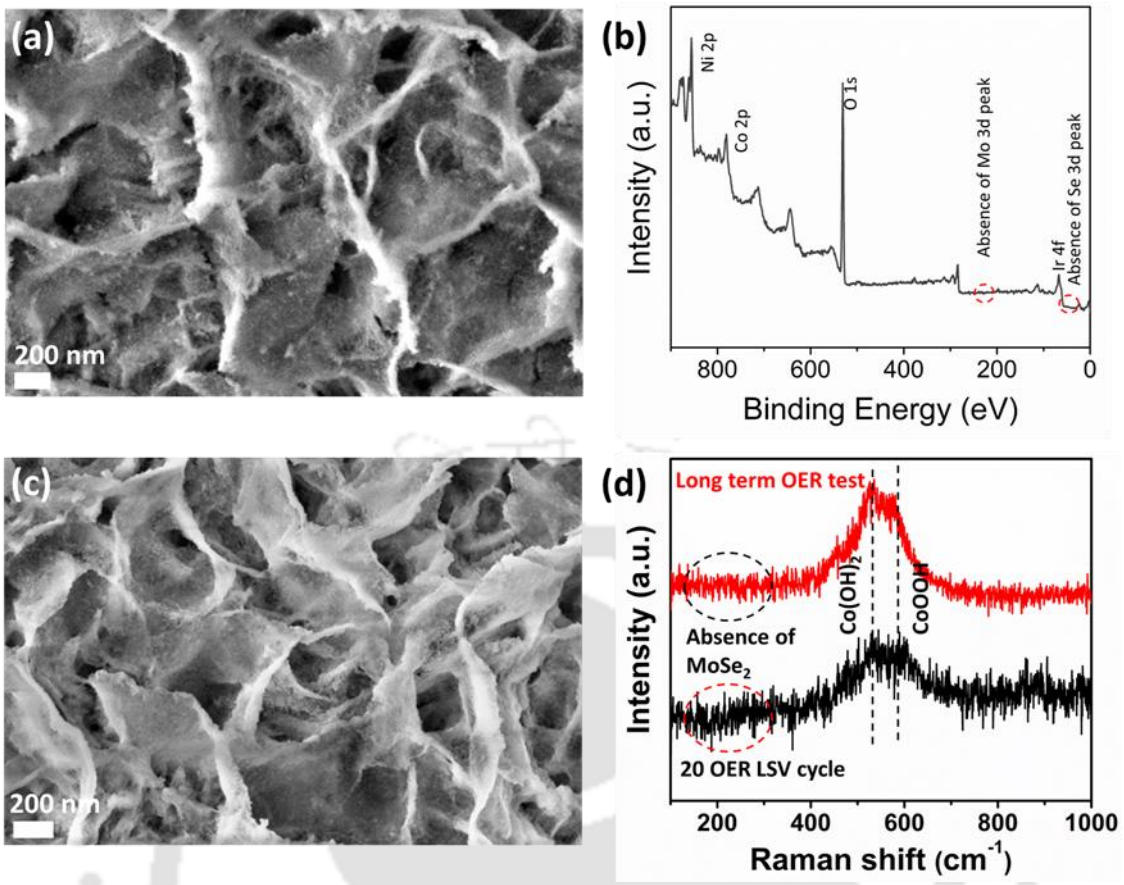

Figure 3.13. (a) FESEM image of Ir-$MoSe_2$@$NiCo_2Se_4$ after chronoamperometry test for 24h at 1.48 V, (b) XPS survey spectra of Ir-$MoSe_2$@$NiCo_2Se_4$ after OER chronoamperometry test showing absence of Mo 3d peak. (c) FESEM image of Ir-$MoSe_2$@$NiCo_2Se_4$ after 20 OER LSV cycle and (d) Raman of Ir-$MoSe_2$@$NiCo_2Se_4$ after chronoamperometry test for 24h at 1.48 V and 20 OER LSV cycles.

Table 3.5. EDX result for atomic percentage of different elements

Samples	Co (%)	Ni (%)	Mo (%)	Ir (%)	Se (%)	O (%)
Ir-$MoSe_2$@$NiCo_2Se_4$	8.0	5.7	7.7	1.5	36.7	40.5
Ir-$MoSe_2$@$NiCo_2Se_4$-Long term OER	4.46	7.14	0.07	1.01	0.22	87.08
Ir-$MoSe_2$@$NiCo_2Se_4$-20 OER LSV cycle	4.2	8.64	0.04	1.06	0.26	85.8

Energy dispersive X-ray analysis (EDS) (Table 3.5) and XPS survey scan (Figure 3.13b) also confirmed the dissolution of molybdenum from the system during OER process. Molybdenum dissolution is further confirmed from inductively coupled plasma mass spectrometry (ICP-OES) where Mo/Co ratio decreases from 76 % to 0.8 % after

24h OER stability test. Raman spectra modification after OER stability tests in Figure 3.13d revels no signature of $MoSe_2$, which further support the phenomenon of surface crystalline modification and subsequent $MoSe_2$ dissolution. To inspect the occasion of molybdenum removal, the sample after 20 cycles of LSV activation were investigated, and there was negligible content of molybdenum in the sample according to EDS (0.04 %), ICP-OES (Mo/Co- 1.1%). There was no signature of $MoSe_2$ related peaks in the Raman spectrum (Figure 3.13d) and small sheets of $MoSe_2$ were also absent in FESEM image (Figure 3.13c). Thus, it can be concluded that OER induced surface reconstruction quickly happens within few LSV cycles only. EDS analysis further revealed that, Ir-$MoSe_2$@$NiCo_2Se_4$ sample after stability test contains negligible selenium content (Table 3.5) and large increase of oxygen content on the surface, indicating surface phase transformation into hydroxide/(oxy)hydroxide. OER catalytic reaction seems to trigger self-activation process to reformulate the surface into hydroxide/(oxy)hydroxide linked SAC-Ir. Considering the poor OER catalysis of pure $MoSe_2$, its dissolution is actually beneficial for OER process as there is minor role of $MoSe_2$ in OER catalysis. Volcano plot, representing the theoretical predicted activity of different catalysts, shows that Ni/Co based catalysts are much more OER active as compared to Mo based ones.[49] Now, dissolution of $MoSe_2$ from surface reconstructed Ni/Co (oxy)hydroxide surface can expose more Ni/Co sites which also contributes to OER activity together with SAC-Ir. In addition, the sites of dissolved $MoSe_2$ now becomes rough (Figure 3.13a), which can also increase the catalytic activity due to increased local concentration of OH^- ions, which can be resulted from increase in local electric field at the nanoscale tips as recently explained by Yang et al.[50]

This surface activation process was further supported by XPS core level 2p spectra of Co and Ni in OER activated Ir-$MoSe_2$@$NiCo_2Se_4$. Together with (oxy)hydroxide related peaks, new doublet corresponding to $Co(OH)_2$ and NiOOH at 782 eV, 797.9 eV and 857.3 eV, 875.4 eV (Figure 3.14a, b) appears respectively at the expense of $NiCo_2Se_4$ related peaks.[30,51] Self-activation of $NiCo_2Se_4$ surface during OER into its hydroxide/(oxy)hydroxide form is also evident from the appearance of continuously increasing peak at around 1.39 V during activation for consecutive LSV cycles (Figure 3.9a) which indicates the rise of (oxy)hydroxide phase and oxidation process of Ni.[52] Ir 4f spectrum of surface activated Ir-NiCoOOH displays doublets centered at 65.2 eV and 62.2 eV suggesting their same high oxidation state (+4) as before OER activation process (Figure 3.14c). This surface self-activation during OER

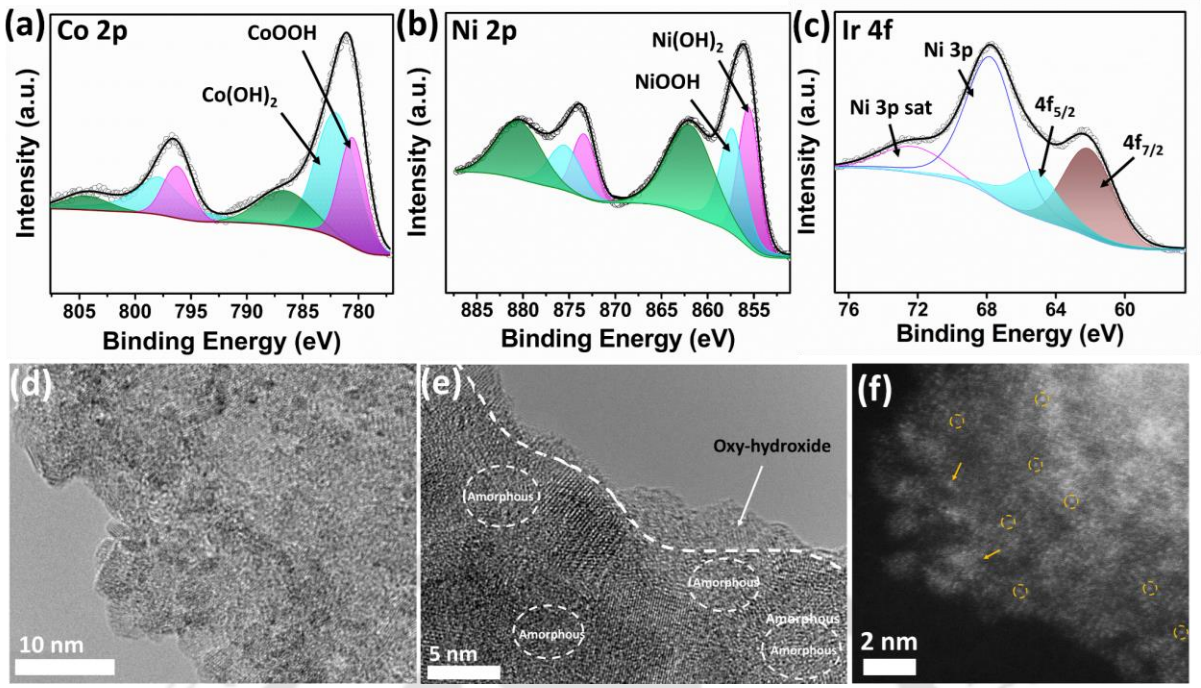

Figure 3.14. High resolution XPS spectra with deconvoluted peak for (a) Co 2p, (b) Ni 2p and (c) Ir 4f of OER activated Ir-NiCoOOH. (d) TEM, (e) HRTEM and (f) HAADF-STEM image of Ir-NiCoOOH.

operation actually helps to improve the catalytic activity as observed from improved slopes of LSV curves in consecutives cycles. HRTEM images (Figure 3.14d, e) of activated sample after stability test, reveals the disappearance of vertical $MoSe_2$ and the formation of amorphous layer as well as amorphous domains. The newly formed amorphous layers and domains can be attributed to Ni/Co- hydroxide/(oxy)hydroxide, matching with the result obtained via aforementioned XPS analysis.

The state of iridium particle after stability test was investigated with HAADF-STEM imaging, XPS, XANES and EXAFS. This surface activation throughout the catalytic operation does not cause any aggregation of Ir single-atom as confirmed from the Figure 3.14f. In addition, no obvious shift of the Ir 4f XPS spectra (Figure 3.14c) and XANES Ir L3- edge (Figure 3.15a) was observed indicating the same valance state of Ir as before OER test. From FT-EXAFS spectra in Figure 3.15b, no shift corresponding to Ir-O bond and no peak related to Ir-Ir have been observed in case of activated sample. This suggests no aggregation of Ir atoms occurs during long term OER stability. In addition, FT-EXAFS spectra of Ir-NiCoOOH catalyst have also been fitted as shown in Figure 3.16 and the fitting suggests Ir is coordinated to four O atoms of oxygen ligands (three oxygen ligands occur from the support NiCoOOH and the fourth

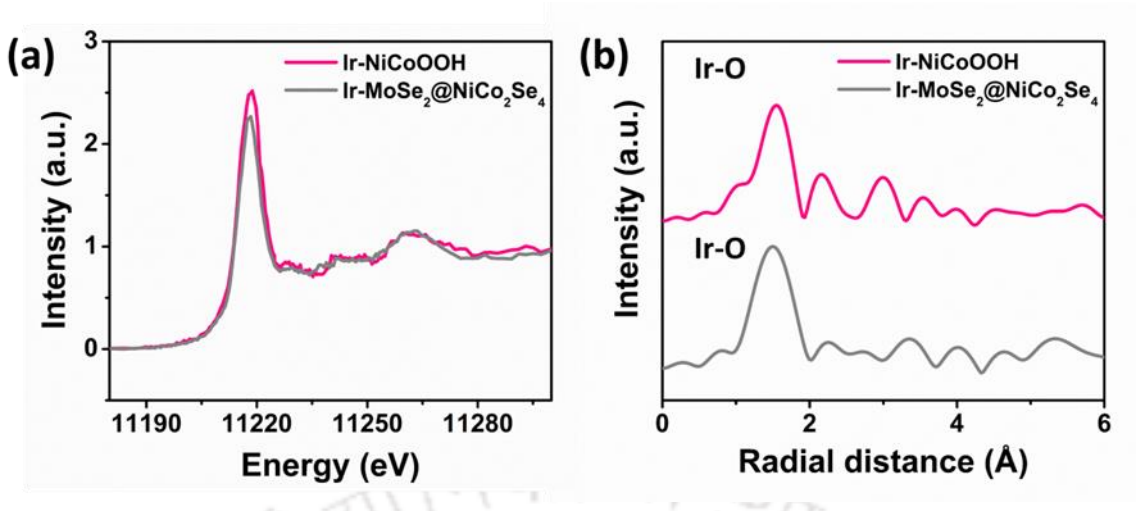

Figure 3.15. (a) Normalised XANES Ir L3-edge of Ir-$MoSe_2$@$NiCo_2Se_4$ and Ir-NiCoOOH and (b) represents corresponding FT-EXAFS spectra.

oxygen ligand is attached to Ir atom in terms of OH) and two O atoms of hydroxyl groups similar to

Table 3.6. Fitting parameters of FT-EXAFS spectra of Ir-NiCoOOH catalyst (CN: coordination number; σ^2: Debye-Waller factor)

Sample	Shell	CN	R (Å)	σ^2 (Å^2)	R-factor
Ir-NiCoOOH	Ir-O	4.3	2.0298	0.0055	0.019
	Ir-O	1.8	2.7000	0.0030	
	Ir-Ni	4.1	3.1096	0.0016	

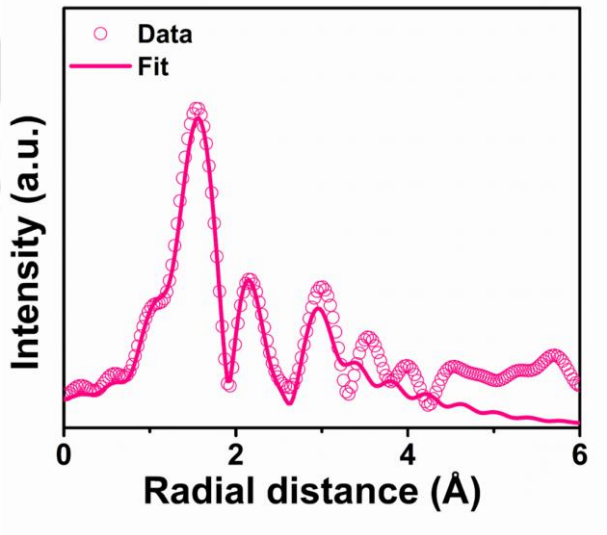

Figure 3.16. FT-EXAFS data fit for Ir-NiCoOOH

Ir-$MoSe_2$@$NiCo_2Se_4$. However, Ir is also interacting with Ni atom at 3.1 Å with a coordination number of 4 (Table 3.6). This suggests that during electrochemical surface reconstruction, the stabilization of SAC-Ir possibly associated with Ir-Ni interaction. The content of iridium remains very similar like the sample before OER induced surface atomic rearrangement confirmed through ICP-OES. Based on the aforementioned analysis, schematic of possible OER induced surface atomic rearrangement and activation process is given in Figure 3.17.

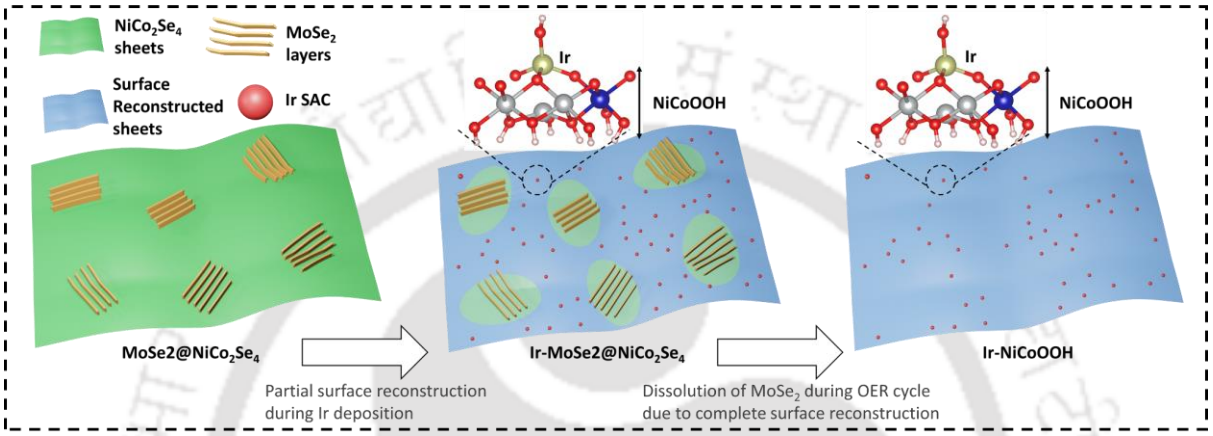

Figure 3.17. Schematic representation of surface reconstructed Ir-$MoSe_2$@$NiCo_2Se_4$ and dissolution of $MoSe_2$ from the heterostructure during OER cycle.

3.3.6 Theoretical calculation of OER

To explore the electronic origin of high OER activity of Ir-$MoSe_2$@$NiCo_2Se_4$, calculation was performed on SAC-Ir linked with NiCo-Oxy(hydroxide) as the surface, which actually play the role of catalysis after surface re-construction during OER. Plot

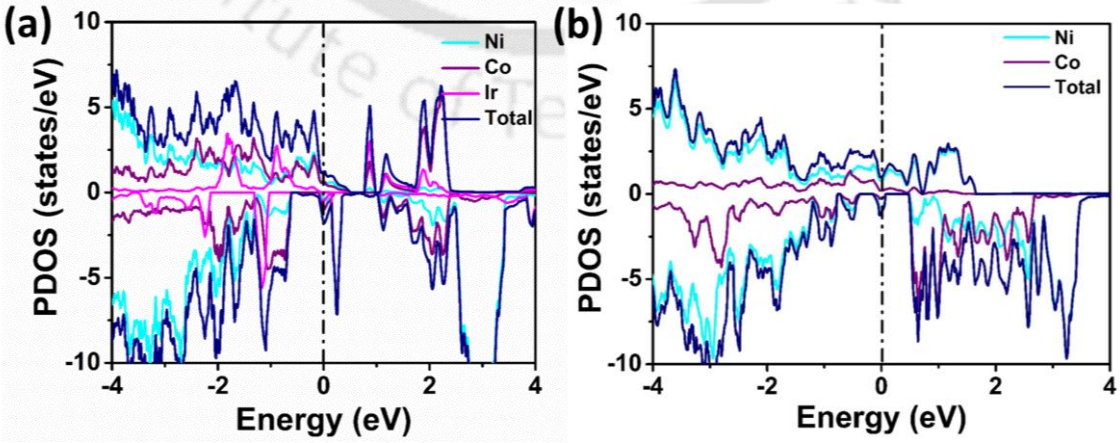

Figure 3.18. DFT calculation for OER: PDOS of (a) Ir-NiCoOOH and (b) NiCoOOH. Fermi level is set to zero in these plots.

of projected density of states (PDOS) (Figure 3.18a, b) shows that SAC-Ir introduces new localised electronic energy levels around the Fermi level of electrochemically activated Ir-NiCoOOH, and hence widen the total density of states (TDOS) around the Fermi level. Appearance of such localised states around Fermi level due to synergistic coupling of SAC-Ir and base NiCoOOH gives rise to the suitable adsorption of

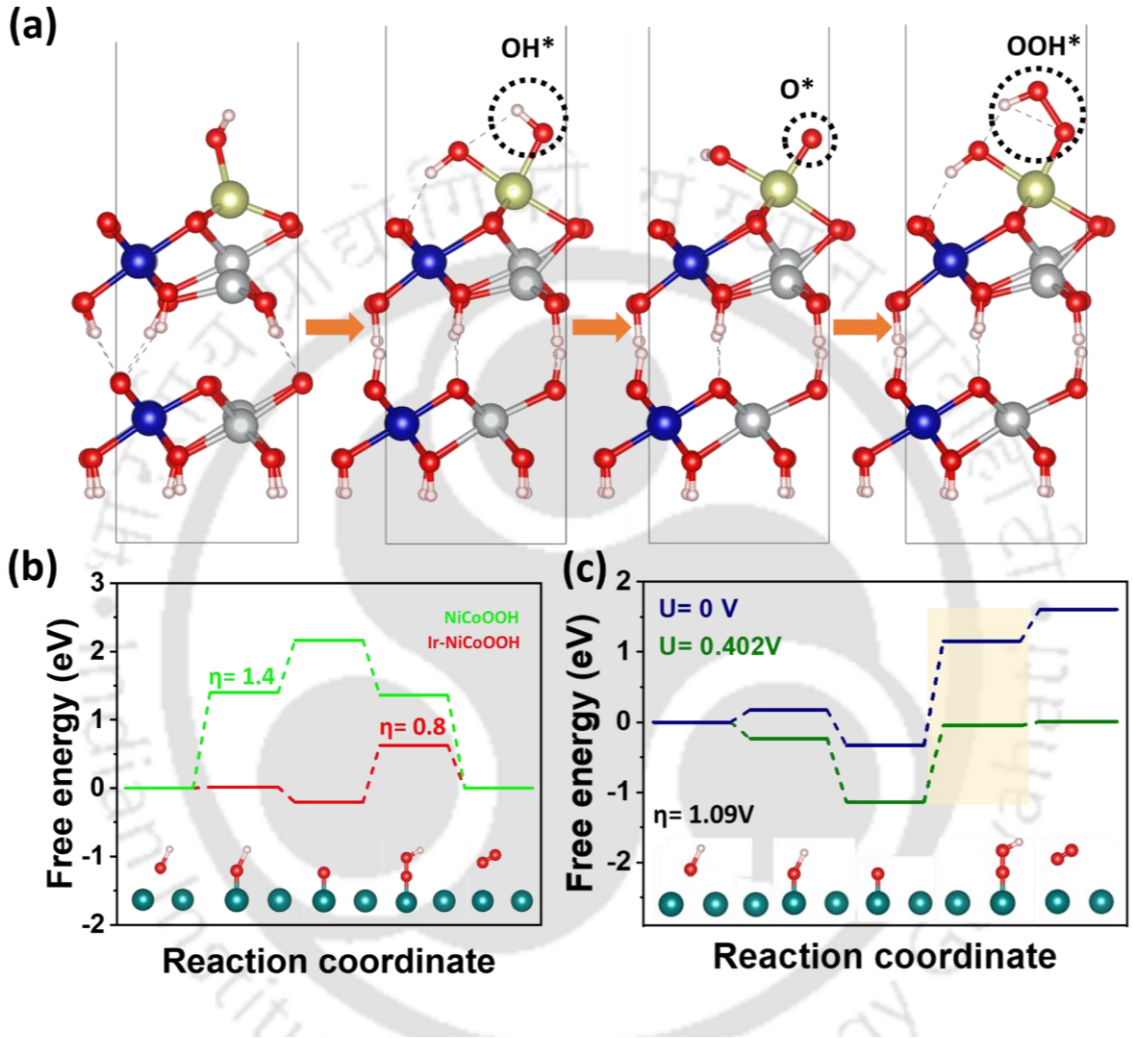

Figure 3.19. DFT calculation for OER: (a) Optimized atomic configuration of the Ir-NiCoOOH with different proposed OER elementary steps and (b) Free energy diagram of the proposed OER elementary steps at NiCoOOH and Ir-NiCoOOH catalyst. (c) Gibbs free energy profile for OER at Ir sites over Ir (001).

intermediate species and thus provide high catalytic activity compared to the base material.[53]

The optimised unit cells at different elementary stage of OER reaction are shown in Figure 3.19a. Calculation shows that Ni for NiCoOOH and Ni, Ir site for Ir-NiCoOOH are the active OER sites, whereas no adsorption of OH was observed on Co site. For OER alkaline condition, the rate determining step here is the formation of adsorbed

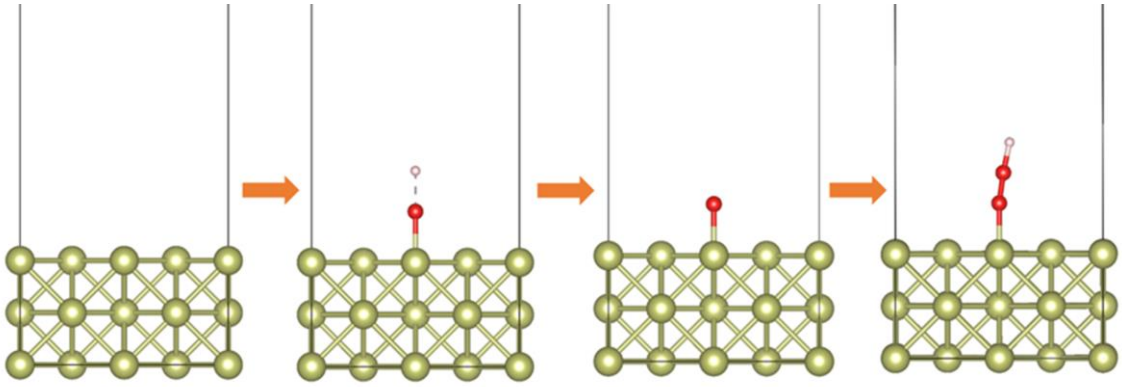

Figure 3.20. DFT calculation for OER: Optimized atomic configuration of the Ir (001) crystal at different proposed OER steps.

hydroxyl ion (OH*) for NiCoOOH and (OOH*) for Ir-NiCoOOH catalyst. Energy pathways of elementary steps (Figure 3.19b) demonstrates the Gibb's free energy for the rate determining step reduces significantly after the incorporation of Ir over NiCoOOH which can be attributed to the increased density of electronic states near the Fermi level. To further highlight the importance of single atom Ir decoration, we compare the catalytic activity of Ir-NiCoOOH with bulk Ir (001) surface. Calculations suggests that Ir-NiCoOOH have much lower Gibbs free energy for the rate determining step than that of Ir atoms in the Ir (001) crystal indicating the importance of single atom Ir decoration over catalytic surfaces (Figure 3.19c, Figure 3.20).

3.4 Conclusion

In summary, we have incorporated single atom iridium (SAC-Ir) to $MoSe_2$@$NiCo_2Se_4$ hybrid via photochemical process, which on electrochemical surface reconstruction turns into highly active OER catalyst. This OER catalyst shows one of the best performances with very low overpotential 200 mV for 10 mA cm^{-2} current density, and small Tafel slope of 42 mV dec^{-1}. Detailed XPS, XANES, EXAFS and TEM investigations reveal extensive in-situ surface reconstruction during OER to dissolute molybdenum from the heterostructure and conversion of selenide base into Ni,Co-hydroxide/oxyhydroxide (NiCoOOH). DFT calculation shows that, SAC-Ir widens the electronic density of states around Fermi level of NiCoOOH, and Gibb's free energy for rate determining step (O*-OOH*) of SAC-Ir site was found to be very low, which leads to high OER activity of Ir-NiCoOOH. $MoSe_2$@$NiCo_2Se_4$ as cathode and Ir-NiCoOOH as anode display very stable overall water splitting, and it requires only 1.51 V cell voltage to get a current density of 10 mA cm^{-2}, which is among the best in this field, including SAC based systems. Thus, in this work, facile photochemical process for single atom linking

and the understanding the state of Ir-SAC during dynamic OER process is expected to trigger new developments in broad area of electrocatalyst.

References

[1] S. Chu, A. Majumdar, *Nat. 2012 4887411* **2012**, *488*, 294.

[2] N.-T. Suen, S.-F. Hung, Q. Quan, N. Zhang, Y.-J. Xu, H. M. Chen, *Chem. Soc. Rev.* **2017**, *46*, 337.

[3] Y. Lee, J. Suntivich, K. J. May, E. E. Perry, Y. Shao-Horn, *J. Phys. Chem. Lett.* **2012**, *3*, 399.

[4] N. Cheng, S. Stambula, D. Wang, M. N. Banis, J. Liu, A. Riese, B. Xiao, R. Li, T. K. Sham, L. M. Liu, G. A. Botton, X. Sun, *Nat. Commun.* **2016**, *7*, 1.

[5] P. Xi, B. Huang, J. Yin, J. Jin, M. Lu, H. Zhang, Y. Peng, C. H. Yan, *J. Am. Chem. Soc.* **2020**, *142*, 18378.

[6] Y. Hou, M. Qiu, M. G. Kim, P. Liu, G. Nam, T. Zhang, X. Zhuang, B. Yang, J. Cho, M. Chen, C. Yuan, L. Lei, X. Feng, *Nat. Commun. 2019 101* **2019**, *10*, 1.

[7] Q. Wang, X. Huang, Z. L. Zhao, M. Wang, B. Xiang, J. Li, Z. Feng, H. Xu, M. Gu, *J. Am. Chem. Soc.* **2020**, *142*, 7425.

[8] H. Jiang, Q. He, X. Li, X. Su, Y. Zhang, S. Chen, S. Zhang, G. Zhang, J. Jiang, Y. Luo, P. M. Ajayan, L. Song, *Adv. Mater.* **2019**, *31*, 1.

[9] B. R. Wygant, K. Kawashima, C. B. Mullins, *ACS Energy Lett.* **2018**, *3*, 2956.

[10] C. Dong, X. Zhang, J. Xu, R. Si, J. Sheng, J. Luo, S. Zhang, W. Dong, G. Li, W. Wang, F. Huang, *Small* **2020**, *16*, 1.

[11] H. J. Monkhorst, J. D. Pack, *Phys. Rev. B* **1976**, *13*, 5188.

[12] A. J. Tkalych, H. L. Zhuang, E. A. Carter, *ACS Catal.* **2017**, *7*, 5329.

[13] F. Costanzo, *Phys. Chem. Chem. Phys.* **2016**, *18*, 7490.

[14] L. Xu, A. R. Tetreault, M. A. Pope, *Chem. Mater.* **2020**, *32*, 148.

[15] X. Li, L. Zhang, M. Huang, S. Wang, X. Li, H. Zhu, *J. Mater. Chem. A* **2016**, *4*, 14789.

[16] J. Yang, C. Yu, X. Fan, C. Zhao, J. Qiu, *Adv. Funct. Mater.* **2015**, *25*, 2109.

[17] J. Guo, Y. Shi, X. Bai, X. Wang, T. Ma, *J. Mater. Chem. A* **2015**, *3*, 24397.

[18] F. Xie, W. C. H. Choy, C. Wang, X. Li, S. Zhang, J. Hou, *Adv. Mater.* **2013**, *25*, 2051.

[19] B. Li, L. Jiang, X. Li, Z. Cheng, P. Ran, P. Zuo, L. Qu, J. Zhang, Y. Lu, *Adv. Funct. Mater.* **2019**, *29*, 1.

[20] M. Xiao, J. Zhu, G. Li, N. Li, S. Li, Z. P. Cano, L. Ma, P. Cui, P. Xu, G. Jiang, H. Jin, S. Wang, T. Wu, J. Lu, A. Yu, D. Su, Z. Chen, *Angew. Chemie - Int. Ed.* **2019**, *58*, 9640.

[21] H. N. Nong, T. Reier, H. S. Oh, M. Gliech, P. Paciok, T. H. T. Vu, D. Teschner, M. Heggen, V. Petkov, R. Schlögl, T. Jones, P. Strasser, *Nat. Catal.* **2018**, *1*, 841.

[22] K. Jiang, M. Luo, M. Peng, Y. Yu, Y. R. Lu, T. S. Chan, P. Liu, F. M. F. de Groot, Y. Tan, *Nat. Commun.* **2020**, *11*, 1.

[23] H. Zhang, X. Li, A. Hähnel, V. Naumann, C. Lin, S. Azimi, S. L. Schweizer, A. W. Maijenburg, R. B. Wehrspohn, *Adv. Funct. Mater.* **2018**, *28*, 1.

[24] S. B. Roy, K. Akbar, J. H. Jeon, S. K. Jerng, L. Truong, K. Kim, Y. Yi, S. H. Chun, *J. Mater. Chem. A* **2019**, *7*, 20590.

[25] W. H. Lai, L. F. Zhang, W. B. Hua, S. Indris, Z. C. Yan, Z. Hu, B. Zhang, Y. Liu, L. Wang, M. Liu, R. Liu, Y. X. Wang, J. Z. Wang, Z. Hu, H. K. Liu, S. L. Chou, S. X. Dou, *Angew. Chemie - Int. Ed.* **2019**, *58*, 11868.

[26] Y. Xue, G. Ma, X. Wang, M. Jin, E. M. Akinoglu, D. Luo, L. Shui, *ACS Appl. Mater. Interfaces* **2021**, *13*, 7334.

[27] Z. Si, Z. Lv, L. Lu, M. Liu, Y. Chen, H. Jin, X. Tian, K. Dai, J. Liu, W. Song, *ChemCatChem* **2019**, *11*, 5457.

[28] J. Yu, J. Yu, X. Wu, D. Guan, Z. Hu, S. C. Weng, H. Sun, Y. Song, R. Ran, W. Zhou, M. Ni, Z. Shao, Z. Shao, *Chem. Mater.* **2020**, *32*, 4509.

[29] C. Zhu, A. L. Wang, W. Xiao, D. Chao, X. Zhang, N. H. Tiep, S. Chen, J. Kang, X. Wang, J. Ding, J. Wang, H. Zhang, H. J. Fan, *Adv. Mater.* **2018**, *30*, 1.

[30] B. Wang, C. Tang, H. F. Wang, X. Chen, R. Cao, Q. Zhang, *Adv. Mater.* **2019**, *31*, 1.

[31] J. Lin, P. Wang, H. Wang, C. Li, X. Si, J. Qi, J. Cao, Z. Zhong, W. Fei, J. Feng, *Adv. Sci.* **2019**, *6*, 1.

[32] J. Zhang, J. Liu, L. Xi, Y. Yu, N. Chen, S. Sun, W. Wang, K. M. Lange, B. Zhang, *J. Am. Chem. Soc.* **2018**, *140*, 3876.

[33] L. Zhang, Y. Jia, G. Gao, X. Yan, N. Chen, J. Chen, M. T. Soo, B. Wood, D. Yang, A. Du, X. Yao, *Chem* **2018**, *4*, 285.

[34] D. Liu, Q. Lu, Y. Luo, X. Sun, A. M. Asiri, *Nanoscale* **2015**, *7*, 15122.

[35] M. Ledendecker, S. Krick Calderón, C. Papp, H.-P. Steinrück, M. Antonietti, M. Shalom, *Angew. Chemie Int. Ed.* **2015**, *54*, 12361.

[36] Z. Pu, Y. Luo, A. M. Asiri, X. Sun, *ACS Appl. Mater. Interfaces* **2016**, *8*, 4718.

[37] Y. Zheng, Y. Jiao, Y. Zhu, Q. Cai, A. Vasileff, L. H. Li, Y. Han, Y. Chen, S.-Z. Qiao, *J. Am. Chem. Soc.* **2017**, *139*, 3336.

[38] J. Wu, R. Xie, X. Hu, Z. Nie, Y. Shi, Y. Yu, N. Yang, *J. Mater. Chem. A* **2021**, 9753.

[39] Y. Wu, Y. Liu, G. D. Li, X. Zou, X. Lian, D. Wang, L. Sun, T. Asefa, X. Zou, *Nano Energy* **2017**, *35*, 161.

[40] S. Zhang, X. Zhang, X. Shi, F. Zhou, R. Wang, X. Li, *J. Energy Chem.* **2020**, *49*, 166.

[41] A. Sivanantham, P. Ganesan, S. Shanmugam, *Adv. Funct. Mater.* **2016**, *26*, 4661.

[42] B. H. R. Suryanto, Y. Wang, R. K. Hocking, W. Adamson, C. Zhao, *Nat. Commun.* **2019**, *10*, 1.

[43] J. Zhang, T. Wang, D. Pohl, B. Rellinghaus, R. Dong, S. Liu, X. Zhuang, X. Feng, *Angew. Chemie - Int. Ed.* **2016**, *55*, 6702.

[44] D. Wang, Q. Li, C. Han, Q. Lu, Z. Xing, X. Yang, *Nat. Commun.* **2019**, *10*, 1.

[45] J. Chen, H. Chen, T. Yu, R. Li, Y. Wang, Z. Shao, S. Song, *Recent Advances in the Understanding of the Surface Reconstruction of Oxygen Evolution Electrocatalysts and Materials Development*, Vol. 4, Springer Singapore, **2021**.

[46] Y. Wang, Y. Zhu, S. Zhao, S. She, F. Zhang, Y. Chen, T. Williams, T. Gengenbach, L. Zu, H. Mao, W. Zhou, Z. Shao, H. Wang, J. Tang, D. Zhao, C. Selomulya, *Matter* **2020**, *3*, 2124.

[47] C. Cai, S. Han, Q. Wang, M. Gu, *ACS Nano* **2019**, *13*, 8865.

[48] Z. Zhang, C. Feng, C. Liu, M. Zuo, L. Qin, X. Yan, Y. Xing, H. Li, R. Si, S. Zhou, J. Zeng, *Nat. Commun. 2020 111* **2020**, *11*, 1.

[49] Z. W. She, J. Kibsgaard, C. F. Dickens, I. Chorkendorff, J. K. Nørskov, T. F. Jaramillo, *Science (80-.).* **2017**, *355*.

[50] P. Liu, B. Chen, C. Liang, W. Yao, Y. Cui, S. Hu, P. Zou, H. Zhang, H. Jin Fan, C. Yang, P. Liu, C. Liang, W. Yao, Y. Cui, S. Hu, P. Zou, C. Yang, B. Chen, H. Zhang, H. Zhang Hong Kong Branch, H. J. Fan, *Adv. Mater.* **2021**, *33*, 2007377.

[51] A. Sikdar, A. Majumdar, A. Gogoi, P. Dutta, M. Borah, S. Maiti, C. Gogoi, K. Anki Reddy, Y. Oh, U. Narayan Maiti, *J. Mater. Chem. A* **2021**, *9*, 7640.

[52] J. Y. C. Chen, L. Dang, H. Liang, W. Bi, J. B. Gerken, S. Jin, E. E. Alp, S. S. Stahl, *J. Am. Chem. Soc.* **2015**, *137*, 15090.

[53] J. Shan, C. Ye, S. Chen, T. Sun, Y. Jiao, L. Liu, C. Zhu, L. Song, Y. Han, M. Jaroniec, Y. Zhu, Y. Zheng, S. Z. Qiao, *J. Am. Chem. Soc.* **2021**, *143*, 5201.

Chapter 4

Microwave Induced Rapid Surface Amorphization of Metal Oxide Nanowire into Sulfides Shell: A New Design Strategy for Electronically Modulated Efficient Hydrogen Evolution Catalyst

Chapter 4

Microwave Induced Rapid Surface Amorphization of Metal Oxide Nanowire into Sulfides Shell: A New Design Strategy for Electronically Modulated Efficient Hydrogen Evolution Catalyst

Order/dis-order atomic arrangements in crystalline/amorphous structure possess a complementing effect in electro-catalysis as the former one can offer a long-range electronic conducting path, whereas the latter is rich with active sites. However, atomic level interfacing of crystalline and amorphous structures is extremely challenging and thus often end-up with uncontrolled secondary deposition one above another. Here, we are presenting second-scale atomic rearrangement of crystalline oxide nanowire surface into amorphous molybdenum sulfide shell that displayed excellent hydrogen evolution activity. Employing transient heating by microwave-activated graphene filament, surface atoms of molybdenum tungsten oxide (MoWO) nanowire can be arrested in either an amorphous or crystalline state during their sulfidation. Such a nanowire structure consisting of crystalline oxide core-amorphous sulfide shell shows excellent catalytic activity for hydrogen evolution reaction (HER) and exhibits an overpotential of 136 mV at 10 mA cm^{-2} in the acid electrolyte, which is much lower than the overpotential of parent oxide nanowire (356 mV) and its fully sulfurized crystalline counterpart (163 mV). As-developed catalyst also shows competitive HER performance with excellent alkaline and neutral electrolytes stability, thereby qualifying it as a pH universal catalyst. A detailed density functional theory calculation reveals oxide core promoted activation of multiple sites of amorphous sulfide phase, which provide key insights of electronic modulation via crystalline/amorphous interfacial structure for HER catalysis. This rapid and highly facile technique can lay the platform for the development of generic crystalline/amorphous core-shell nanostructure and their possible use as cost-effective and efficient catalysts.

4.1 Introduction:

The availability of low-cost and highly efficient catalysts for electrolytic hydrogen generation is critical for the large-scale implementation of green fuel-based hydrogen economy. Precious platinum noble metal gives state-of-the-art hydrogen evolution performance due to the suitable position of its 'd' band center close to Fermi Level and consequent perfect balance of adsorption/desorption energy of the elementary catalytic processes, but it's very high cost and scarcity limit large scale commercial use.[1–3] Tremendous research efforts have been paid to

develop suitable non-precious alternatives that can efficiently generate hydrogen at an affordable cost and also remains highly durable in operational condition.

Molybdenum sulfide is one of the most attractive candidates in this regard due to its natural abundance, resistance to corrosions, and high activity.[4] However, weak hydrogen adsorption over the basal plane of crystalline MoS_2 in the stable 2H phase makes the major portion of the materials dead/inactive, and activity is only limited to its edges.[5,6] This inactivity of the basal plane is associated with the fully occupied valance state of its sulfur atom, whereas under-coordinated sulfur atoms at the edges offer a partially occupied valance state which allows efficient hydrogen adsorption.[7,8] Efforts have been made to engineer MoS_2 to expose edges predominantly;[9] however, the generation of edge-dominated structures is difficult to realize.[10] In parallel, much emphasis has been paid to activating the sulfur sites of basal planes of MoS_2, and hence optimising the adsorption/desorption process by partially vacating their valance states via doping or incorporation of sulfur vacancy.[7,8,11] Nevertheless, controlled incorporation of such crystalline defects or dopants for suitable electronic tuning is still a highly challenging task. In contrast to the edge-specific activity of crystalline molybdenum sulfide, its amorphous form (a-MoS_x) having a disordered structure, offers numerous active sites throughout its surface and thus has gained much interest.[12–14] Nonetheless, very limited efforts have been made to tune and uplift the intrinsic activity of amorphous molybdenum sulfide.[15,16]

Core-shell nanowire heterostructure is a suitable platform to synergistically enhance the catalytic activity of the shell via electronic coupling while maintaining structural advantage of nanowires; however, for molybdenum/tungsten sulfide all the reports are limited to their crystalline form, not of their amorphous phase. For example, Jaramillo group developed vertically oriented crystalline MoO_3-MoS_2 core-shell heterostructure through high-temperature sulfidation under flowing hydrogen sulfide gas. This heterostructure showed an efficient hydrogen evolution reaction (HER) due to its facile charge transfer property of core MoO_3 and excellent HER catalytic activity of shell MoS_2.[17] A similar gas-phase controlled sulfidation strategy was also employed by Schmuki et al. to develop crystalline MoO_3-MoS_2 core-shell heterostructure from electrochemically grown MoO_3 nanowires grown with anodic alumina oxide (AAO) nanochannels. The obtained structure showed good HER activity, which gets benefited from its high density of stacking faults.[18] In another work, Jung et al. fabricated WO_3-WS_2 core-shell structure by two-step spontaneous oxidation and sulfurization of tungsten foil.[19] However, crystalline core-amorphous shell structure with amorphous a-MoS_x remains

an elusive goal as regular high-temperature methods favour crystalline structures, and conventional processing of such amorphous phase, like acidic precipitation or electrochemical process, does not process the high level of nanoscale controllability required for this kind of advanced structure. These are vast reasons amorphous a-MoS_x systems were never actively investigated for their full potential.

Here, we present a unique strategy to grow ultrathin a-MoS_x shell within seconds over crystalline molybdenum tungsten oxide (MoWO) nanowire core. High microwave absorption ability of partially reduced graphene oxide was utilized for radiative heating and transient surface reaction of MoWO with the sulfur source which gave rise to crystalline/amorphous core-shell structure. Surface atoms of nanowire react with hydrogen sulfide and undergo rapid rearrangement during this graphene filament involved transient heating process (GFTH), and the surface atomic arrangements can be arrested in an amorphous state depending on the GFTH timing. This unique amorphization of surface atoms shows highly stable and excellent HER activity requiring an overpotential of 136 mV to get a current density of 10 mA cm^{-2} in 0.5 M H_2SO_4 electrolyte, which is much better active as compared to their oxide (356 mV) and fully converted crystalline sulfide form (163 mV). Further, the catalysts also show good HER activity in alkaline and neutral electrolytes with excellent long-term operational stability, which makes it important for widespread pH conditions. Unlike the crystalline counterpart, the understanding of the origin of catalytic activity of amorphous molybdenum sulfide is very poor to date. A comprehensive understanding of the site-specific catalytic activity of amorphous a-MoS_x and the role of crystalline MoWO core in promoting the activity of different sites have been presented here. This fast, simple, and cost-effective process is expected to serve as a practical technology for core-shell-based active HER catalysts development. Furthermore, understanding of promoted catalysis will reveal the underlying principle governing the catalytic interaction on the surface of amorphous domains which will guide further development in this direction.

4.2 Experimental Section:

4.2.1 Materials:

Ammonium heptamolybdate tetrahydrate ($(NH_4)_6Mo_7O_{24}.4H_2O$) and sodium tungstate dihydrate ($Na_2WO_4.2H_2O$) were purchased from Sigma-Aldrich. Thiourea (CH_4N_2S) was bought from Alfa-Aesar. Hydrochloric acid (HCl) was purchased from Merck. Carbon cloth (CC) was obtained from Zoltek.

4.2.2 Synthesis of MoWO nanowire:

To eliminate surface contaminants, CC was first cleaned with ethanol and water under ultrasonication for 15 minutes each. To synthesize MoWO nanowires 0.8 g of $(NH_4)_6Mo_7O_{24}.4H_2O$ and 0.74 g of $Na_2WO_4.2H_2O$ were mixed in 60 ml distilled water and pH of the solution was changed to 3.0 with 5 M HCl under stirring. The mixed solution, along with the washed CC, was then transferred to a 100 ml autoclave and kept at 180°C for 6 hours. Once the reaction autoclave was cooled to room temperature, the growing sample over CC was washed with distilled water and ethanol and dried in a vacuum oven at room temperature.

4.2.3 Synthesis of a-MoS_x@MoWO and c-MoWS:

For microwave-assisted sulfidation of MoWO, first graphene oxide (GO) was prepared through modified Hummers' method and dried in a freeze dryer. This dried GO foam with the help of some graphite powder was partially reduced by microwave irradiation for 5s in a household microwave oven (1250 W). Then a piece of MoWO grown on CC was placed in a lab-made microwave reactor surrounded by partially reduced graphene foam mixed with CH_4N_2S and irradiated with microwave for a different time. Depending on time a-MoS_x@MoWO (8s) and c-MoWS (12s) were obtained which were then rinsed with distilled water and ethanol and dried in a vacuum oven.

4.2.4 Material characterisations:

Powder XRD patterns were done by Rigaku X-ray diffractometer with Cu Kα radiation (λ=1.5418 Å). Zeiss Sigma 300 FE-SEM was used to take FESEM images, while energy dispersive X-ray spectroscopy was carried out in an Ametek EDAX equipped with a Zeiss Sigma 300 FE-SEM. For HRTEM and STEM analysis, a Titan TM 80-300 (FEI) with probe Cs corrector was used. For elemental analysis and surface chemistry, XPS was conducted in ESCALAB Xi+ (Thermo Fisher) instrument.

4.2.5 Electrochemical measurements:

In a PARSTAT 3000A-DX potentiostat, electrocatalytic HER was performed using a three-electrode configuration with Ag/AgCl (saturated calomel electrode) as reference electrode, graphite rod as counter electrode, and 0.5 M H_2SO_4 (1M KOH and 1M PBS) as electrolyte. To measure the performance 1×1 cm^2 of synthesized samples on CC were immersed in the electrolyte as working electrode. All polarisation curves were collected

at a scan rate of 5 mV s^{-1} and then adjusted using iR compensation. All the potentials were calibrated against reversible hydrogen electrode (RHE) according to the formula,

$$E_{RHE} = E_{Ag/Agcl\ or\ SCE} + 0.059 \times pH + E_{CE}$$

Where, E_{CE} is the potential shift of counter electrode against RHE.

Impedance spectroscopy of samples was performed at an AC amplitude of 10 mV throughout a frequency range of 10 kHz to 0.1 Hz.

The double layer capacitance (C_{dl}) was determined using cyclic voltammetry curves (CV) in the 0.1-0.2 V potential range vs. RHE. At a potential of 0.15 V vs. RHE, half of the difference in anodic current (J_a) and cathodic current (J_c) was plotted. The slope of the above curve yields the C_{dl} value which is also proportional to ECSA of the catalysts.

4.2.6 Computational details for HER

Quantum Espresso package with ultrasoft pseudopotentials was used to carry out all the spin polarised DFT calculations.[20] Plane-wave (PW) method with generalised gradient approximation (GGA) based on Perdew-Burke-Ernzerhof exchange correlation functional was employed for the calculations. A kinetic energy cut-off of 1020 eV was used for the plane waves. Integration in the Brillouin zone was done using a 5 × 5 × 1 Monkhorst-Pack k-point mesh for geometric optimization and a 15 × 15 × 1 mesh for density of states (DOS). MoWO was modelled by replacing 4 alternative Mo atoms with 4 W atoms of a monoclinic MoO_3 unitcell having optimized lattice parameters of a = 8.09 Å, b = 7.80 Å, c = 7.36 Å (32 atoms). Mo_3S_9 cluster (12 atoms) was used as a motif of amorphous molybdenum sulphide (a-MoS_x).[21,22] The heterostructure model of HER catalyst a-MoS_x@MoWO was built using MoWO as the core and putting a-MoS_x cluster (12 atoms) over the (001) plane of MoWO (32 atoms) supercell. Atomic positions and lattice constants of all the model structures were fully optimized until the residual forces were less than 0.025 eV/Å. A vacuum of 15 Å was applied in all structures to avoid periodic image interaction along the surface. In all structures S-sites were considered as the hydrogen adsorption sites. The hydrogen adsorption free energy (ΔG_{H*}) was calculated by using the following equation

$$\Delta G_{H*} = \Delta E_{H*} + \Delta E_{ZPE} - T\Delta S_{H*} \qquad 4.1$$

Where, the hydrogen chemisorption energy of the catalyst, ΔE_{H*} is defined as,

$$\Delta E_{H*} = E_{H*} - E_* - \frac{1}{2}E_{H_2} \quad 4.2$$

Where, E_{H*} , E_* are the total energies of surface with and without adsorbed H atom respectively and E_{H_2} is the total energy of H_2 molecule in the gas phase. ΔE_{ZPE} and ΔS_{H*} is the zero-point energy and entropy difference between adsorbed hydrogen and hydrogen in the gas phase respectively. Hence, the Gibbs free energy for hydrogen adsorption can be written as,[23]

$$\Delta G_{H*} = \Delta E_{H*} + 0.24 \quad 4.3$$

4.3 Results and Discussions

The process of microwave-involved surface amorphization of nanowire has been presented schematically in Figure 4.1. Molybdenum tungsten oxide nanowire (MoWO) grown over carbon cloth was sandwiched between partially reduced graphene oxide aerogels (prGO), in which sulfur precursor (thiourea) was mixed with the lower part of aerogel. The entire system was then placed within a glass vial, and the microwave heating was done under N_2 condition in a microwave oven (detail in the experimental section). It is important to use prGO for this purpose, as its free electrons can efficiently absorb microwave radiation to induce eddy current, and its low conductivity can ensure fast resistive heating up to a very high temperature (~1500°C).[24,25] The high temperature of prGO quickly decomposes thiourea to generate hydrogen sulfide gas (H_2S) which start reacting with surface of MoWO nanowire.[26] Once the microwave was turned off after few seconds, the graphene filament got cooled in ultrafast rate.[25] This transient heating and cooling process leaves the reacting surface atoms in the disordered amorphous state as they do not get sufficient time to crystallize, hence lead to crystalline/amorphous core-shell structure. Interestingly, for a reaction time of 8s, surface molybdenum atoms of MoWO nanowires turn into amorphous sulfide whereas tungsten remains in the oxide state. This has been confirmed by XPS analysis and will be discussed in

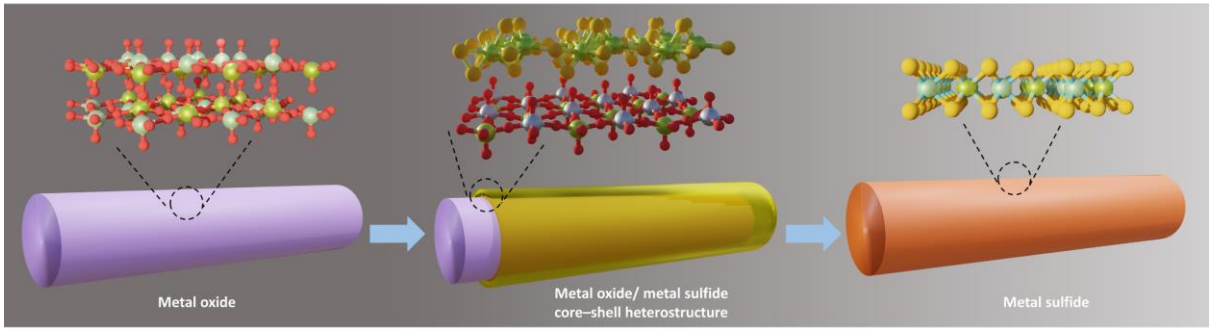

Figure 4.1. Schematic diagram of phase evolution during microwave irradiation.

the subsequent sections, and henceforth this sample will be termed as a-MoS_x@MoWO. Allowing the reaction to continue for few more seconds (12s) leads to near full conversion into crystalline MoW-sulfide (c-MoWS). This reactive surface amorphization/crystalline process under GFTH condition is presented schematically in Figure 4.1.

4.3.1 XRD analysis:

To implement the concept of crystalline/amorphous core-shell nanowire structure molybdenum tungsten oxide (MoWO) was chosen as the core material. Ultrathin nanowires of MoWO were grown over carbon cloth substrate via hydrothermal technique (Detail in experimental section). X-diffraction patterns (Figure 4.2) give an insight of the crystalline phase conversion process

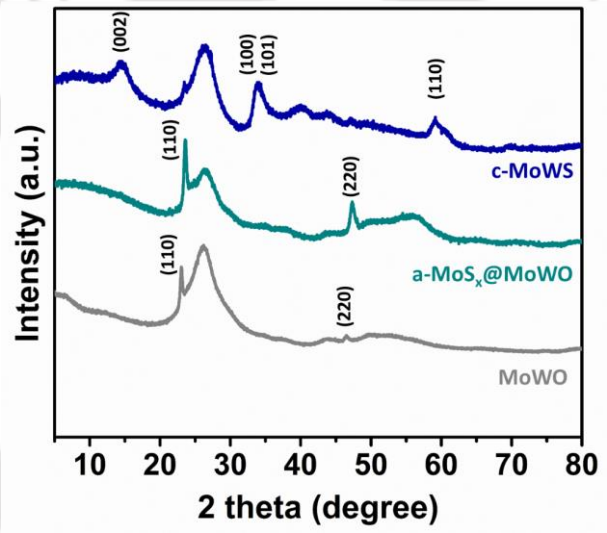

Figure 4.2. XRD pattern of MoWO, a-MoS_x@MoWO, c-MoWS.

during the GFTH. The XRD patterns of hydrothermally synthesized MoWO contain peaks at 2θ =23.03° corresponding to $Mo_{0.5}W_{0.5}O_3$ phase (JCPDS no. 028-0667) along with a broad peak at 26.2 coming from carbon cloth (CC) substrate. At lower GFTH time (8s), no additional peaks except MoWO related peaks were detected. XRD analysis indicates that either no change in crystalline phase happens for 8s GFTH or an amorphous phase may appear which is undetectable under XRD. Interestingly, increase of GFTH duration to 12s leads to near disappearance of MoWO related peaks, and emergence of additional peaks at 2θ values of 14.40°, 33.91° and 59.17° (Figure 4.2). Out of these, a peak at 33.91° can be assigned to either (100) planes of MoS_2 (JCPDS no. 37-1492) or (101) planes of WS_2 (JCPDS card no. 01-84-1398). On the other hand, other two peaks at 14.40° and 59.17° are related to (002) and (110) planes of either MoS_2 or WS_2 as both phases have peaks at the same position. XRD analysis of the sample corresponding to 12s GFTH confirms the evolution of crystalline sulfide structure.

Interestingly, EDS elemental analysis (Table 4.1) shows continuous increase of sulfur content in the structure with increase of GFTH time, indicating continuous phase evolution. Considering the EDS result (presence of sulphur) and XRD pattern (absence of crystalline sulphide peaks) suggest that 8s GFTH sample may form amorphous sulfide phase (a-MoS_x) while crystalline phase appears at higher GFTH time (12s) sample.

Table 4.1: Atomic percentage of elements in different synthesized samples from EDS analysis

Samples	Mo	W	S	O
MoWO	5.72	6.32	-	87.95
a-MoS_x@MoWO	9.64	10.68	16.37	63.29
c-MoWS	14.66	16.12	58.5	10.7

4.3.2 Morphological analyses:

Conformal growth of thin and uniform MoWO nanowires over each fibre of the cloths can be seen from its FESEM images (Figure 4.3a, inset shows the low magnification image). When the as-grown oxide nanowire is subjected to controlled graphene filament based transient

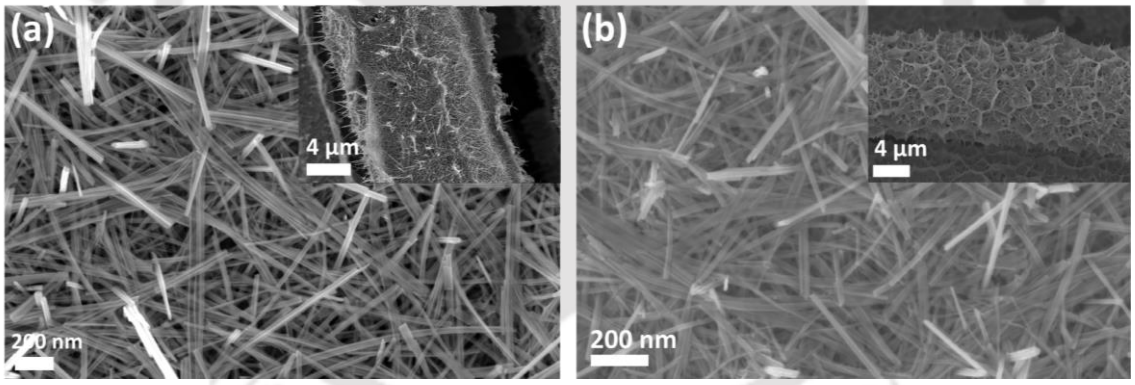

Figure 4.3. FESEM images of (a) MoWO and (b) a-MoS_x@MoWO. Inset shows the low magnification images

microwave heating (GFTH), no apparent morphological change was observed (Figure 4.3b, low magnification image in the inset). Low-resolution transmission electron microscopy confirms the nanowire structure of MOWO (Figure 4.4a) and its high-resolution transmission electron microscopy (HRTEM) reveals that parallel lattice fringes correspond to (110) planes (spacing 0.39 nm) of monoclinic $Mo_{0.5}W_{0.5}O_3$ (Figure 4.4b). The crystalline phase evolutions were further analysed with HRTEM investigation. GFTH treatment does not change the overall nanowire morphology (Figure 4.5a), however, interesting crystalline structure variations among the samples obtained with different GFTH treatment can be seen from their TEM &

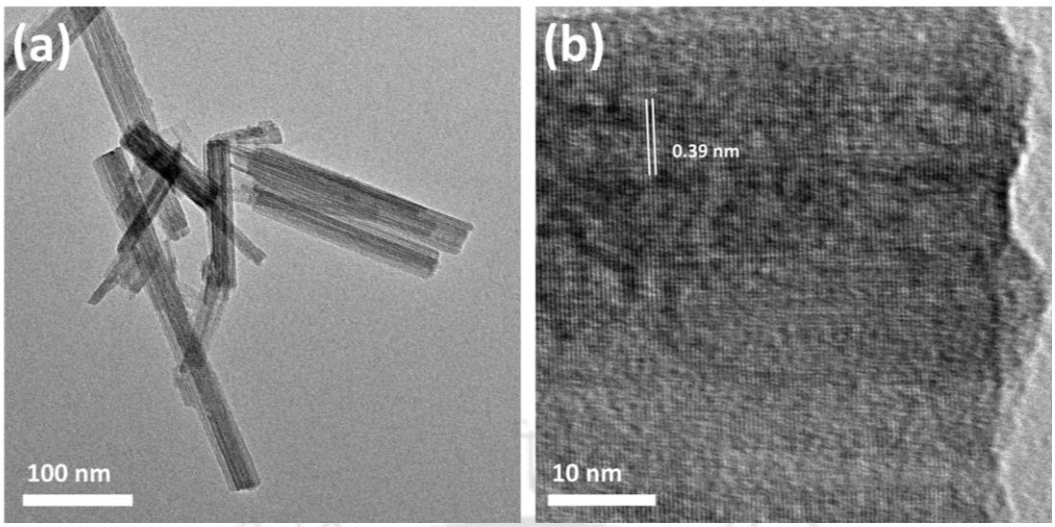

Figure 4.4. (a) TEM and (b) HRTEM image of MoWO

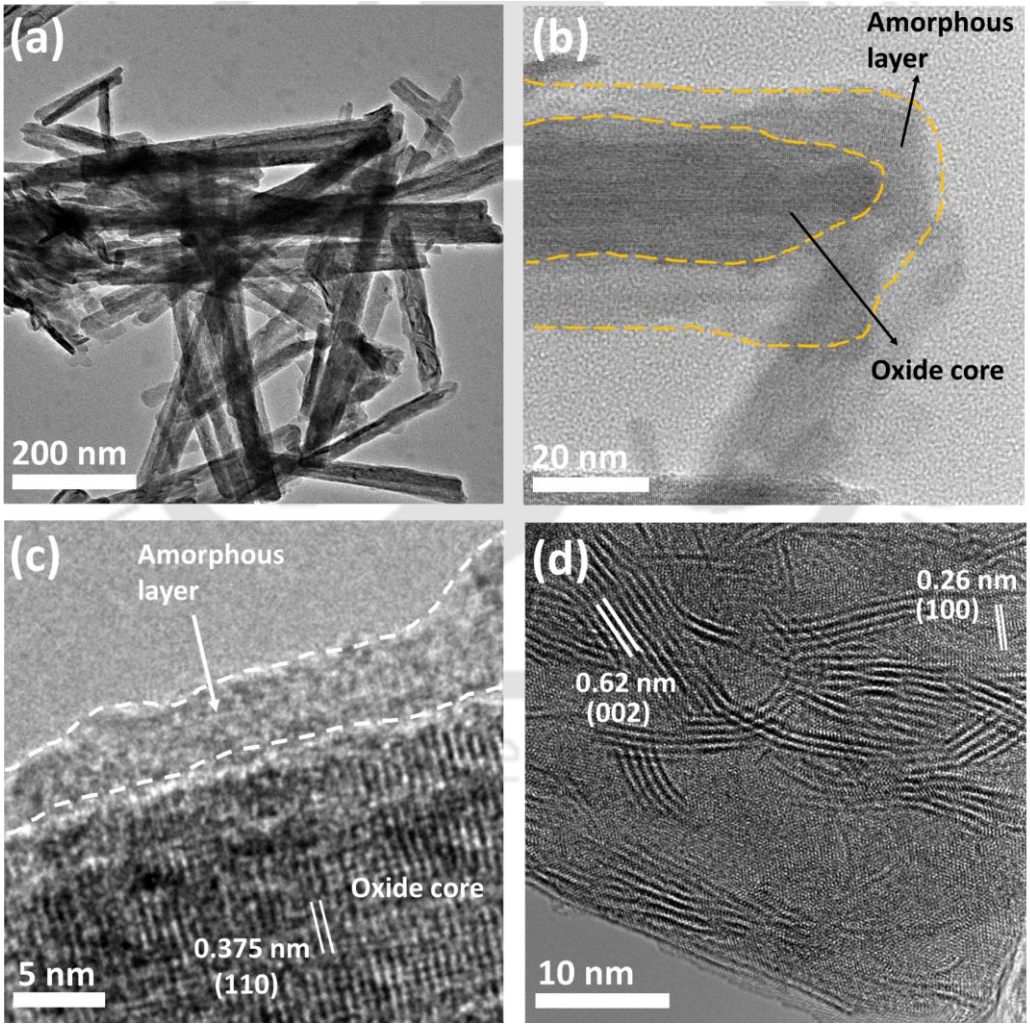

Figure 4.5. (a) Low resolution, (b) high resolution TEM of a-MoS_x@MoWO. HRTEM images of (c) a-MoS_x@MoWO and (d) c-MoWS.

HRTEM images (Figure 4.5b-d). Amorphous shell of low thickness (~3-7 nm) can be detected

over crystalline core of 8s GFTH treated sample as is evident from TEM & HRTEM image (Figure 4.5b, c). The inter-planar spacing of core is consistent with parent MoWO nanowire, and the shell can be identified as the amorphous sulfide layer. Thus, combining XRD and HRTEM analysis we can conclude that amorphous shell grows over GFTH treatment of 8s, and the amorphous layer is that of sulfide as confirmed by EDS. In sharp contrast, sample developed at higher GFTH time (12s) shows the evolution of crystalline phases, as is evident from clearly visible lattice fringes with inter-planar distances of 0.62 nm and 0.26 nm correspond to MoS_2 /WS_2 which confirms phase conversion into crystalline sulfide structure, consistent with XRD analysis (Figure 4.5d).

4.3.3 XPS analysis:

To highlight the changes in the chemical state of surface and shade light on the phase evolution during GFTH induced sulfidation the samples were investigated with X-ray photoelectron spectroscopy (XPS). The deconvoluted XPS spectra of W 4f, Mo 3d and S 2p before and after GFTH treatment were presented in Figure 4.6a-c. An important observation is that W 4f core level XPS spectra of MoWO and a-MoS_x@MoWO are nearly identical which signifies that tungsten remains in the same state in both the cases (Figure 4.6a). Thus, the amorphous sulfide shell over oxide core of a-MoS_x@MoWO cannot be that of tungsten-based sulfide. Change of chemical state of W happens for the case of c-MoWS, as characteristic peaks related to crystalline WS_2 at 32.9 ($4f_{7/2}$) and 35 eV ($4f_{5/2}$) can clearly be observed in W 4f XPS spectra (Figure 4.6a).[27] Unlike tungsten, the spectral feature of XPS Mo 3d peak shows obvious changes in a-MoS_x@MoWO. This 8s GFTH treated sample exhibits three doublet peaks at 229.8 eV/ 232.9 eV, 230.8 eV/ 234 eV and 233 eV/ 236.1 eV which correspond to Mo^{4+} of molybdenum sulfide, Mo^{5+} of Mo^{V} defect centres of molybdenum sulfide and Mo^{6+} of MoO_3 respectively (Figure 4.6b).[12,28,29] The presence of Mo^{4+} states of its sulfide while absence of W related sulfide phase suggests that the amorphous shell of 8s GFTH can be associated with molybdenum sulfide phase. For c-MoWS, XPS doublets due to Mo^{6+} of MoO_3 and Mo^{4+} (229.7 eV/ 232.7 eV) of molybdenum sulfide can only be found without any Mo^{V} defect centres, which indicates possible formation of crystalline MoS_2 phase and is also consistent with crystalline information obtained from HRTEM. A better idea about the amorphous and crystalline phase in a-MoS_x@MoWO and c-MoWS samples can be gained from the positions and the intensity ratio of the characteristic doublets of XPS of S2p.[22,30] The deconvoluted S 2p XPS spectra of a-MoS_x@MoWO comprise two sets of spin splitted doublets ($2p_{3/2}$ & $2p_{1/2}$) (Figure 4.6c), higher binding energy (S_{HBE}) doublets at 164 eV/ 165.1 eV can be attributed to

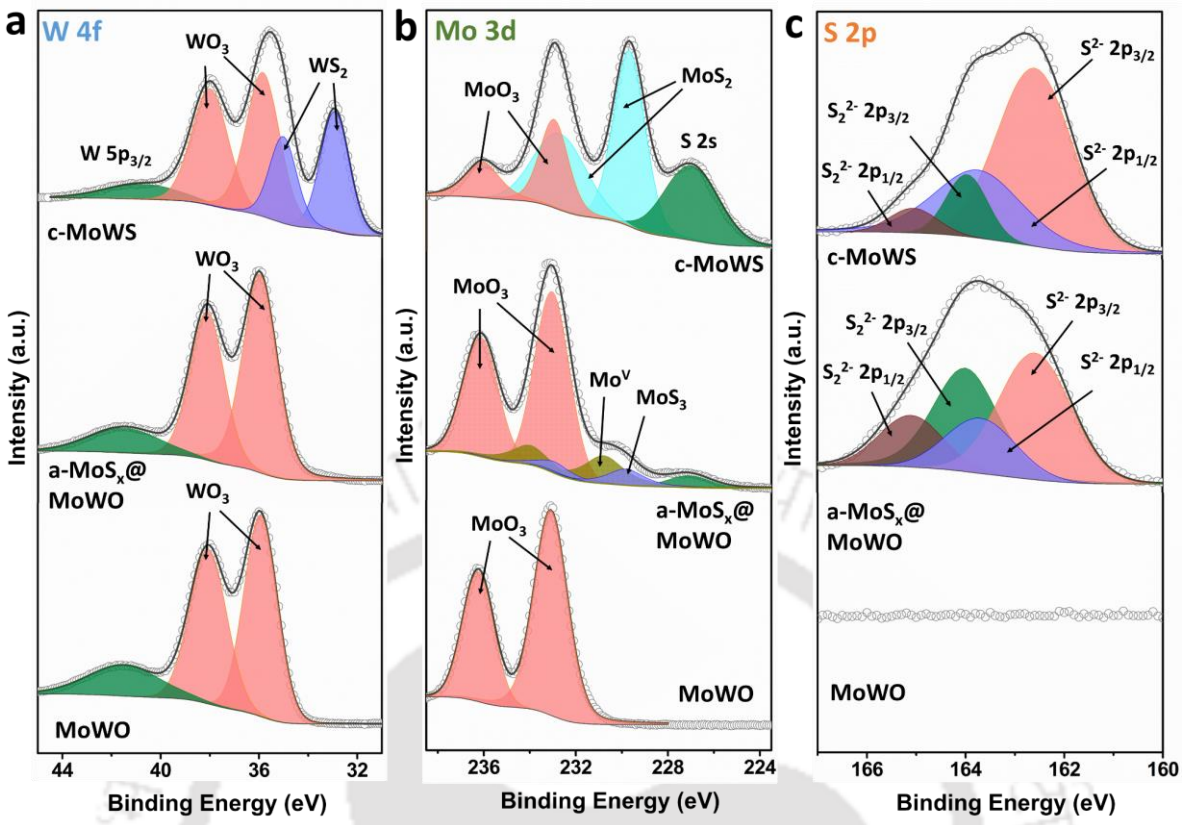

Figure 4.6. High resolution XPS spectra with fitting for: (a) W 4f, (b) Mo 3d and (c) S 2p of MoWO, a-MoS_x@MoWO and c-MoWS

apical S^{2-} and bridging S_2^{2-} of amorphous molybdenum sulfide (a-MoS_x) whereas lower binding energy (S_{LBE}) doublets at 162.6 eV/ 163.7 eV can be attributed to its unsaturated S^{2-} and/or terminal S_2^{2-} sites.[31] The intensity ratio of S_{LBE} to S_{HBE} was determined from the XPS peaks to be 5:4, which is a characteristic feature of amorphous form of MoS_3, indicating the existence of amorphous molybdenum sulphide in the structure.[22,30] Amorphous MoS_3 is an aggregation of {S-Mo-S_2} units in the form of {Mo_3-S_9} cluster type, which has a possible four triangular structure.[22] In these possible structures, triangles with bridging S_2^{2-} and S^{2-} ligands between two Mo atoms along with apical sulfur atom (bonded to three Mo atoms) are possible as shown in Figure 4.7. On the other hand, S 2p XPS spectrum of the c-MoWS sample shows two doublets at 162.5 eV/ 163.7 eV (S_{LBE}) and 164.1 eV/ 165.2 eV (S_{HBE}). The intensity ratio of S_{LBE} and S_{HBE} in this case was found to be 5:1, which is different corresponding to MoS_3 structure having a ratio of 5:4. This indicates that the molybdenum sulfide in this sample (c-MoWS) is not amorphous, which is also consistent with XRD and HRTEM observations. In this sample, the lower binding energy peaks can be attributed to S^{2-} species in the crystalline MoS_2 basal plane, whereas the higher binding energy peaks can be owing to bridging disulfide S_2^{2-} ligands on the MoS_2 edge, which are widely recognised as unsaturated sulphur edges.[32]

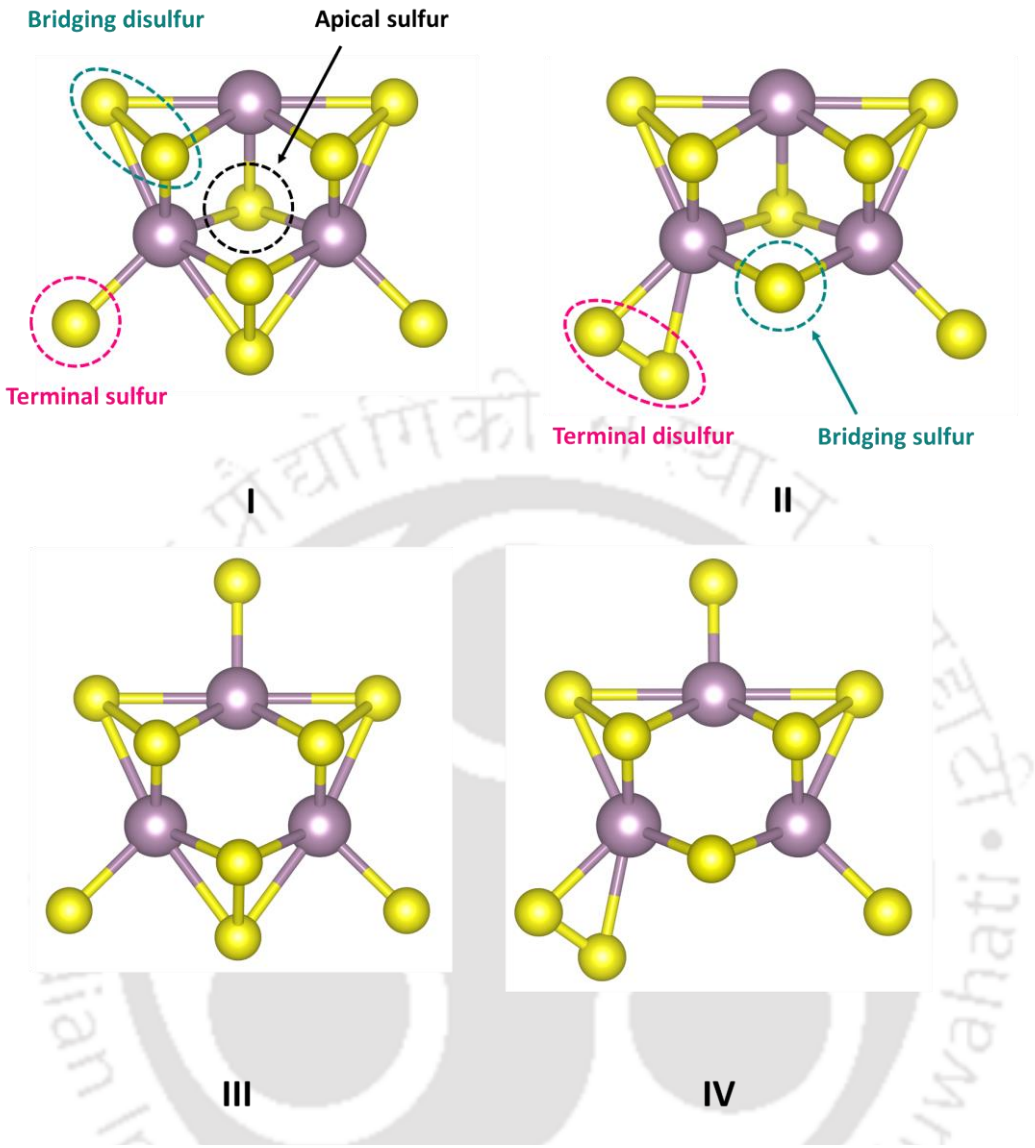

Figure 4.7. Possible {Mo_3-S_9} clusters to represent MoS_3 structure

These observations taken together signify that molybdenum is easily sulfurized at lower GFHT time of 8s whereas sulfidation of tungsten atoms requires higher time (12s). Based on the aforesaid finding, it can be concluded that the absence of tungsten sulphide peaks and the existence of amorphous a-MoS_x along with MoWO in 8s GFTH treated sample points to the creation of a-MoS_x and MoWO heterostructure (a-MoS_x@MoWO).

4.3.4 HER catalytic performance in 0.5 M H_2SO_4:

The amorphous sulfide shell over crystalline oxide nanowire is expected to serve as an excellent hydrogen evolution catalyst due to the presence of numerous active sites on the surface and possible interfacial synergy. HER performances of a-MoS_x@MoWO, c-MoWS,

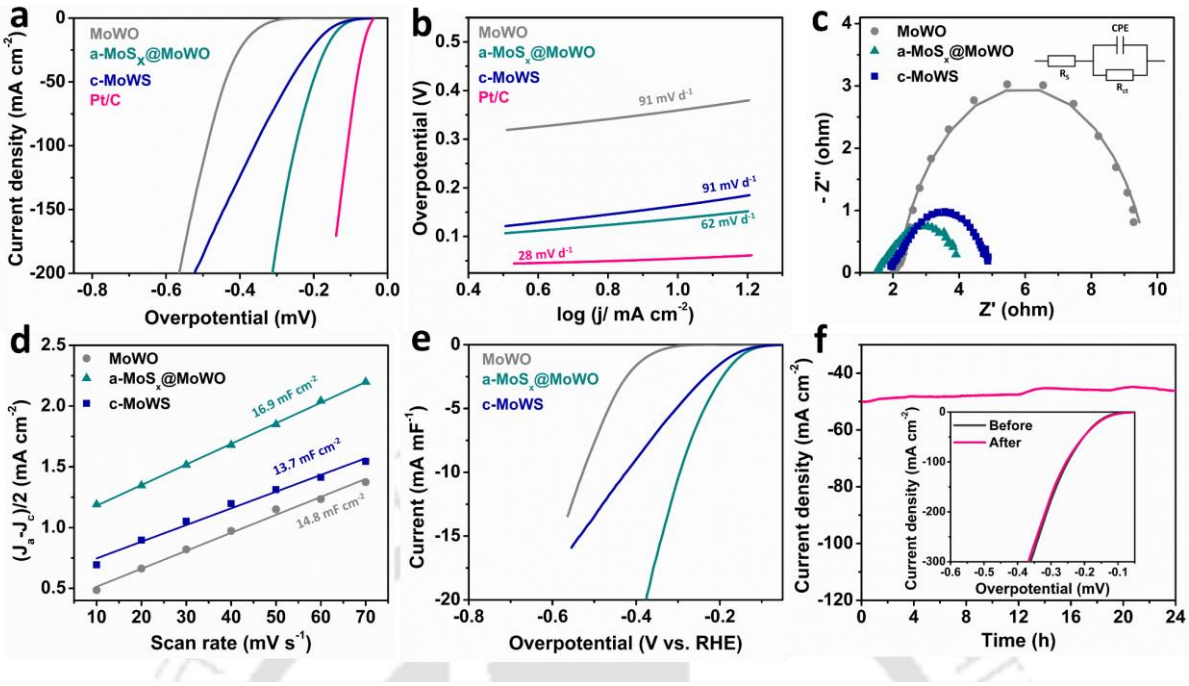

Figure 4.8. (a) LSV curves, (b) corresponding Tafel slopes of MoWO, a-MoS_x@MoWO, c-MoWS and Pt/C in 0.5 M H_2SO_4. (c) Nyquist plots of the catalysts. (d) ECSA and (e) ECSA normalised LSV curves of catalysts. (f) Chronoampeometry curve of a-MoS_x@MoWO with comparison of LSV curve before and after test in inset.

along with commercial Pt/C as reference were tested in 0.5 M H_2SO_4 electrolyte in a three-electrode configuration. Linear sweep voltammetry (LSV) curves (Figure 4.8a) display that the HER activity of a-MoS_x@MoWO is much better than MoWO nanowire and c-MoWS. The required overpotential (η) to achieve HER current density of 10 mA cm^{-2} is only 136 mV for a-MoS_x@MoWO, which is 200 mV lower than the parent oxide sample MoWO (356 mV) (Table 4.2). Besides, the value of η is also much better than c-MoWS (163 mV) and comparable to best-performing molybdenum sulfide-based acidic HER catalysts (Table 4.3). To further understand the reaction kinetics, Tafel slope has been determined from Tafel plots (η vs $log\ J$) in Figure 4.8b. The lowest Tafel slope of a-MoS_x@MoWO (62 mV dec^{-1}) compared to other samples, MoWO (91 mV dec^{-1}) and c-MoWS (91 mV dec^{-1}) indicate faster reaction kinetics in the 8s sulfurized sample. The origin of faster HER kinetics can better be understood from the detailed analysis of impedance analysis through the Nyquist plot (Figure 4.8c). The fitting of these plots has been done with the circuit diagram as denoted in inset of Figure 4.8c where R_{ct} represent charge transfer resistance, R_s is the solution resistance, and CPE represents constant phase element, and the values are given in Table 4.2. The determined R_{ct} value of a-MoS_x@MoWO is the lowest (2.74 Ω) as compared to MoWO (7.63 Ω) and c-MoWS (3.08 Ω). Lowest R_{ct} value of a-MoS_x@MoWO indicates facile charge transfer between electrode and

electrolyte during HER process. Electrochemical surface area (ECSA) of the developed catalysts was compared

Table 4.2: HER metrices for different samples in 0.5 M H_2SO_4 electrolyte

Samples	η_{10} (mV)	Tafel slope (mV dec^{-1})	R_s (Ω)	R_{ct} (Ω)
MoWO	356	91	2.13	7.63
a-MoS_x@MoWO	136	62	1.54	2.74
c-MoWS	163	91	1.95	3.08

Table 4.3: Comparison of HER overpotentials and Tafel slope for various reported electrocatalysts in 0.5 M H_2SO_4

Samples	η_{10} (mV)	Tafel slope (mV dec^{-1})	Reference
a-MoS_x@MoWO	136	62	**This work**
MoS_2/graphite rod	177	67	[33]
MoS_2/CNT	194	52.7	[34]
MoS_2/3D porous carbon nanosheets	162*	38	[35]
MoS_2/nanocarbon hybrid network	186	53	[36]
Monolayer MoS_2	183	77.6	[37]
MoS_2 microflakes	174	62	[38]
Amorphous MoS_3	200	60	[12]
1T-MoS_2 nanostructure	187	43	[39]
N-doped MoS_2	168	40.5	[40]
WS_2 on nanofibers	280	60	[41]

**Data has been measured from the given LSV curve*

by comparing their electrical double layer capacitances (C_{dl}) obtained from corresponding cyclic voltammograms at different scan rates. The measured C_{dl} values for a-MoS_x@MoWO (16.9 mF cm^{-2}) is comparable to MoWO (14.8 mF cm^{-2}) and c-MoWS (13.7 mF cm^{-2}) owing to their similar kind of nanowire structure (Figure 4.8d). To compare the intrinsic HER activities, ECSA-normalized LVS curves are plotted in Figure 4.8e. The a-MoS_x@MoWO has a greater ECSA normalised current at any given potential as compared to MoWO and c-MoWS

samples, as can be seen from Figure 4.8e. This shows that after heterostructure development, a-MoS_x@MoWO possesses greater intrinsic HER catalytic activity, which can be attributable to a large number of active sites of amorphous a-MoS_x phase and synergist coming from amorphous-crystalline heterostructure formation. The stability of an electrode during electrochemical measurement is also very important for long-term use. Stability of the best performing sample, a-MoS_x@MoWO displays excellent stability at a high current density of 50 mA cm^{-2} for a duration of 24h without any decay in current density as shown in Figure 4.8f. The LSV curves before and after HER stability test nearly overlap each other, which also suggests high operational stability of a-MoS_x@MoWO. From the structural, ECSA and impedance analysis, it can be concluded that the better HER performance of a-MoS_x@MoWO is associated with i) large catalytic active sites of amorphous a-MoS_x shell, ii) beneficial charge transfer kinetics in the core-shell structure as evident from lowest R_{ct} value.

4.3.5 HER catalytic performance in 1 M KOH and 1 M PBS solution:

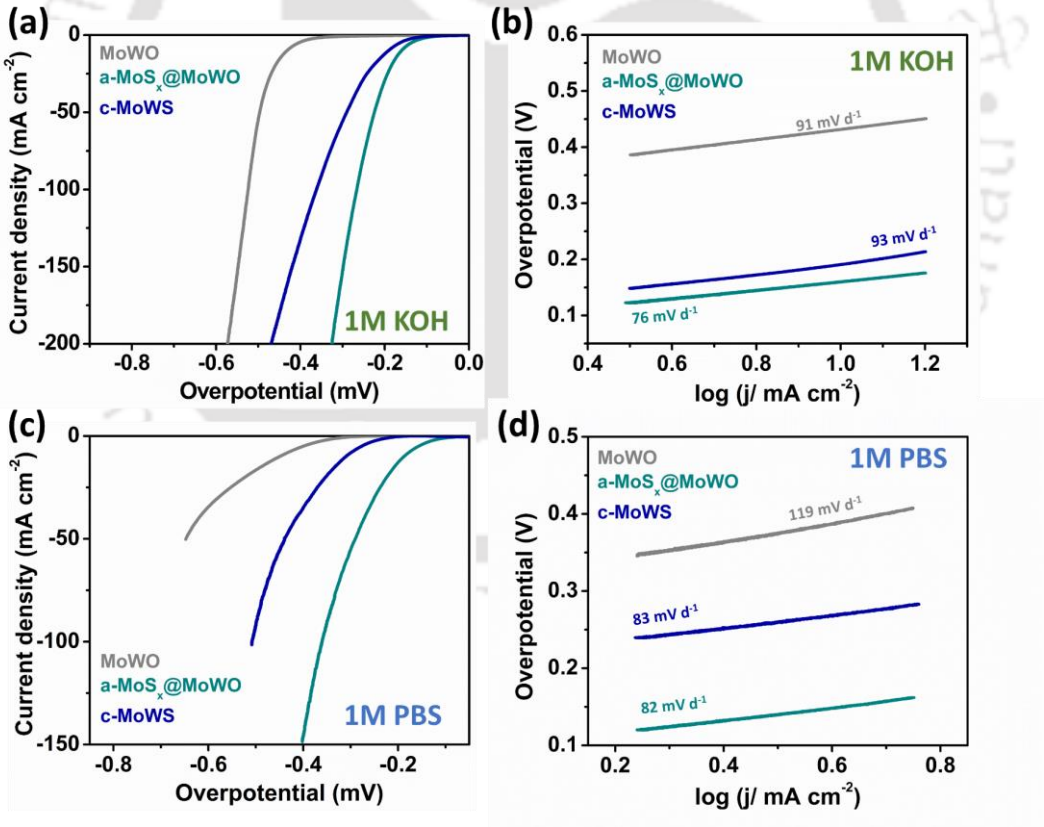

Figure 4.9. (a) LSV curve and (b) Tafel slpoe of a-MoS_x@MoWO in 1 M KOH solution. (c) LSV curve and (d) Tafel slpoe of a-MoS_x@MoWO in 1 M PBS solution.

Molybdenum-based catalysts are known to perform better in acidic electrolytes but their performance is generally worse in alkaline or neutral electrolytes.[42,43] However, often

electrolyser cells are implemented in alkaline or neutral electrolytes to match the performance of the catalysts in both HER and OER half-reactions and address the stability of the catalysts. To use the developed materials as pH universal HER catalysts, performance as well as long-term stability were evaluated in alkaline (1M KOH) and neutral (1M PBS) electrolytes. Figure 4.9a (& Table 4.4) shows the LSV curves of catalysts in KOH medium, which suggest a low overpotential of 160 mV to achieve a current density of 10 mA cm^{-2} for a-MoS_x@MoWO compared to other synthesized samples. Similar to acidic electrolyte, faster HER kinetics of a-MoS_x@MoWO is also evident from its lowest Tafel slope (Figure 4.9b & Table 4.4). Same

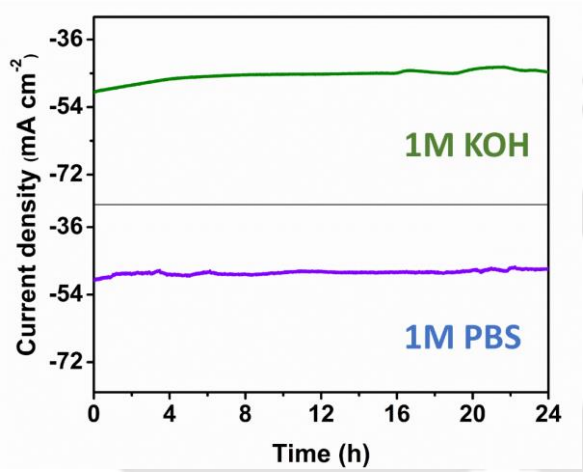

Figure 4.10. Chronoampeometry curve of a-MoS_x@MoWO in 1 M KOH and 1 M PBS electrolyte.

trend can also be seen in the case of 1 M PBS electrolyte where a-MoS_x@MoWO requires only 188 mV overpotential to reach 10 mA cm^{-2} current density with a low Tafel slope of 82 mV dec^{-1} (Figure 4.9c, d). More importantly, chronoamperometric test as shown in Figure 4.10 suggests its operational stability at a current density of 50 mA cm^{-2} for a duration of 24h for both basic and neutral conditions. The performance metric in alkaline and neutral electrolytes are comparable to recent reports for molybdenum sulfide-based systems (Table 4.5). Facile

Table 4.4: HER metrices for different samples at different pH medium

Sample	1 M KOH		1M PBS	
	η_{10} (mV)	**Tafel slope (mV dec^{-1})**	**η_{10} (mV)**	**Tafel slope (mV dec^{-1})**
MoWO	432	91	478	154
a-MoS_x@MoWO	160	76	188	76
c-MoWS	190	93	309	83

processing, excellent stability with good performance in pH universal conditions qualify this crystalline/amorphous core-shell structure as attractive low-cost candidate for widespread practical durable use.

Table 4.5: Comparison of HER overpotentials for various reported electrocatalysts in basic and neutral electrolyte

Samples	η_{10} (mV) in 1M KOH	η_{10} (mV) in 1M PBS	Reference
a-MoS_x@MoWO	160	188	**This work**
1T-2H MoS_2	290	-	[44]
MoS_2/Black Phosphorus Heterostructure	237	258	[45]
Mo-W carbide on carbon shells	179	221	[46]
MoP microparticle	190	330	[47]
WP nanorods	150	200	[48]
B-Mo_2C nanosheet	112	-	[49]
WP_2 submicroparticles	153	244	[50]
Bulk Mo_2C	-	200	[51]
Bulk Mo_2B	-	250	[51]
Bulk MoB	225	-	[51]

4.3.6 Theoretical calculation of HER

A detailed analysis of density functional theory (DFT) was undertaken to explain the origin of high HER activity of a-MoS_x@MoWO heterostructure (Figure 4.11a). Unlike crystalline MoS_2, where the genesis of catalytic activity is well understood, the electronic origin of amorphous a-MoS_x is poorly understood.[52,53] Moreover, there is no theoretical study on amorphous a-MoS_x based heterostructure till date. Here, DFT based understanding of a-MoS_x@MoWO is done in two steps: first, electronic origin of higher catalytic activity of a-MoS_x has been disclosed. In the second step, the role of crystalline MoWO core in promoting the activity of amorphous shell has been revealed. Gibbs free energy of hydrogen adsorption (ΔG_{H*}), which is a relevant descriptor for HER activity has been calculated (Figure 4.11b, Table 4.6).[54,55] For high HER activity, the strength of hydrogen adsorption over catalytic surface

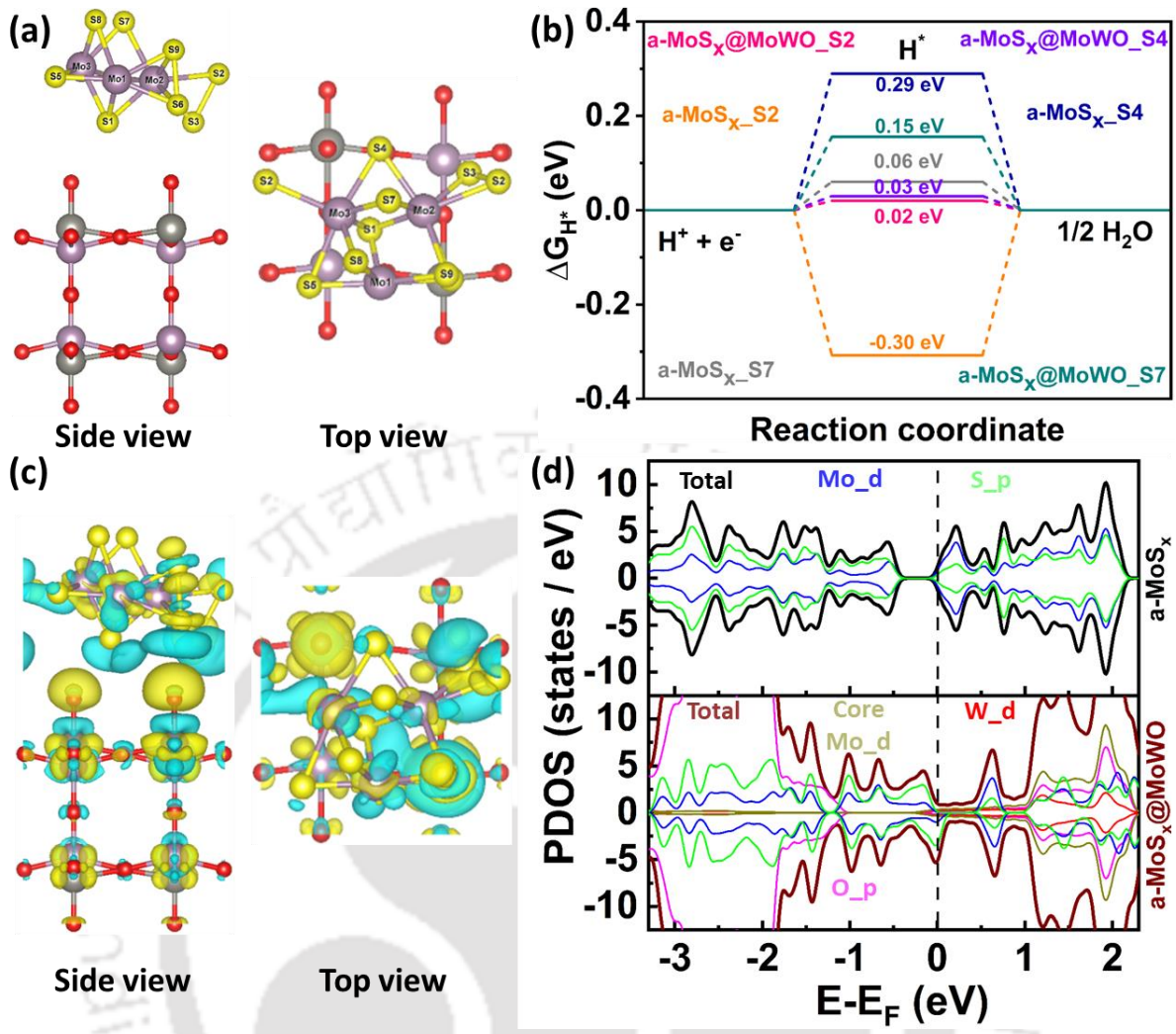

Figure 4.11. Analysis of HER activity of a-MoS_x@MoWO heterostructure using DFT: (a) Structural model of a-MoS_x@MoWO after relaxation; (b) Free energy diagram of HER pathways for the catalysts at various sites; (c) Interfacial charge transfer as obtained from Bader charge analysis, yellow color denotes charge deficiency and green color denotes charge accumulation; (d) PDOS of a-MoS_x and a-MoS_x@MoWO.

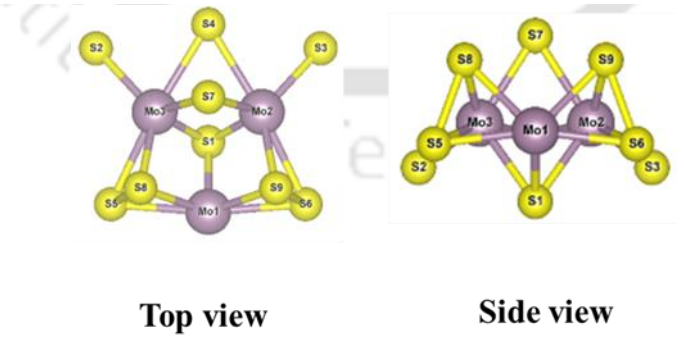

Figure 4.12. Relaxed structure of a-MoS_x.

should not be too strong or too weak (Sabatier's principle), this gives rise to the condition for optimum HER activity ($\Delta G_{H*} \approx 0$).[56]

Table 4.6: H-adsorption free energies (ΔG_{H*}) of different catalysts.

Structure	H-adsorption free energy (ΔG_{H*}) at different sites						
	Mo1	**S1**	**S2**	**S4**	**S7**	**S8**	**S9**
a-MoS_x	0.80 eV	1.65 eV	-0.30 eV	0.29 eV	0.06 eV	-0.78 eV	-0.78 eV
a-MoS_x@MoWO	-	-	**0.02 eV**	**0.03 eV**	**0.15 eV**	**0.06 eV**	**0.11 eV**
MoS_2	-	1.89 eV					

Amorphous a-MoS_x, which has the form of MoS_3 in our sample, consists of different sulfur and molybdenum sites, namely apical sulfur (S1), bridging sulfur (S4, S7), bridging disulfur (S5, S6, S8, S9) and terminal sulfur (S2, S3) as depicted in Figure 4.12.[22] Out of these sites, S8 and S9 are equivalent by symmetry, similarly S2 & S3 and S5 & S6 are also equivalent in this a-MoS_x structure. Calculation of site-specific catalytic activity of a-MoS_x alone reveals that the value of ΔG_{H*} is the lowest for bridging site S7 (0.06eV), and it is very close to thermoneutral binding energy of hydrogen (Figure 4.11b). The magnitude of ΔG_{H*} for other sulfur and molybdenum sites follow the order S4 (0.29 eV) < S2 (-0.30 eV) < S8 (-0.78 eV) < Mo1 (0.80 eV) < S1 (1.65 eV) (Fig. 4b & Table 4.6) in which S1 & Mo1 shows very poor activity due to very high ΔG_{H*} values and thus, those sites will not be considered in the case of heterostructure. This activity trend is very different from commonly studied hexagonal (2H) MoS_2, in which basal plane sulfur sites are inactive towards hydrogen evolution reaction, as has been reflected in their very high ΔG_{H*} value (1.89 eV) (Table 4.6). Surprisingly, remarkable improvement in the activity of multiple sulfur sites has been identified in a-MoS_x@MoWO heterostructure. In a-MoS_x@MoWO, the sites S2, S4, S7, S8 and S9 all attain very low values of ΔG_{H*} (0.02 eV, 0.03 eV, 0.15 eV, 0.06 eV and 0.11 eV respectively) as presented in free

energy diagrams (Figure 4.11b & Table 4.6), which signifies that, multiple sites are highly HER active in heterostructure as compared to primary S7 site of a-MoS_x alone. To inspect the origin of high activity of multiple sites in the heterostructure, we have done Bader charge analysis which shows significant interfacial charge transfer from core MoWO nanowire to surface a-MoS_x (Figure 4.11c). This interfacial electronic modification can lead to redistribution of charges over the a-MoS_x shell, which leads to improvement in catalytic activity of multiple sites. To elucidate the electronic origin of high catalytic activity, the electronic structure of both a-MoS_x and a-MoS_x@MoWO heterostructure have been calculated. From the plot of total density of states, it can be concluded that both of them show metallic conductivity having partially filled topmost electronic bands (Figure 4.11d). This metallic property is beneficial for HER activity, as there will be less resistive energy loss across the nanostructure body when electron passes from external current collector to surface active sites.

The difference in activity of different sulfur sites was further inspected by calculating the projected density of states (PDOS) contributed by individual sites (Figure 4.13a, b). Significant variations in the density of filled states below the Fermi level can be seen from the

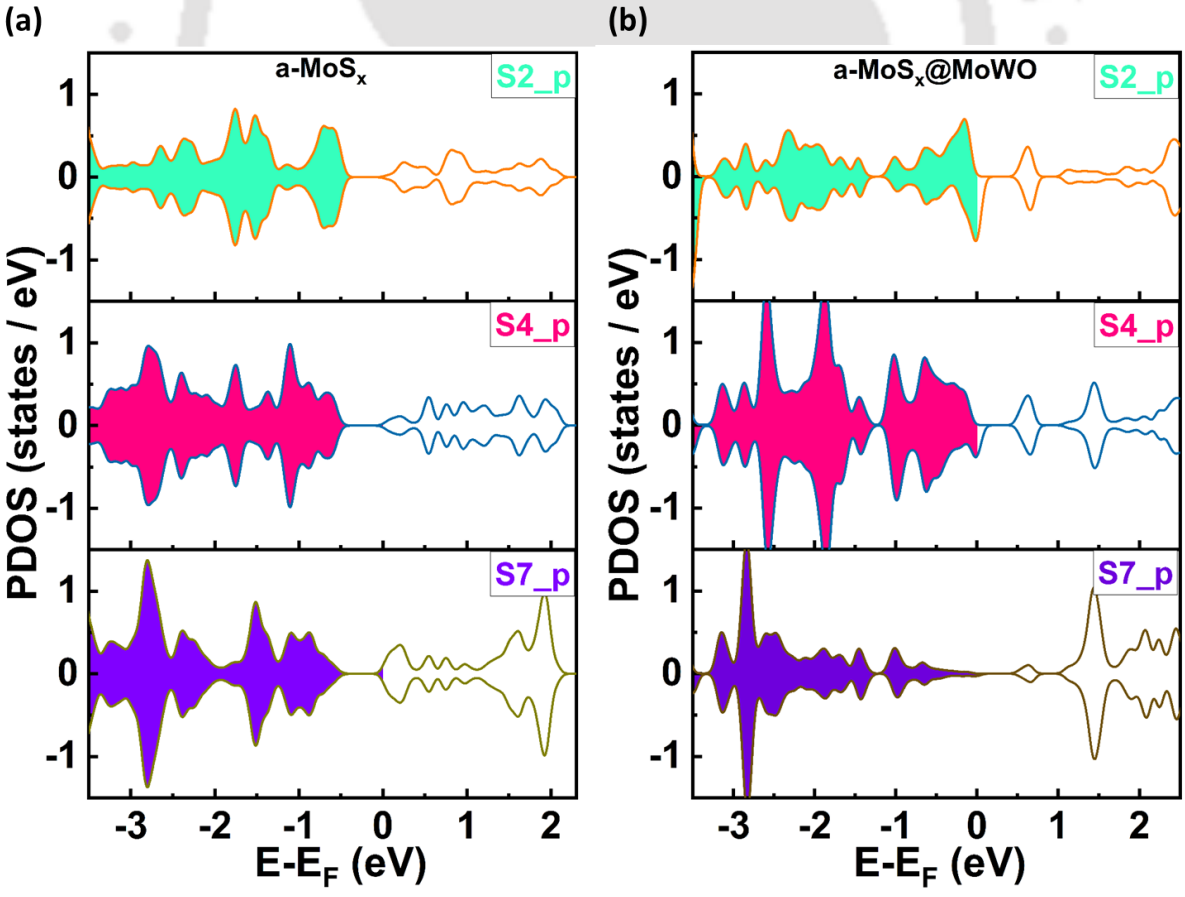

Figure 4.13. Site specific PDOS of 3p orbital of S2, S4 and S7 sites for (a) a-MoS_x and (b) a-MoS_x@MoWO.

plots, the variation is more prominent within the range of -2 eV to 0 eV. It is also evident that higher the number of states in the front of the lower filled band better is the activity observed, which can explain the variation in activity of S1 and other S-sites of a-MoS_x (Figure 4.13a). For quantitative analysis of this observation, these p-states close to Fermi level are considered as the 'active p-states' for hydrogen binding.[57,58] The variation in activity of different sites can easily be understood considering the position of 'centre of active p-states' (E_p) (within 2 eV below Fermi level) which is presented in Table 4.7. From the table, it is evident that the position of $|E_p|$ follows same trend as the activity of different sites having the order S7 < S4 < S2 < S8 < S1, thus this can be taken as the descriptor to explain the catalytic trend of different sites in a-MoS_x. In the case of a-MoS_x@MoWO heterostructure, density of p-states close to Fermi level of different sulfur sites changes significantly as can be seen from Figure 4.13b. This change leads to upshift of 'centre of active p-states' (E_p) of S2, S4 and S8, (Table 4.8) thereby activating those sites for HER by lowering the required value of ΔG_{H*} Nevertheless, slight increase in value of ΔG_{H*} for S7 site of heterostructure is also consistent with its downward shifted 'centre of active p-states' as compared to that of a-MoS_x. In addition to the discussion above, large increase in the density of states at the Fermi level contributed by S2, S4 and S8 lead to higher HER activity which is attributable to beneficial H-adsorption and better conductivity of the heterostructure.[59–61]

In practice, a catalyst's ability can be boosted in two ways: by increasing the number of active sites and improving the activity of each site. From the above results estimated from DFT calculations, it could be concluded that the strategy of core-shell a-MoS_x@MoWO structure prepared from surface amorphization is an effective way to uplift the intrinsic HER activity of the catalyst. In 2H-MoS_2, in terms of HER performance, only the Mo-edge sites are active but all the basal S sites are inert.[52,53] According to the DFT analysis, for amorphous a-MoS_x, only one S site is active. On the other hand, in core-shell a-MoS_x@MoWO, not only each site exhibits high activity but also shows large number of active sites due to synergistic electronic interaction between core and shell.

Table 4.7: Band Centers (E_p) for different sites of a-MoS_x.

Range	Band center				
Full	-3.57	-3.47	-2.87	-2.76	-4.19
-2 to 0	-1.47	-1.26	-1.23	-1.22	-1.30
ΔG_{H*}(eV)	1.65	-0.30	0.29	0.06	-0.78

Table 4.8: Band Centers (E_p) for different sites of a-MoS_x@MoWO

Range	Band center				
Full	-2.94	-1.77	-2.80	-2.75	-3.09
-2 to 0	-0.84	-1.17	-1.31	-1.19	-1.26
ΔG_{H^*}(eV)	0.02	0.03	0.15	0.06	0.11

4.4 Conclusion

A rapid and facile microwave-involved dry process has been presented for controlled reactive sulfidation and surface atomic rearrangement over molybdenum tungsten oxide nanowires. Partially reduced graphene foam placed both sides of oxide nanowire sample, and rapidly heated up by absorbing microwave irradiation which dissociates thiourea to hydrogen sulfide gas and this gas reacts with surface atoms of the nanowires. The atomic rearrangement can be tuned to get an amorphous or crystalline sulfide structure depending on the duration of this graphene filament-involved transient heating process (GFTH). GFTH of eight seconds leads to a nanowire structure consisting of crystalline MoWO core and amorphous a-MoS_x shell, which displayed excellent catalytic hydrogen evolution reaction. A DFT-based comprehensive understanding has been presented to elucidate the origin of high catalytic activity as developed crystalline/amorphous core-shell structure. The calculation reveals that multiple sulfur sites (bridging & terminal S) of amorphous a-MoS_x of different coordination show low hydrogen adsorption free energy (ΔG_{H*}), which get lowered significantly due to structural change and charge transfer at the interface of MoWO nanowire core, thus displaying high catalytic activity. This fast and very simple process is possible to extend to generate a variety of chalcogenide, phosphide, and nitride-based core-shell structures, highlighting the importance of this protocol. Furthermore, a detailed understanding of catalytic activity of a-MoS_x and its heterostructure, which is rarely reported, can give a practical guideline to design efficient HER catalysts.

Reference

[1] Q. Xu, G. Li, Y. Zhang, Q. Yang, Y. Sun, C. Felser, *ACS Catal.* **2020**, *10*, 5042.

[2] S. Trasatti, *J. Electroanal. Chem. Interfacial Electrochem.* **1972**, *39*, 163.

[3] Y. Lee, J. Suntivich, K. J. May, E. E. Perry, Y. Shao-Horn, *J. Phys. Chem. Lett.* **2012**, *3*, 399.

[4] X. Zhang, F. Jia, S. Song, *Chem. Eng. J.* **2021**, *405*, 127013.

[5] T. F. Jaramillo, K. P. Jørgensen, J. Bonde, J. H. Nielsen, S. Horch, I. Chorkendorff, *Science (80-.).* **2007**, *317*, 100.

[6] J. Zhu, Z. C. Wang, H. Dai, Q. Wang, R. Yang, H. Yu, M. Liao, J. Zhang, W. Chen, Z. Wei, N. Li, L. Du, D. Shi, W. Wang, L. Zhang, Y. Jiang, G. Zhang, *Nat. Commun. 2019 101* **2019**, *10*, 1.

[7] L. Li, Z. Qin, L. Ries, S. Hong, T. Michel, J. Yang, C. Salameh, M. Bechelany, P. Miele, D. Kaplan, M. Chhowalla, D. Voiry, *ACS Nano* **2019**, *13*, 6824.

[8] C. Tsai, H. Li, S. Park, J. Park, H. S. Han, J. K. Nørskov, X. Zheng, F. Abild-Pedersen, *Nat. Commun.* **2017**, *8*, 1.

[9] A. Majumdar, P. Dutta, A. Sikdar, H. Lee, D. Ghosh, S. Nath Jha, S. Tripathi, Y. Oh, U. Narayan Maiti, A. Majumdar, P. Dutta, A. Sikdar, U. N. Maiti, H. Lee, Y. Oh, D. Ghosh, S. N. Jha, S. Tripathi, *Small* **2022**, *18*, 2200622.

[10] J. Kibsgaard, Z. Chen, B. N. Reinecke, T. F. Jaramillo, *Nat. Mater. 2012 1111* **2012**, *11*, 963.

[11] Z. Luo, Y. Ouyang, H. Zhang, M. Xiao, J. Ge, Z. Jiang, J. Wang, D. Tang, X. Cao, C. Liu, W. Xing, *Nat. Commun. 2018 91* **2018**, *9*, 1.

[12] J. D. Benck, Z. Chen, L. Y. Kuritzky, A. J. Forman, T. F. Jaramillo, *ACS Catal.* **2012**, *2*, 1916.

[13] X. Ge, L. Chen, L. Zhang, Y. Wen, A. Hirata, M. Chen, M. W. Chen, X. Ge, + L Chen, + L Zhang, Y. Wen, A. Hirata, *Adv. Mater.* **2014**, *26*, 3100.

[14] H. Vrubel, X. Hu, *ACS Catal.* **2013**, *3*, 2002.

[15] D. J. Li, U. N. Maiti, J. Lim, D. S. Choi, W. J. Lee, Y. Oh, G. Y. Lee, S. O. Kim, *Nano Lett.* **2014**, *14*, 1228.

[16] K. C. Pham, Y. H. Chang, D. S. McPhail, C. Mattevi, A. T. S. Wee, D. H. C. Chua, *ACS Appl. Mater. Interfaces* **2016**, *8*, 5961.

[17] Z. Chen, D. Cummins, B. N. Reinecke, E. Clark, M. K. Sunkara, T. F. Jaramillo, *Nano Lett.* **2011**, *11*, 4168.

[18] B. Jin, X. Zhou, L. Huang, M. Lickleder, M. Yang, P. Schmuki, *Angew. Chemie Int. Ed.* **2016**, *55*, 12252.

[19] N. Choudhary, C. Li, H. S. Chung, J. Moore, J. Thomas, Y. Jung, *ACS Nano* **2016**, *10*, 10726.

[20] P. Giannozzi, S. Baroni, N. Bonini, M. Calandra, R. Car, C. Cavazzoni, D. Ceresoli, G.

L. Chiarotti, M. Cococcioni, I. Dabo, A. Dal Corso, S. De Gironcoli, S. Fabris, G. Fratesi, R. Gebauer, U. Gerstmann, C. Gougoussis, A. Kokalj, M. Lazzeri, L. Martin-Samos, N. Marzari, F. Mauri, R. Mazzarello, S. Paolini, A. Pasquarello, L. Paulatto, C. Sbraccia, S. Scandolo, G. Sclauzero, A. P. Seitsonen, A. Smogunov, P. Umari, R. M. Wentzcovitch, *J. Phys. Condens. Matter* **2009**, *21*, 395502.

[21] L. Wu, A. Longo, N. Y. Dzade, A. Sharma, M. M. R. M. Hendrix, A. A. Bol, N. H. de Leeuw, E. J. M. Hensen, J. P. Hofmann, *ChemSusChem* **2019**, *12*, 4383.

[22] T. Weber, J. C. Muijsers, J. W. Niemantsverdriet, *J. Phys. Chem* **1995**, *99*, 9194.

[23] J. K. Nørskov, T. Bligaard, A. Logadottir, J. R. Kitchin, J. G. Chen, S. Pandelov, U. Stimming, *J. Electrochem. Soc.* **2005**, *152*, J23.

[24] S. Xu, G. Zhong, C. Chen, M. Zhou, D. J. Kline, R. J. Jacob, H. Xie, S. He, Z. Huang, J. Dai, A. H. Brozena, R. Shahbazian-Yassar, M. R. Zachariah, S. M. Anlage, L. Hu, *Matter* **2019**, *1*, 759.

[25] Y. Liu, Y. Zhang, Y. Liu, J. Zhu, Z. Ge, Z. Li, Y. Chen, *Carbon N. Y.* **2021**, *173*, 809.

[26] Z. D. Wang, M. Yoshida, B. George, *Comput. Theor. Chem.* **2013**, *1017*, 91.

[27] B. Mahler, V. Hoepfner, K. Liao, G. A. Ozin, *J. Am. Chem. Soc.* **2014**, *136*, 14121.

[28] B. Li, L. Jiang, X. Li, Z. Cheng, P. Ran, P. Zuo, L. Qu, J. Zhang, Y. Lu, B. Li, L. Jiang, X. Li, P. Ran, P. Zuo, Z. Cheng, L. Qu, J. Zhang, Y. Lu, *Adv. Funct. Mater.* **2019**, *29*, 1806229.

[29] X. Wen Lou, H. Chun Zeng, **2003**.

[30] H. Vrubel, D. Merki, X. Hu, *Energy Environ. Sci.* **2012**, *5*, 6136.

[31] L. R. L. Ting, Y. Deng, L. Ma, Y. J. Zhang, A. A. Peterson, B. S. Yeo, *ACS Catal.* **2016**, *6*, 861.

[32] Q. Xu, Y. Liu, H. Jiang, Y. Hu, H. Liu, C. Li, *Adv. Energy Mater.* **2019**, *9*, 1802553.

[33] Z. Sun, M. Yang, Y. Wang, Y. H. Hu, *ACS Appl. Energy Mater.* **2019**, *2*, 1102.

[34] X. Qiu, Y. Huang, Z. Nie, B. Ma, Y. Tan, Z. Wu, N. Zhang, X. Xie, *Nanoscale* **2020**, *12*, 1109.

[35] D. Ko, X. Jin, K. dong Seong, B. Yan, H. Chai, J. M. Kim, M. Hwang, J. Choi, W. Zhang, Y. Piao, *Appl. Catal. B Environ.* **2019**, *248*, 357.

[36] A. K. Kunhiraman, S. Ramanathan, B. Pullithadathil, *Electrochim. Acta* **2018**, *264*, 329.

[37] C. C. Cheng, A. Y. Lu, C. C. Tseng, X. Yang, M. N. Hedhili, M. C. Chen, K. H. Wei, L. J. Li, *Nano Energy* **2016**, *30*, 846.

[38] D. Kiriya, P. Lobaccaro, H. Y. Y. Nyein, P. Taheri, M. Hettick, H. Shiraki, C. M. Sutter-Fella, P. Zhao, W. Gao, R. Maboudian, J. W. Ager, A. Javey, *Nano Lett.* **2016**, *16*, 4047.

[39] M. A. Lukowski, A. S. Daniel, F. Meng, A. Forticaux, L. Li, S. Jin, *J. Am. Chem. Soc.* **2013**, *135*, 10274.

[40] R. Li, L. Yang, T. Xiong, Y. Wu, L. Cao, D. Yuan, W. Zhou, *J. Power Sources* **2017**, *356*, 133.

[41] S. Yu, J. Kim, K. R. Yoon, J. W. Jung, J. Oh, I. D. Kim, *ACS Appl. Mater. Interfaces* **2015**, *7*, 28116.

[42] G. Li, D. Zhang, Y. Yu, S. Huang, W. Yang, L. Cao, *J. Am. Chem. Soc.* **2017**, *139*, 16194.

[43] J. Qin, C. Xi, R. Zhang, T. Liu, P. Zou, D. Wu, Q. Guo, J. Mao, H. Xin, J. Yang, *ACS Catal.* **2021**, *11*, 4486.

[44] S. Wang, D. Zhang, B. Li, C. Zhang, Z. Du, H. Yin, X. Bi, S. Yang, *Adv. Energy Mater.* **2018**, *8*, 1.

[45] T. Liang, Y. Liu, Y. Cheng, F. Ma, Z. Dai, *ChemCatChem* **2020**, *12*, 2840.

[46] L. Wang, Z. Li, K. Wang, Q. Dai, C. Lei, B. Yang, Q. Zhang, L. Lei, M. K. H. Leung, Y. Hou, *Nano Energy* **2020**, *74*, 104850.

[47] T. Wang, K. Du, W. Liu, Z. Zhu, Y. Shao, M. Li, *J. Mater. Chem. A* **2015**, *3*, 4368.

[48] Z. Pu, Q. Liu, A. M. Asiri, X. Sun, *ACS Appl. Mater. Interfaces* **2014**, *6*, 21874.

[49] F. X. Ma, H. Bin Wu, B. Y. Xia, C. Y. Xu, X. W. Lou, *Angew. Chemie Int. Ed.* **2015**, *54*, 15395.

[50] Z. Xing, Q. Liu, A. M. Asiri, X. Sun, *ACS Catal.* **2015**, *5*, 145.

[51] H. Vrubel, X. Hu, *Angew. Chemie Int. Ed.* **2012**, *51*, 12703.

[52] P. Raybaud, J. Hafner, G. Kresse, S. Kasztelan, H. Toulhoat, *J. Catal.* **2000**, *189*, 129.

[53] J. D. Benck, T. R. Hellstern, J. Kibsgaard, P. Chakthranont, T. F. Jaramillo, *ACS Catal.* **2014**, *4*, 3957.

[54] J. Greeley, T. F. Jaramillo, J. Bonde, I. Chorkendorff, J. K. Nørskov, *Nat. Mater.* **2006**, *5*, 909.

[55] B. Hinnemann, P. G. Moses, J. Bonde, K. P. Jørgensen, J. H. Nielsen, S. Horch, I. Chorkendorff, J. K. Nørskov, *J. Am. Chem. Soc.* **2005**, *127*, 5308.

[56] J. K. Nørskov, T. Bligaard, J. Rossmeisl, C. H. Christensen, *Nat. Chem.* **2009**, *1*, 37.

[57] Y. Ouyang, C. Ling, Q. Chen, Z. Wang, L. Shi, J. Wang, *Chem. Mater.* **2016**, *28*, 4390.

[58] M. Liu, M. S. Hybertsen, Q. Wu, *Angew. Chemie* **2020**, *132*, 14945.

[59] B. Hammer, J. K. Nørskov, *Adv. Catal.* **2000**, *45*, 71.

[60] Y. Liu, J. Wu, K. P. Hackenberg, J. Zhang, Y. M. Wang, Y. Yang, K. Keyshar, J. Gu, T. Ogitsu, R. Vajtai, J. Lou, P. M. Ajayan, B. C. Wood, B. I. Yakobson, *Nat. Energy* **2017**, *2*, 1.

[61] J. K. Nørskov, F. Abild-Pedersen, F. Studt, T. Bligaard, *Proc. Natl. Acad. Sci. U. S. A.* **2011**, *108*, 937.

Chapter 5

Microwave Induced Rapid Recrystallization process for Universal Development of Metal Chalcogenides and Phosphides Towards Outstanding Oxygen Evolution Reaction

Chapter 5

Microwave Induced Rapid Recrystallization process for Universal Development of Metal Chalcogenides and Phosphides Towards Outstanding Oxygen Evolution Reaction

Lowering the production cost while maintaining the superb activity of catalysts for sluggish oxygen evolution reaction (OER) is the utmost challenge; however, it remains the decisive factor for the success of the electrolytic hydrogen-based green economy. Here, we present a fast (seconds) and very low energy-expensive recrystallization strategy for the universal development of nickel-iron-based sulfide, selenide and phosphide nanostructures that perform state-or-the-art OER activity. Amorphous and irregular bulk morphology of the surface of iron nitrate treated nickel foam rapidly recrystallizes into uniform nanostructures of chalcogenide and phosphide phases under graphene-involved microwave treatment. As-developed nanosheets of iron-doped Ni_3S_2/NiS in-plane heterostructure show exceptionally high OER activity, with an overpotential of only 187 mV at 10 mA cm^{-2}. It requires only 289 mV to achieve a very high current density of 500 mA cm^{-2} which is well below the much-talked target value (<300 mV) required for commercial use. Comprehensive analysis shows that NiS phase of Ni_3S_2/NiS selectively transforms into an amorphous (oxy)hydroxide phase under OER condition to in-situ generate iron-doped Ni_3S_2/NiOOH heterostructure, which displays high activity. Fast phase evolution and recrystallization into nanostructures of the protocol not only interesting for generating diverse crystalline phases, but also highly important for their low-cost practical applications.

5.1 Introduction

The oxygen evolution reaction (OER), which creates molecular oxygen by the electrolysis of water, is a significant component of water splitting technology and is utilized in numerous renewable energy systems, such as fuel cells and metal-air batteries.[1] However, the multi-step electron transfer processes of large energy barriers make the OER kinetics sluggish and thus require highly efficient catalysts.[1,2] In this regard, Ir and Ru-based noble-metal catalysts are frequently employed, but their scarcity and very high price practically limit widespread commercial use.[3] In a search for cheap alternatives, earth-abundant 3d-transition metal (TM) chalcogenide/phosphide-based catalysts have been explored extensively, and significant

progress in OER catalysis has been registered. In particular, chalcogenides like sulfides/selenides and phosphides of transition metals emerge as front runners. They display top-tier performance on behalf of their high intrinsic conductivity and in-situ surface activation during OER process.[4,5]

The TM-chalcogenide-based OER catalysts are mostly produced either via solution phase techniques or through high-temperature vapor transport methods. In solution phase techniques, hydrothermal/solvothermal methods were used either to directly synthesize TM-sulfides/selenides/phosphides in single-step or two-step protocols like the growth of oxide in the first stage and sulfidation/selenization/phosphidation in the second step were adopted. Notably, the two-step protocols often exhibit highly enhanced activity due to suitable phase and morphological evolutions.[6,7] In contrast, vapor transport process for the development of sulfide/selenide/phosphide based OER catalyst is invariably two stage protocol. In the first stage, nanostructures of transition metal-based compounds are produced via solution phase and the sulfidation/selenization/phosphidation are conduced within a temperature-controlled chemical vapour deposition (CVD) system.[8,9] Both these processes for developing TM-chalcogenide/phosphide based OER catalysts require a significant thermal budget for hours of reactions and involves complexity to control each stage of synthesis. Nevertheless, despite all these efforts the single-phase chalcogenides give performances which cannot satisfy the practical demand.[10] Thus, dedicated efforts have been made to enhance their performance by suitable heterostructure formation, heteroatom doping, in-situ etching of selective elements, and so on.[11–13] For example, Hu et al., developed a heterostructure of $NiFe(OH)_x$/FeS in which the base FeS provides a wide surface area and high conductivity to catalytically active $NiFe(OH)_x$ to achieve low OER overpotential of 245 mV at 10 mA cm^{-2} and 304 mV for 500 mA cm^{-2}.[14] The heterostructure has been developed in two step process: first FeS has been grown hydrothermally over an iron foam at 120º C for a long time of 12 h and then the surface of the structure has been corotated in a corrosive solution to generate $NiFe(OH)_x$/FeS heterostructure. As opposed to vertical heterostructure, Wu et al. have developed a heterostructure of Ni_3N and 2H-MoS_2 in 3-step process where Ni_3N was synthesized in solution method, 2H-MoS_2 was produced by hydrothermally and finally the interface engineering between the two structure was created by hydrothermal method again.[15] Synergistically this structure showed excellent OER activity and required only 299 mV to reach a current density of 500 mA cm^{-2}. In another work, Wang et al. first made hydrophilic carbon cloth (CC) by tris-Cl solution deposition and then through high temperature annealing.[16] This hydrophilic CC

was then used as a substrate to grow NiCo based hydroxide via hydrothermal method which again sulfurized hydrothermally to obtain $CoNi_2S_4$ on CC. Finally, another hydrothermal reaction was done to generate $CoNi_2S_4$/NiMn LDH on CC for highly efficient OER catalysis which needed 312 mV overpotential for high current density 500 mA cm^{-2}. By in-situ etching of NiFe LDHs Cai et al. have produced a highly active OER catalyst requiring 206 and 305 mV overpotential to achieve 10 and 500 mA cm^{-2} current densities.[17] To realize the structure, they have grown NiFe LDH on Ni foam substrate via electrochemical deposition under continuous N_2 flow which after selectively etched by polyoxometallic acids to get final catalyst. Such processes are much complicated and in many cases the improvement is minimal.[18,19] Only handful of TM-chalogenide based catalysts were able to achieve extremely high OER activity, for example exhibiting 10 mA cm^{-2} below 200 mV and 500 mA cm^{-2} close to 300 mV overpotentials which are considered as gold standard in this field.[20,21] Particularly, achieving very high current at low overpotentials is highly demanding as commercial electrolyzers need to operate at high currents to get sufficient hydrogen evolution. Unfortunately, most of these OER catalysts require 330 mV or higher to achieve 500 mA cm^{-2} current.[22,23] In this current situation, it is highly demanding to develop TM-chalcogenide/phosphide OER catalysts that are not only cheap and facile to produce, but also can meet the highest standard of OER catalysis.

Herein, we present a versatile, low cost and very fast strategy involving domestic microwave for the development of highly efficient metal sulphide, selenide and phosphide-based OER catalysts. The strategy was planned by considering the fact that partially reduced graphene oxide (p-rGO) can efficiently absorb microwave and get rapidly heated up to 1500° C in matter of seconds and cools down at an ultrafast rate (~10^4 K s^{-1}) once the microwave is OFF.[24,25] Such microwave-involved strategy was previously successfully used to heal the defects of reduced graphene oxide and recently used for the generation of graphene-based composites.[26,27] However, we propose to employ this microwave-involved strategy to bypass the complicated chemical vapour deposition process to develop highly OER active diverse chalcogenide/phosphide phases over nickel foam substrate. In this proposal, p-rGO can serve the two purposes: firstly, quickly decompose the chalcogen precursors mixed with it, and secondly, initiate rapid crystallization and phase transformation in chalcogenides over surface treated nickel foam placed near to it through transient radiative heating. To implement this strategy, commercially available nickel foam was first dipped in iron nitrate solution at ambient condition to develop amorphous Ni-Fe-hydroxide phases, and this treated foam was subjected

to this proposed microwave treatment for few seconds only. This unique process turned the irregular amorphous Ni-Fe-hydroxide phase into crystalline sulfide, selenide and phosphide phases within seconds. The only energy cost for the entire process starting from nickel foam happens during microwave heating for few seconds which is ~10^3-10^4 orders of magnitude lower as compared to several hours long hydrothermal or CVD processes. Significantly, this fast crystallization leads to iron-doped bi-phasic systems like Ni_3S_2/NiS, Ni_3Se_2/$NiSe_2$ and $Ni_{12}P_5$/Ni_2P, unlike hydrothermal/CVD process, which commonly results in single phases. In this process, the random morphology over nickel foam turns into uniform nanostructures. Importantly, all these developed bi-phasic chalcogenides and phosphides exhibit excellent OER catalytic activity and can deliver 500 mA cm^{-2} current at lower overpotentials as compared to most of the previous reports. In particular, Fe-doped sulfide shows in-plane heterostructure of tetragonal Ni_3S_2 and hexagonal NiS phases, which display exceedingly high OER activity requiring overpotential of only 187 mV and 289 mV to achieve 10 mA cm^{-2} and 500 mA cm^{-2}, which is one of the best performances as compared to any other non-noble metal catalysts reported thus far. The origin of this very high OER activity has been investigated in details and been correlated with this unique heterostructure and the in-situ phase evolution during OER.

5.2 Experimental Section

5.2.1 Materials

Iron nitrate nonahydrate $Fe(NO_3)_3.9H_2O$ and sodium hypophosphite (NaH_2PO_2) were purchased from Sigma-Aldrich. Thiourea (CH_4N_2S) and selenium powder were bought from Alfa-Aesar. Potassium hydroxide pellets (KOH) and hydrochloric acid (HCl) were purchased from Merck. Nickel foam (NF) has been purchased from MTI.

5.2.2 Synthesis of Fe-NF

First NF was cleaned with 3M HCl, ethanol and water under ultrasonication for 15 minutes each to remove surface impurities. Then to synthesize Fe-NF, a piece of washed NF was dipped in a solution of $Fe(NO_3)_3.9H_2O$ (0.525 g in 15 ml water) and kept there for 10 minutes. After the stipulated time, dipped NF was washed with water and ethanol and dried in a vacuum oven at room temperature to obtain brown coloured Fe-NF.

5.2.3 Synthesis of iron doped nickel sulfide, selenide and phosphide via rapid microwave induced generic phase evolution process (RMP)

First via Hummers' method graphene oxide (GO) was prepared and dried in a freeze dryer. This dried GO was then partially reduced in a domestic microwave oven with the help of graphite powder. Then for the rapid microwave induced phase evolution process, a piece of previously synthesized Fe-NF was placed in lab-made microwave reactor with partially reduced graphene surrounding. Different sources were then mixed with the graphene surrounding for sulfidation (CH_4N_2S), selenization (Se powder) and phosphidation (NaH_2PO_2). Depending on the source and time of reaction (5s for sulfidation and selenization, 8s for phosphidation) metal sulfide, selenide and phosphides were prepared. These developed samples were washed with water and ethanol to remove any unreacted sources and dried in vacuum oven at room temperature.

5.2.4 Synthesis of iron doped nickel sulfide via hydrothermal and CVD method

To synthesize iron doped nickel sulfide hydrothermally, a piece of Fe-NF was placed in an autoclave containing 0.3 g thiourea dissolved in 15 ml water and kept in an oven at 150º C for 10 h. After the reaction, the sample was washed with water and ethanol and then dried under vacuum at room temperature

To prepare Fe doped nickel sulfide via CVD method, a piece of Fe-NF was placed on a porcelain boat with CH_4N_2S on upstream side. The samples were then heated to 300º C temperature with a heating rate of 5º C min^{-1}. After the reaction when the temperature of the system came down to room temperature, the sample was washed with water, ethanol and dried in a vacuum oven at room temperature.

5.2.5 Material characterizations

Powder XRD patterns were taken by Rigaku X-ray diffractometer with Cu Kα source (λ=1.5418 Å). Field emission scanning electron microscopy (FESEM) images were captured by Zeiss Sigma 300 FESEM. For HRTEM and STEM analysis, Titan TM 80-300 (FEI) was used. ESCALAB Xi+ made by Thermo Fisher was utilized to conduct XPS of the samples.

5.2.6 Electrochemical measurements

The electrocatalytic OER performance was measured in 1 M KOH solution with a three-electrode cell having saturated calomel electrode as reference and platinum wire as counter electrodes (CE) with the help of PARSTAT 3000A-DX potentiostat. 1×1 cm^2 of developed samples were dipped in the electrolyte as a working electrode. Polarisation curves were taken at a standard scan rate of 5 mV s^{-1} and then corrected with iR compensation. The recorded potentials (E_{SCE}) were readjusted against reversible hydrogen electrode (RHE),

$$E_{RHE} = E_{SCE} + 0.059 \times pH + E_{RE}$$

Where, E_{RE} represents the potential of reference electrode against RHE.

Electrochemical impedance measurements of the catalysts were done in a frequency range of 10 kHz to 0.1 Hz at an AC amplitude of 10 mV. Cyclic voltammetry (CV) curves were taken in a voltage window of 0.1-0.2 V against RHE to calculate double layer capacitance (C_{dl}) which is also correlated to ECSA of the catalysts.

5.3 Results and discussions

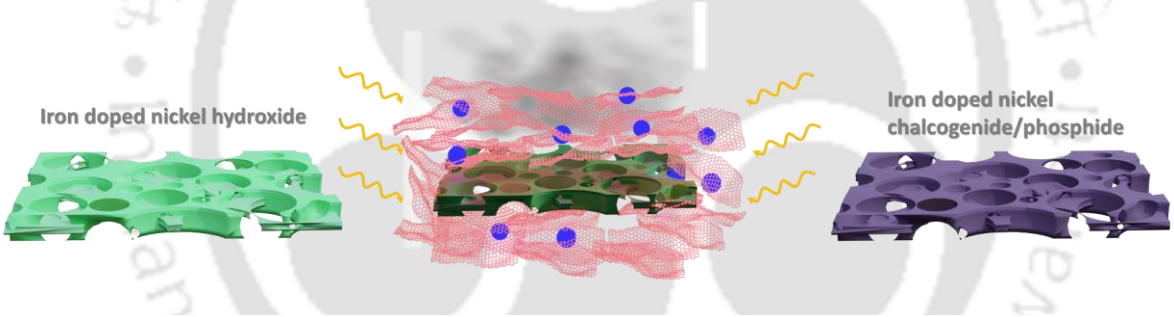

Figure 5.1. Schematic diagram of sulfidation/selenization/phosphidation of metal hydroxide through rapid microwave induced generic phase evolution process (RMP).

This rapid microwave-induced generic phase evolution process (RMP) for recrystallization was done within a customized domestic microwave oven. At first, an amorphous hydroxide phase of nickel and iron was prepared over nickel foam surface by simply dipping the foam within iron nitrate aqueous solution for few minutes. As-developed amorphous Ni/Fe hydroxide was crystalized to sulfide, selenide and phosphide nanostructures in seconds through microwave technique involving reduced graphene oxide in presence of desired chalcogen and phosphorous precursors (thiourea (TU), selenium powder (SP), sodium hypophosphite (SHP)). Reduced graphene is known to get rapidly heated by absorbing microwave and very high temperature as high as 1500^o C can be reached with partially reduced GO (p-rGO). The rapid self-heating of p-rGO under microwave was used for both the decomposition of TU/SP/SHP to generate gaseous species and gas phase reaction with Ni/Fe-hydroxide phase. The entire processing was

done by flowing nitrogen gas to a glass vial reactor to avoid the development of oxidative species. The schematic of the processing and phase evolution has been presented in Figure 5.1. Surprisingly, well-crystalline Ni/Fe-based sulfide, selenide and phosphide phases evolved within just a few seconds which otherwise require hours of gas phase or hydrothermal treatment involving large energy costs and processing complexity. Importantly, the energy cost is only 1.8 W for 8s treatment at 800 W of microwave, which is ~10^3-10^4 orders of magnitude lower as compared to conventional thermal/hydrothermal processes.

5.3.1 FESEM analysis

The recrystallization process was reflected in the radical morphological evolution during the microwaving process. Taking the Ni-Fe based sulfide as an example, the completely irregular bulk morphology of Ni-Fe hydroxide (Figure 5.2a), which evolve over smooth nickel foam surface on $Fe(NO_3)_3$ treatment, evolves into uniform lamellar structure made of highly interconnected sheets in only 5s of RMP treatment (Figure 5.2b). The structure turns into a uniform and continuous lamellar structure. The structure can also be thought of as continuous interconnected sheets (figure 5.2b), and the vertically protruding edges have a thickness of only ~5 nm. These sheets remain interconnected to each other to form an open porous network which is highly beneficial gas-releasing structure in OER process. The rapid recrystallization strategy was further extended for phosphide and selenide development to establish the generic nature

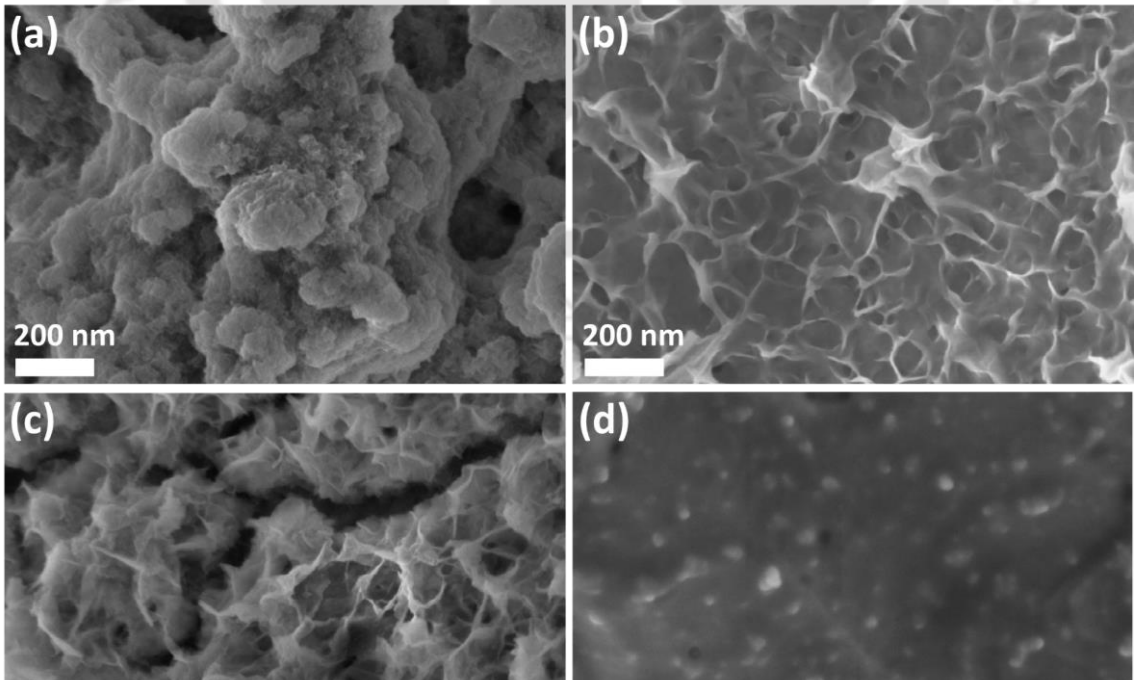

Figure 5.2. FESEM images of (a) Fe-NF, (b) Fe doped nickel sulfide, (c) Fe doped nickel selenide and (d) Fe doped nickel phosphide via RMP process.

of this process. For the case of selenide, decomposition of SP and gas phase reaction leads to highly dense and oriented sheet structure with an average thickness of ~ 5 nm (Figure 5.2c). On the other hand, reaction with source of phosphorous drastically changes irregular morphology of Ni-Fe-hydroxide into uniform nanoparticles of average diameter ~ 27 nm dispersed over highly smooth surface (Figure 5.2d).

5.3.2 XRD analysis

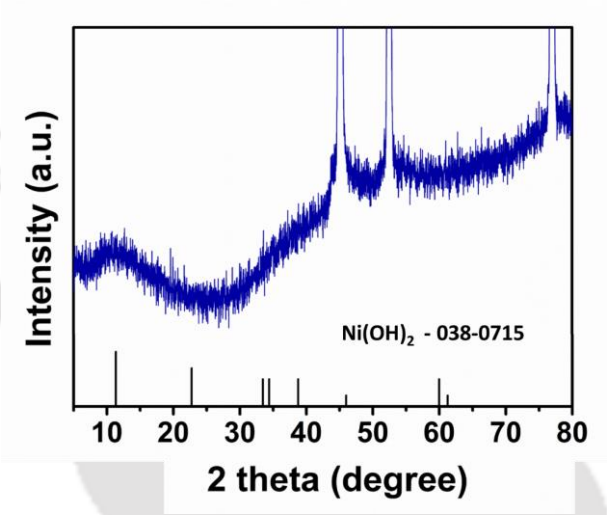

Figure 5.3. XRD pattern of Fe-NF

The rapid evolution of crystalline phases is evident from the XRD patterns as given in Figures 5.3 & 5.4. The XRD pattern in Figure 5.3 reveals that $Fe(NO_3)_3$ treatment does not give rise to any crystalline phases in which the peaks of nickel substrate at 45.2º, 52.6º and 77º are only visible. However, small broad hump appears at ~ 11.1º which can be assigned to

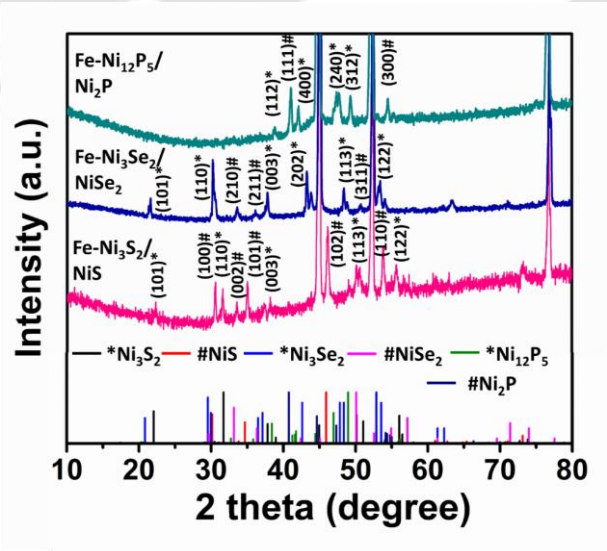

Figure 5.4. XRD pattern of Fe-Ni_3S_2/NiS, Fe-Ni_3Se_2/$NiSe_2$ and Fe-$Ni_{12}P_5$/Ni_2P

amorphous/poorly crystalline Ni-Fe hydroxide phase. The XRD pattern further reveals rapid crystallization of this amorphous phase into sulfide, selenide and phosphide phases within just 8 seconds. The sulfide structure consists of mixture of two different crystalline phases namely tetragonal Ni_3S_2 (JCPDS- 01-075-6275) and hexagonal NiS (JCPDS- 01-075-0613) having peaks at 22.3º, 31.6º, 38.2º, 50.6º, 55.6º and 30.6º, 33.6º, 35º, 46.1º, 53.9º respectively. The as-developed selenide and phosphides also show the bi-phasic structures, and the two sets of peaks are matching with Ni_3Se_2 (JCPDS- 01-077-3110) & $NiSe_2$ (JCPDS- 008-0423) and $Ni_{12}P_5$ (JCPDS- 01-074-138) & Ni_2P (JCPDS- 01-072-2514) phases respectively.

5.3.3 TEM analysis

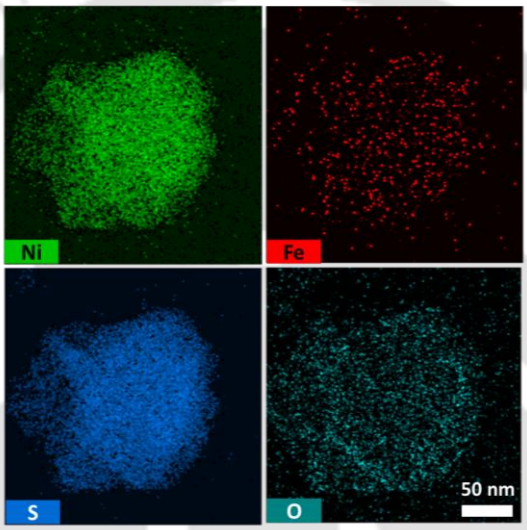

Figure 5.5. TEM elemental mapping of Fe-Ni_3S_2/NiS

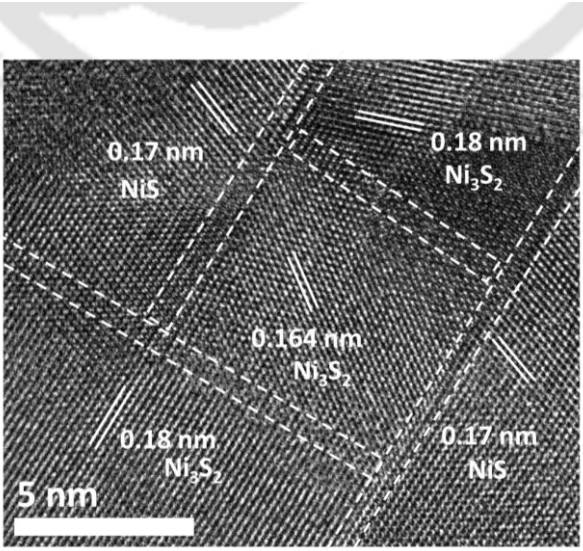

Figure 5.6. HRTEM image of Fe-Ni_3S_2/NiS

The TEM elemental mapping shows uniform distribution of Ni, Fe and S throughout the sample, which signifies that Fe remains as a dopant within the sulfide structure (Figure 5.5). The crystalline structure of Ni_3S_2/NiS biphasic nanosheets was examined with atomic resolution transmission electron microscope and is presented in Figure 5.6. The TEM image reveals highly crystalline domains which are separated by sharp atomic boundaries. The domains with inter-planner spacing of 0.18 nm and 0.164 nm correspond to (113) and (122) planes of Ni_3S_2 respectively, whereas the domain having lattice spacing of 0.17 nm corresponds to (110) plane of NiS phase. This HRTEM image establishes that the second-scale recrystallization and phase evolution resulted in Ni_3S_2/NiS in-plane heterostructures. These characterizations establish that dramatic morphological and crystalline evolution can be done within seconds by this p-rGO-involved reactive microwave technique RMP, and all of these materials can display high catalytic activity, which will be discussed in the subsequent sections.

5.3.4 XPS analysis

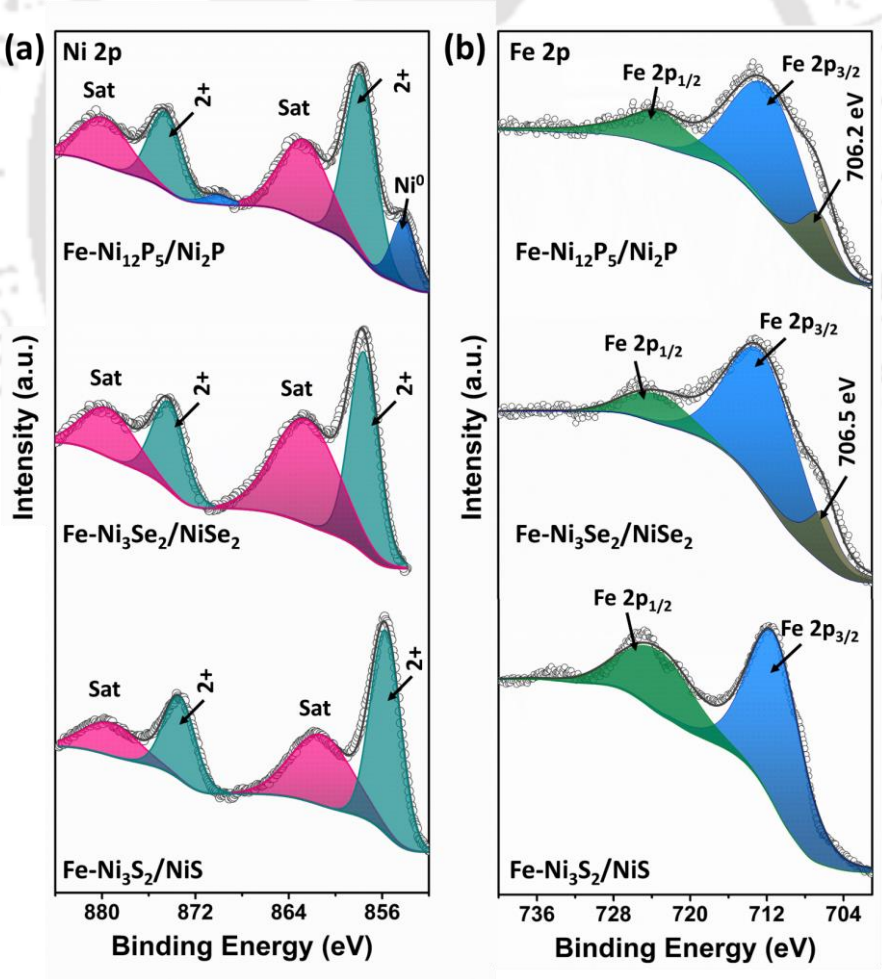

Figure 5.7. high resolution XPS spectra for (a) Ni 2p, (b) Fe 2p of Fe-Ni_3S_2/NiS, Fe-Ni_3Se_2/$NiSe_2$ and Fe-$Ni_{12}P_5$/Ni_2P.

To analyse the surface chemical state and oxidation nature of the metallic species state the as-developed samples have been investigated by X-ray photoelectron spectroscopy (XPS). The high resolution XPS spectra corresponding to Ni 2P orbital of as-developed Fe-Ni_3S_2/NiS, Fe-Ni_3Se_2/$NiSe_2$ and Fe-$Ni_{12}P_5$/Ni_2P show very similar features (Figure 5.7a). For all the cases, the Ni 2P peaks can be deconvoluted into a doublet and a two shakeup satellite. The doublets correspond to spin-orbit splitted $2p_{3/2}$ and $2p_{1/2}$ peaks. The position of $2p_{3/2}$/$2p_{1/2}$ at 855.8 eV/ 873.4 eV, 856 eV/ 873.7 eV and 856.2 eV/ 874 eV correspond to Ni^{2+} state and matches well with the reported nickel based sulfide, selenide and phosphide phases.[28–30] In addition, an extra doublet peak at 852.4 eV/ 869.2 eV could be observed in Ni 2p XPS spectra of Fe-$Ni_{12}P_5$/Ni_2P which corresponds to the Ni^0 of $Ni_{12}P_5$/Ni_2P heterostructure.[30] The XPS spectra of Fe 2p spectrum of all the phases (Figure 5.7b) on deconvolution reveal spin-orbit splitted ($2p_{3/2}$ & $2p_{1/2}$) peaks at 711.7 eV / 724.6 eV, 712.8 eV/ 724.5 eV and 712.3 eV / 724.3 eV corresponding to Fe^{3+} of Fe-Ni_3S_2/NiS, Fe-Ni_3Se_2/$NiSe_2$ and Fe-$Ni_{12}P_5$/Ni_2P respectively.[28,31] However, no peaks related to satellite can be detected in the Fe 2p XPS spectra suggesting Fe^{3+}

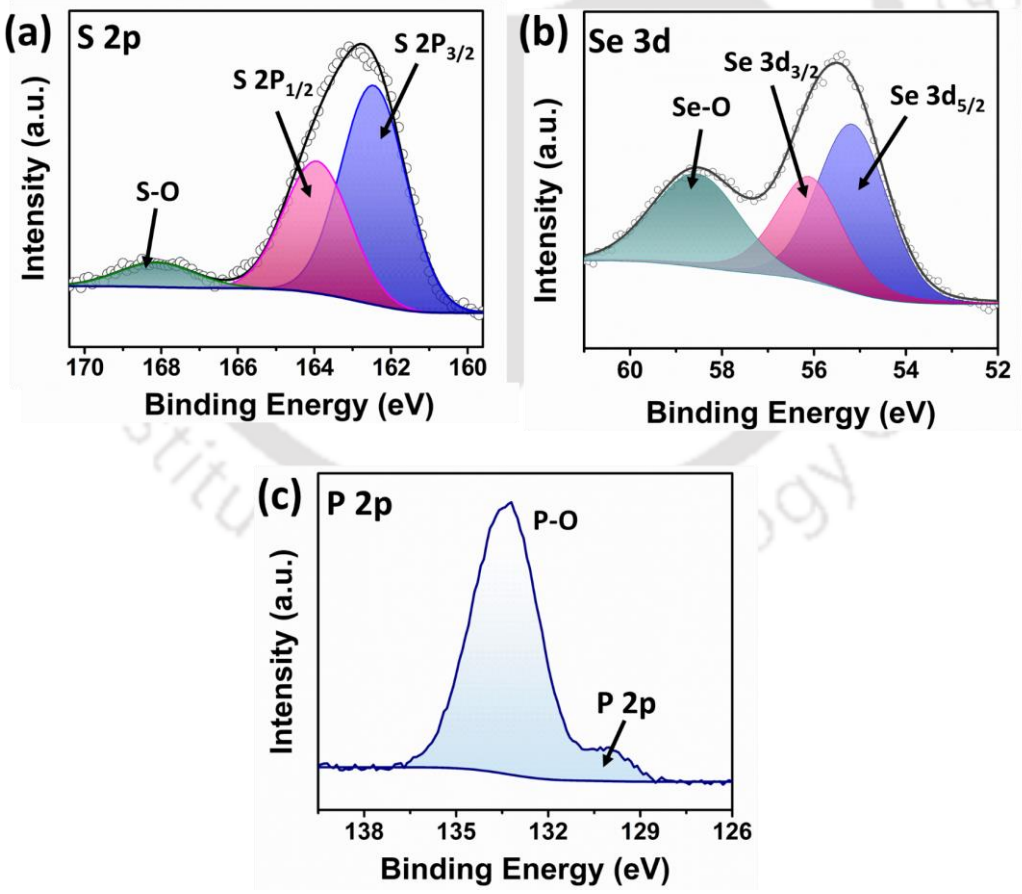

Figure 5.8. high resolution XPS spectra for (a) S 2p XPS spectra of Fe-Ni_3S_2/NiS (b) Se 3d XPS spectra of Fe-Ni_3Se_2/$NiSe_2$ and (c) P 2p XPS spectra of Fe-$Ni_{12}P_5$/Ni_2P.

mainly remain as a dopant in the nickel sulfide, selenide and phosphide lattice.[28,32] Additional peaks at 706.5 eV for Fe-Ni_3Se_2/$NiSe_2$ and 706.1 eV for Fe-$Ni_{12}P_5$/Ni_2P can be observed which are the pre-peaks of Fe $2p_{3/2}$.[31,33] The deconvoluted S 2p XPS spectra as shown in Figure 5.8a consists of two spin splitted peaks ($2p_{3/2}$ & $2p_{1/2}$) at 162.5 eV & 163.9 eV which corresponds to S^{2-} state, and a low intensity peak at 168.1 eV corresponding to surface oxidized metal sulfide species. To support the conversion, XPS has been further employed, as shown in Figures 5.8b, c. Se 3d core-level spectra consist of two characteristic peaks at 55.2 eV and 56.1 eV associated with Se $3d_{5/2}$ and Se $3d_{3/2}$ and a peak at 58.4 eV corresponding to Se-O bond suggesting that surface Se species have been partially oxidized in the air to form SeO_x (Figure 5.8b).[29,34] Similarly, P 2p XPS spectra consist of a characteristic peak at 129.8 eV related to $Ni_{12}P_5$/Ni_2P and the signal at 133.4 eV corresponding to P-O surface oxidation possibly formed by exposure to air and very common in $Ni_{12}P_5$ and Ni_2P samples (Figure 5.8c).[30,35,36]

5.3.5 OER catalytic performance

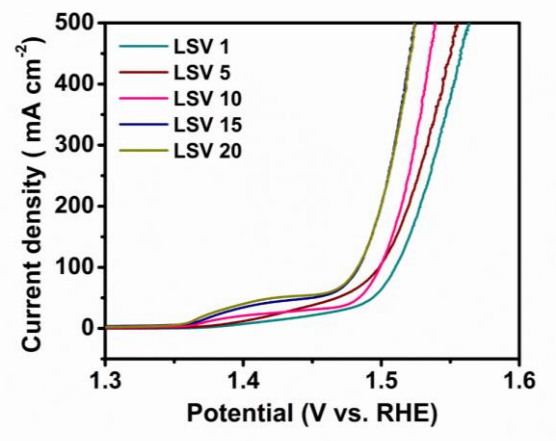

Figure 5.9. OER LSV cycles (without *iR* correction) for activating Fe-Ni_3S_2/NiS.

The four-electron transfer process of oxygen evolution reaction makes this process sluggish, and it requires large overpotential to cross the surface energy barriers. As-developed fast-crystallization sulfide, selenide and phosphide nanostructures were found to show superb OER activities and require low overpotentials even to achieve high current density. The linear sweep voltammetry (LSV) polarization curves exhibited dynamic changes in successive scans in 1 M KOH electrolytes and then stabilize after few scans (Figure 5.9). This dynamic changes of LSV curves in transition metal-based chalcogenides are associated with in-situ oxidation and surface reconstruction into (oxy)hydroxide phases.[5,12] The evaluation of OER performance was done after all the samples had undergone these dynamic changes during first few LSV cycles and no further modification was detected in consecutive LSV curves. Figure 5.10a shows the LSV

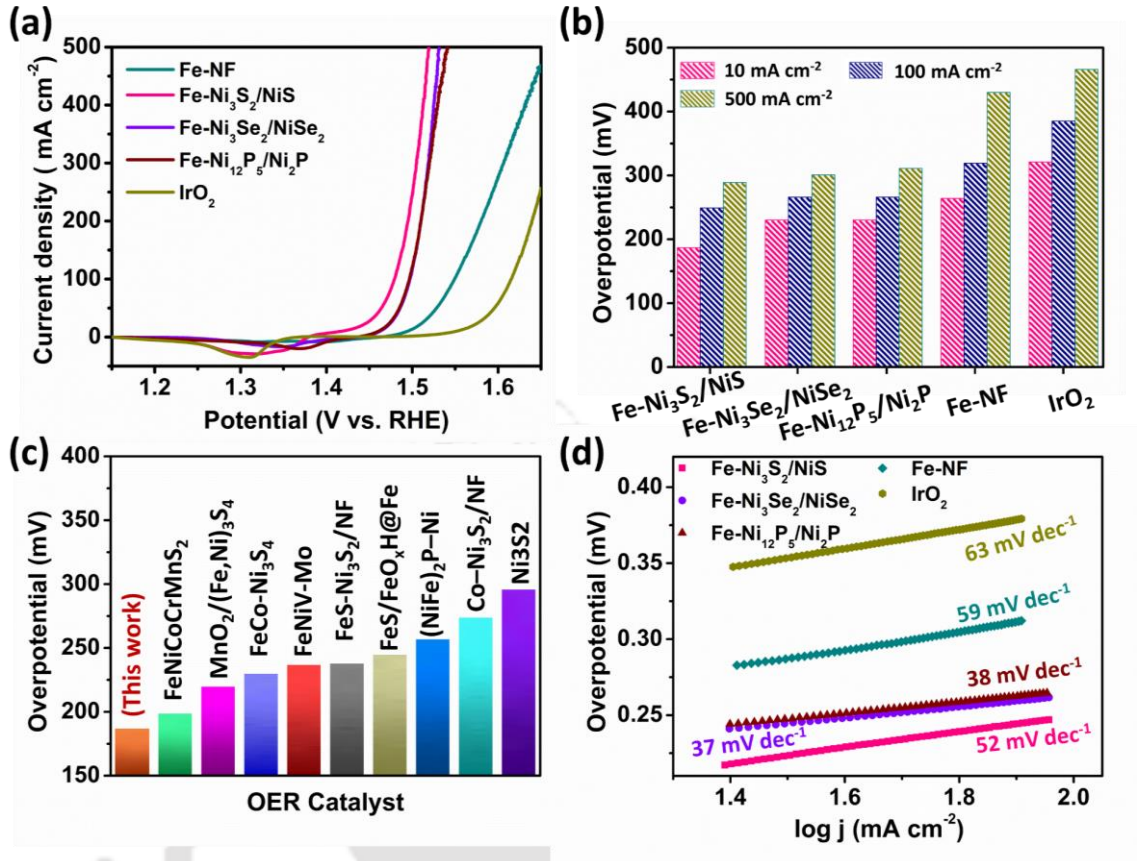

Figure 5.10. (a) OER Polarisation curves for Fe-NF, Fe-Ni_3S_2/NiS, Fe-Ni_3Se_2/$NiSe_2$, Fe-$Ni_{12}P_5$/Ni_2P and IrO_2 with *iR* compensation and their (b) overpotential for different current densities 10, 100 and 500 mA cm^{-2}. (c) Comparison of OER overpotential at 10 mA cm^{-2} for Fe-Ni_3S_2/NiS with previously reported catalysts (d) Tafel plots of Fe-NF, Fe-Ni_3S_2/NiS, Fe-Ni_3Se_2/$NiSe_2$, Fe-$Ni_{12}P_5$/Ni_2P and IrO_2.

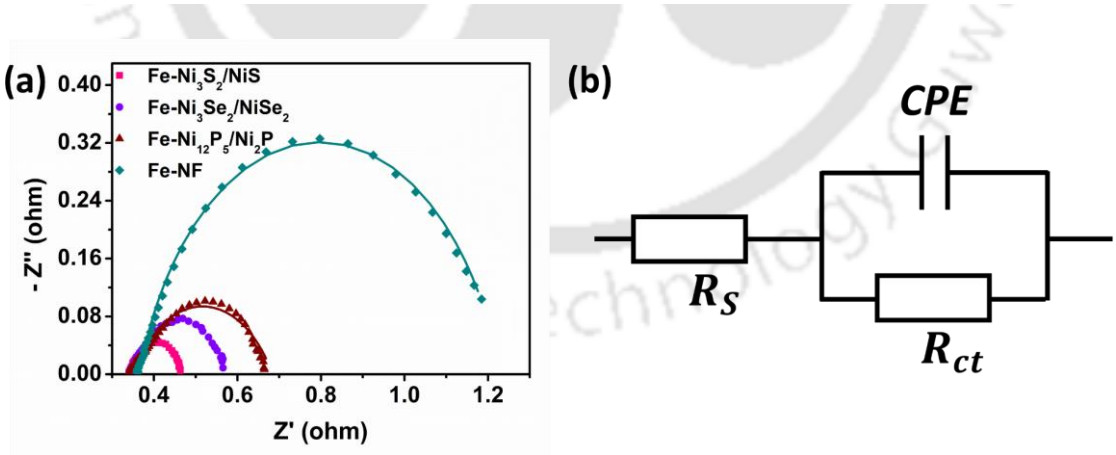

Figure 5.11. (a) EIS curves of the corresponding materials with fitting according to the model as shown in (b).

polarization curves of Fe-NF and as-developed Fe-Ni_3S_2/NiS, Fe-Ni_3Se_2/$NiSe_2$ and Fe-$Ni_{12}P_5$/Ni_2P samples together with benchmark noble metal-based catalysts IrO_2. The required overpotentials to deliver current densities of 10 mA cm^{-2}, 100 mA cm^{-2} and 500 mA cm^{-2} are

Table 5.1. Summary of OER performance of different synthesized catalysts

Samples	η_{10} (mV)	η_{100} (mV)	η_{500} (mV)	Tafel slope (mV dec^{-1})	R_s (Ω)	R_{ct} (Ω)
Fe-Ni_3S_2/NiS	187	249	289	52	0.34	0.13
Fe-Ni_3Se_2/$NiSe_2$	230	266	301	37	0.34	0.24
Fe-$Ni_{12}P_5$/Ni_2P	232	267	311	37	0.35	0.34
Fe-NF	264	319	-	59	0.34	0.92
Fe-NiS-CVD	248	307	356	63	0.35	0.47
Fe-Ni_3S_2-HT	292	358	433	69	0.35	0.61

Table 5.2. OER performance of recently reported non-noble metal based electrocatalysts

Samples	η_{10} (mV)	η_{100} (mV)	η_{500} (mV)	Tafel slope (mV dec^{-1})	Reference
Fe-Ni_3S_2/NiS	187	249	289	52	**This work**
FeS-Ni_3S_2/NF	238	290	-	44	[37]
$Fe_{0.8}Ni_{0.15}S_{1.05}$	228	324	-	53	[38]
$Ni_3Fe_{0.5}V_{0.5}$	200	264	291	39	[39]
Acetylene black@$NiFeS_x$	232	329[a)]	-	35	[40]
$Ni_{0.9}Fe_{0.1}MoO_4$	299	443[a)]	-	63	[41]
Fe-NiP/NiS	204	256	-	54	[42]
FeS/FeO_xH@Fe nanosheets	245	276	376	71	[22]
FeCo-Ni_3S_4	230	280	393	63	[23]
$Fe_{0.9}Ni_{2.1}S_2$@NF	-	252	294	64	[43]
Mo–Ni_3S_2/NF	218	280	-	42	[44]
MnO_2/$(Fe,Ni)_3S_4$	220	268	325	45	[45]
FeOOH–CoS	-	260	306	61	[46]
Co-Fe-S NFs@MS/NF	223	281	300[a)]	43	[47]
FeNiV-Mo5%	237	288	412	38	[48]

$FeNiCoCrMnS_2$	199	246	283	39	[49]
Fe-NiTe–$Ni_{12}P_5$	275 (η_{20})	340	-	66	[36]

[a] *(Data have been collected from LSV curve)*

given in Figure 5.10b and Table 5.1. Significantly, the required overpotential (η_{10}) to deliver 10 mA cm^{-2} current density is only 187 mV for the case of Fe-Ni_3S_2/NiS, which is among the one of the lowest values ever reported with earth-abundant transition metal-based catalysts. Besides, the selenide and phosphide counterparts also exhibit excellent OER activity with η_{10} values are 230 mV and 232 mV respectively, which are far superior as compared to η_{10} value of 264 mV and 321 mV for Fe-NF sample and benchmark IrO_2 catalyst. More remarkably, only small overpotentials of 289, 301 and 311 mV corresponding to sulfide, selenide and phosphide phases can drive high current density of 500 mA cm^{-2}. These very low values of η_{500} are not only significantly lower as compared to IrO_2 (466 mV) and Fe-NF (430 mV) catalysts, but also lower than most of the reported data in the literature (Figure 5.10c and Table 5.2).[22,23,37,45,48–52] Reaction kinetics of the catalysts were further judged by determining Tafel plots (η vs *log J*) as shown in Figure 5.10d. RMP processed samples Fe-Ni_3S_2/NiS (52 mV dec^{-1}), Fe-Ni_3Se_2/$NiSe_2$ (37 mV dec^{-1}) and Fe-$Ni_{12}P_5$/Ni_2P (38 mV dec^{-1}) show very low Tafel slope value compared to Fe-NF (59 mV dec^{-1}) and IrO_2 (63 mV dec^{-1}). The lowest Tafel slope of RMP processed samples indicates faster reaction kinetics of these samples. The aforementioned results establish that our second-scale recrystallization and phase evolution turn the Fe-NF into highly active OER catalysts, particularly, the performance of Fe-Ni_3S_2/NiS is the state-of-the art in this field.

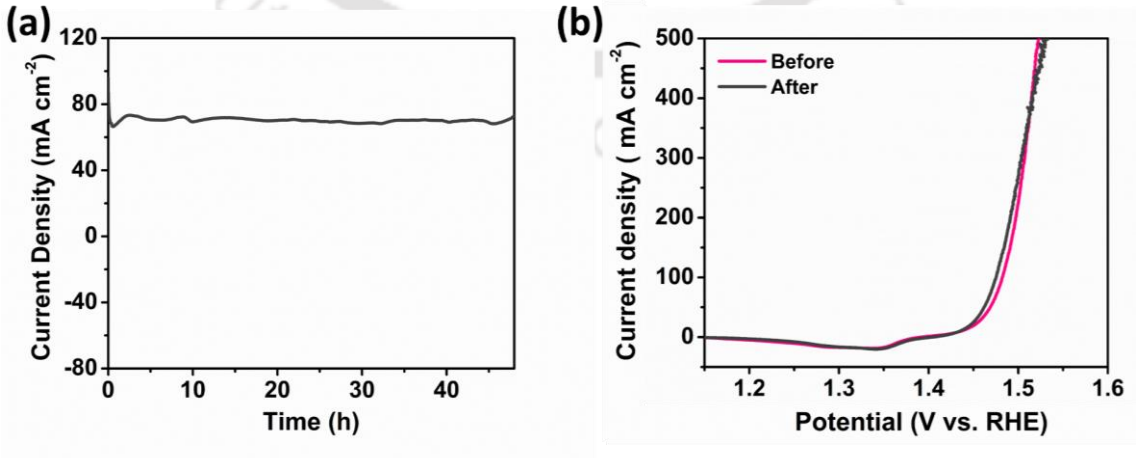

Figure 5.12. (a) Chronoamperometric test for OER of Fe-Ni_3S_2/NiS at 1.47 V for a long time of 48 h and (b) shows comparison of its polarisation curve before and after stability test.

To inspect the origin of high OER activity of the developed catalysts, electrochemical impedance measurement was performed and presented in Nyquist plots (Figure 5.11a). The circuit diagram shown in Figure 5.11b was used to fit these graphs, with R_{ct}, R_s and CPE representing charge transfer resistance, solution resistance and constant phase element, and the values are listed in Table 5.1. The table displays that all phases of the samples possess low R_{ct} values as compared to that of Fe-NF sample (0.92 Ω). Such a significant decrease in R_{ct} values indicate that our recrystallization process turns Fe-NF into generic phases having active surfaces endowed with facile charge transfer characteristics between electrode and electrolyte. Especially the lowest R_{ct} value of only 0.13 Ω for Fe-Ni_3S_2/NiS sample signifies its superior charge transfer characteristics, and it is consistent with its outstanding OER activity. Furthermore, the as-developed catalysts show long-term operational stability (Figure 5.12a), retaining 50 mA cm^{-2} current density at a constant potential of 1.47 V against RHE for 48 hours. The LSV curve does not degrade following the stability test (Figure 5.12b), demonstrating that it is suitable for long-term use.

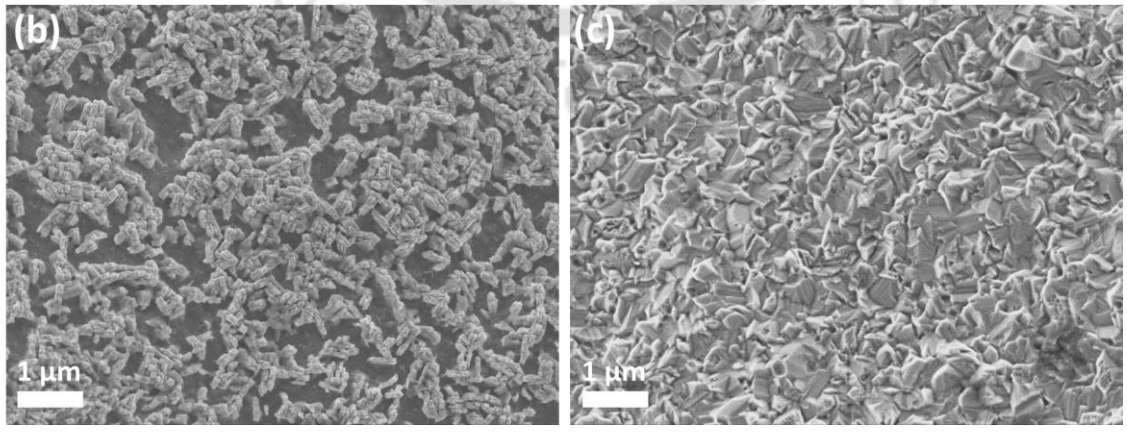

Figure 5.13. (a) XRD pattern of Fe doped Ni sulfide developed via high temperature annealing by CVD and hydrothermally. FESEM images of (b) Fe-NiS-CVD and (c) Fe-Ni_3S_2-HT.

The outstanding OER activity of rapidly crystalized Fe-Ni_3S_2/NiS phase raises a relevant query about whether similar performance can also be realized through conventional sulfidation strategies like hydrothermal or high-temperature chemical vapour transport methods (CVD). To shed light on this question, the Fe-NF was subjected to hydrothermal treatment in TU solution and thermal treatment with TU in CVD furnace (experimental section). Interestingly, the crystalline phases of the resultant sulfides are very different as compared to our RMP-based crystallization technique. Unlike Ni_3S_2/NiS phase, the vapour thermal method (CVD) generates highly crystalline hexagonal NiS phase, whereas the hydrothermal process produces trigonal Ni_3S_2 phase (Figure 5.13a). Not only the crystalline phases, the morphologies of the hydrothermal and vapour thermal converted samples are very different, the former one displays sheetlike morphology, whereas the latter one does not show any regular structure (Figure 5.13b, c). The LSV polarization curves (Figure 5.14a) of OER exhibit that the sulfide phase of RMP method is far superior to hydrothermal or vapour thermal sulfides, as is evident from its much lower onset potential and steeper rise. These overpotentials to achieve 10 mA cm^{-2} and 500 mA cm^{-2} OER currents are far lower in Fe-Ni_3S_2/NiS (187 and 289 mV) than that required for sulfide samples obtained through hydrothermal (292 and 433 mV), vapour thermal (248 and 356 mV) methods (Table 5.1). The calculated Tafel slope of RMP sulfide (52 mV dec^{-1}) is much lower as compared to hydrothermal and vapour thermal samples (69 and 63 mV/dec respectively), which evidences its much faster reaction kinetics (Figure 5.14b). The electrochemical surface area ECSA of the samples was estimated from cyclic voltammograms in the non-Faradic regions and the measured electrical double layer capacitance does not show significant variations (Figure 5.15a). To inspect the variation in their intrinsic activity ECSA normalized LSV curves were

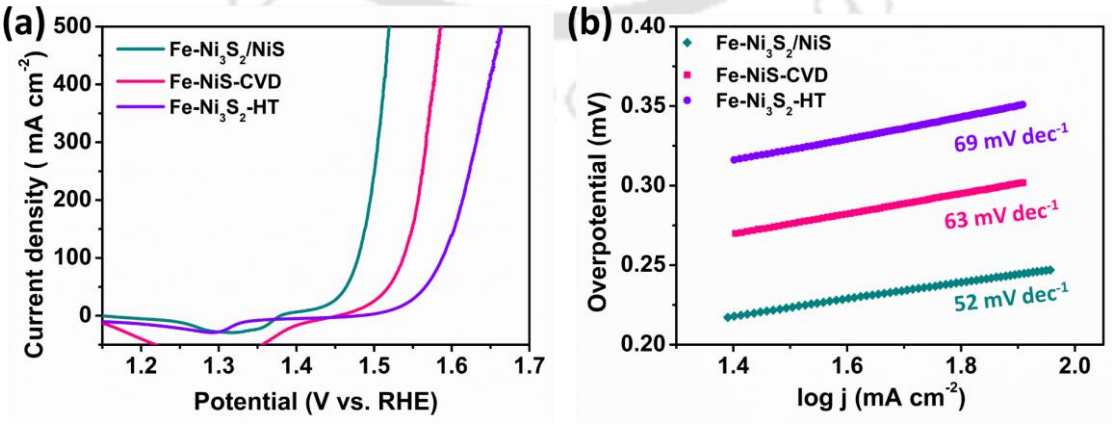

Figure 5.14. (a) OER Polarisation curves for Fe-Ni_3S_2/NiS, Fe-NiS-CVD and Fe-Ni_3S_2-HT with *iR* compensation, their (b) corresponding Tafel plots.

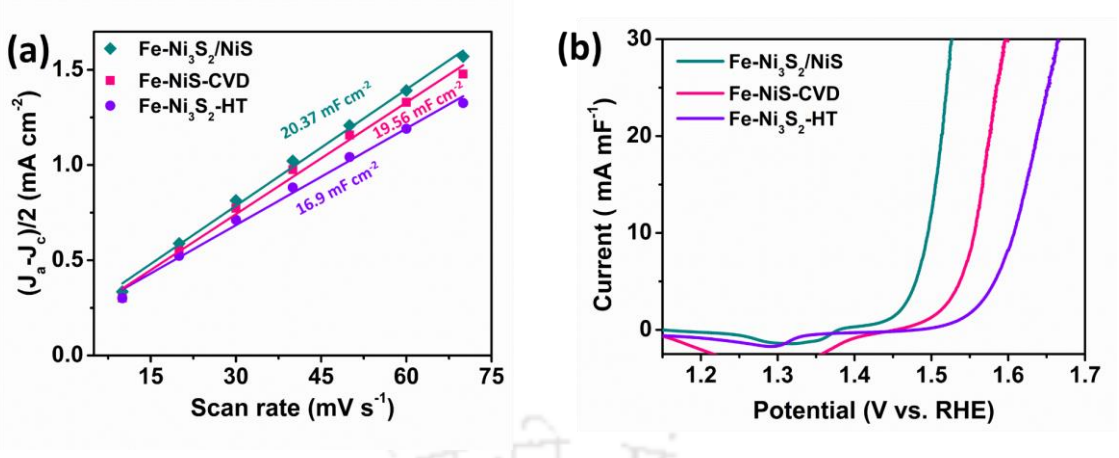

Figure 5.15. (a) Estimated C_{dl} of ECSA for Fe-Ni_3S_2/NiS, Fe-NiS-CVD and Fe-Ni_3S_2-HT and (b) ECSA normalised LSV curves.

presented (Figure 5.15b) and compared. When compared to other sulfide samples synthesized via conventional procedures, RMP sulfide displays the maximum current at any given potential, indicating that this catalyst has a higher intrinsic OER activity. The origin of higher activity of RMP-based samples can be better understood using Nyquist plots and extensive impedance analysis (Figure 5.16). The RMP sulfide has the lowest R_{ct} value (0.13 Ω) when compared to samples synthesized through hydrothermal (0.47 Ω) and vapour thermal (0.61 Ω) processes, indicating facile charge transfer between electrode and electrolyte for the former (Figure 5.16). This comparative investigation highlights the importance of this unique microwave-involved rapid crystallization strategy in developing crystalline phases having very high catalytic activity.

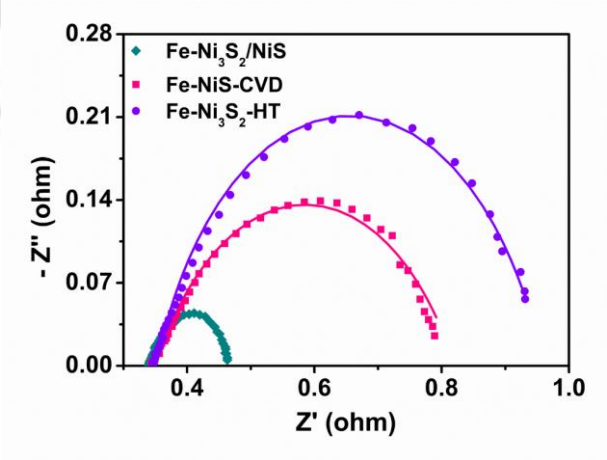

Figure 5.16. EIS curves of Fe-Ni_3S_2/NiS, Fe-NiS-CVD and Fe-Ni_3S_2-HT with fitting according to the model as shown in Figure 5.11b.

5.3.6 Post-OER characterizations

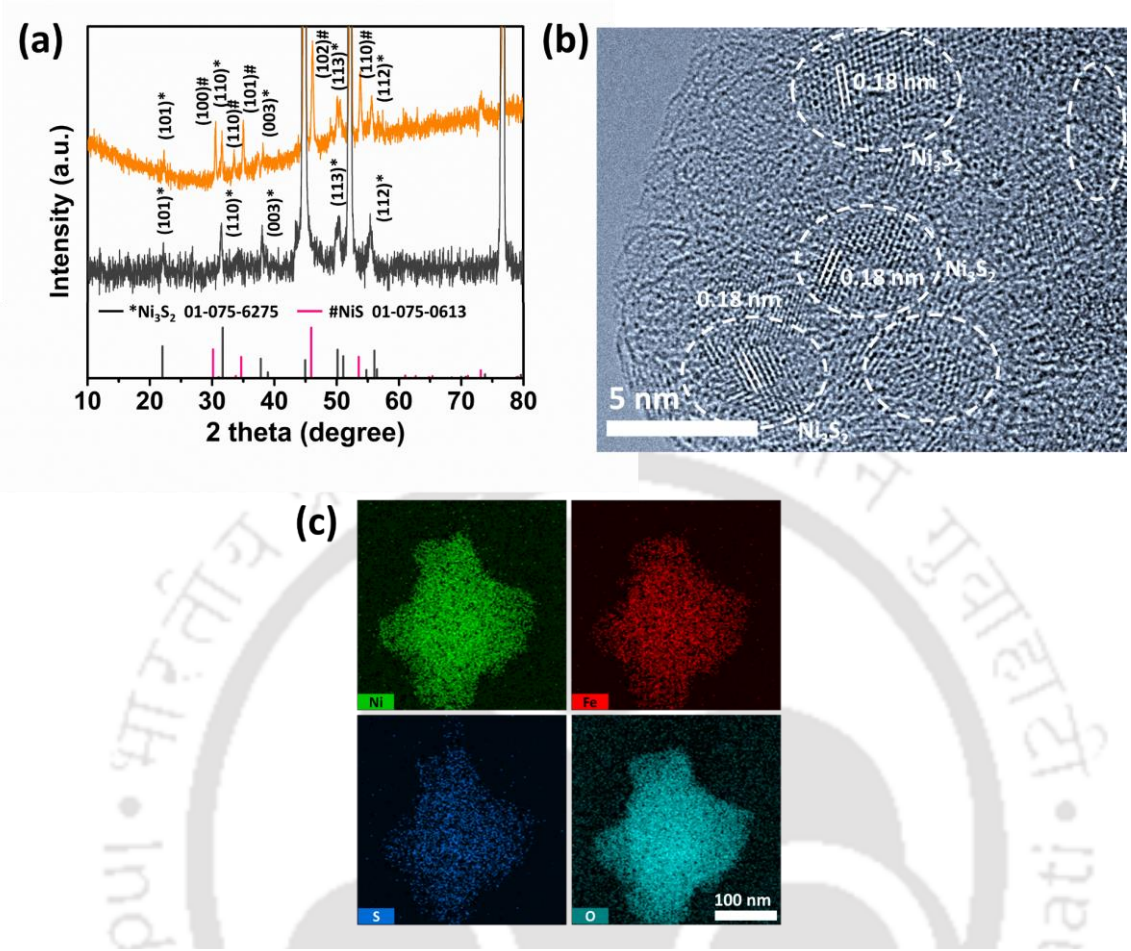

Figure 5.17. (a) XRD pattern of Fe-Ni_3S_2/NiS and Fe-Ni_3S_2/NiOOH. (b) HRTEM image and (c) TEM mapping of Fe-Ni_3S_2/NiOOH.

Considering the unmatched high performance of Fe-Ni_3S_2/NiS, it was further investigated to reveal the origin of its excellent OER activity. The LSV curves were continuously showing improvement in the consecutive cycles before being stabilized during 20 cycles, this observation indicates that there might have been some surface modification and in-situ activation of the catalyst during first few cycles of OER process (Figure 5.9). To enquire any such in-situ modification, the XRD pattern of as developed Fe-Ni_3S_2/NiS before and after 20 LSV cycles of OER were compared (Figure 5.17a). Importantly, it was found that the XRD peaks related to NiS completely disappear after self-activation during OER; however, peaks of Ni_3S_2 are clearly visible. From this XRD it can be inferred that only NiS component of Fe-Ni_3S_2/NiS heterostructure is fully reconstructed to produce some amorphous phases during electrochemical activation process. The HRTEM investigation of the sample after OER test indeed confirms the absence of NiS phase and the presence of lattice fringes with inter-planner separation of 0.18 nm corresponding to Ni_3S_2, together with the occurrence of amorphous

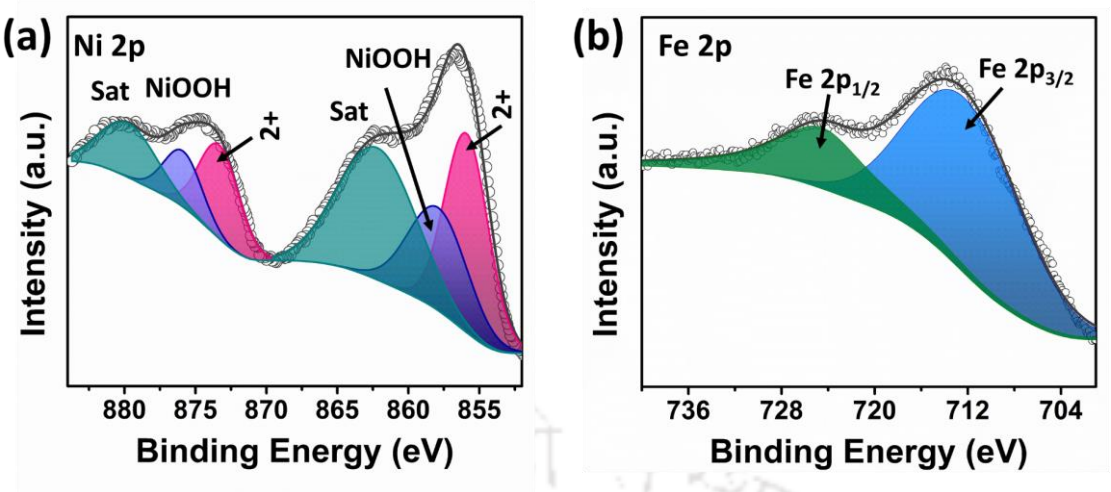

Figure 5.18. (a) Ni 2p and (b) Fe 2p XPS spectra of Fe-Ni_3S_2/NiOOH.

regions (Figure 5.17b). The TEM mapping analysis after OER test shows substantial decrease in sulfur and consequent increase of oxygen content in the sample (Figure 5.17c). This indicates possible phase transformation of NiS into hydroxide/(oxy)hydroxide species.

The deconvoluted Ni 2p XPS spectra, as presented in Figure 5.18a shows that together with a peak of Ni^{2+} similar to before OER sample, an additional peak to 858.2 eV/ 876.2 eV appears after OER test, which can be assigned to nickel (oxy)hydroxide phase (NiOOH). Thus, combining XRD, HRTEM and XPS analysis, it can be concluded that NiS phase of Fe-Ni_3S_2/NiS heterostructure converted into NiOOH phase during the self-activation process during OER catalysis. The as-activated Fe-Ni_3S_2/NiOOH in-plane heterostructure is responsible for the observed superb oxygen evolution activity. The XPS analysis further shows the peak profile of Fe 2p changes significantly, and its deconvolution discloses the shift of Fe^{3+} to higher binding energy of 713.3 eV/ 725.5 eV in after OER sample as compared to position at 711.7 eV/ 724.6 eV in before OER sample (Figure 5.18b). This shift of binding energy of Fe^{3+} dopant can be linked with the change in its chemical environment due to the oxidation of its sulfide host.

Recent theoretical and experimental studies have revealed that a high OER catalytic activity can stem from one or more of the following characteristics of catalysts: (i) suitable electronic property offering low energy barriers to elementary steps in OER, (ii) good electrical conductivity for easy charge transport to the active sites with the minimal resistive energy loss, (iii) suitable morphology of catalytic electrode for easy O_2 release, which otherwise can block the active sites, and (iv) tip curvature of the catalysts. Noticeably, our Fe-Ni_3S_2/NiS in-plane heterostructure catalyst satisfies all these beneficial characteristics and has manifold role in

enhancing the OER activity. Firstly, Fe-Ni_3S_2/NiS quickly converts into the ideal Fe-Ni_3S_2/NiOOH heterostructure, where Fe-doped NiOOH provides the most suitable electronic structure among various non-noble metal catalysts that can activate OER process at a low overpotential [53,54]. Through in-situ Raman measurement, Louie et al. attributed the enhanced OER performance of Fe-doped NiOOH to significant local environmental modification of Ni-O as proven by in-situ Raman spectroscopy [55]. In the case of Fe-doped NiOOH, it has been reported that Fe^{3+} site is the main active site for OER which is proven to take a higher oxidation state (Fe^{4+}) during OER condition as proven by Chen et al. through in-situ Mössbauer spectroscopy [56,57]. In addition to it, Fe enhances the activity of the catalyst by increasing the conductivity of Fe-NiOOH compared to only NiOOH catalyst, and the present Fe^{3+} in the structure assist to induce more Ni^{3+} in the structure, thus increasing the OER activity of the material [58]. Although Fe doping improves the conductivity of Fe-NiOOH, it still has less electrical conductivity compared to chalcogenides [59]. However, the structural advantage of in-plane heterostructure can preserve overall conducting channels. In this in-plane heterostructure, domains of Ni_3S_2 and Fe-NiOOH form percolated conducting network in which electrons from current collector (nickel foam substrate) can be easily delivered to the active Fe-NiOOH phase along metallic Ni_3S_2, thus facilitating the OER process. Moreover, Ni_3S_2 in this heterostructure is itself a good OER catalyst. Thus, both Fe-NiOOH and Ni_3S_2 act as active OER catalysts with advantageous in-plane heterostructure configuration ensuring good overall electrical conductivity. In addition, the open cellular morphology of the as-developed catalyst without complex porosity can guarantee the easy release of generated O_2 gas from the electrode; thus, this can minimize the blocking of active sites with the generated O_2. It has been recently found that a high curvature of catalysts is highly beneficial for OER process, as the applied electric field can be concentrated [60]. This amplification of electric field can enhance the local concentration of OH^- ions around the tips and thereby increase the reaction kinetics. The tip curvature of our catalysts is only ~5 nm to induce an unusually high local field and OH^- ion concentration, which might be a nonnegligible origin for the highly boosted OER activity.

5.4 Conclusion

In summary, we report a generic phase evolution strategy in which unique bi-crystalline phases develop over nickel foam through rapid microwave-involved technique. Just room temperature dipping of commercial nickel foam in iron nitrate and subsequent gas phase chalcogenization/ phosphidation in a domestic microwave oven for only few seconds lead to development of unique phases like iron doped Ni_3S_2/NiS, Ni_3Se_2/$NiSe_2$, and $Ni_{12}P_5$/Ni_2P. Out of the developed

catalysts, Fe-Ni_3S_2/NiS displays state-of-the art OER activity requiring an overpotential of 187, 249 and 289 mV to achieve a current density of 10 mA cm^{-2}, 100 mA cm^{-2} and 500 mA cm^{-2} respectively, and having superb operational stability. Values of required overpotential are significantly lower as compared to nearly all the non-noble catalysts developed so far, and at par with the few best results reported thus far. The other chalcogenides like metal selenide (Fe-Ni_3Se_2/$NiSe_2$), metal phosphide (Fe-$Ni_{12}P_5$/Ni_2P) also require a low overpotential of only 301 and 311 mV respectively to achieve a very high current density of 500 mA cm^{-2}. Importantly, the development does not require any complicated equipment or complex processing. Further, this second scale process requires orders of magnitude lower thermal budget as compared to conventional techniques like thermal vapour transport method or hydrothermal techniques. We believe that the generic nature of the process for crystalline phase transformation, ultrafast processing and very low cost can guide the development of low cost catalysts for commercial use.

Reference

[1] N.-T. Suen, S.-F. Hung, Q. Quan, N. Zhang, Y.-J. Xu, H. M. Chen, *Chem. Soc. Rev.* **2017**, *46*, 337.

[2] B. M. Hunter, H. B. Gray, A. M. Müller, *Chem. Rev.* **2016**, *116*, 14120.

[3] S. Park, Y. Shao, J. Liu, Y. Wang, *Energy Environ. Sci.* **2012**, *5*, 9331.

[4] W. Li, D. Xiong, X. Gao, L. Liu, *Chem. Commun.* **2019**, *55*, 8744.

[5] B. R. Wygant, K. Kawashima, C. B. Mullins, *ACS Energy Lett.* **2018**, *3*, 2956.

[6] A. Majumdar, P. Dutta, A. Sikdar, H. Lee, D. Ghosh, S. Nath Jha, S. Tripathi, Y. Oh, U. Narayan Maiti, A. Majumdar, P. Dutta, A. Sikdar, U. N. Maiti, H. Lee, Y. Oh, D. Ghosh, S. N. Jha, S. Tripathi, *Small* **2022**, *18*, 2200622.

[7] X. Xu, F. Song, X. Hu, *Nat. Commun. 2016 71* **2016**, *7*, 12324.

[8] S. Chu, W. Chen, G. Chen, J. Huang, R. Zhang, C. Song, X. Wang, C. Li, K. (Ken) Ostrikov, *Appl. Catal. B Environ.* **2019**, *243*, 537.

[9] H. Zhang, X. Li, A. Hähnel, V. Naumann, C. Lin, S. Azimi, S. L. Schweizer, A. W. Maijenburg, R. B. Wehrspohn, *Adv. Funct. Mater.* **2018**, *28*, 1706847.

[10] X. Xiao, D. Huang, Y. Fu, M. Wen, X. Jiang, X. Lv, M. Li, L. Gao, S. Liu, M. Wang, C. Zhao, Y. Shen, *ACS Appl. Mater. Interfaces* **2018**, *10*, 4689.

[11] J. Yu, T. A. Le, N. Q. Tran, H. Lee, *Chem. - A Eur. J.* **2020**, *26*, 6423.

[12] J. Chen, H. Chen, T. Yu, R. Li, Y. Wang, Z. Shao, S. Song, *Recent Advances in the Understanding of the Surface Reconstruction of Oxygen Evolution Electrocatalysts and Materials Development*, Vol. 4, Springer Singapore, **2021**.

[13] H. Jiang, Q. He, X. Li, X. Su, Y. Zhang, S. Chen, S. Zhang, G. Zhang, J. Jiang, Y. Luo, P. M. Ajayan, L. Song, *Adv. Mater.* **2019**, *31*, 1805127.

[14] S. Niu, W.-J. Jiang, T. Tang, L.-P. Yuan, H. Luo, J.-S. Hu, S. Niu, W. Jiang, T. Tang, L. Yuan, H. Luo, J. Hu, *Adv. Funct. Mater.* **2019**, *29*, 1902180.

[15] T. Wu, E. Song, S. Zhang, M. Luo, C. Zhao, W. Zhao, J. Liu, F. Huang, *Adv. Mater.* **2022**, *34*, 2108505.

[16] P. Wang, J. Qi, C. Li, W. Li, T. Wang, C. Liang, *Electrochim. Acta* **2020**, *345*, 136247.

[17] Z. Cai, P. Wang, J. Zhang, A. Chen, J. Zhang, Y. Yan, X. Wang, *Adv. Mater.* **2022**, *34*, 2110696.

[18] Y. Liu, X. Luo, C. Zhou, S. Du, D. Zhen, B. Chen, J. Li, Q. Wu, Y. Iru, D. Chen, *Appl. Catal. B Environ.* **2020**, *260*, 118197.

[19] Y. Fang, Y. Xue, L. Hui, H. Yu, Y. Liu, C. Xing, F. Lu, F. He, H. Liu, Y. Li, *Nano Energy* **2019**, *59*, 591.

[20] P. Zhai, Y. Zhang, Y. Wu, J. Gao, B. Zhang, S. Cao, Y. Zhang, Z. Li, L. Sun, J. Hou, *Nat. Commun.* **2020**, *11*, 5462.

[21] J. Yuan, X. Cheng, H. Wang, C. Lei, S. Pardiwala, B. Yang, Z. Li, Q. Zhang, L. Lei, S.

Wang, Y. Hou, *Nano-Micro Lett.* **2020**, *12*, 104.

[22] Y. Tan, X. Xu, Q. Li, X. Chen, Q. Che, Y. Chen, Y. Long, *J. Colloid Interface Sci.* **2021**, *594*, 575.

[23] X. Mao, Y. Liu, Z. Chen, Y. Fan, P. Shen, *Chem. Eng. J.* **2022**, *427*, 130742.

[24] G. He, M. Yan, H. Gong, H. Fei, S. Wang, *Int. J. Extrem. Manuf.* **2022**, *4*, 032003.

[25] Y. Liu, Y. Zhang, Y. Liu, J. Zhu, Z. Ge, Z. Li, Y. Chen, *Carbon N. Y.* **2021**, *173*, 809.

[26] O. K. Park, N. H. Kim, J. H. Lee, *Carbon N. Y.* **2022**, *187*, 330.

[27] F. Meng, H. Wang, F. Huang, Y. Guo, Z. Wang, D. Hui, Z. Zhou, *Compos. Part B Eng.* **2018**, *137*, 260.

[28] C. Z. Yuan, Z. T. Sun, Y. F. Jiang, Z. K. Yang, N. Jiang, Z. W. Zhao, U. Y. Qazi, W. H. Zhang, A. W. Xu, *Small* **2017**, *13*, 1604161.

[29] Z. Ran, C. Shu, Z. Hou, L. Cao, R. Liang, J. Li, P. Hei, T. Yang, J. Long, *J. Power Sources* **2020**, *468*, 228308.

[30] H. Shi, Q. Yu, G. Liu, X. Hu, *Int. J. Hydrogen Energy* **2021**, *46*, 17097.

[31] Z. Zou, X. Wang, J. Huang, Z. Wu, F. Gao, *J. Mater. Chem. A* **2019**, *7*, 2233.

[32] M. Wang, L. Zhang, J. Pan, M. Huang, H. Zhu, **2021**, *14*, 4740.

[33] Z. Wu, Z. Zou, J. Huang, F. Gao, *J. Catal.* **2018**, *358*, 243.

[34] F. Zhang, Y. Pei, Y. Ge, H. Chu, S. Craig, P. Dong, J. Cao, P. M. Ajayan, M. Ye, J. Shen, *Adv. Mater. Interfaces* **2018**, *5*, 1701507.

[35] Y. Pan, Y. Liu, J. Zhao, K. Yang, J. Liang, D. Liu, W. Hu, D. Liu, Y. Liu, C. Liu, *J. Mater. Chem. A* **2014**, *3*, 1656.

[36] Y. J. Tang, Y. Zou, D. Zhu, *J. Mater. Chem. A* **2022**, *10*, 12438.

[37] F. Wu, X. Guo, G. Hao, Y. Hu, W. Jiang, F. Wu, X. Guo, G. Hao, Y. Hu, W. Jiang, *Adv. Mater. Interfaces* **2019**, *6*, 1900788.

[38] Z. Jing, Q. Zhao, D. Zheng, L. Sun, J. Geng, Q. Zhou, J. Lin, *J. Mater. Chem. A* **2020**, *8*, 20323.

[39] J. Jiang, F. Sun, S. Zhou, W. Hu, H. Zhang, J. Dong, Z. Jiang, J. Zhao, J. Li, W. Yan, M. Wang, *Nat. Commun. 2018 91* **2018**, *9*, 2885.

[40] Q. Wu, S. Wang, J. Guo, X. Feng, H. Li, S. Lv, Y. Zhou, Z. Chen, **2022**, *15*, 1901.

[41] J. Chen, G. Zhao, Y. Chen, K. Rui, H. Mao, S. X. Dou, W. Sun, *Chem. – A Eur. J.* **2019**, *25*, 280.

[42] J. Zhang, H. Yu, J. Yang, X. Zhu, M. Hu, J. Yang, *J. Alloys Compd.* **2022**, *924*, 166613.

[43] B. Fei, Z. Chen, J. Liu, H. Xu, X. Yan, H. Qing, M. Chen, R. Wu, B. Fei, Z. Chen, J. Liu, H. Xu, X. Yan, H. Qing, M. Chen, R. Wu, *Adv. Energy Mater.* **2020**, *10*, 2001963.

[44] C. Lan, H. Xie, Y. Wu, B. Chen, T. Liu, *Energy and Fuels* **2022**, *36*, 2910.

[45] X. Zhang, Z. Song, Q. Yan, W. Cong, L. Yang, K. Zhu, K. Ye, J. Yan, D. Cao, G. Wang, *J. Power Sources* **2021**, *515*, 230627.

[46] G. Deng, J. Zhao, H. S. Hu, X. Y. Wang, M. Zhu, Y. Y. Feng, *Int. J. Hydrogen Energy* **2021**, *46*, 37333.

[47] W. Yang, Q. Zhang, S. S. Siwal, Y. Hua, C. Xu, *Electrochim. Acta* **2020**, *361*, 137038.

[48] Z. Wu, J. Yang, W. Shao, M. Cheng, X. Luo, M. Zhou, S. Li, T. Ma, C. Cheng, C. Zhao, *Adv. Fiber Mater.* **2022**, *4*, 774.

[49] T. X. Nguyen, Y.-H. Su, C.-C. Lin, J.-M. Ting, T. X. Nguyen, Y.-H. Su, C.-C. Lin, J.-M. Ting, *Adv. Funct. Mater.* **2021**, *31*, 2106229.

[50] X. Tong, Y. Li, N. Pang, Y. Qu, C. Yan, D. Xiong, S. Xu, L. Wang, P. K. Chu, *Chem. Eng. J.* **2021**, *425*, 130455.

[51] J. Chen, Y. Li, G. Sheng, L. Xu, H. Ye, X. Z. Fu, R. Sun, C. P. Wong, *ChemCatChem* **2018**, *10*, 2248.

[52] L. Li, C. Sun, B. Shang, Q. Li, J. Lei, N. Li, F. Pan, *J. Mater. Chem. A* **2019**, *7*, 18003.

[53] S. Lee, L. Bai, X. Hu, *Angew. Chemie* **2020**, *132*, 8149.

[54] J. R. Swierk, S. Klaus, L. Trotochaud, A. T. Bell, T. D. Tilley, *J. Phys. Chem. C* **2015**, *119*, 19022.

[55] M. W. Louie, A. T. Bell, *J. Am. Chem. Soc.* **2013**, *135*, 12329.

[56] D. Friebel, M. W. Louie, M. Bajdich, K. E. Sanwald, Y. Cai, A. M. Wise, M. J. Cheng, D. Sokaras, T. C. Weng, R. Alonso-Mori, R. C. Davis, J. R. Bargar, J. K. Nørskov, A. Nilsson, A. T. Bell, *J. Am. Chem. Soc.* **2015**, *137*, 1305.

[57] J. Y. C. Chen, L. Dang, H. Liang, W. Bi, J. B. Gerken, S. Jin, E. E. Alp, S. S. Stahl, *J. Am. Chem. Soc.* **2015**, *137*, 15090.

[58] L. Trotochaud, S. L. Young, J. K. Ranney, S. W. Boettcher, *J. Am. Chem. Soc.* **2014**, *136*, 6744.

[59] L. L. Feng, G. Yu, Y. Wu, G. D. Li, H. Li, Y. Sun, T. Asefa, W. Chen, X. Zou, *J. Am. Chem. Soc.* **2015**, *137*, 14023.

[60] P. Liu, B. Chen, C. Liang, W. Yao, Y. Cui, S. Hu, P. Zou, H. Zhang, H. Jin Fan, C. Yang, P. Liu, C. Liang, W. Yao, Y. Cui, S. Hu, P. Zou, C. Yang, B. Chen, H. Zhang, H. Zhang Hong Kong Branch, H. J. Fan, *Adv. Mater.* **2021**, *33*, 2007377.

Chapter 6

Summary and Outlook

Chapter 6

Summary and Outlook

6.1 Summary and highlights of the thesis

The brief summary and the main conclusions of this thesis work are highlighted in this chapter. This thesis has carried out development of efficient heterostructures and single-atom catalysts (SACs) to address the main challenges in the field of water electrolysis to achieve a green hydrogen-based economy. The goal of this thesis was to design catalysts based on the practical applicability of these materials and methodologies, in addition to satisfying the demand for high-performance electrocatalysts. Simple catalyst development process, new design strategies and in-depth understanding of the active catalyst material are the important criteria for development of an efficient electrocatalyst whereas requirement of low overpotential, low Tafel slope, high current density, long-term stability is the practical consideration for development of efficient electrocatalysts which have been adapted in this thesis. Here, six major findings of this thesis have been organized together, i) Development of an electronically tuned $MoSe_2$@$NiCo_2Se_4$ heterostructure via simple atomic rearrangement of mixed metal oxide/hydroxide nanosheet; ii) Stabilization of iridium SAC on dynamically reconstructed $MoSe_2$@$NiCo_2Se_4$ support; iii) Strong electronic tuning between amorphous shell a-MoS_x and crystalline core MoWO to construct a core-shell heterostructure via rapid microwave induced graphene filament involved transient heating process (GFTH); iv) Generic energy-efficient recrystallization process to develop metal sulfides/selenides/phosphides from metal hydroxides; v) Achievement of low overpotential, low Tafel slope, high current density and long-term stability from developed electrocatalysts; vi) Density function theory (DFT) calculation-based theoretical understanding for the improvement in electrocatalytic efficiency caused by heterostructure adaptability and SAC.

i) Development of an electronically tuned $MoSe_2$@$NiCo_2Se_4$ heterostructure via simple atomic rearrangement of mixed metal oxide/hydroxide nanosheet

To address the challenge of sequential deposition of components in a heterostructure, in chapter 2 we have adapted selenization induced atomic rearrangement of mixed metal oxide/hydroxide nanosheets (MoO_3/Ni-$Co(OH)_2$). Due to variation in atomic radius, at high temperature molybdenum come out of the structure and form a heterostructure of $MoSe_2$ and $NiCo_2Se_4$. Our result suggest that selenization of MoO_3/Ni-$Co(OH)_2$

nanosheets result in growth of longitudinal $MoSe_2$ nanosheet arrays perpendicular to the $NiCo_2Se_4$ nanosheet substrate. The interlayer distance of $MoSe_2$ in heterostructure is higher compared to its bulk form. With its vertical orientation and interlayer expanded structure, the $MoSe_2$ layer structure ensures a large surface area with accessible catalytic edges. In addition, as opposed to standard $MoSe_2$ structures that are parallel to the current collector, vertically oriented arrangements allow electrons to directly reach the catalytic edges of $MoSe_2$ from the base $NiCo_2Se_4$ and thus preventing a high energy loss. Therefore, due to its structural advantages, it is expected to show good catalytic activity towards hydrogen evolution reaction (HER).

ii) Stabilization of iridium SAC on dynamically reconstructed $MoSe_2$@$NiCo_2Se_4$ support

In chapter 3, we have photochemically incorporated iridium single atoms over the surface of $MoSe_2$@$NiCo_2Se_4$ heterostructure. From several characterization single atomic nature was confirmed and EXAFS result suggested that this SAC-Ir is coordinated with four nearest neighbour oxygen (O) atoms, out of which three can be offered by oxygen ligand of oxyhydroxide/hydroxide of Co (Ni) support and the fourth one can be –OH ligand over Ir-atom. These oxygen rich ligands for the stabilization of SAC-Ir on the heterostructure is provided by the partial surface reconstruction of the support in aqueous KOH medium during the deposition. Additionally, during the OER process, the surface of transition metal-based sulfide, selenide, and phosphides undergo reconstruction by simultaneously leaching certain lattice ions or by producing highly active amorphous hydroxide/(oxy)hydroxide phases on the surface. Therefore, extensive post-OER characterizations like XPS, XANES, EXAFS and TEM has been done which reveal extensive in-situ surface reconstruction during OER to dissolute molybdenum from the heterostructure and conversion of selenide base into Ni,Co-hydroxide/oxyhydroxide (NiCoOOH). EXAFS fitting suggests, iridium not only coordinated to four O atoms of oxygen ligands similar to Ir-$MoSe_2$@$NiCo_2Se_4$ but also interacting with Ni atoms thus stabilizing over the reconstructed surface by making an Ir-Ni interaction. This Ir-SAC incorporated reconstructed structure has shown an excellent performance for OER process.

iii) Strong electronic tuning between amorphous shell a-MoS_x and crystalline core MoWO to construct a core-shell heterostructure via rapid microwave induced graphene filament involved transient heating process (GFTH)

Core-shell nanowire heterostructure is a good platform for synergistically enhancing the catalytic activity of the shell through electronic coupling. However, all reports on molybdenum/tungsten sulphide have only dealt with their crystalline form, not their amorphous phase. Therefore, in chapter 4, we have presented a microwave induced novel method for growing an ultrathin a-MoS_x shell above crystalline molybdenum tungsten oxide (MoWO) nanowire core in a matter of seconds. Partially reduced graphene oxide was used as a filament for this purpose as it can efficiently absorb microwaves and can decompose sulfur source at a very high temperature in a few seconds. After a short while, when the microwave was turned off, the graphene filament cooled down really quickly. Because the reacting surface atoms do not have enough time to crystallize during this transient heating and cooling process, crystalline/amorphous core-shell structure is produced. Atomic interfacing of crystalline core and amorphous shell structure possesses strong electronic interaction between the components as observed from different investigations. Increasing the reaction time can also convert the oxides into crystalline sulfides. Thus, this kind of controllability can assist in the development of highly catalytic active catalysts.

iv) Generic energy-efficient recrystallization process to develop metal sulfides/selenides/phosphides from metal hydroxides

Conventional methods for the development of metal chalcogenides/ phosphides are non-energy efficient, time consuming and involve complex multi-step processing. Therefore, in chapter 5, we have designed a microwave induced universal, low-cost processing for rapid recrystallization of metal hydroxide structure to in-situ generated metal chalcogenides and phosphides. Rapid heating and cooling characteristic of graphene was used here for two reasons, firstly to decompose the chalcogen and phosphorous sources in seconds scale and then secondly for the rapid phase evolution process. Thus, just room temperature dipping of commercial nickel foam in iron nitrate and subsequent gas phase chalcogenization/ phosphidation in a domestic microwave oven for only few seconds led to development of unique phases like iron doped Ni_3S_2/NiS, Ni_3Se_2/$NiSe_2$, and $Ni_{12}P_5$/Ni_2P. This type of biphasic systems can provide high activity in catalysis process.

v) Achievement of low overpotential, low Tafel slope, high current density and long-term stability from developed electrocatalysts:

In chapter 2, developed sheet-on-sheet heterostructure shows excellent HER performance, requiring an overpotential of 89 mV to get a current density 10 mA cm^{-2}, and a Tafel slope of

65 mV dec^{-1}, which is substantially lower than the overpotential required for MoO_3@Ni-$Co(OH)_2$ (189 mV). Additionally, $MoSe_2$@$NiCo_2Se_4$ achieves a very high current density of 100 and 500 mA cm^{-2} with just 156 and 227 mV, respectively, demonstrating remarkable HER catalytic activity. The origin of high HER activity is correlated to low charge transfer resistance, high specific activity calculated by ECSA normalised current density and structural advantages like layer expansion of $MoSe_2$ sheets and its vertical orientation. Importantly, the as-developed $MoSe_2$@$NiCo_2Se_4$ heterostructure displays excellent operational stability for long duration, maintaining 50 mA cm^{-2} current density throughout the 24 h operation.

In chapter 3, Ir-$MoSe_2$@$NiCo_2Se_4$ structure on electrochemical surface reconstruction displays outstanding OER activity, requiring only 200 mV and 313 mV overpotentials for 10 mA cm^{-2} and 500 mA cm^{-2} current densities respectively which is significantly lower than $MoSe_2$@$NiCo_2Se_4$ (255 and 411 mV), MoO_3@Ni-$Co(OH)_2$ (280 and 450 mV) and commercial IrO_2 (318 and 466 mV). In addition, Ir-$MoSe_2$@$NiCo_2Se_4$ has the lowest Tafel slope (42 mV dec^{-1}) of all the aforementioned catalysts, including commercial IrO_2. This higher intrinsic activity can be associated with low charge transfer resistance, high activity of linked SAC- Ir, and promotional effect coming from its base which gets activated in-situ to generate Ni,Co-(oxy)hydroxide. This catalyst has also displayed an excellent stability confirmed from chronoamperometric test and multi-step chronoamperometric test at high current density. Furthermore, $MoSe_2$@$NiCo_2Se_4$ as the cathode and Ir-NiCoOOH as the anode exhibit extremely steady overall water splitting and just 1.51 V of cell voltage is needed to achieve a current density of 10 mA cm^{-2}, which is among the best in this sector, including SAC-based systems.

In chapter 4, a-MoS_x@MoWO shows highly stable and excellent HER activity requiring an overpotential of 136 mV to get a current density of 10 mA cm^{-2} in 0.5 M H_2SO_4 electrolyte. This is significantly more active than their oxide (356 mV) and fully converted crystalline sulphide forms (163 mV). Additionally, the catalysts exhibit great long-term operating stability and good HER activity in neutral and alkaline electrolytes as well, which is significant for using it in a universal pH condition. Better HER performance of a-MoS_x@MoWO is associated with large catalytic active sites of amorphous a-MoS_x shell and beneficial charge transfer kinetics in the core-shell structure as observed from lowest R_{ct} value.

In chapter 5, all the phase evolved samples i.e., iron doped Ni_3S_2/NiS, Ni_3Se_2/$NiSe_2$, and $Ni_{12}P_5$/Ni_2P display outstanding OER performance in alkaline solution requiring only 289, 301 and 311 mV overpotential to achieve high current density of 500 mA cm^{-2}. These values are significantly lower than state-of-the-art electrocatalysts and most of the earth-abundant transition metal-based catalysts. The origin of high catalytic activity can be correlated to in-situ surface reconstruction of NiS phase to highly active NiOOH phase to form an in-plane heterostructure of Fe-Ni_3S_2/NiOOH.

vi) Density function theory (DFT) calculation-based theoretical understanding of the improvement in electrocatalytic efficiency caused by heterostructure adaptability and SAC

In chapter 2, it was found that: i) both of the heterostructure's components, $MoSe_2$ and $NiCo_2Se_4$, contribute to HER activity; ii) the metallic nature of base $NiCo_2Se_4$ provides an electronic highway for charge carriers to reach the $MoSe_2$ edge site; and iii) layer expansion and edge-oriented structure dramatically decrease the adsorption energy barrier for hydrogen, benefiting HER activity. The combination of the aforementioned findings result in significant HER activity.

In chapter 3, the importance of single atom Ir decoration has been shown by calculating Gibbs's free energy for different OER intermediates of surface reconstructed Ir-NiCoOOH and bulk Ir surface which suggesting lower value for Ir-NiCoOOH. Additionally, SAC-Ir increases activity of Ir-NiCoOOH by reducing the Gibb's free energy for the rate-determining step (O*-OOH*) of the SAC-Ir site and widening the electronic density of states around the Fermi level of NiCoOOH.

In chapter 4, from DFT analysis we found that only one sulfur site is active for amorphous a-MoS_x. However, after core-shell a-MoS_x@MoWO heterostructure formation, multiple sulfur sites (bridging & terminal S) of amorphous a-MoS_x get activated by significantly lowering hydrogen adsorption free energy (ΔG_{H*}) via charge transfer at the interface of MoWO nanowire core and a-MoS_x shell. In addition, density of state has been substantially increased near Fermi level after core-shell structure formation which helps in optimum hydrogen binding to the catalyst surface thus reducing the overpotential for HER.

6.2 Future Scope

The focus of this thesis is to develop efficient heterostructures and incorporation of single atom catalysts on a proper support with in-depth understanding of the origin of high catalytic activity. However, there is still a great deal of room to extend this present work in different range of applications along with electrolysis of water.

- Although we have designed an amorphous-crystalline core-shell heterostructure for molybdenum and tungsten-based sulfides. This surface amorphization strategy can also be extended for other materials. At present, there are huge number of catalysts being used for different catalysis processes. Now generating an amorphous-crystalline heterostructure for other catalysis processes is expected to give synergistic efficiency. In addition, it is very important to know the theoretical background for the origin of high catalytic activity of the material. As to date very poor theoretical understanding has been provided for amorphous structures and amorphous based heterostructures. Here, we have explored the synergistic effect of amorphous-crystalline core-shell heterostructure in hydrogen evolution through theoretical understanding. So, our experimental process can be used to generate other amorphous-crystalline heterostructures and the theoretical understanding can lay the platform to understand the promotional effects of the components of a heterostructure in catalysis. So, it can give the guideline for the development of further catalysts.
- For the stabilization of single atoms on the surface of metal chalcogenides, there are two competitive processes: stabilization of single atoms and surface reconstruction of metal chalcogenides in oxidative OER condition. Therefore, it is highly important to know if single atoms are stable after catalysis process. Here, we have shown how iridium single atoms are being stabilized with the help of oxygen ligands of in-situ reconstructed metal sulfide surface. However, how these single atoms can be stabilized with other different ligands is still unknown. If the same strategy that we have taken to stabilize Ir SACs can be extended to other metal chalcogenides/phosphide surfaces or to stabilize other noble metals (where different interaction between metal and support is expected) are also unknown. To answer these questions, it is highly important to perform characterizations of the catalyst before and after the catalysis process. Further, operando synchrotron spectroscopy can also be used to understand the dynamic behaviour of the catalyst during the whole catalysis process. In addition, the unique photochemical method that we have adapted here can be extended for other noble metals also for SACs development. Also, the

same Ir SAC catalyst that we have grown for OER can also be directly used in other applications like oxygen reduction reaction, CO_2 reduction and metal-air batteries.

- Rather than depositing different components sequentially for the development of heterostructure, the in-situ dealloying process for phase conversion that we have used can be extended to synthesize other heterostructures on demand. The design principle should be directed by the final application perspective. Here, our motivation was to develop an efficient HER catalyst, so we started with a material having molybdenum content. However, for other applications, the starting material can be varied to get optimum performance. Though we have only synthesized heterostructures based on selenide structure, it is expected to synthesize other chalcogenides and phosphides through this process. We have also provided theoretical calculation that shows high HER catalytic activity with the regulation of layer expansion of molybdenum selenides. However, it will be very interesting to know if the same mechanism is also true for other sulfide, phosphides-based materials.
- In case of microwave induced recrystallization strategy, we have observed the generation of in-plane heterostructures of sulfide/ selenide/ phosphide biphasic systems. This process can also be extended to develop other biphasic materials as well. In addition, this strategy is very energy and time efficient and can be used as a scalable process. Dedicated research is highly required to tally the cost of material synthesis and to make it a scalable one compared to the conventional material synthesis process for establishing this as one of the best catalysts.
- The majority of the globe is covered by the ocean, which is generally more accessible than fresh water in some regions. The direct splitting of saltwater to produce hydrogen is therefore more advantageous from a practical and financial standpoint. Although the efficiency of the existing electrocatalyst for water electrolysis in both alkaline and acidic electrolyte is good, the more useful seawater electrolysis is still inefficient. This is a result of seawater's low conductivity as an electrolyte, ionic toxicity, and high corrosivity. On the other hand, chlorine evolution reaction frequently takes place at the anode during seawater electrolysis, which significantly lowers the process's overall efficiency of seawater splitting. In order to further develop electrocatalysts for sea water splitting, high selectivity, high conductivity, and high activity with new design strategies are highly required.
- Bifunctional electrocatalysts for water splitting can also be applied in other applications like metal-air batteries, fuel cells. However, their actual usage in those applications is

severely constrained by the lack of efficient bifunctional electrocatalysts. Therefore, it is highly desirable to develop bifunctional catalysts with high activity, selectivity, and stability for various applications.

Permissions and Attributions

- The content of chapters 2 and 3 are based on the published work
  Small, 2022, 18, 2200622, in collaboration with Pronoy Dutta, Anirban Sikdar, Heehyeon Lee, Debasis Ghosh, Sambhu Nath Jha, Shilpa Tripathi, Yongtak Oh and Uday Narayan Maiti.

- The content of chapter 4 is based on the published work
  Catalysis Today, https://doi.org/10.1016/j.cattod.2022.11.023, in collaboration with Golam Masud Karim, Pronoy Dutta, Heehyeon Lee, Sujit Kumar Deb, Anirban Sikdar, Yongtak Oh and Uday Narayan Maiti.

- The content of chapter 5 is based on the published work
  Applied Surface Science, https://doi.org/10.1016/j.apsusc.2023.156622, in collaboration with Pronoy Dutta, Yunho Kang, Golam Masud Karim, Sujit Kumar Deb, Sang Ouk Kim and Uday Narayan Maiti.